

2016

Surface analysis of model systems: from a metal-graphite interface to an intermetallic catalyst

Emma J. Kwolek
Iowa State University

Follow this and additional works at: <https://lib.dr.iastate.edu/etd>

 Part of the [Inorganic Chemistry Commons](#)

Recommended Citation

Kwolek, Emma J., "Surface analysis of model systems: from a metal-graphite interface to an intermetallic catalyst" (2016). *Graduate Theses and Dissertations*. 15030.
<https://lib.dr.iastate.edu/etd/15030>

This Dissertation is brought to you for free and open access by the Iowa State University Capstones, Theses and Dissertations at Iowa State University Digital Repository. It has been accepted for inclusion in Graduate Theses and Dissertations by an authorized administrator of Iowa State University Digital Repository. For more information, please contact digirep@iastate.edu.

Surface analysis of model systems: From a metal-graphite interface to an intermetallic catalyst

by

Emma J. Kwolek

A dissertation submitted to the graduate faculty
in partial fulfillment of the requirements for the degree of

DOCTOR OF PHILOSOPHY

Major: Inorganic Chemistry

Program of Study Committee:
Patricia A. Thiel, Major Professor
James W. Evans
Gordon J. Miller
Michael C. Tringides
Javier Vela-Becerra

Iowa State University

Ames, Iowa

2016

Copyright © Emma J. Kwolek, 2016. All rights reserved.

Dedicated to my parents.

TABLE OF CONTENTS

	Page
ABSTRACT.....	viii
CHAPTER 1. GENERAL INTRODUCTION	1
1. Metals on Graphite.....	1
2. Gold Catalysts and Beyond.....	3
3. Instrumentation	5
4. Data Processing and Analysis.....	7
5. Dissertation Organization	8
Figures	9
References.....	11
CHAPTER 2. ADSORPTION OF DYSPROSIUM ON THE GRAPHITE (0001)	
SURFACE: NUCLEATION AND GROWTH AT 300 K	17
Abstract.....	17
1. Introduction.....	18
2. Description of Methods.....	19
2.1. Experimental details.....	19
2.2. Computational details: DFT.....	20
3. Computational Results: Adsorption Energy and Diffusion Barrier	21
4. Experimental Results: Island Characteristics.....	23
4.1. Island shapes	23
4.2. Island densities and size distributions.....	25
5. Theoretical Analysis of Island Formation for Deposition of Dy/Graphite	25
5.1. Island densities.....	25
5.2. Island size distribution	27
5.3. Layer distributions	28
6. Discussion.....	31
7. Conclusions.....	34

Acknowledgements.....	34
Figures.....	35
Appendix 1. Additional Notes on Layer Occupations.....	43
Appendix 2. Ion Damage.....	43
Appendix 3. Anneals after Deposition.....	50
Appendix 4. Oxygen Exposure after Deposition.....	58
References.....	61
CHAPTER 3. THE (111) SURFACE OF NAAU ₂ : STRUCTURE, COMPOSITION, AND STABILITY	64
Abstract.....	64
1. Introduction.....	65
2. Experimental Details.....	67
3. Experimental Results	68
3.1. Composition from XPS and XRD.....	68
3.2. Surface characterization <i>before</i> Na depletion	70
3.3. Surface characterization <i>after</i> Na depletion.....	71
3.4. Evidence regarding mechanisms of Na depletion.....	72
4. Discussion.....	73
5. Conclusion	76
Acknowledgements.....	76
Figures.....	77
Appendix. Surface Morphology.....	85
References.....	107
CHAPTER 4. INTERACTION OF OXYGEN WITH THE (111) SURFACE OF NAAU ₂	109
Abstract.....	109
1. Introduction.....	110
2. Experimental Details.....	112
3. Experimental Results	114

3.1. Composition of the initial surface.....	114
3.2. Oxygen exposure at 300 K.....	117
3.3. Effects of heating to temperatures below and above the Na desorption onset	119
3.4. Oxygen adsorption at 425 K.....	121
3.5. Oxygen adsorption on Na-depleted surfaces at 300 K.....	122
4. Discussion.....	123
5. Conclusions.....	125
Acknowledgements.....	126
Figures.....	127
Appendix 1. Supplementary Information.....	140
Appendix 2. Experimental Parameters.....	145
Appendix 3. Oxygen Adsorbed on NaAu ₂ (111).....	145
References.....	154

CHAPTER 5. INTERACTION OF WATER, CARBON MONOXIDE, AND CARBON

DIOXIDE WITH THE (111) SURFACE OF NAAU ₂	157
Abstract.....	157
1. Introduction.....	158
2. Experimental Details.....	160
3. Experimental Results.....	162
3.1. Cleaned surface composition.....	162
3.2. Water exposure at 300 K.....	163
3.3. Effects of heating to temperatures below and above the Na desorption onset	165
3.4. Carbon monoxide exposures at 300 K and 500 K.....	166
3.5. Carbon dioxide exposures at 300 K.....	167
4. Discussion.....	168
4.1. Water.....	169
4.2. Carbon monoxide.....	171
4.3. Carbon dioxide.....	171
5. Conclusions.....	172
Acknowledgements.....	173

Figures.....	174
Appendix. Experimental Parameters	182
References.....	182

CHAPTER 6. PRINCIPLES OF ANALYZING X-RAY PHOTOELECTRON

SPECTROSCOPY DATA	186
Abstract.....	186
1. Introduction.....	186
2. Spectrum Acquisition.....	187
2.1. X-ray photoelectron spectroscopy	187
2.2. X-ray sources	190
2.3. Auger electron spectroscopy.....	191
3. Spectrum Analysis	192
3.1. Scofield cross-sections.....	192
3.2. Inelastic mean free path	193
3.3. Chemical shifts.....	194
3.4. Errant peaks	195
3.4.1. Sample plate peaks.....	196
3.4.2. Satellite peaks	197
3.4.3. “Ghost” peaks	198
4. Example Analysis	200
4.1. Single peak.....	201
4.2. Convolutd peaks.....	202
4.3. Atomic composition.....	202
5. Conclusions.....	204
Acknowledgements.....	204
Figures.....	205
References.....	219

APPENDIX A. ADSORPTION OF AU AND PT ON THE GRAPHITE (0001)

SURFACE.....	221
--------------	-----

APPENDIX B. E-BEAM HEATER TEMPERATURE CALIBRATION.....	236
APPENDIX C. EXPERIMENTAL DATABASE	241
ACKNOWLEDGEMENTS.....	285

ABSTRACT

This thesis summarizes research completed on two different model systems. In the first system, we investigate the deposition of the elemental metal dysprosium on highly-oriented pyrolytic graphite (HOPG) and its resulting nucleation and growth. The goal of this research is to better understand the metal-carbon interactions that occur on HOPG and to apply those to an array of other carbon surfaces. This insight may prove beneficial to developing and using new materials for electronic applications, magnetic applications and catalysis.

In the second system, we investigate the intermetallic single crystal NaAu_2 . We conducted a characterization of the clean (111) surface along with a determination of the effects of gas exposures on the surface. No surfaces of bulk NaAu_2 have been previously characterized, although the closely related system of Na films on Au(111) has been investigated. NaAu_2 is an active catalyst for CO oxidation. To better understand the catalytic reaction occurring, we studied the NaAu_2 surface after exposure to $\text{O}_{2,g}$, CO_g , $\text{CO}_{2,g}$ and H_2O_g . The goal of this research is to find a possible alternative for supported gold catalysts by utilizing an Au-rich intermetallic compound and to determine how its catalytic reaction proceeds. This insight may be valuable in determining other catalytic alternatives as well as helping understand catalytic reactions that occur with other intermetallic compounds.

In order to characterize and examine these systems, we utilized several ultrahigh vacuum (UHV) techniques, including scanning tunneling microscopy (STM), X-ray photoelectron spectroscopy (XPS) and low-energy electron diffraction (LEED).

CHAPTER 1

GENERAL INTRODUCTION

This thesis work presents investigations on two different model systems. The first system examines the rare earth metal, dysprosium, and its nucleation and growth upon deposition onto graphite. The second system examines the intermetallic single crystal, NaAu_2 , characterizing the clean surface as well as analyzing what happens on the surface after various gas exposures.

1. Metals on Graphite

Natural and synthetic graphite has been used in various applications throughout industry for several hundred years, but it has only been in the last forty years that the scientific community has begun to study graphite in detail. Highly-oriented pyrolytic graphite (HOPG) is one of the most extensively studied forms of synthetic graphite. Today graphite is used in electrodes,¹⁻³ catalyst supports,⁴⁻⁷ batteries,⁸⁻¹¹ analytical sensors,¹² x-ray diffraction,^{13,14} and lubricants.^{15,16} HOPG is an ideal material to use since it is fairly inexpensive and inert. The conductivity within each layer of HOPG is close to that of noble metals,¹⁷ which makes it a prospective candidate to replace current metals used in industry that are rare, expensive, and potentially toxic to the environment.

Studying the interaction of metals with graphite can give insight into several research topics involving carbon materials. It is known that some metals, alkali, alkali earths and lanthanides, intercalate (move from the surface to subsurface layers) in carbon materials.¹⁸⁻²² Some metals also form nanowires/nanowiskers after deposition onto silicon and/or carbon

based substrates at elevated temperatures.²³⁻²⁶ Therefore, developing an understanding of how those specific metals interact with thick carbon films can be beneficial. Information can be gathered on how metals bind to the graphite surface and how this can affect electronic and magnetic properties of both the graphite and the metal. There is potential for this research to broaden the understanding of metal-carbon interactions on an array of carbon surfaces.

Scanning tunneling microscopy (STM) studies of metals on HOPG have become more common in the ultra-high vacuum (UHV) community within the last twenty five years. Noble metals (e.g. silver, gold, platinum) are the most common group that have been investigated on HOPG, due to their resistance to oxidation and corrosion in air as well as their use in catalysis. Researchers have found that the metals tend to form small 2D and 3D clusters on the surface,²⁷⁻²⁹ although gold and platinum can also form dendritic structures.^{27,29} Figure 1 illustrates these features. The noble metals preferentially nucleate at step edges²⁸⁻³¹ and defect sites,^{29,31,32} and only nucleate on terraces at higher coverages.²⁸⁻³¹ This preferential nucleation is due to the weak metal-HOPG bonding interaction, especially on flat terraces, and the low sticking coefficient of the metal.^{27,28,31,33} Researchers have found that this weak interaction causes difficulty in imaging the surface because as the STM tip rasters across the surface it can cause sintering and shearing of the metal islands.^{27,31,34} Figure 2 illustrates these scanning issues. Adjusting the tip tunneling parameters helps to alleviate this issue.

HOPG with intercalated rare earth metals is of interest due to the resulting 2D structure as well as the anisotropic electronic properties, which have potential for new applications in electronic materials development,^{17,35,36} spintronics,³⁷ and magnetic materials.^{38,39} The 2D structures vary due to the staging of the metal between the graphene layers with the intercalated metal layers separated by one to three graphene layers.^{17,36}

Conductivity within each graphene layer and each intercalated metal layer is still present, but the addition of the intercalated metal promotes conductivity between the graphene sheets as electrons move between the metal atoms and the π bands of HOPG.^{35,40} These changes in conductivity may prove useful for industry, especially for electronic applications.

The main focus of this experimental research was STM studies on the nucleation and growth of the rare earth metal dysprosium (Dy) on HOPG. Since little was known about how Dy may behave on HOPG, the results of this study provided a guide for continued research into Dy on HOPG at elevated temperatures and on other carbon surfaces. In addition, other rare earth metals may be investigated to provide further insight on metal-graphite interactions as well as a comparison with Dy on HOPG. Continuing insight into interactions between metals and carbon surfaces can be beneficial to the materials industry, as metals on surfaces continue to be utilized for electronic applications, catalysis and future uses yet to be discovered.

2. Gold Catalysts and Beyond

Single crystal gold surfaces have long been considered poor catalysts as their inert surfaces do not readily absorb molecules. However, in 1987, Haruta and co-workers discovered that supported gold nanoparticles were catalytically active at low temperatures.⁴¹ Metal oxides are the typical support for gold nanoparticles and common ones include TiO_2 , Al_2O_3 and SiO_2 .⁴²⁻⁴⁶ Since then, researchers have found that supported gold nanoparticles are catalytically active for many reactions including CO oxidation,⁴⁷⁻⁴⁹ propene oxidation,⁴² NO reduction,⁴³ hydrogenation of acetylene, butadiene and CO_2 ,^{44,45} hydrochlorination of ethyne

and acetylene,^{46,50} and decomposition of Freon-12 (CCl_2F_2) and methyl chloride.⁵¹

Researchers have also discovered catalytic activity in nanoporous gold solids and foams.⁵²⁻⁵⁵

Scientists believe that the small size of the gold nanoparticles, typically 2 – 10 nm in diameter, is the main factor that promotes catalysis. Answering the question of why this is the case has not been as simple and researchers have collectively hypothesized three possible explanations. The first theory involves the interaction between the underlying metal oxide support and the gold nanoparticles. Here, the metal oxide influences the electronic state of the gold nanoparticle via charge transfer between the two which promotes catalytic activity.⁵⁶⁻⁵⁸ The second, and most likely theory, involves the coordination number (or number of nearest neighbors) of the gold atoms in the nanoparticle. A nanoparticle typically has a coordination number of 3-4, while a close packed surface (e.g. an fcc or hcp single crystal) has a surface coordination number of 7-9. A low coordination number leads to higher unsaturation in the gold atoms and thus more binding sites for catalytic activity.^{52,59,60} The final theory involves the quantum effects due to the size of the nanoparticle. It is speculated that the electronic band structure is altered from the bulk band structure thus allowing a higher reactivity.⁶¹⁻⁶³ Additional experimental work and theoretical calculation need to be conducted before a conclusion can be reached.

Alternatives to supported metal nanoparticles are becoming more desirable as they eliminate the need for the supports, allowing the catalysts to be more versatile. Intermetallic compounds are becoming increasingly popular in this realm of catalysis as possible replacements for these supported metal nanoparticle catalysts. For instance, quasicrystalline $\text{Ti}_{70}\text{Zr}_{10}\text{Co}_{20}$ is an active catalyst for oxidation of cyclohexane and Pd-Ga compounds show reactivity for selective hydrogenation of alkynes.^{64,65} Intermetallic compounds are comprised

of two or more metallic elements that have an ordered crystal structure and a fixed stoichiometry. Xiao and co-workers recently discovered that the single crystal intermetallic NaAu_2 is an active catalyst for low temperature CO oxidation.⁶⁶ Powdered NaAu_2 showed catalytic activity down to 30°C ($\sim 300\text{ K}$)⁶⁶ which is much lower than the temperature of 300°C ($\sim 575\text{ K}$) that Haruta and co-workers reported for unsupported Au powder.⁴¹ The intermetallic nature of the compound, specifically the sodium, plays a key role in increasing the catalytic activity. This result shows promise that Au-rich intermetallics may be a viable alternative to supported gold nanoparticles.

The main focus of this experimental research was to determine the morphology of the $\text{NaAu}_2(111)$ single crystal as well as conduct X-ray photoelectron spectroscopy (XPS) studies both before and after gas exposures (specifically reactant and product gases in CO oxidation). In addition, the techniques of low-energy electron diffraction (LEED) and STM were used to develop a better picture of the surface morphology. There have been no previous studies of bulk NaAu_2 characterization. However, Barth and co-workers studied Na films on Au(111). They found that upon heating the samples after deposition from 300 K to 600 K, Na and Au react to form films and multilayers of NaAu_2 which exhibit a (111) surface orientation.^{67,68} Studying the interactions between the Na, Au and gases can give insight into how the reaction proceeds and what role the intermetallic, especially sodium, plays in increasing the catalytic activity.

3. Instrumentation

Ultrahigh vacuum (UHV), at pressures typically between 10^{-10} and 10^{-11} mbar, is used to study surfaces because it allows us to control the sample's environment and remove

potential sources of contamination, which include oxygen and carbon. UHV is also required for electron based techniques used to study the surface.

Scanning tunneling microscopy (STM) is a nondestructive technique that provides a topographic image of a sample's surface. An atomically sharp metal tip is brought within 0.5 nm to 1 nm of the surface and electrons tunnel between the sample and the tip. When a bias voltage is applied, a net current flow occurs and is measured. The tip is rastered across the sample and records the measured current, which creates an electron density contour map of the surface. STM is generally used to image atomically flat surfaces and 2D structures on surfaces (i.e. islands and step-terraces).

X-ray photoelectron spectroscopy (XPS) provides both quantitative and characteristic information on sample composition and elemental chemical states. An X-ray source irradiates a sample surface which then emits characteristic core electrons that are detected and recorded. These recorded electrons produce an energy spectrum of intensity versus binding energy with peaks that correspond to the characteristic core electrons. From this spectrum, a user can determine which elements are present (via peak binding energy) as well as the surface composition (via integration of area under the peaks). Peak binding energies can also reveal the chemical state of an element. For example, a pure metal is typically at a lower binding energy than a metal oxide. A detailed description of XPS is given in Chapter 6.

Low-energy electron diffraction (LEED) provides a 2D structure, in reciprocal space, of the top ~1 nm (4 to 5 atomic layers) of a sample. Low-energy electrons (30 eV to 200 eV) are required because they have a short mean free path (which limits detection to the top ~1 nm) and wavelengths on the order of, or smaller than, atomic separations. An electron gun produces these low-energy electrons which bombard the sample surface, collide with atoms,

and elastically scatter. Those electrons which scatter back toward the gun are accelerated into a phosphor screen. The impact sites on the screen fluoresce and a pattern of spots is produced. This pattern represents a 2D structure in reciprocal space, which can be converted into real space and provide lattice parameters and crystal orientation of the surface. LEED is typically used for ordered crystals (e.g. a single crystal sample) because such samples have defined atom locations which produce a pattern with sharp bright spots and a low background.

4. Data Processing and Analysis

WSxM software was used to process and analyze all acquired STM images.⁶⁹ In many cases, the STM tip is not perpendicular to the sample while scanning a surface for several reasons, including sample tilt or scanner bow, causing the acquired image to have a slope. The two most common image processing procedures to correct these issues are plane and flatten. The plane feature, whether global (entire surface) or local (selected region), fits a plane to the image and subtracts this from the original image. This preserves the original height information as well. The flatten feature, considered a form of filtering, subtracts a function from each scan line. Different applications within the flatten feature can be used to preserve height information, dependent on the original image topography. Other image processing procedures utilized include the Fast Fourier Transform (FFT) filter to remove noise from images, equalize to enhance image contrast, and remove lines to minimize streaks by islands. Plane, flatten, and equalize are frequently used for all STM images shown in this dissertation. Any additional image processing is noted in the figure caption.

CasaXPS software was used to process and analyze all acquired XPS spectra.⁷⁰ A Shirley background subtraction was used for the majority of peak integrations, as it is ideal for integrating single peaks and small energy ranges.^{71,72} Microsoft Excel software was used for numerical analysis and graphing.

5. Dissertation Organization

This dissertation includes two published papers, one accepted paper and one paper in preparation. The first published paper, Chapter 3: “The (111) Surface of NaAu₂: Structure, Composition, and Stability” appears in the journal of *Inorganic Chemistry*, volume 54, year 2015 on page 1159. The second published paper, Chapter 4: “Interaction of Oxygen with the (111) Surface of NaAu₂” appears in the journal of *Surface Science*, In Press, year 2016. The submitted paper, Chapter 2: “Adsorption of Dy on the Graphite (0001) Surface: Nucleation and Growth at 300 K” has been accepted for publication in *The Journal of Chemical Physics*, year 2016. The paper in preparation is Chapter 5: “Interaction of Water, Carbon Monoxide, and Carbon Dioxide with the (111) Surface of NaAu₂”.

Chapter 2 focuses on the rare earth metal dysprosium and its adsorption, nucleation and growth on HOPG when deposited at room temperature. Chapters 3, 4, and 5 focus on the intermetallic single crystal, NaAu₂, specifically in regards to its clean surface composition and structure, the effects oxygen has on the surface and the effects water, carbon monoxide, and carbon dioxide have on the surface, respectively. Chapter 6 gives a comprehensive look at XPS from how it works to analyzing acquired spectra. Following the chapters are appendices that briefly discuss two other metals (Au and Pt) deposited on HOPG, a temperature calibration for annealing in the manipulator, and an experimental database.

Figures

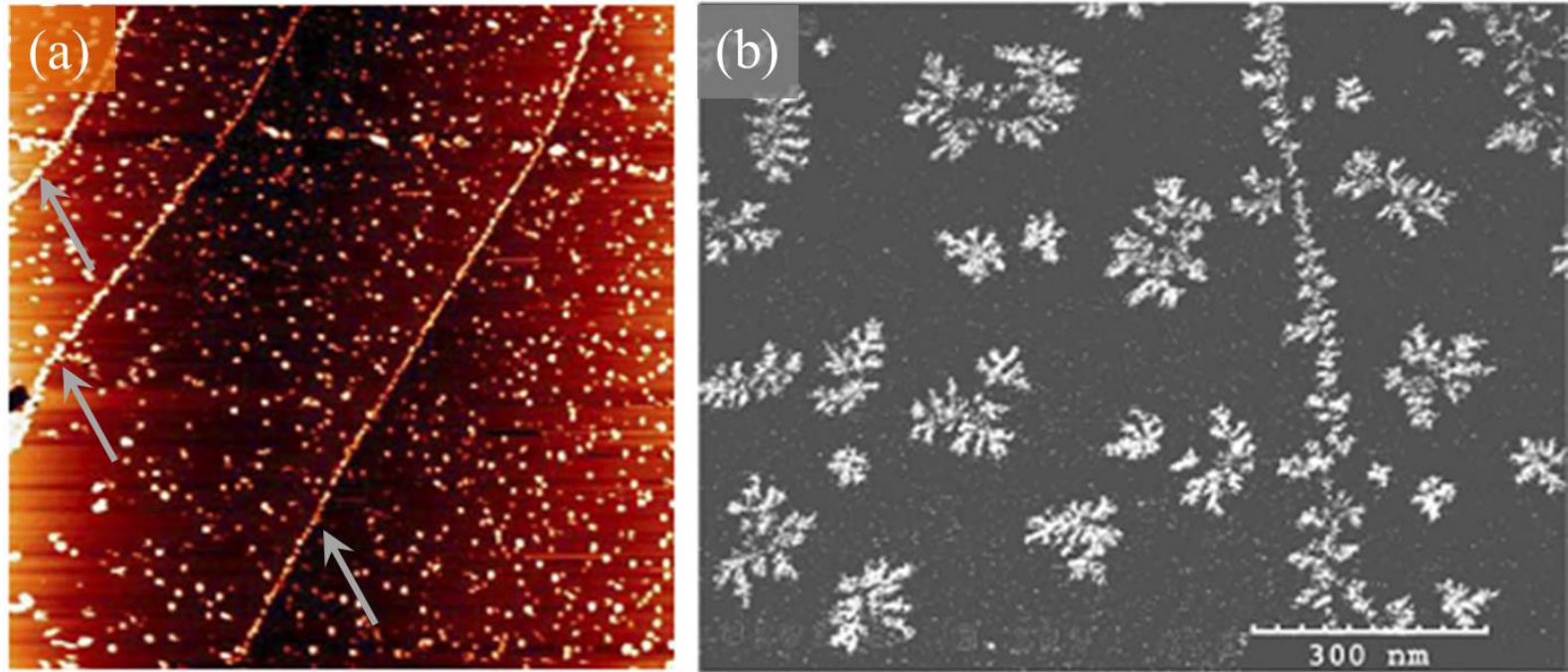


Figure 1. Images of typical metal nucleation on HOPG (a) Ag on HOPG, 870 nm x 870 nm, reproduced from Reference [31], with permission from Elsevier; (b) Pt on HOPG, 844 nm x 1095 nm, reproduced from Reference [32], with permission from Elsevier; Step edges are indicated by the gray arrows in (a).

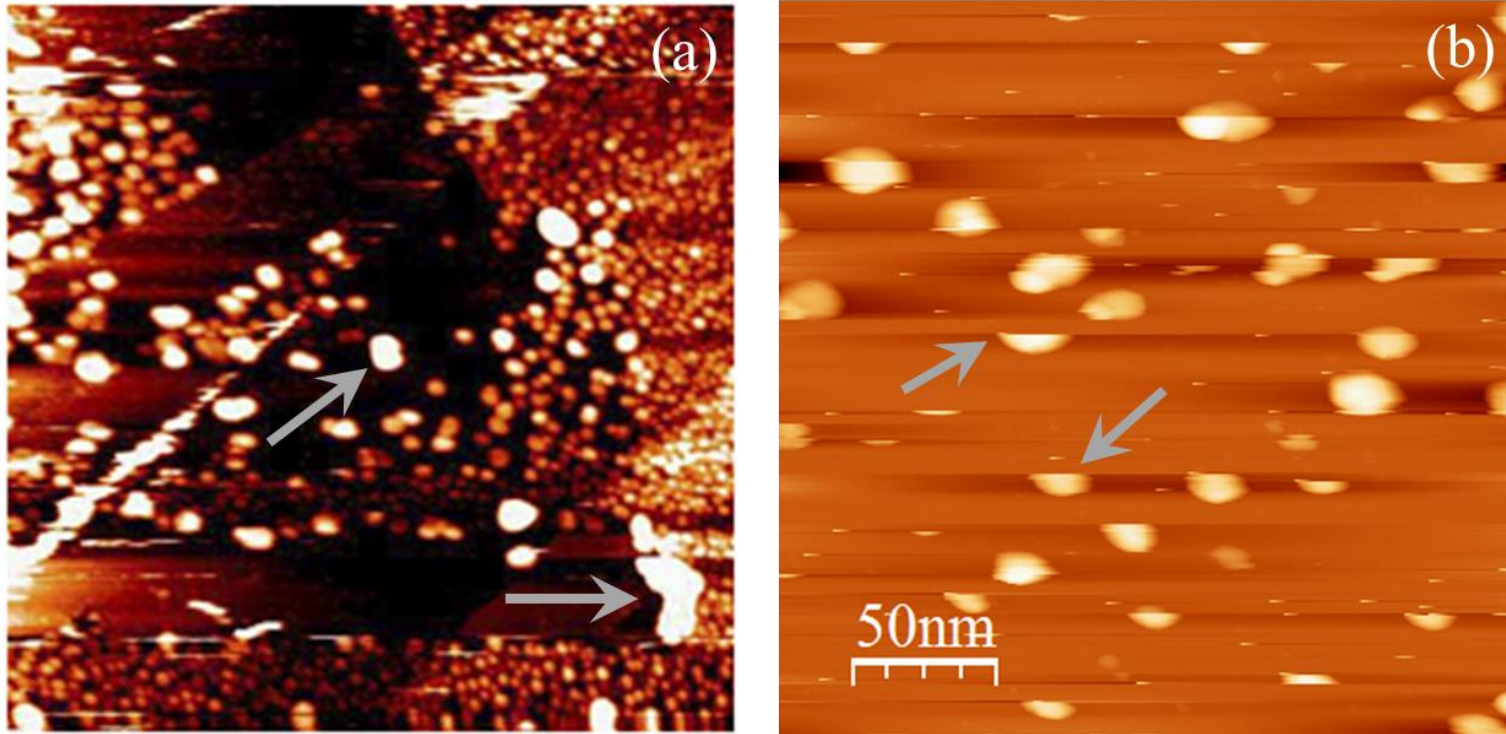


Figure 2. STM images showing examples of (a) sintering and (b) shearing of metal islands on HOPG caused by tip tunneling effects. (a) Ag on HOPG, 600 nm x 600 nm, reproduced from Reference [31], with permission from Elsevier; (b) Cu on HOPG, 250nm x 250nm. Sintered islands are denoted by the gray arrows in (a) and sheared islands are denoted by the gray arrows in (b).

References

- ¹X. Yanpeng, A. Taleb and P. Jegou, "Electrodeposition of cobalt films with an oriented fir tree-like morphology with adjustable wetting properties using a self-assembled gold nanoparticle modified HOPG electrode," *Journal of Materials Chemistry A* **1**, 11580 (2013).
- ²C. I. Vázquez and G. I. Lacconi, "Nucleation and growth of silver nanostructures onto HOPG electrodes in the presence of picolinic acid," *Journal of Electroanalytical Chemistry* **691**, 42 (2013).
- ³J. Qiao, Y. Liu, F. Hong and J. Zhang, "A review of catalysts for the electroreduction of carbon dioxide to produce low-carbon fuels," *Chemical Society Reviews* **43**, 631 (2014).
- ⁴C. M. Whelan and C. J. Barnes, "An STM study of structural transitions during the nucleation and growth of Pd and Cu cluster catalysts on HOPG," *Applied Surface Science* **119**, 288 (1997).
- ⁵D. V. Demidov, I. P. Prosvirin, A. M. Sorokin and V. I. Bukhtiyarov, "Model Ag/HOPG catalysts: preparation and STM/XPS study," *Catalysis Science & Technology* **1**, 1432 (2011).
- ⁶F. Rodríguez-Reinoso, "The role of carbon materials in heterogeneous catalysis," *Carbon* **36**, 159 (1998).
- ⁷Y. Yao, Q. Fu, Z. Zhang, H. Zhang, T. Ma, D. Tan and X. Bao, "Structure control of Pt–Sn bimetallic catalysts supported on highly oriented pyrolytic graphite (HOPG)," *Applied Surface Science* **254**, 3808 (2008).
- ⁸S.-K. Jeong, M. Inaba, R. Mogi, Y. Iriyama, T. Abe and Z. Ogumi, "Surface Film Formation on a Graphite Negative Electrode in Lithium-Ion Batteries: Atomic Force Microscopy Study on the Effects of Film-Forming Additives in Propylene Carbonate Solutions," *Langmuir* **17**, 8281 (2001).
- ⁹G. Radhakrishnan, J. D. Cardema, P. M. Adams, H. I. Kim and B. Foran, "Fabrication and Electrochemical Characterization of Single and Multi-Layer Graphene Anodes for Lithium-Ion Batteries," *Journal of the Electrochemical Society* **159**, A752 (2012).
- ¹⁰R. Wen, M. Hong and H. R. Byon, "In Situ AFM Imaging of Li–O₂ Electrochemical Reaction on Highly Oriented Pyrolytic Graphite with Ether-Based Electrolyte," *Journal of the American Chemical Society* **135**, 10870 (2013).
- ¹¹L. Wang, D. Deng, L. C. Lev and S. Ng, "In-situ investigation of solid-electrolyte interphase formation on the anode of Li-ion batteries with Atomic Force Microscopy," *Journal of Power Sources* **265**, 140 (2014).
- ¹²D. A. C. Brownson, R. V. Gorbachev, S. J. Haigh and C. E. Banks, "CVD graphene vs. highly ordered pyrolytic graphite for use in electroanalytical sensing," *Analyst* **137**, 833 (2012).

- ¹³M. A. Havstad, M. A. Schildbach and W. I. McLean, *The optical constants and spectral specular reflectivity of highly oriented pyrolytic graphite (HOPG). Revision 1*, (1993).
- ¹⁴X. Zhang, J. Zhang, G. Yang, M. Wei, G. Hu, B. Zhao and J. Zheng, "A High-Efficiency X-Ray Crystal Spectrometer for X-Ray Thomson Scattering," *Plasma Science and Technology* **15**, 755 (2013).
- ¹⁵N. Espallargas, L. Vitoux and S. Armada, "The wear and lubrication performance of liquid–solid self-lubricated coatings," *Surface and Coatings Technology* **235**, 342 (2013).
- ¹⁶S. Srikan, K. Ramji, B. Satyanarayana and S. Ramana, "Investigation on turning of AISI 1040 steel with the application of nano-crystalline graphite powder as lubricant," *Proceedings of the Institution of Mechanical Engineers, Part C: Journal of Mechanical Engineering Science* (2013).
- ¹⁷S. L. Molodtsov, C. Laubschat, M. Richter, T. Gantz and A. M. Shikin, "Electronic structure of Eu and Yb graphite intercalation compounds," *Physical Review B* **53**, 16621 (1996).
- ¹⁸M. Caragiu and S. Finberg, "Alkali metal adsorption on graphite: a review," *Journal of Physics: Condensed Matter* **17**, R995 (2005).
- ¹⁹W. E. Craven and W. Ostertag, "Rare earth graphite intercalation compounds," *Carbon* **4**, 223 (1966).
- ²⁰J. F. Hamilton and P. C. Logel, "Nucleation and growth of Ag and Pd on amorphous carbon by vapor deposition," *Thin Solid Films* **16**, 49 (1973).
- ²¹L. Huang, Y. Pan, L. Pan, M. Gao, W. Xu, Y. Que, H. Zhou, Y. Wang, S. Du and H. J. Gao, "Intercalation of metal islands and films at the interface of epitaxially grown graphene and Ru(0001) surfaces," *Applied Physics Letters* **99**, 163107 (2011).
- ²²Y. Wang, P. Puech, I. Gerber and A. Pénicaud, "Resonant Raman scattering of graphite intercalation compounds KC_8 , KC_{24} , and KC_{36} ," *Journal of Raman Spectroscopy* **45**, 219 (2014).
- ²³G. Richter, K. Hillerich, D. S. Gianola, R. Mönig, O. Kraft and C. A. Volkert, "Ultrahigh Strength Single Crystalline Nanowhiskers Grown by Physical Vapor Deposition," *Nano Letters* **9**, 3048 (2009).
- ²⁴M. Kolb and G. Richter, "Growth Of Single Crystalline Copper Nanowhiskers," *AIP Conference Proceedings* **1300**, 98 (2010).
- ²⁵M. Suzuki, K. Hamachi, K. Nagai, R. Kita, K. Nakajima and K. Kimura, "Growth of Nanowhiskers of Al, Ti, Cr, Mn, Fe, Co, Ni, Zn, Cu, Ag and Au by High-Temperature Glancing Angle Deposition," *ECS Transactions* **33**, 41 (2010).

- ²⁶M. Schamel, C. Schopf, D. Linsler, S. T. Haag, L. Hofacker, C. Kappel, H. P. Strunk and G. Richter, "The filamentary growth of metals," *International Journal of Materials Research* **102**, 828 (2011).
- ²⁷E. Ganz, K. Sattler and J. Clarke, "Scanning tunneling microscopy of Cu, Ag, Au, and Al adatoms, small clusters, and islands on graphite," *Surface Science* **219**, 33 (1989).
- ²⁸G. M. Francis, I. M. Goldby, L. Kuipers, B. von Issendorff and R. E. Palmer, "Deposition and growth of noble metal clusters on graphite," *Journal of the Chemical Society - Dalton Transactions* 665 (1996).
- ²⁹A. Stabel, K. Eichhorst-Gerner, J. P. Rabe and A. R. González-Elipe, "Surface Defects and Homogeneous Distribution of Silver Particles on HOPG," *Langmuir* **14**, 7324 (1998).
- ³⁰L. L. Wang, X. C. Ma, Y. Qi, P. Jiang, J. F. Jia, Q. K. Xue, J. Jiao and X. H. Bao, "Controlled growth of uniform silver clusters on HOPG," *Ultramicroscopy* **105**, 1 (2005).
- ³¹I. Lopez-Salido, D. C. Lim and Y. D. Kim, "Ag nanoparticles on highly ordered pyrolytic graphite (HOPG) surfaces studied using STM and XPS," *Surface Science* **588**, 6 (2005).
- ³²A. R. Howells, L. Hung, G. S. Chottiner and D. A. Scherson, "Effects of substrate defect density and annealing temperature on the nature of Pt clusters vapor deposited on the basal plane of highly oriented pyrolytic graphite," *Solid State Ionics* **150**, 53 (2002).
- ³³E. Ganz, K. Sattler and J. Clarke, "Scanning tunneling microscopy of the local atomic structure of two-dimensional gold and silver islands on graphite," *Physical Review Letters* **60**, 1856 (1988).
- ³⁴G. W. Clark and L. L. Kesmodel, "Ultrahigh vacuum scanning tunneling microscopy studies of platinum on graphite," *Journal of Vacuum Science & Technology B* **11**, 131 (1993).
- ³⁵S. Danzenbächer, S. L. Molodtsov, J. Boysen, T. Gantz, C. Laubschat, A. M. Shikin, S. A. Gorovikov and M. Richter, "Electronic structure of graphite intercalation compounds of rare-earths and uranium," *Physica B: Condensed Matter* **259–261**, 1153 (1999).
- ³⁶M. S. Dresselhaus and G. Dresselhaus, "Lattice Mode Structure of Graphite Intercalation Compounds" in *Intercalated Layered Materials*, edited by F. Lévy (Springer Netherlands, Dordrecht, 1979), pp. 423.
- ³⁷C. Vo-Van, Z. Kassir-Bodon, H. Yang, J. Coraux, J. Vogel, S. Pizzini, P. Bayle-Guillemaud, M. Chshiev, L. Ranno, V. Guisset, P. David, V. Salvador and O. Fruchart, "Ultrathin epitaxial cobalt films on graphene for spintronic investigations and applications," *New Journal of Physics* **12**, 103040 (2010).
- ³⁸B. Uchoa, T. G. Rappoport and A. H. Castro Neto, "Kondo Quantum Criticality of Magnetic Adatoms in Graphene," *Physical Review Letters* **106**, 016801 (2011).

- ³⁹H. Sevinçli, M. Topsakal, E. Durgun and S. Ciraci, "Electronic and magnetic properties of 3d transition-metal atom adsorbed graphene and graphene nanoribbons," *Physical Review B* **77**, 195434 (2008).
- ⁴⁰H. Suematsu, K. Ohmatsu and R. Yoshizaki, "Magnetic properties of Europium-graphite intercalation compound C₆Eu," *Solid State Communications* **38**, 1103 (1981).
- ⁴¹M. Haruta, T. Kobayashi, H. Sano and N. Yamada, "Novel Gold Catalysts for the Oxidation of Carbon Monoxide at a Temperature far Below 0°C," *Chemistry Letters* **16**, 405 (1987).
- ⁴²T. Hayashi, K. Tanaka and M. Haruta, "Selective Vapor-Phase Epoxidation of Propylene over Au/TiO₂Catalysts in the Presence of Oxygen and Hydrogen," *Journal of Catalysis* **178**, 566 (1998).
- ⁴³A. Ueda and M. Haruta, "Nitric Oxide Reduction with Hydrogen, Carbon Monoxide, and Hydrocarbons over Gold Catalysts," *Gold Bulletin* **32**, 3 (1999).
- ⁴⁴G. C. Bond, P. A. Sermon, G. Webb, D. A. Buchanan and P. B. Wells, "Hydrogenation over supported gold catalysts," *Journal of the Chemical Society, Chemical Communications* 444b (1973).
- ⁴⁵H. Sakurai and M. Haruta, "Synergism in methanol synthesis from carbon dioxide over gold catalysts supported on metal oxides," *Catalysis Today* **29**, 361 (1996).
- ⁴⁶G. J. Hutchings, "Gold catalysis in chemical processing," *Catalysis Today* **72**, 11 (2002).
- ⁴⁷M. Haruta, "When Gold Is Not Noble: Catalysis by Nanoparticles," *The Chemical Record* **3**, 75 (2003).
- ⁴⁸G. C. Bond and D. T. Thompson, "Gold-catalysed oxidation of carbon monoxide," *Gold Bulletin* **33**, 41 (2000).
- ⁴⁹M. Haruta, N. Yamada, T. Kobayashi and S. Iijima, "Gold catalysts prepared by coprecipitation for low-temperature oxidation of hydrogen and of carbon monoxide," *Journal of Catalysis* **115**, 301 (1989).
- ⁵⁰B. Nkosi, N. J. Coville, G. J. Hutchings, M. D. Adams, J. Friedl and F. E. Wagner, "Hydrochlorination of acetylene using gold catalysts: A study of catalyst deactivation," *Journal of Catalysis* **128**, 366 (1991).
- ⁵¹T. Aida, R. Higuchi and H. Niiyama, "Decomposition of Freon-12 and Methyl Chloride over Supported Gold Catalysts," *Chemistry Letters* **19**, 2247 (1990).
- ⁵²B. Hvolbæk, T. V. W. Janssens, B. S. Clausen, H. Falsig, C. H. Christensen and J. K. Nørskov, "Catalytic activity of Au nanoparticles," *Nano Today* **2**, 14 (2007).

- ⁵³A. Wittstock, V. Zielasek, J. Biener, C. M. Friend and M. Baeumer, "Nanoporous gold catalysts for selective gas-phase oxidative coupling of methanol at low temperature," *Science* **327**, 319 (2010).
- ⁵⁴V. Zielasek, B. Jürgens, C. Schulz, J. Biener, M. M. Biener, A. V. Hamza and M. Bäumer, "Gold Catalysts: Nanoporous Gold Foams," *Angewandte Chemie International Edition* **45**, 8241 (2006).
- ⁵⁵M. Haruta, "New Generation of Gold Catalysts: Nanoporous Foams and Tubes—Is Unsupported Gold Catalytically Active?," *ChemPhysChem* **8**, 1911 (2007).
- ⁵⁶A. Sanchez, S. Abbet, U. Heiz, W.-D. Schneider, H. Häkkinen, R. N. Barnett and U. Landman, "When gold is not noble: Nanoscale gold catalysts," *The Journal of Physical Chemistry A* **103**, 9573 (1999).
- ⁵⁷M. Haruta and M. Daté, "Advances in the catalysis of Au nanoparticles," *Applied Catalysis A: General* **222**, 427 (2001).
- ⁵⁸D. Ricci, A. Bongiorno, G. Pacchioni and U. Landman, "Bonding Trends and Dimensionality Crossover of Gold Nanoclusters on Metal-Supported MgO Thin Films," *Physical Review Letters* **97**, 036106 (2006).
- ⁵⁹C. Lemire, R. Meyer, S. Shaikhutdinov and H.-J. Freund, "Do Quantum Size Effects Control CO Adsorption on Gold Nanoparticles?," *Angewandte Chemie International Edition* **43**, 118 (2004).
- ⁶⁰N. Lopez, T. V. W. Janssens, B. S. Clausen, Y. Xu, M. Mavrikakis, T. Bligaard and J. K. Nørskov, "On the origin of the catalytic activity of gold nanoparticles for low-temperature CO oxidation," *Journal of Catalysis* **223**, 232 (2004).
- ⁶¹M. Valden, X. Lai and D. W. Goodman, "Onset of Catalytic Activity of Gold Clusters on Titania with the Appearance of Nonmetallic Properties," *Science* **281**, 1647 (1998).
- ⁶²X. Lai and D. W. Goodman, "Structure–reactivity correlations for oxide-supported metal catalysts: new perspectives from STM," *Journal of Molecular Catalysis A: Chemical* **162**, 33 (2000).
- ⁶³Z. Yang, R. Wu and D. W. Goodman, "Structural and electronic properties of Au onTiO₂(110)," *Physical Review B* **61**, 14066 (2000).
- ⁶⁴J. Hao, J. Wang, Q. Wang, Y. Yu, S. Cai and F. Zhao, "Catalytic oxidation of cyclohexane over Ti–Zr–Co catalysts," *Applied Catalysis A: General* **368**, 29 (2009).
- ⁶⁵K. Kovnir, M. Ambrüster, D. Teschner, T. V. Venkov, F. C. Jentoft, A. Knop-Gericke, Y. Grin and R. Schlögl, "A new approach to well-defined, stable and site-isolated catalysts," *Science and Technology of Advanced Materials* **8**, 420 (2007).

- ⁶⁶C. Xiao, L.-L. Wang, R. V. Maligal-Ganesh, V. Smetana, H. Walen, P. A. Thiel, G. J. Miller, D. D. Johnson and W. Huang, "Intermetallic NaAu₂ as a Heterogeneous Catalyst for Low-Temperature CO Oxidation," *Journal of the American Chemical Society* **135**, 9592 (2013).
- ⁶⁷J. V. Barth, R. J. Behm and G. Ertl, "Adsorption, surface restructuring and alloy formation in the NaAu(111) system," *Surface Science* **341**, 62 (1995).
- ⁶⁸J. V. Barth, H. Brune, R. Schuster, G. Ertl and R. J. Behm, "Intermixing and two-dimensional alloy formation in the Na/Au(111) system," *Surface Science* **292**, L769 (1993).
- ⁶⁹I. Horcas, R. Fernandez, J. M. Gomez-Rodriguez, J. Colchero, J. Gomez-Herrero and A. M. Baro, "WSXM: A software for scanning probe microscopy and a tool for nanotechnology," *Review of Scientific Instruments* **78**, (2007).
- ⁷⁰CasaXPS: Processing Software for XPS, AES, SIMS and More; www.CasaXPS.com, (October 19, 2014).
- ⁷¹M. Repoux, "Comparison of background removal methods for XPS," *Surface and Interface Analysis* **18**, 567 (1992).
- ⁷²T. Heizo, I. Naganori, N. Katsumi, K. Satoru and T. Takuei, "The Comparison of the Background Removal Methods in XPS Spectra," *Japanese Journal of Applied Physics* **29**, 2512 (1990).

CHAPTER 2**ADSORPTION OF DYSPROSIUM ON THE GRAPHITE (0001) SURFACE:
NUCLEATION AND GROWTH AT 300 K**

A paper published in *The Journal of Chemical Physics*

Emma J. Kwolek,^{1,2} Huaping Lei,^{1,3,5} Ann Lii-Rosales,^{1,2} Mark Wallingford,¹ Yinghui Zhou,^{1,6} Cai-Zhuang Wang,^{1,3} Michael C. Tringides,^{1,3} James W. Evans,^{1,3} and P. A. Thiel^{1,2,4}

¹The Ames Laboratory, Ames, Iowa 50011, USA

²Department of Chemistry, Iowa State University, Ames, Iowa 50011, USA

³Department of Physics & Astronomy, Iowa State University, Ames, Iowa 50011, USA

⁴Department of Materials Science & Engineering, Iowa State University, Ames, Iowa 50011,
USA

⁵Current address: Key Laboratory of Materials Physics, Institute of Solid State Physics, CAS,
China

⁶Permanent address: Department of Physics, Xiamen University, Xiamen 361005, China

Abstract

We have studied nucleation and growth of Dy islands on the basal plane of graphite at 300 K using scanning tunneling microscopy (STM), density functional theory (DFT) in a form that includes van der Waals interactions, and analytic theory. The interaction of atomic Dy with graphite is strong, while the diffusion barrier is small. Experiment shows that at 300 K, the density of nucleated islands is close to the value predicted for homogeneous

nucleation, using critical nucleus size of 1 and the DFT-derived diffusion barrier.

Homogeneous nucleation is also supported by the monomodal shape of the island size distributions. Comparison with the published island density of Dy on graphene shows that the value is about two orders of magnitude smaller on graphite, which can be attributed to more effective charge screening in graphite. The base of each island is 3 atomic layers high and atomically ordered, forming a coincidence lattice with the graphite. Islands resist coalescence, probably due to multiple rotational orientations associated with the coincidence lattice. Upper levels grow as discernible single-atom layers. Analysis of the level populations reveals significant downward interlayer transport, which facilitates growth of the base. This island shape is metastable, since more compact three-dimensional islands form at elevated growth temperature.

1. Introduction

The interaction of magnetic materials with graphitic surfaces, from single-layer graphene to few-layer graphene to bulk graphite, holds possibilities for designing and controlling magnetic properties at the nanoscale. For graphene, in particular, it has been proposed that the carbon sheet may play a valuable role in new spintronics devices, or as a support or modifier of magnetic materials.¹⁻⁵ In most cases, it is necessary to achieve good contact between the magnetic material and the carbonaceous substrate, in the form of a thin, essentially two-dimensional (2D) metal layer.¹ However, this has proven difficult since the adsorption energy of a metal on a graphitic surface is often much less than its cohesive energy, a factor which promotes three-dimensional (3D) growth of metals.⁶

In terms of magnetic properties, rare earths such as Dy attract special interest because of their high magnetic moment. This paper is a study of Dy islands that form when Dy is deposited on bulk graphite at room temperature. It sheds light on the fundamental energetics and mechanisms involved in adsorption, diffusion, nucleation, and growth, which may contribute to an ability to predict and manipulate Dy nanostructures, and the conditions under which they form.

There are two prior sets of studies of Dy's interaction with related substrates. In one set, the substrate was graphene grown on SiC(0001).⁷⁻⁹ There, it was shown that deposition of Dy at 660 K produced compact 3D islands, with (mainly) triangular shapes indicative of fcc atomic structure, rather than the bulk hcp structure.⁷ Smaller, more irregular islands formed at 300 K, and were very stable against coarsening when annealed at 600 K.^{8,9} In the second set, the substrate was highly-oriented pyrolytic graphite (HOPG).¹⁰ A 20 nm film of Dy was deposited, corresponding to about 70 atomic layers if distributed uniformly. Annealing to 1200 K produced a carbide-like surface species, consistent with the high propensity for rare earths to form carbides.¹¹

2. Description of Methods

2.1. Experimental details

The experiments were performed in an ultrahigh vacuum (UHV) chamber with base pressure 5×10^{-11} mbar. The graphite samples were HOPG of grade ZYA in experiments at low coverage, i.e. below 0.8 monolayer (ML) of Dy, or ZYB in experiments at higher coverage. The clean graphite surface was prepared by tape-cleavage in air, followed by transfer into the UHV chamber where all subsequent experiments took place. Samples were

heated in the manipulator to either 800 K for 60 minutes (low coverage experiments) or 1000 K for 20 minutes (high coverage experiments) in UHV to remove contaminants and then transferred to the scanning tunneling microscopy (STM) stage for subsequent Dy deposition and STM imaging. Dy was deposited via physical vapor deposition from a Mantis QUAD-EV-C Mini e-beam evaporator, using a Mo crucible lined with pyrolytic boron nitride. For heating, the crucible was biased at +2 kV with respect to an electron filament mounted parallel to and near the top of the evaporation target, with total power typically 25 W.

In a study of Cu/graphite, we showed that this evaporator, under similar conditions, produced a significant fraction of metal ions that damaged the graphite surface and influenced nucleation. We also showed that this could be circumvented by heating the evaporator, then shutting off the high voltage and/or filament current during deposition, with only a small drop in flux over times up to 10 s.¹² For all experiments reported herein, we employed this protocol. The deposition time was constant at 10 s; coverage was varied by adjusting power and hence flux.

In STM, tunneling parameters were typically in the range -1.0 V to -1.2 V tip bias and 0.15 nA to 0.25 nA tunneling current for low coverage experiments, and 0.70 V to 1.3 V and 0.13 nA to 0.77 nA for higher coverage experiments. The STM tip was electrochemically-etched W. All STM images were planed for data analysis. Other details of STM experiments and data analysis were the same as reported elsewhere.¹²

2.2. Computational details: DFT

First-principles energy calculations with non-local van der Waals correction were performed based on density functional theory (DFT) using VASP.^{13,14} The exchange and

correlation energy functional adapted the opt-B88 scheme developed by Klimes et al.¹⁵⁻¹⁷ This functional has been verified to describe accurately the energy and other properties of graphite and metals.^{15,17} The electron-ion interaction was described by the projector augmented wave method.¹⁸ The energy cutoff for the plane wave basis set used in the calculation was 600 eV. The calculated fundamental properties of graphite agreed well with the corresponding experimental values.¹⁹ The calculated lattice constants of hexagonally-close-packed Dy were 0.357 nm for a and 0.558 nm for c , respectively, in good agreement with experimental data of 0.359 nm for a and 0.565 nm for c .²⁰ The calculated cohesive energy was 3.58 eV/atom, somewhat larger than the experimental value, 3.04 eV/atom.²⁰

The graphite substrate was modeled by a slab with a 6×6 unit cell in the xy plane and four layers along the (0001) direction, plus enough vacuum (1.57 nm) to avoid interaction between the slab and its images under the periodic boundary condition. Spin polarization and dipole correction were considered in all calculations. A Γ -centered k -point grid of $15 \times 15 \times 1$ was used for Brillouin zone sampling to ensure energetic convergence. During geometric optimization, the bottom three layers were fixed at their bulk positions, while carbon atoms in the top layer and metal adatom were relaxed fully with a force tolerance of 0.1 eV/nm.

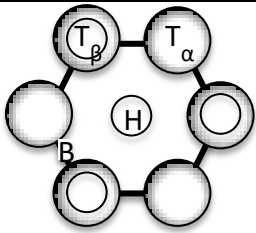
3. Computational Results: Adsorption Energy and Diffusion Barrier

Table 1 shows calculated values of the adsorption energy of a Dy atom at different sites on the graphite surface. The adsorption energy at the favored site is 1.90 eV. This is higher than the value of 1.47 eV calculated for Dy on graphene,²¹ which reinforces a trend noted elsewhere: For a given metal, its calculated adsorption energy on graphite exceeds that on graphene.¹⁹ The adsorption energy is about 2/3 the cohesive energy of bulk Dy, 3.04 eV.

The adsorption energy falls in the range of chemisorption, and implies an essentially infinite surface lifetime for a Dy atom at 300 K. By all measures, the interaction of Dy with graphite is reasonably strong.

The Dy atom is most stable at the hollow (H) site, in the center of the hexagon of carbon atoms. (See inset in Table 1 for identification of adsorption sites.) This is the same as the site predicted for Dy and other rare earths on free-standing graphene.⁹ The diffusion barrier, E_d , can be approximated as the difference in adsorption energies along a path that links minimum-energy sites. In this case that path leads from the H site, over T_α and back to H. The energy difference between the H and T_α sites is 0.048 eV.

Table 1. DFT results for a Dy atom adsorbed on graphite. A schematic of atoms in the (0001) graphite plane is shown in top left, where large circles represent top-layer C atoms and smaller circles represent second-layer C atoms. Four high-symmetry adsorption sites are identified: two top (T) sites, which differ in occupation of the second-layer site; hollow (H); and bridge (B).

				
	T_α	T_β	Bridge (B)	Hollow (H)
Adsorption Energy (eV)	-1.85	-1.83	-1.83	-1.90
Height above carbon atom plane (nm)	0.241	0.242	0.239	0.214

4. Experimental Results: Island Characteristics

4.1. Island shapes

Figure 1 shows representative STM images of Dy islands on graphite terraces, for coverages spanning 0.12 to 2.5 ML. The islands consistently have a flat base with an irregular footprint. The flat base is decorated with smaller upper features, many of which are found near the island edges. The base is 0.87 ± 0.02 nm high, based on a sample size, N , of 36 islands. This height is invariant with island size. To first order, it can be compared with the 0.282 nm spacing between close-packed planes in bulk Dy, which yields a thickness of 3 atomic layers. Thus, the base can be described as quasi two-dimensional (2D), which is not unreasonable in light of the relatively high adsorption energy found in Section 3.

In many cases a honeycomb pattern with amplitude 0.04 ± 0.01 nm ($N = 144$ islands) can be observed on the base, as shown in Figure 2. This is a moiré pattern between the Dy film and the graphite support, which indicates that the Dy film is atomically well-ordered. The modulation periodicity is 1.23 nm, which is close to 3.4 times the periodicity of the underlying graphite. In moiré patterns such as this, a rotation between the unit cell vectors of the overlayer and the substrate, along with possible distortion of the overlayer, brings the two lattices into coincidence. There must be 6 rotational orientations, given the 3-fold symmetry of the graphite substrate. Unfortunately, atomic-scale resolution of the graphite support could not be obtained in the presence of Dy islands, so the rotational angle is unknown. However, the existence of a coincidence lattice provides further evidence of significant interaction between Dy and the carbon substrate.

At high Dy coverage, Dy islands become very close but often retain their individual identity, as illustrated in Figure 3. For example, the oval in Figure 3(a) encompasses 3 islands

separated by thin gaps, indicating a barrier to coalescence. We attribute this to the different epitaxial orientations of the Dy base, associated with the moiré pattern. Only when orientations happen to match can adjacent islands merge easily.

The bases often have taller dot-like features around their edges. The height of these dots corresponds to 1 atomic layer above the base. Examples are visible in Figure 1 and Figure 4. Larger, layer-like features can also cover part of the islands' interiors. These are 1.13 ± 0.02 nm and 1.42 ± 0.02 nm above the graphite. Figure 4 provides examples of these features, including line profiles that illustrate heights. The fact that each layer is higher by 0.28 nm indicates that single Dy layers are populated successively, above the base. With increasing Dy coverage, it becomes more probable to find these partially-filled layers. The layers can exist near the center of an island, or emanate from an edge. When more than one layer exists atop the base, layers are stacked in a wedding-cake morphology such that each level below the top one is partially exposed.

For comparison, Figure 5 shows the result when Dy is deposited at 800 K. Now the Dy islands are much taller and more three-dimensional; the three-layer mesa-like base is no longer evident. This indicates that the quasi-2D shape at 300 K is metastable. Indeed, the equilibrated Wulff shape of crystalline islands should be relatively tall compared to their width for a metal weakly bound to the substrate. The footprint should also be geometric, e.g., hexagonal for hcp crystal structure. Presumably, upward diffusion beyond the first three layers becomes facile at the higher temperature, allowing islands to achieve a more equilibrated shape during growth, than that which can be attained at 300 K.

4.2. Island densities and size distributions

The island density, N_{isl} , is shown as a function of Dy coverage in Figure 6. The density increases from a value of $(2.4 \pm 0.3) \times 10^{-4} \text{ nm}^{-2}$ at 0.12-0.15 ML, and saturates at $6.0 \times 10^{-4} \text{ nm}^{-2}$ at 1.2 ML.

The island size distribution is shown in Figure 7 for two coverages, 0.13 and 1.2 ML. In both cases the distribution is monomodal.

These observations are analyzed in the following section.

5. Theoretical Analysis of Island Formation for Deposition of Dy/Graphite

5.1. Island densities

First we assess the island nucleation mechanism by comparing the observed value of N_{isl} and its coverage dependence for deposition at 300 K with theories for homogeneous nucleation. It is useful to note that the area of the surface unit cell for graphite is $\Omega = 0.052 \text{ nm}^2$. Multiple experiments for deposition of 0.12-0.15 ML provide quite consistent estimates for N_{isl} (see Figure 6). Averaging this data yields $N_{isl} = (2.4 \pm 0.3) \times 10^{-4} \text{ nm}^{-2}$ (or 1.3×10^{-5} per unit cell or per adsorption site) for coverage $\theta = 0.13 \pm 0.1 \text{ ML}$ corresponding to a deposition flux of $F = 0.013 \text{ ML/s}$.

To analyze this behavior, we use the estimate for the terrace diffusion barrier of $E_d \approx 48 \text{ meV}$, obtained from DFT analysis described in Section 3. Assuming an attempt frequency of $\nu = 10^{12.5}/\text{s}$ yields a rate of $h = \nu \exp[-E_d/(k_B T)]$ for adatom hopping associated with terrace diffusion. A key parameter for nucleation is h/F . Using the experimental values of $T = 300 \text{ K}$ and $F = 0.013 \text{ ML/s}$, one has $h = 10^{11.7}/\text{s}$ and $h/F = 10^{13.6}/\text{s}$. For homogeneous nucleation and

growth of islands with critical size i (where islands of size $> i$ atoms are stable), the island density satisfies $N_{isl} \sim \theta^{(1-\chi)/2} (h/F)^\chi$ where $\chi = i/(i+2)$ in the regime of low coverage.²²

For this system, it is reasonable to anticipate that homogeneous nucleation and growth of islands is at least close to irreversible, corresponding to critical size $i = 1$. Theoretical analysis indicates that the temperature for transition to reversible island formation is proportional to $E_{rev} = (2/3)E_d + E_{NN}$, where $E_{NN} > 0$ is the strength of the nearest-neighbor interaction.²² More precisely, to ensure a transition temperature above 300 K for a standard deposition flux of 0.005 ML/s and attempt frequency of $\nu = 5 \times 10^{12}$ /s, one requires that $E_{rev} \approx 0.55$ eV or above. Thus, for Dy on HOPG with $E_d \approx 0.05$ eV, one requires that $E_{NN} \approx 0.52$ eV or above. A crude estimate of E_{NN} and 1/6 of the bulk cohesive energy yields a value of 0.51 eV, and it is plausible that the true E_{NN} for a pair of Dy on HOPG is stronger.

For $i = 1$, one has that $N_{isl} \sim (h/F)^{-1/3}$ for fixed coverage, and simulations indicate that $N_{isl} \approx 2.18 \times 10^{-5}$ per site for $\theta = 0.13$ ML.^{22,23} Thus, the experimental value of N_{isl} , 1.26×10^{-5} per site, is close to but slightly reduced from classic $i = 1$ prediction (reduced by a factor of $r = 0.58$).

The lower experimental value could be achieved by choosing an attempt frequency which is higher by a factor of 5.1. Such a prefactor, just above 10^{13} /s, cannot be excluded, but one generally expects low prefactors for low diffusion barriers (as in this system).

Alternatively, the lower experimental N_{isl} could be naturally explained by deviations from classic $i = 1$ behavior due to either significant mobility of adsorbed Dy dimers (and perhaps other small Dy clusters) or due to the onset of reversibility in island formation. To obtain a sense of the impact of dimer mobility or reversibility in reducing N_{isl} , we note the following.

If monomers and dimers have comparable mobility, then $N_{isl} \sim (h/F)^{-2/5}$ ^{22,24} which implies a

reduction in N_{isl} from the classic $i = 1$ value by a factor of $r = (h/F)^{-1/15} = 0.12$ for the above $h/F = 10^{13.6}$, i.e. the reduction is too strong. For facile dissociation of dimers but stable trimers corresponding to $i = 2$, one has that $N_{isl} \sim (h/F)^{-1/2}$, reducing N_{isl} for the classic $i = 1$ value by a factor of $r = (h/F)^{-1/6} = 0.005$, which is much too strong. In conclusion, the observed reduction by $r = 0.58$ relative to classic $i = 1$ could be induced by some dimer mobility²⁴ (still significantly lower than adatom mobility), or by slight reversibility in island formation.

Another way of accounting for these effects is by introducing a slight increase $\delta\chi = \chi - 1/3$ in the scaling exponent χ relative to $i = 1$, so that $(h/F)^{-\delta\chi} = r = 0.58$. This implies that $\delta\chi = 0.018$ so $\chi = 0.351$ and $(1-\chi)/2=0.325$. As a result, $N_{isl} = c(h/F)^{-0.351}\theta^{0.325}$. Choosing c to recover the experimental N_{isl} at 0.13 ML, and recognizing that $F=\theta/10$ in experiment, one obtains $N_{isl} \approx 5.01 \times 10^{-4} \theta^{0.676}$ per site, which should apply in the lower coverage regime where the footprint of the islands covers a small fraction of the substrate area (i.e., the “point island” regime²²). This curve is shown in Figure 6 up to a coverage of 0.4 ML, beyond which one expects that the point island model will significantly overestimate N_{isl} because it underestimates the capture probability at existing islands. (We emphasize that for the Dy islands with a 3-layer base, the areal coverage or fraction of the substrate covered is only $\sim \theta/3$ in contrast to θ for 2D islands. Thus, nucleation persists to higher coverages.) There is good agreement between the model and the data in this regime.

5.2. Island size distribution

Next, we analyze experimental observations for the island size distribution, N_s , which gives the density of islands of s atoms, so that $N_{isl} = \sum_{s>1} N_s$ and $\theta = \sum_s sN_s$. If $s_{av} \approx \theta/N_{isl}$

denotes the average island size (measured in atoms), then the island size distribution is naturally written in scaled form, $N_s \approx (N_{isl}/s_{av})f(s/s_{av}, \theta)$, where the scaling or shape function $f(x)$ satisfies $\int_{x>0} dx f(x) = 1$ and $\int_{x>0} dx xf(x) = 1$.²² For homogeneous nucleation at lower coverages around 0.1 ML, $f(x)$ is monomodal with a peak height around $x = 1$ increasing from about 0.75 for $i = 1$ to 1.1, 1.3, and 1.5 for $i = 2, 3,$ and 6 , respectively (and also $f(x)$ narrows with increasing i). The peak also increases to about 1.1 with high dimer mobility.²⁴ There is a significant population of smaller islands reflected in $f(0) \approx 0.3$ for $i = 1$, with $f(0)$ quickly decreasing with increasing i (e.g., to 0.15 for $i = 1$). The experimental $f(x)$ shown in Figure 7(a) for 0.13 ML has a peak height around 1.0 consistent with slight deviations from classic $i = 1$ behavior. However, there is a significant depletion in the population of small islands relative to classic $i = 1$ behavior. This feature together with an increase in peak height and shift to smaller x -values has been seen previously and attributed to post-deposition diffusion and coalescence of small clusters.²⁵ Figure 7(b) shows the experimental $f(x)$ for a much higher coverage of 1.2 ML. The peak height is similar to 0.13 ML, but the peak and the weight of the distribution has shifted to higher (scaled) island sizes. This feature might be expected, as inspection of STM images reveals that island growth is impeded by impingement upon other islands (without coalescence) in this regime. As noted in Section 4, we attribute this to epitaxial mismatch between different islands. This would tend to induce a sharper cut-off on the right side of the distribution.

5.3. Layer distributions

Despite the complexity of multilayer growth in this system (described in more detail below), simplified modeling can produce significant insights, e.g., into the extent of

interlayer transport. To provide some context, such models have been traditionally developed for systems with equivalent layers where growth in higher layers proceeds before lower layers are complete. If θ_j denotes the coverage of layer j , then $P_j = \theta_j - \theta_{j+1}$ denotes the exposed fraction of layer j . In the extreme case where interlayer transport is absent, one finds a Poisson distribution for P_j and film roughness W satisfies $W^2 = d^2 \theta$, where d is the interlayer spacing.²² This modeling has been refined to account for downward interlayer transport by specifying that a fraction, α , of atoms deposited in each layer reach the next lower layer (so $\alpha = 0$ recovers the above case).²⁶⁻²⁸ Then, for rough growth with small α , one can show that $W^2 \approx (1-2\alpha)\theta d^2$.^{27,28} Although not well-recognized, this result must be modified for larger α [see Appendix 1].

A special feature of the Dy/graphite system is that atoms deposited on the substrate form bases consisting of three atomic layers (rather than single layer islands). This implies facile transport from the substrate upward to the second and third layers. However, on top of these bases, growth occurs in single layers. Thus, it is convenient to refer to the fraction, P_j , of exposed level, j (rather than layer), where $j = 0$ is the substrate, $j = 1$ is the top of the 3-layer base, $j = 2$ is the top of the single layer island on the base, etc. Experimental values for these populations or fractions of exposed levels for coverage $\theta = 1.2$ ML are given in Table 2.

Table 2. Layer distributions in Dy islands at 1.2 ML. P_j is the fraction of area exposed for each level j , where $j = 0$ indicates the graphite substrate, $j = 1$ is the top of the Dy base, $j = 2$ is the first Dy layer atop the base, and $j = 3$ is the second Dy layer above the base. The

parameters α and α^* are defined in Figure 8. The experimental values were obtained by analyzing a total area of $1.38 \times 10^6 \text{ nm}^2$, which included 792 Dy islands.

	<i>Experiment</i>	<i>Model:</i> $\alpha^* = \alpha = 0$	<i>Model:</i> $\alpha^* = \alpha = 0.65$	<i>Model:</i> $\alpha^* = 0.69$ $\alpha = 0.85$
P_0	0.631	0.670	0.634	0.631
P_1	0.276	0.185	0.278	0.281
P_2	0.0904	0.096	0.072	0.081
P_3	0.0024	0.036	0.015	0.006

To elucidate this behavior, we develop a theory in the spirit of the more traditional one mentioned above, for multilayer growth with equivalent layers. However, here we naturally specify that all atoms deposited on the graphite substrate are incorporated immediately into 3-layer bases. A fraction α^* of atoms deposited on top of bases hop down to become incorporated in the base and the remainder stay on top of the base forming single-layer islands. Of atoms deposited in higher layers, a fraction α hop down to be incorporated in the next lower layer, and the remainder stay in the layer where they were deposited, forming or joining single-layer islands in that layer. See the schematic in Figure 8. With this prescription, the rate equations describing the evolution of the level populations are:

$$d/d\theta P_0 = -P_0/3 - \alpha^*P_1/3, \quad d/d\theta P_1 = P_0/3 + \alpha^*P_1/3 - (1-\alpha^*)P_1 - \alpha P_2,$$

$$d/d\theta P_2 = (1-\alpha^*)P_1 + \alpha P_2 - (1-\alpha)P_2 - P_3, \quad d/d\theta P_{j \geq 4} = (1-\alpha)P_{j-1} - (1-2\alpha)P_j - \alpha P_{j+1}.$$

Simple modification of these equations is possible if one wishes to exclude population of level 4 (i.e., to enforce $P_4 = 0$) consistent with experiment.

It is natural to first consider the extreme case of no interlayer transport (other than upward transport of atoms deposited on the substrate to form 3-layer bases). In this case $\alpha^* =$

$\alpha = 0$, and the above equations partially decouple in the sense that P_j is coupled only to $P_{k < j}$ so they can be recursively solved exactly to obtain

$$P_0 = \exp(-\theta/3), \quad P_1 = [\exp(-\theta/3) - \exp(-\theta)]/2,$$

$$P_2 = (3/4)[\exp(-\theta/3) - \exp(-\theta)] - \theta \exp(-\theta)/2, \text{ etc.}$$

As shown in Table 2, the resultant values of P_j agree roughly with experimental values, but the fact that P_0 is higher in the model than in experiment (0.670 vs. 0.631, respectively) is a clear indication that net downward transport is operative in the Dy/graphite system.

To refine the above simplest model, we introduce interlayer transport, initially setting $\alpha^* = \alpha$. We also enforce $P_4 = 0$. Numerical integration of the associated rate equations indicates that good agreement with experiment comes from choosing $\alpha = 0.65$, with the resultant values of P_j shown in Table 2. A slightly better fit is achieved by allowing independent values $\alpha^* = 0.69$ and $\alpha = 0.85$. In either case, this analysis indicates that there is significant net downward transport in the Dy/graphite system, which impacts the film height distribution.

The existence of small single-layer features at the edges of islands was noted in Section 4. Their presence indicates that nucleation is somewhat more likely near islands' edges than in islands' interiors. This could divert some Dy atoms from reaching and crossing over the edge of the base, leading to $\alpha^* < \alpha$ as suggested by the modeling.

6. Discussion

One major conclusion from this work is that Dy island nucleation is homogeneous. This is based upon the measured value of N_{isl} at 0.13 ML, in comparison with the value predicted from a point-island growth model using the diffusion barrier from DFT and $i = 1$.

The agreement is quite good, with the experimental value being slightly lower than the predicted value. Elsewhere, we have argued that homogeneous nucleation of metals on graphite terraces may be less common than previously thought, with heterogeneous nucleation playing a larger role than expected due to the susceptibility of graphite substrates to inadvertent ion beam damage.¹² We have argued that if the measured island density is significantly higher than the predicted value, then heterogeneous nucleation should be considered. If the opposite is true, as in this case, then homogeneous nucleation is viable with some adjustments. Here, we have shown that the degree of adjustment is too extreme if $i = 2$ or if dimer diffusion is fully operative, though a small contribution from one or both of these mechanisms could explain the discrepancy.

The island size distributions are also consistent with homogeneous nucleation. Their monomodal shapes are quite different from the monotonically-decreasing shape found in our previous study of Cu on graphite, where Cu ions in the metal atom flux introduced defects in the graphite surface during deposition. Precautions are taken in the present work to prevent such damage, consistent with the radically-different distributions observed.

As noted in Section 1, Hupalo et al. studied a related system, Dy deposited on monolayer graphene supported on SiC, at 300 K.⁸ They reported $N_{isl} = 2 \times 10^{-2} \text{ nm}^{-2}$ at 0.4 ML, which is two orders of magnitude higher than our value of N_{isl} at 0.13 ML. While a somewhat higher value of $E_d = 0.125 \text{ eV}$ was calculated for that system, this and other differences—in experimental flux and coverage—are insufficient (by far) to explain the difference in N_{isl} . Instead, we propose that the explanation lies in the influence of the number of carbon layers, n , on nucleation, growth, and stability of metal nanoclusters. There is now broad evidence for this dependence, with N_{isl} generally decreasing as n increases.⁶ This has

been demonstrated in studies of Au, Ag, and Pd nanoclusters on n -layer graphene sheets supported on SiO₂/Si substrates. This trend, decreasing N_{isl} with increasing n , describes exactly the trend in going from Dy/graphene ($n = 1$) in the prior work, to Dy/graphite ($n \rightarrow \infty$) in this study. One explanation involves charge transfer from the metal to the underlying carbon and consequent Coulomb and dipole repulsion terms, which have significant effect at small n due inefficient screening.²⁹

Finally, we comment on the morphology of the Dy islands. Experiment indicates that growth is quasi-2D. The islands exhibit a 3-layer base, and single atomic layers grow on top of the base. DFT shows that the interaction between Dy and the graphite is reasonably strong, providing a rationale for the quasi-2D base. Analysis of the level populations reveals significant downward interlayer transport, which facilitates growth of the base. On the other hand, the quasi-2D structure is metastable, based on comparison with the taller, more compact 3D islands that form at 800 K; the most natural explanation is that upward transport (beyond the 3-layer base) is kinetically limited at 300 K.

It is possible that the base is limited to 3 atomic layers because of strain between Dy and graphite lattices. It is well-established that strain influences growth in heteroepitaxial systems. For the growth mode known as Stranski-Krastanov (SK), the film wets the substrate (growth is smooth) up to a critical thickness, beyond which growth is 3D.^{30,31} In SK systems strain is often manifest in a moiré pattern at or below the critical thickness.³²⁻³⁵ Strictly speaking, SK is a thermodynamic (equilibrium) picture of growth, but the same factors that lead to SK growth can influence structures formed under kinetically-limited conditions.

7. Conclusions

We have shown that experimental measurements of the value of Dy island density, and coverage-dependence of Dy island density at low coverage, are well described by analytic theory for homogeneous nucleation, using energetics provided by DFT. The Dy islands have a quasi-2D 3-layer base which exhibits atomic order coincident with the graphite substrate. This natural tendency toward quasi-2D growth may be useful in situations where good contact between a magnetic metal and a graphitic substrate is desired.

Acknowledgements

The experimental and DFT components of this work (Sections 3 and 4) were conducted by the following authors: EJK, HL, ALR, MW, YZ, CZW, MCT, and PAT. Experimental and DFT effort was supported by the US Department of Energy (DOE), Office of Science, Basic Energy Sciences, Materials Sciences and Engineering Division. Research was performed in part at the Ames Laboratory, which is operated by Iowa State University under contract # DE-AC02-07CH11358. DFT was performed, in part, with a grant of computer time at the National Energy Research Scientific Computing Centre (NERSC). NERSC is a DOE Office of Science User Facility supported by the Office of Science of the U.S. Department of Energy under Contract No. DE-AC02-05CH11231. HL's DFT was supported in part by the National Science Foundation of China (NSFC) Grant No. 11575230, and YZ's participation in the experimental effort was supported by the China Scholarship Council. The modeling and analyses described in Section 5 were performed by JWE, with support from NSF Grant CHE-1111500.

Figures

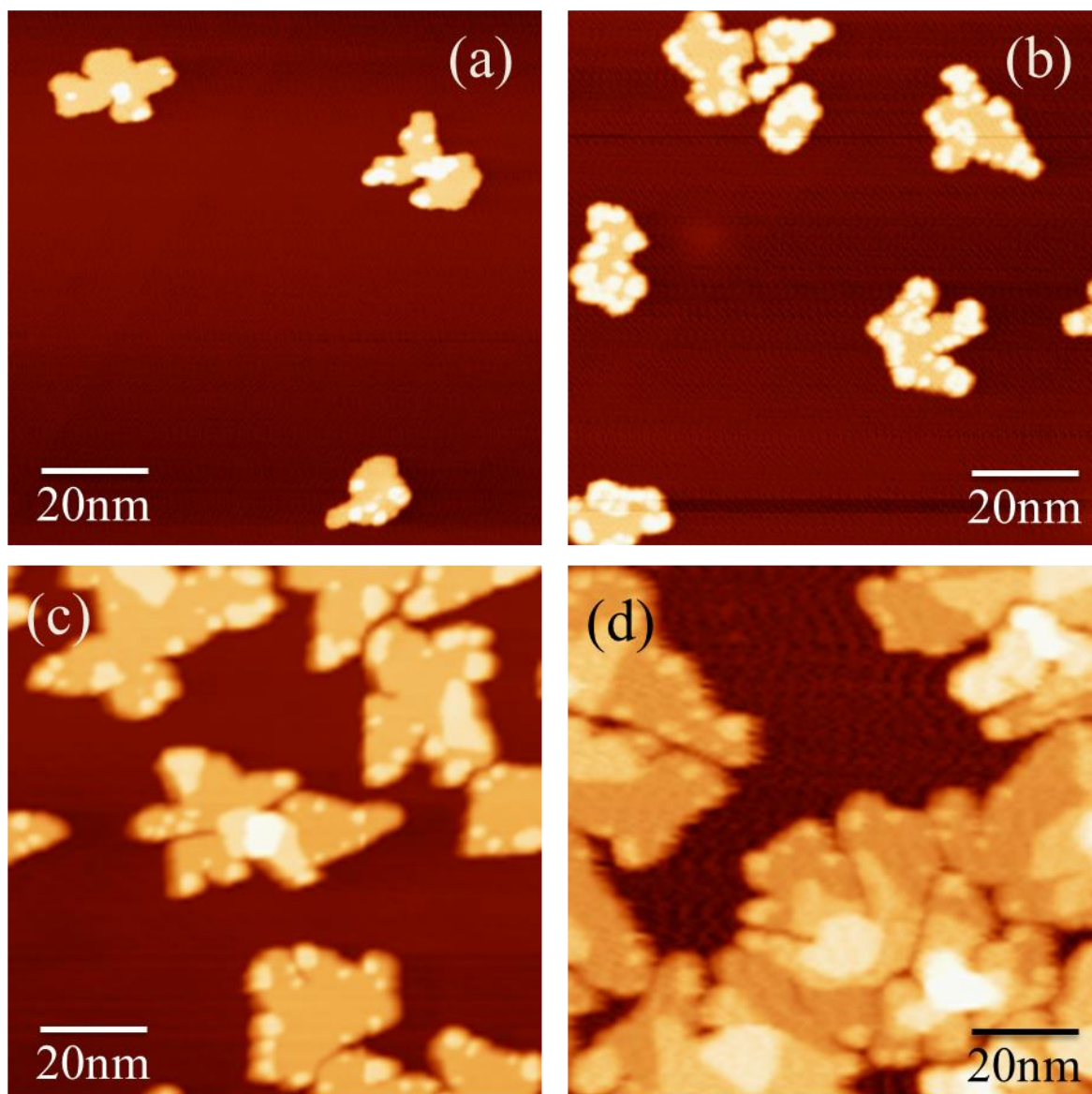


Figure 1. STM images of Dy islands on HOPG terraces, 100 nm x 100 nm. Coverages are: (a) 0.12 ML; (b) 0.28 ML; (c) 1.2 ML; (d) 2.5 ML. Noise is reduced in (d) using a fast Fourier transform (FFT) filter.

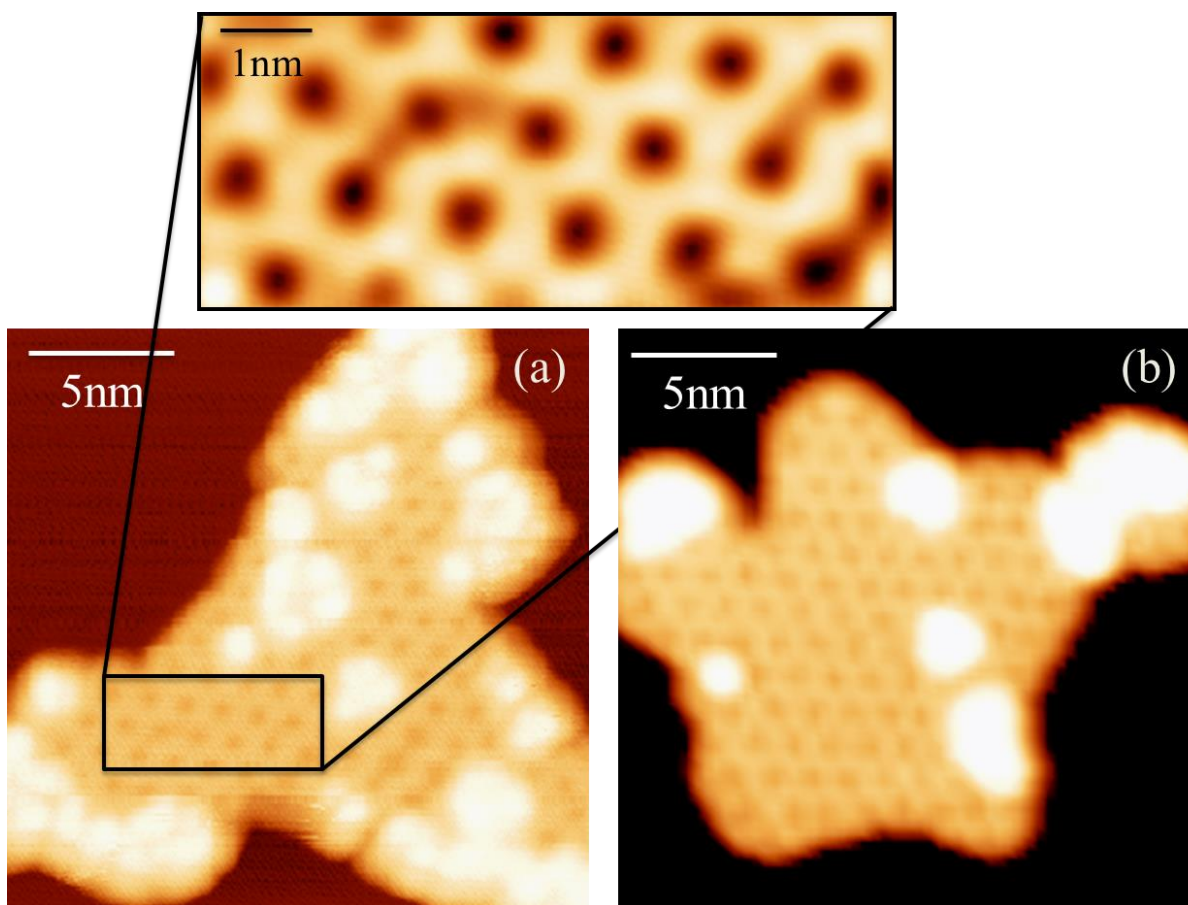


Figure 2. STM images of Dy islands, 20 nm x 20 nm, at (a) 0.28 ML and (b) 0.12 ML. The enlargement shows the honeycomb pattern visible on the base of (a), 7.5 nm x 3.2 nm. The enlargement is shown after FFT filtering.

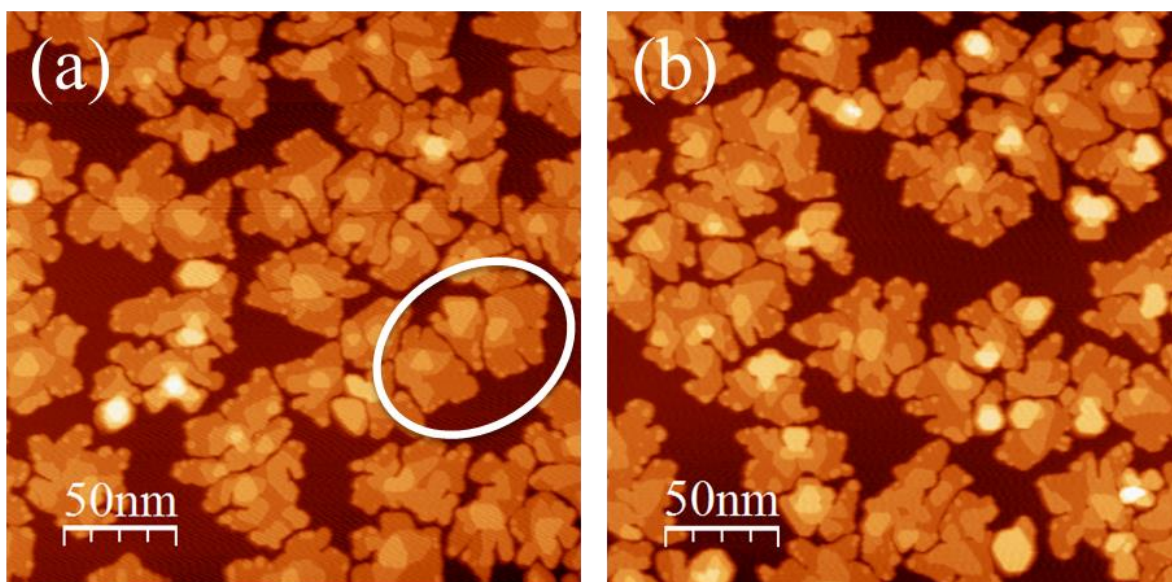


Figure 3. STM images of Dy islands at 2.5 ML. Image sizes are 250 nm x 250 nm. The white oval in (a) shows three islands that are very close but still separated.

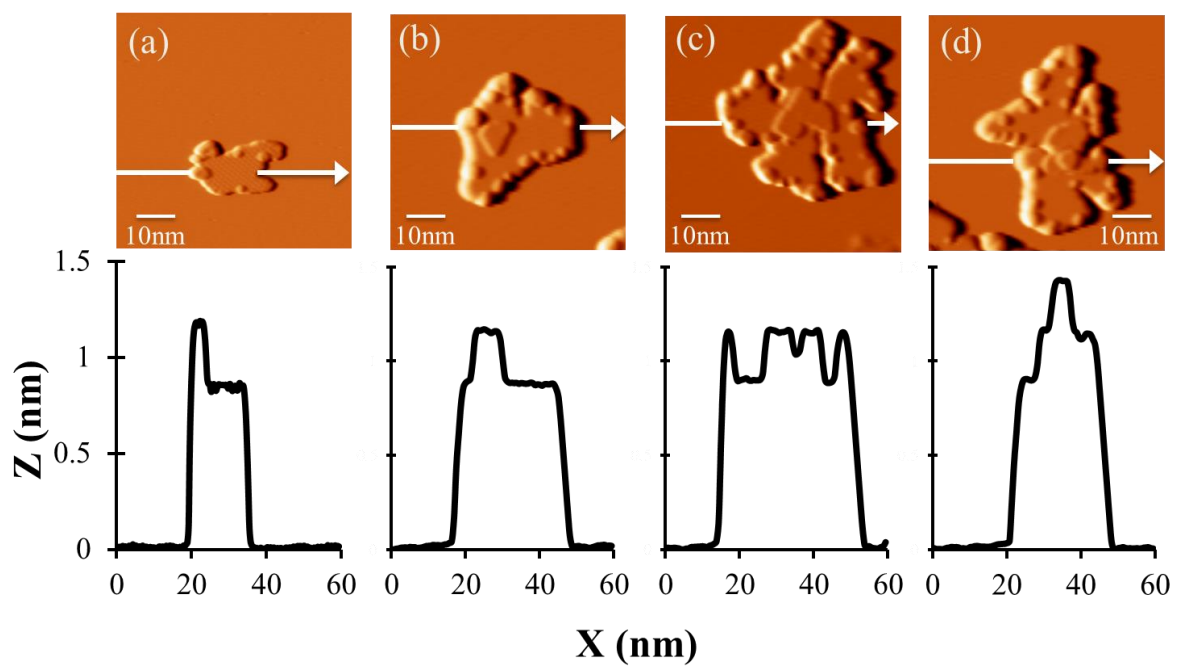


Figure 4. STM images of Dy islands on graphite terraces, with line profiles. Each image has been derived to facilitate viewing of small features on different levels. Image size is 60 nm x 60 nm. (a) 0.14 ML (b)-(d) 1.2 ML.

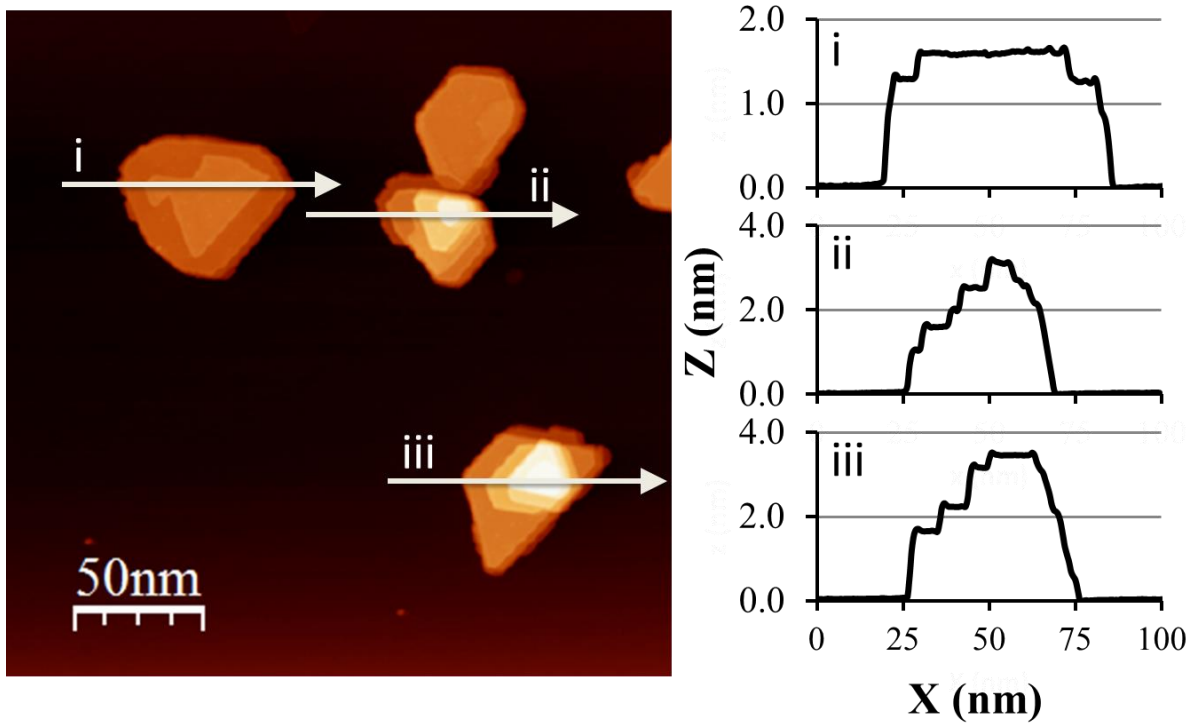


Figure 5. Topographic STM image of Dy islands on a graphite terrace after deposition at 800 K, with associated line profiles. Image size is 250 nm x 250 nm, and tunneling conditions are 1.3 V, 0.15 nA.

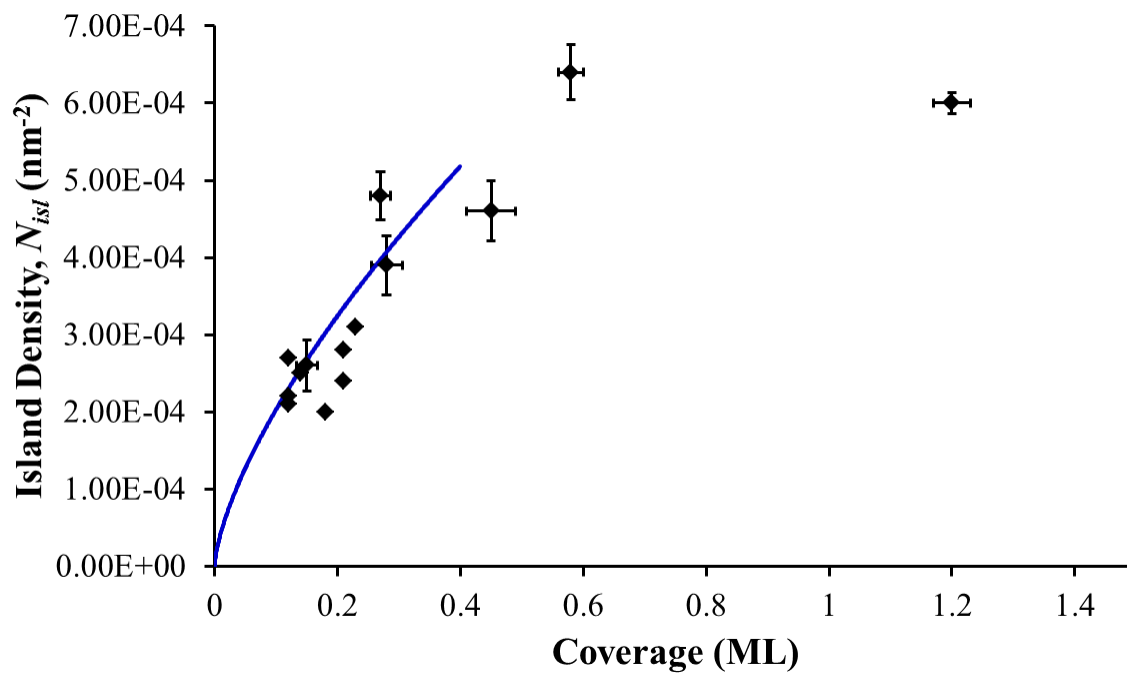


Figure 6. Dy island density as a function of Dy coverage. The curve represents the “point island” model described in the text, with N_{isl} (in units of nm^{-2}) = $9.633 \times 10^{-4} \theta^{0.676}$. Error bars reflect the standard error of the mean, calculated from the set of images available within each experiment, and do not reflect variations between different experiments.

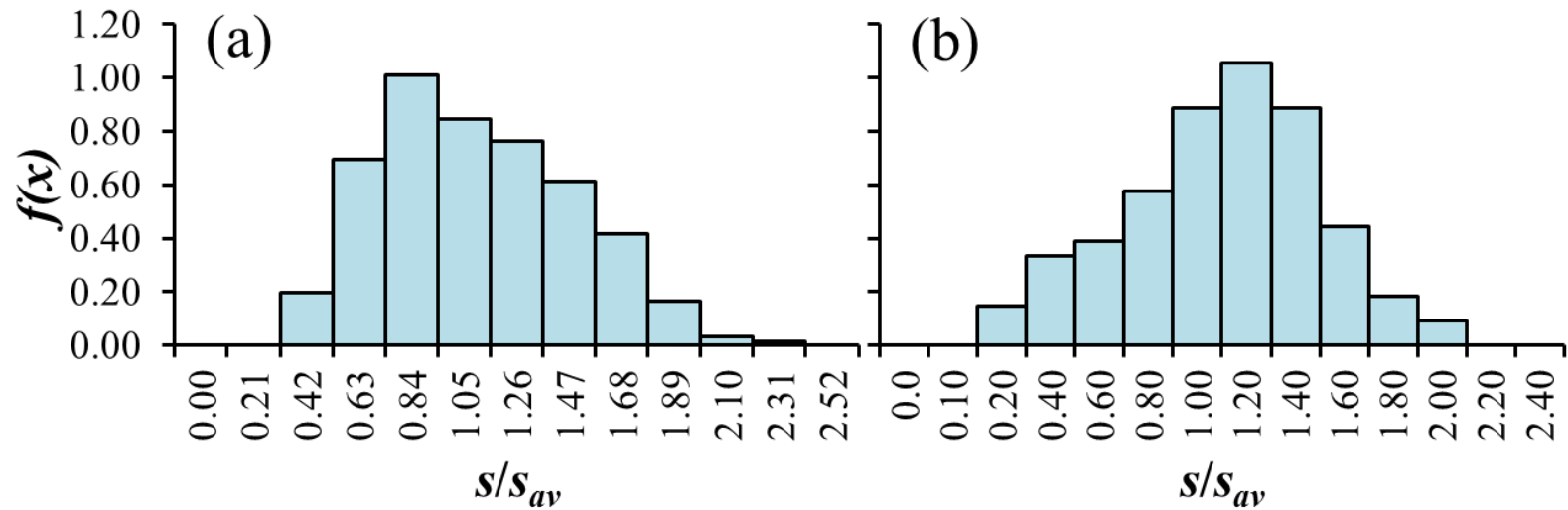


Figure 7. (a) 0.13 ML $s_{av} = 4827$ with bin size = 0.21 . The bin size is chosen to correspond to 1000 atoms/bin. The histogram represents 287 islands. (b) 1.2 ML $s_{av} = 20434$ with bin size = 0.20 . The bin size is chosen to correspond to 4000 atoms/bin. The histogram represents 270 islands.

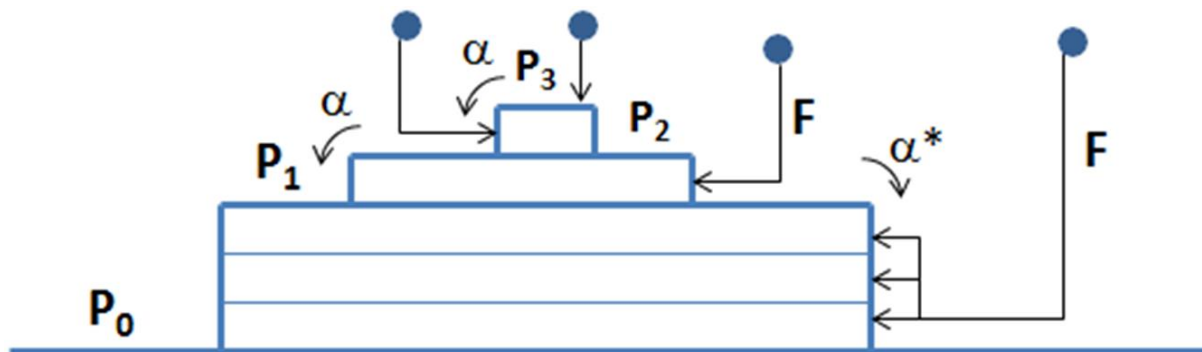


Figure 8. Schematic of model for multilayer growth.

Appendix 1. Additional Notes on Layer Occupations

For equivalent layers with deposition at rate F so $\theta = Ft$ and a fraction α of deposited atoms reaching the next lower layer, one has that:

$$d/d\theta \theta_j = P_{j-1} - \alpha P_{j-1} + \alpha P_j \text{ or } d/d\theta P_j = (1-\alpha)P_{j-1} - (1-2\alpha)P_j - \alpha P_{j+1} \text{ for } j > 1.$$

Separate equations are needed for $j = 0$ and $j = 1$. Neglecting these different equations yields the simple result for $W^2 = (1-2\alpha)\theta d^2$ quoted in the text. However, reliable results for smoother growth with larger α must account for the modified equations, noting that clearly this expression for W^2 cannot apply for $\alpha > 1/2$.

Appendix 2. Ion Damage

1. Initial experiments

A previous Cu/graphite study¹² on the Mantis QUAD-EV-C Mini e-beam evaporator used for these Dy depositions, showed that this evaporator produces a significant fraction of metal ions that damage the graphite surface. This evaporator operates via thermionic emission. A hot filament emits electrons and these electrons are accelerated toward the crucible, which is at a bias (or high voltage, HV) of +2 kV. Metal ions are generated by these filament electrons and accelerated by the HV on the crucible, causing ion damage on the graphite surface. These metal ions are only formed when both the filament and HV are on.

Initial Dy on graphite experiments were conducted leaving both the HV and filament on during deposition. This resulted in surface defects from ion damage produced by the evaporator.¹² The approximated fraction of the flux is estimated from Dy deposition experiments involving ion damage. We assume one ion causes one defect on the surface and all defects become a nucleation site. The ionized fraction = # islands/total atoms and can be

calculated from the slope of the island density vs. coverage plot (Figure A2.1). At 1 ML, the number of islands is estimated at 6.1×10^{-3} islands/nm². Using the surface density of Dy atoms in the hcp(0001) unit cell (4.5 atoms/nm²) we obtain:

$$(6.1 \times 10^{-3} \text{ islands/nm}^2)(1 \text{ nm}^2/4.5 \text{ atoms}) = 1.3 \times 10^{-3} \text{ islands/atom}$$

Thus the ionized fraction of our flux is approximately 1/750.

These experiments resulted in two different types of nucleated islands on the surface. The first type was an island with a flat base and additional growth on top of the island, not unlike the islands described in the main text (cf. Section 4.1). The island density of this flat base island decreases with increasing coverage (and thus increasing ion damage). Between 0 ML and 0.45 ML in coverage, 19-30% of total islands present are this type. Between 0.45 ML and 0.9 ML in coverage, 8-16% of total islands present are this type. Above 1.5 ML in coverage, less than 7% of total islands present are this type. The second type of island was a compact island which is circular in shape and has an average height of $1.4 \text{ nm} \pm 0.1 \text{ nm}$ ($N = 5,200$ islands). This height, compared with the 0.282 nm spacing between close-packed planes in bulk Dy, gives 5 layers of Dy. Figure A2.2 shows examples of the island morphology at various coverages when defects are present. The Dy atoms also decorate the step edge, shown in Figure A2.2(e). While the majority of the compact islands are circular in morphology, some are hexagonal in morphology. These islands are illustrated in Figure A2.3. The nucleation point for each island is believed to be a defect on the surface. To test this theory, we conducted an experiment looking at ion damaged and non-ion damaged surfaces.

2. Ion damage experiments

We conducted a set of experiments for Dy on graphite in order to study how island morphology depended on surface ion damage. Control experiments, which entailed leaving both the HV and filament on during deposition, were conducted before and after the tailored experiments. The tailored experiments entailed shutting off either the HV or the filament or both during deposition. Due to the similar ion damage nature from the evaporator, we hypothesized Dy would act comparable to Cu on a graphite surface without ion damage defects and preferentially adsorb at the step edges with no island nucleation on the terraces.¹² Figure A2.4 shows the results of these experiments. The island morphology drastically changed from that of the ion damage defect surface. The results show only nucleation of the flat base with additional growth Dy islands on the terraces and decoration of the step edges (not shown in the figure). These experiments led to the conclusion that the compact islands seen in initial deposition experiments undergo heterogeneous nucleation, where Dy adsorbs at the defect sites on the surface. The flat base islands then are the result of homogenous nucleation. Remaining experiments, as described in the main text, utilized the conditions for homogeneous nucleation.

Figures

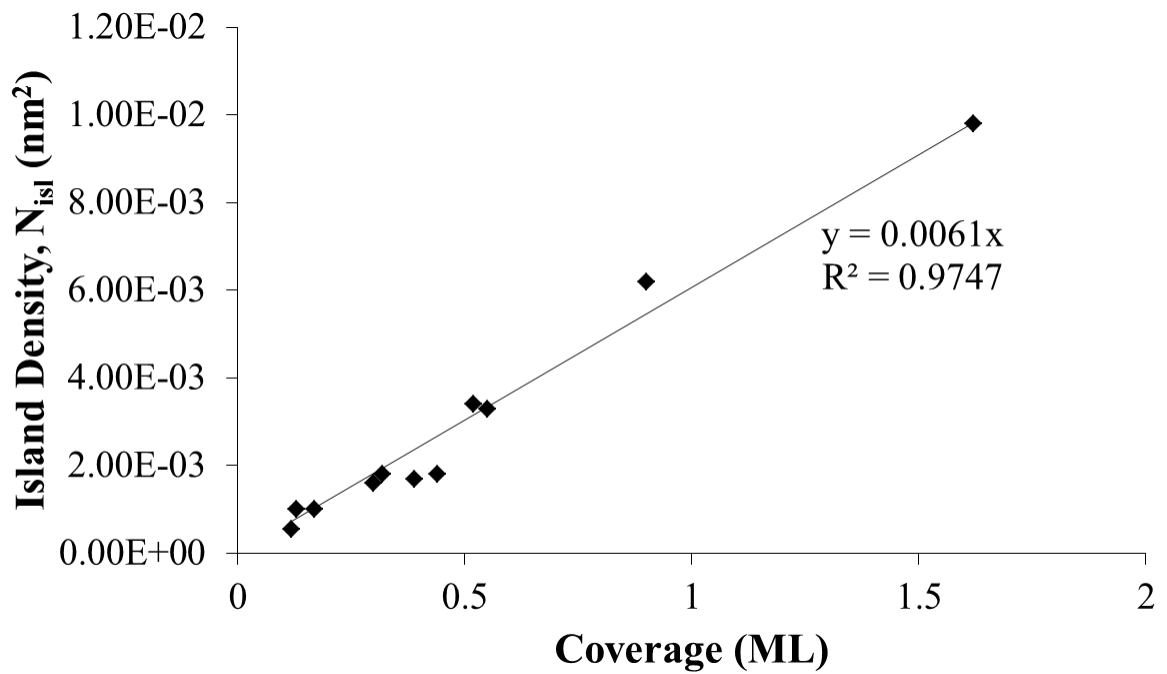


Figure A2.1. Dy island density as a function of Dy coverage with surface ion damage.

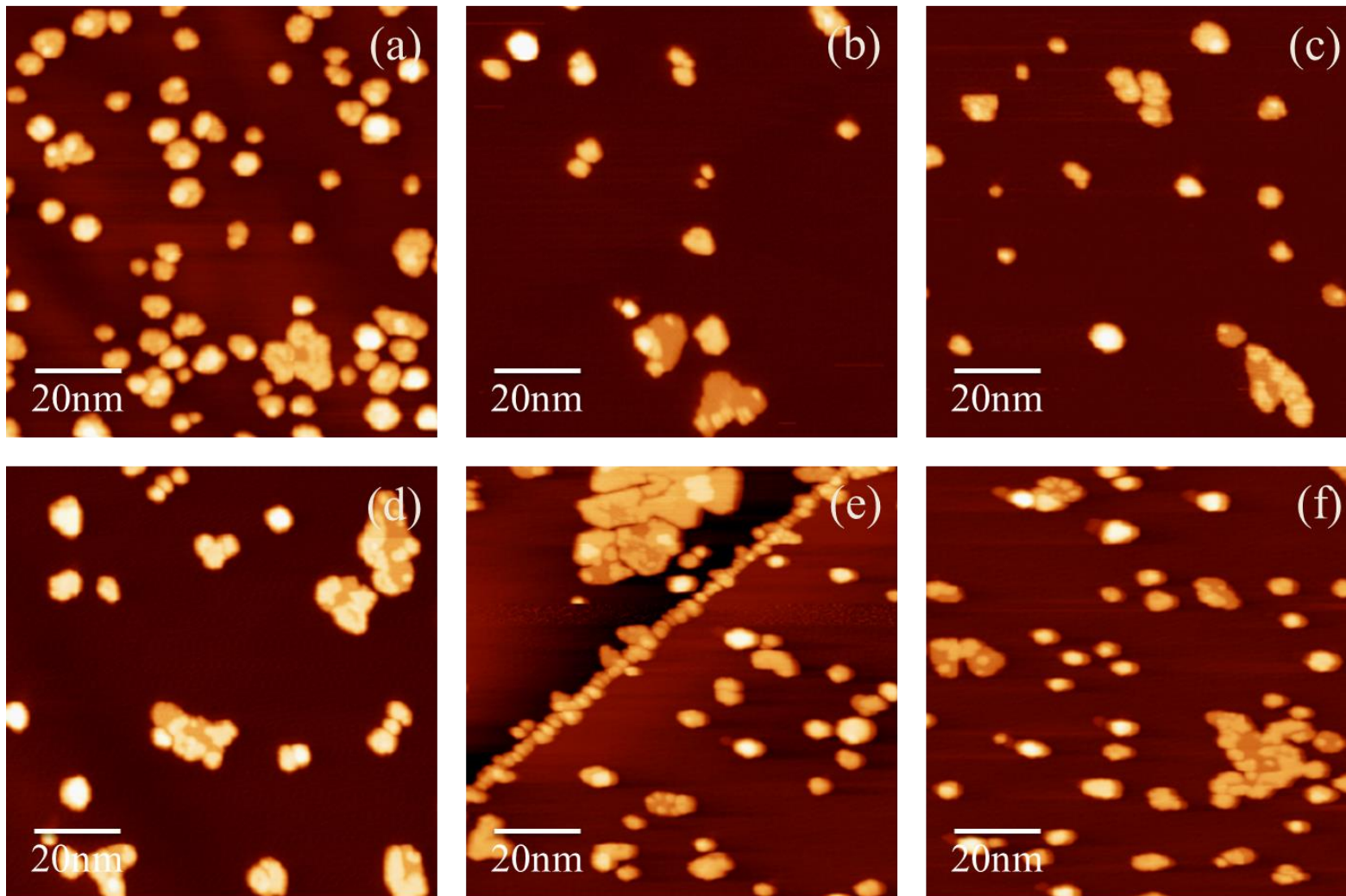


Figure A2.2. STM images of island morphology on the ion damage defect graphite surface at various coverages. (a) 0.9 ML (b) 0.17 ML (c) 0.30 ML (d) 0.44 ML (e) 0.52 ML (f) 0.52 ML. All images 100 nm x 100 nm. Scanning parameters 0.21 nA to 0.27 nA, -0.5 V to -1.0 V.

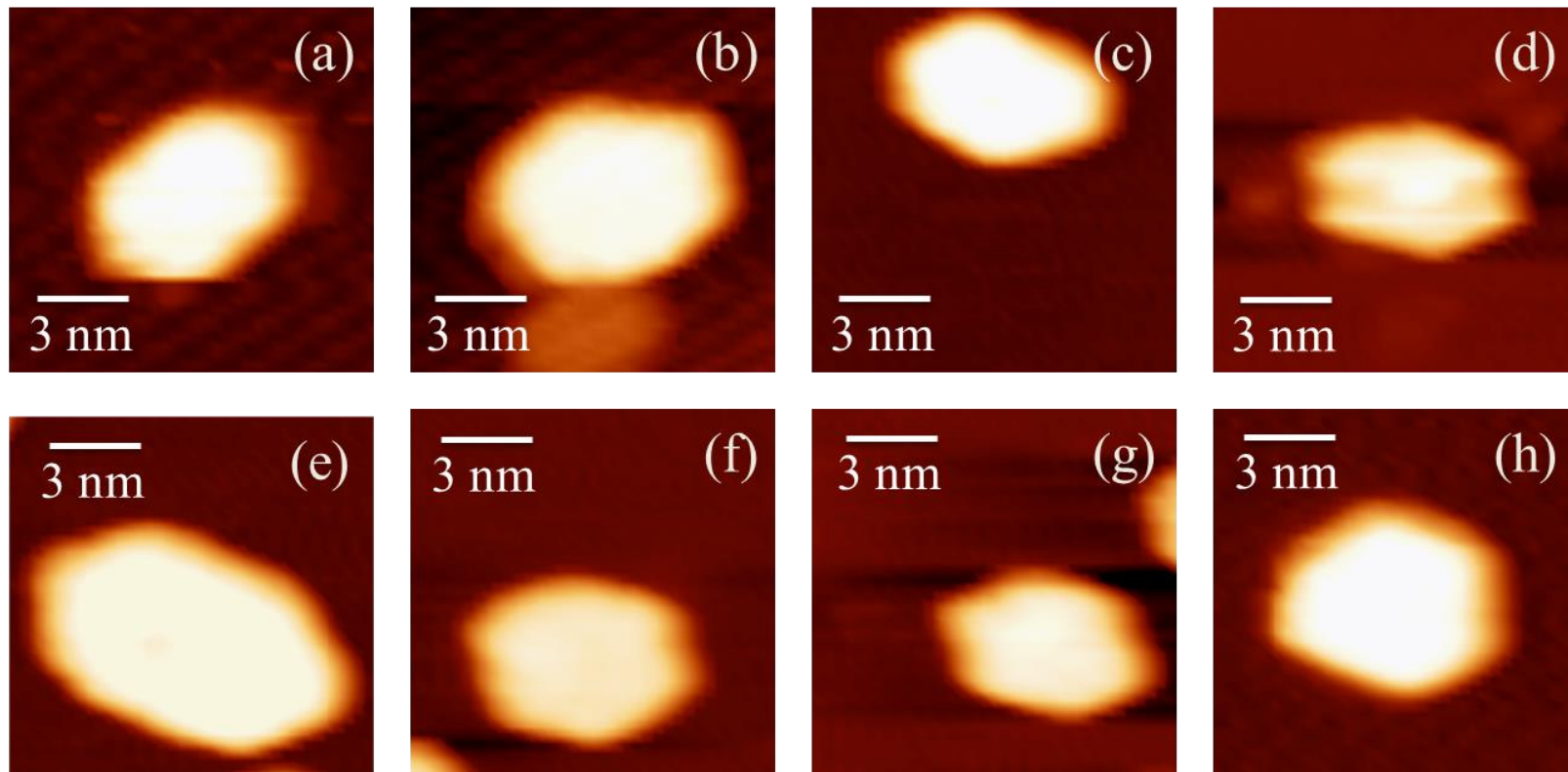


Figure A2.3. STM images of hexagonal island morphology present on the ion damage defect graphite surface. All images 12 nm x 12 nm. Scanning parameters 0.27 nA to 0.37 nA, -0.57 V to -0.88 V.

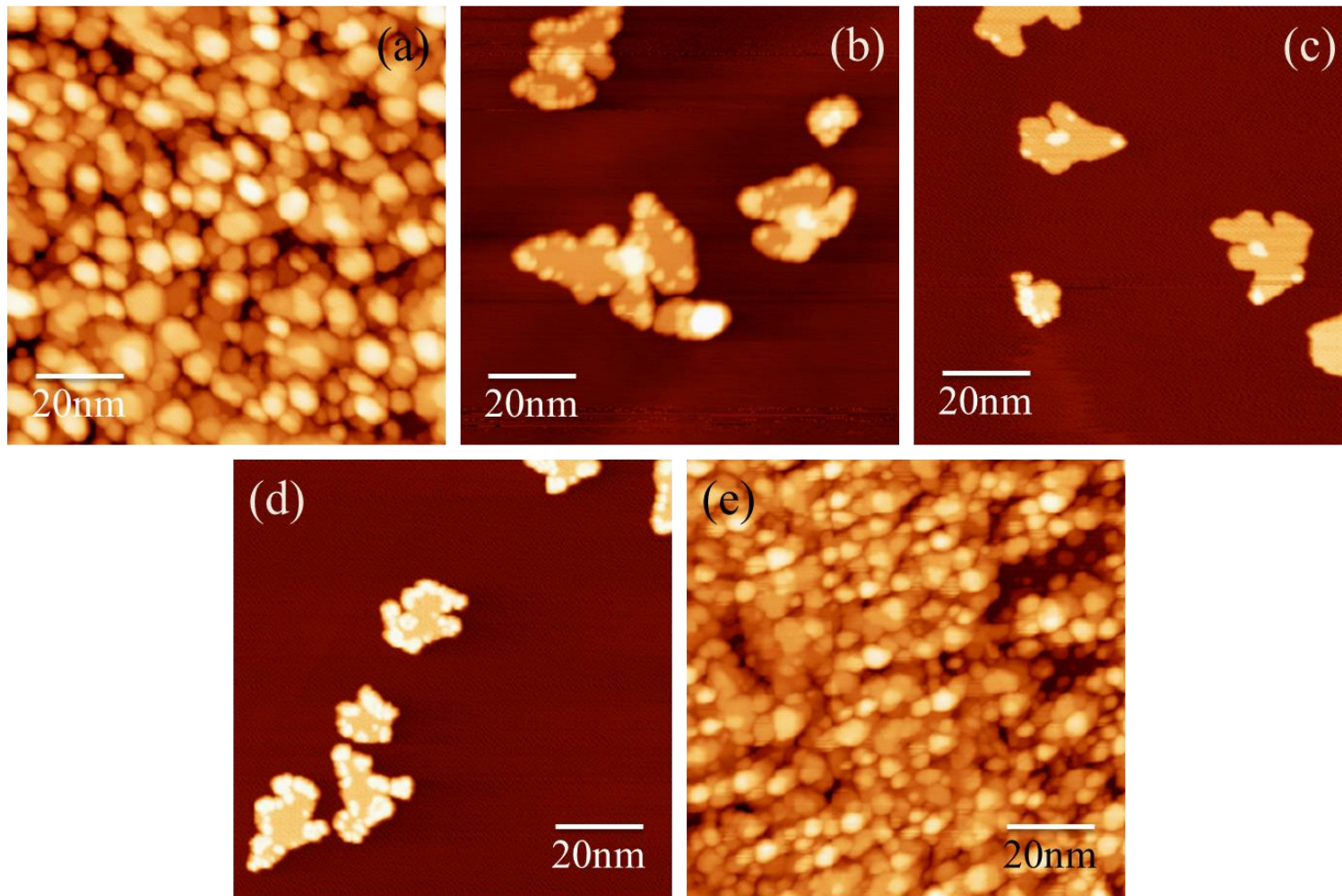


Figure A2.4. STM images from the ion damage experiments showing variations of high voltage (HV) and filament turned on or off. (a) HV On, Filament On (control). (b) HV Off, Filament On. (c) HV On, Filament Off. (d) HV Off, Filament Off. (e) HV On, Filament On (control). All images are 100 nm x 100 nm. Scanning parameters 0.15 nA to 0.26 nA, -1.0 V to -1.2 V.

Appendix 3. Anneals after Deposition

We annealed HOPG samples, after deposition at room temperature, to study Dy desorption and island morphology transformation.

1. With ion damage

We conducted three separate experimental anneals, one slightly above room temperature and two at higher temperatures, on graphite samples with Dy deposited at room temperature with ion damage from the evaporator. For the first experiment, the sample was held at 400 K for 15 minutes. Island density (2.0×10^{-3} islands/nm²) and island heights (flat base islands: 0.85 nm; compact islands: 1.4 nm) remain the same before and after heating. There is little to no change in island morphology as shown in Figure A3.1(a)-(b). 400 K is too low to initiate coarsening on, or loss of Dy from, the terraces.

The next experimental anneal was 750 K for 15 minutes. Island density decreases slightly from 3.0×10^{-3} islands/nm² to 2.0×10^{-3} islands/nm² suggesting coarsening of some islands. The flat base islands decrease in size while increasing in height to that of a compact island (~1.4 nm). The flat base island morphology also becomes more circular (or occasionally hexagonal) in nature. These changes are illustrated in Figure A3.1(c)-(d). Annealing to 750 K appears to promote island coarsening on the terraces.

The final experimental anneal was 1100 K for 1 minute. Island density decreases by an order of magnitude from 3.0×10^{-3} islands/nm² to 2.0×10^{-4} islands/nm² suggesting Dy island coarsening on, or loss of Dy from, the terraces. The islands remaining on the post-annealed surface are circular in morphology and range in height from 1.9 nm to 2.5 nm. Figure A3.2 illustrates these changes. The step edge decoration typically seen after a room

temperature deposition is absent after 1100 K, as shown in Figure A3.2(b). Annealing to 1100 K causes a loss of Dy from the terraces and coarsening of the remaining islands.

2. Without ion damage

We conducted three separate higher temperature anneals on Dy deposited on graphite at room temperature without surface ion damage. The first experiment was 600 K for 5 minutes. Island density remains the same at 4.5×10^{-4} islands/nm² after annealing. The islands decrease in size while increasing in height to that of the taller dot like features first described in Section 4.1 of the main text. This suggests the Dy atoms are moving from the flat base layer to the top most island layer. Figure A3.3 illustrates the changes that occur after annealing. The step edge remains decorated, similar to the decoration seen in all room temperature depositions. The morphology of the islands changes in two ways, either they become more circular in nature or the lobes become elongated. These changes are highlighted in Figure A3.3(b) with gray boxes. Annealing to 600 K appears to promote island self-coarsening with little to no island coarsening on the terraces or loss of Dy.

The next anneal was 700 K for 5 minutes. As with the 600 K anneal the island density remains constant at 2.0×10^{-4} islands/nm². The islands again decrease in size while increasing in height. The island heights range from 1.4 nm to 2.0 nm. Figure A3.4 shows these changes. The morphology of the islands also becomes more compact and circular in shape. The step edges remain decorated as well. Annealing to 700 K seems to promote island self-coarsening as it did at 600 K, but to a greater extent as the islands become smaller in size and taller in height. There is little to no island coarsening or loss of Dy.

The final anneal was 800 K for 5 minutes. The island density decreases slightly from 3.0×10^{-4} islands/nm² to 2.0×10^{-4} islands/nm² suggesting possible Dy desorption. As with the 600 K and 700 K anneals, the islands decrease in size and increase in height. The island heights range from 1.2 nm to 1.4 nm and the morphology is similar to the 600 K anneal wherein the islands become more circular or the lobes elongate. These island heights are not quite as tall as the 700 K anneal, suggesting that there is some loss of Dy via desorption. Figure A3.5 illustrates these changes. The 800 K anneals appears to promote island self-coarsening as seen with the previous anneals. Overall, there appears to be some Dy desorption as post-anneal island heights are lower and the island density has decreased. There is little to no island coarsening.

Figures

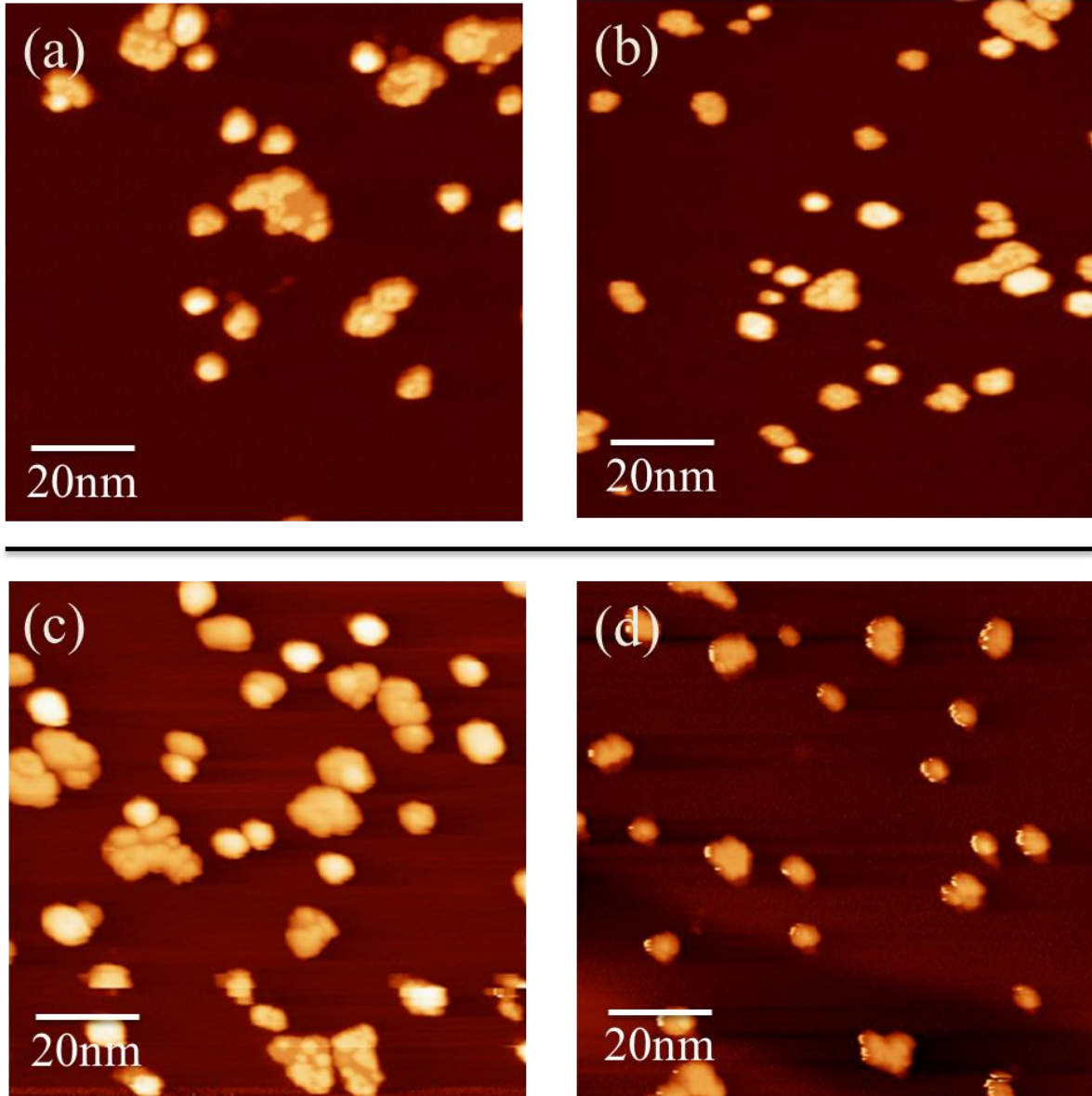


Figure A3.1. STM images illustrating the effects of annealing ion damage defect samples to 400 K and 750 K after a room temperature deposition. (a) 300 K (b) 400 K (c) 300 K (d) 750 K. All images 100 nm x 100 nm. Scanning parameters 0.21 nA to 0.27 nA, -0.8 V to -1.1 V.

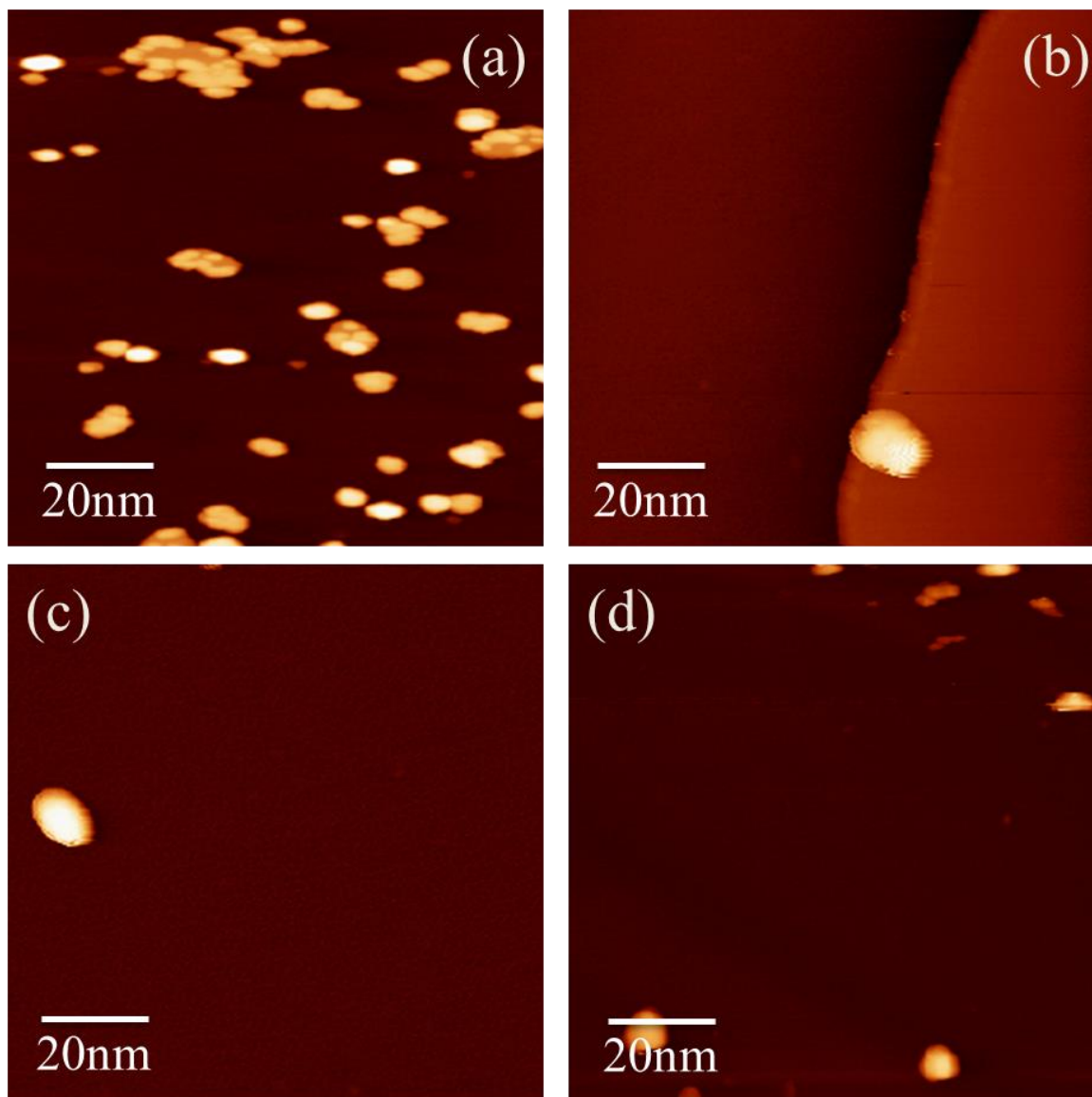


Figure A3.2. STM images illustrating the effects of annealing an ion damage defect sample to 1100 K after a room temperature deposition. (a) 300 K (b)-(d) 1100 K. All images 100 nm x 100 nm. Scanning parameters 0.21 nA to 0.40 nA, -0.20 V to -1.3 V.

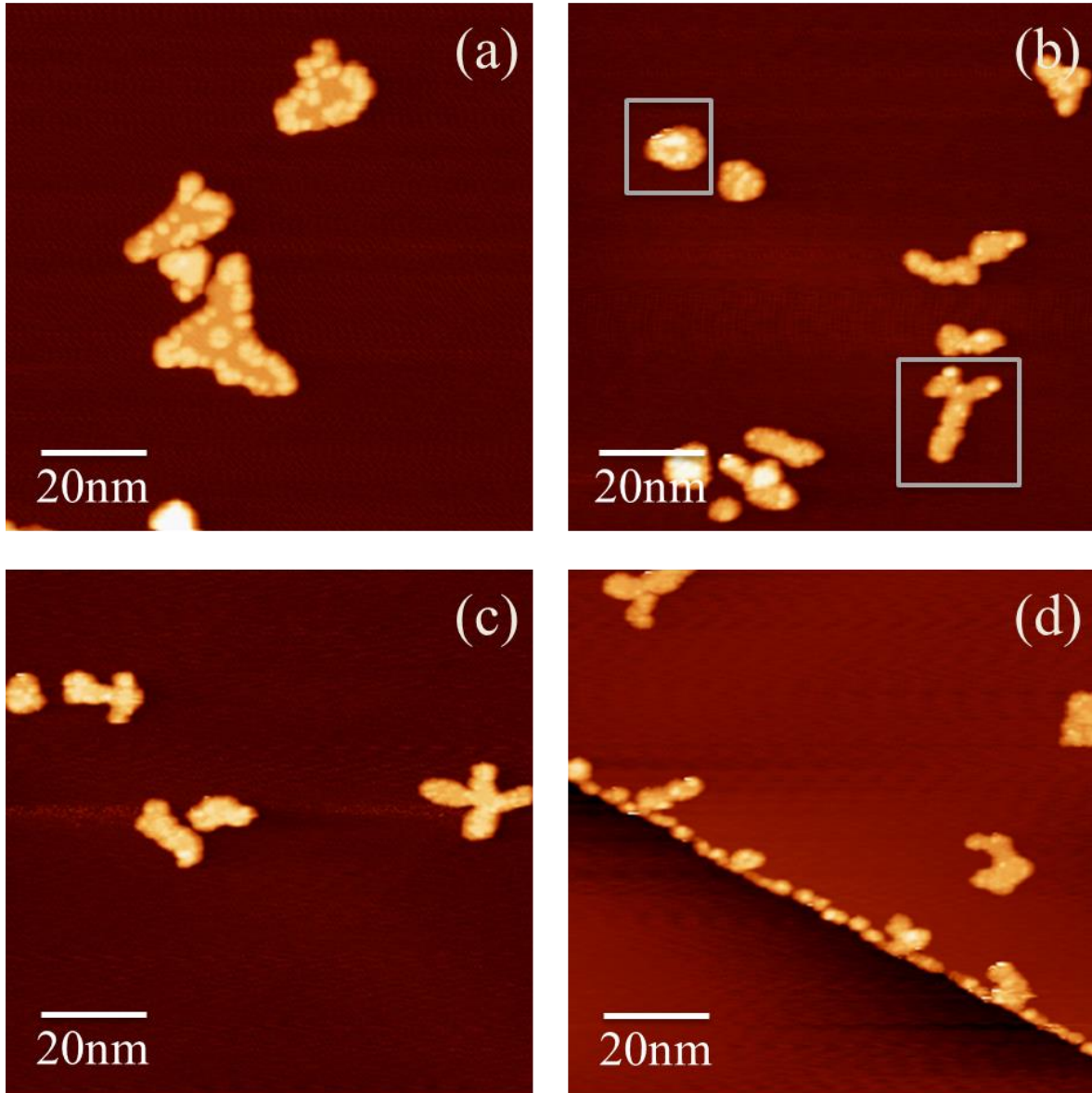


Figure A3.3. STM images illustrating the effects of annealing a graphite sample without ion damage defects to 600 K after a room temperature deposition. (a) 300 K (b)-(d) 600 K. The gray boxes in (b) illustrate the change in island morphology to circular or elongated lobes. All images 100 nm x 100 nm. Scanning parameters 0.21 nA, -1.1 V to -1.2 V.

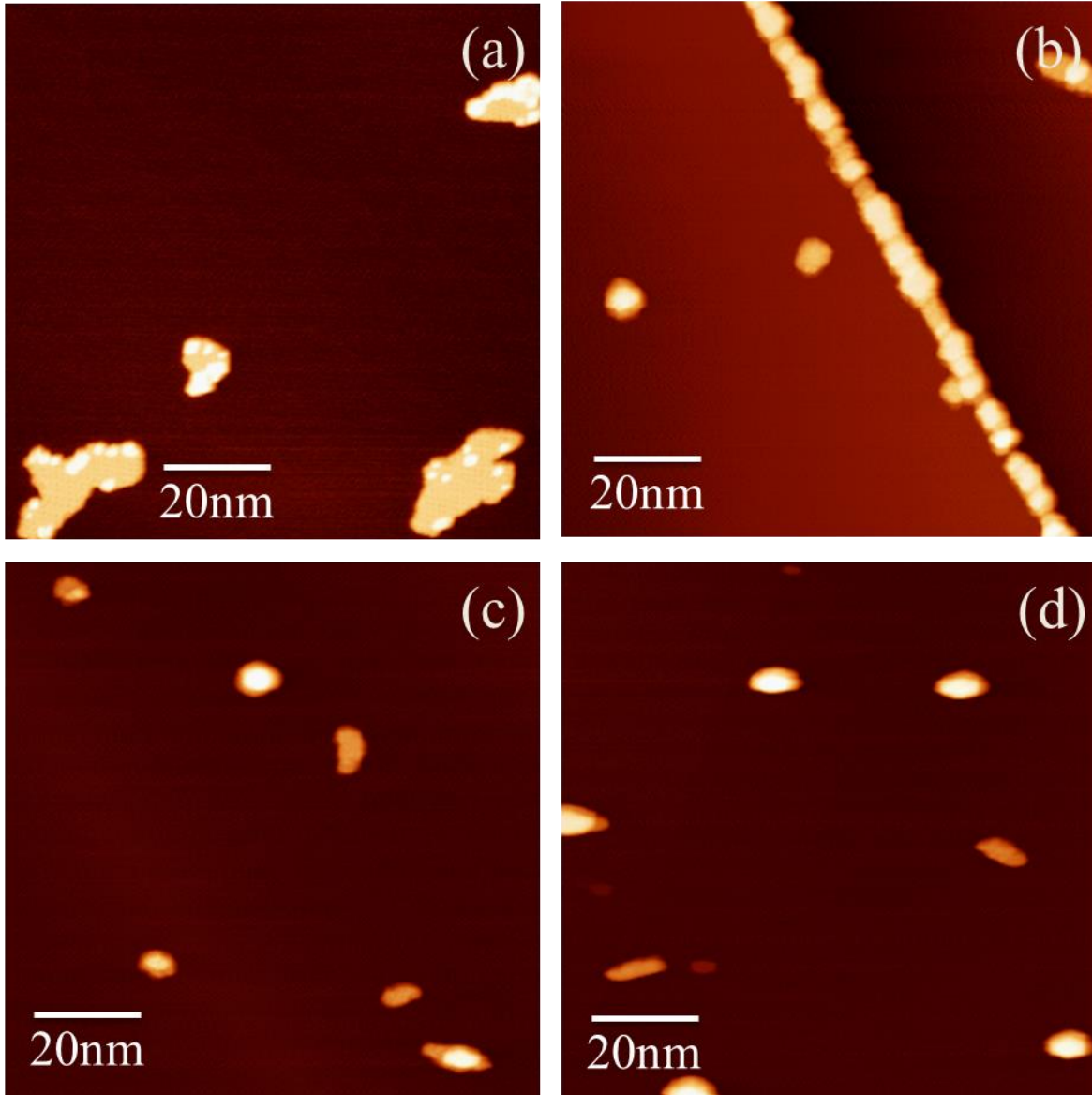


Figure A3.4. STM images illustrating the effects of annealing a graphite sample without ion damage defects to 700 K after a room temperature deposition. (a) 300 K (b)-(d) 700 K. All images 100 nm x 100 nm. Scanning parameters 0.19 nA, -1.1 V.

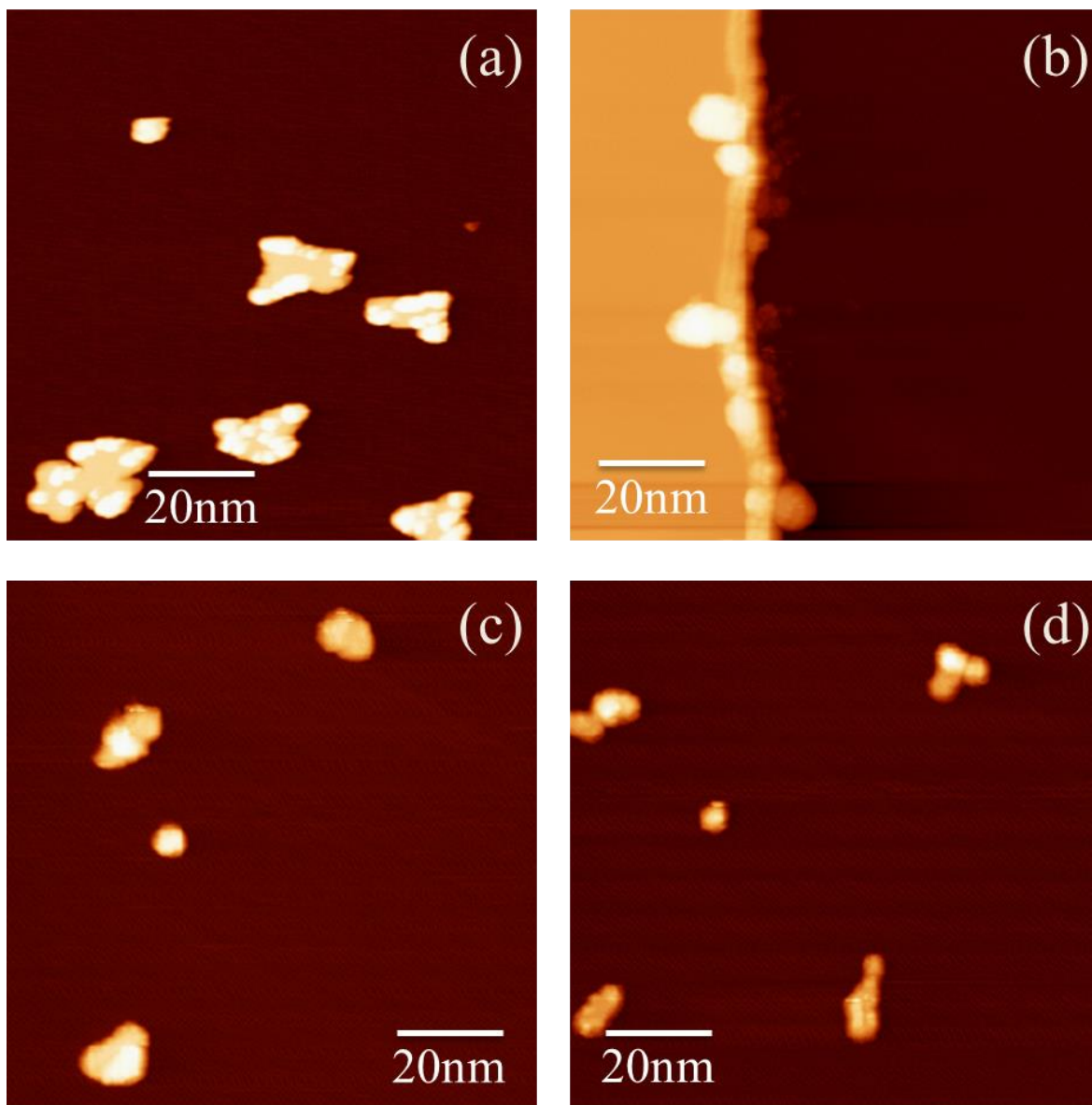


Figure A3.5. STM images illustrating the effects of annealing a graphite sample without ion damage defects to 800 K after a room temperature deposition. (a) 300 K (b)-(d) 800 K. All images 100 nm x 100 nm. Scanning parameters 0.23 nA, -1.1 V to -1.2 V.

Appendix 4. Oxygen Exposure after Deposition

Dy is known to readily react with oxygen in air and form a metal oxide. To study this effect, we exposed Dy supported on graphite in UHV to oxygen and analyzed the resulting surface.

20 Langmuirs (L) of oxygen was exposed to non-ion damaged graphite surfaces at room temperature (300 K) with adsorbed Dy islands in two separate experiments. Figure A4.1 illustrates the effects of these oxygen exposures. In both cases, the islands have coarsened to form larger rough islands which are most likely dysprosium oxide. This coarsening is reflected in the island density which decreases from 2.2×10^{-4} islands/nm² to 1.3×10^{-4} islands/nm². The rough island surfaces make height determination impractical. The presence of oxygen also causes a large double tip effect. An example of a double tip effect is highlighted in Figure A4.1(e) by the gray box.

A third separate oxygen exposure was performed while the graphite sample with Dy islands was held at 400 K during exposure. Figure A4.2 illustrates the effects of this elevated sample temperature oxygen exposure. As with the room temperature exposures, the island coarsen to form larger rough islands. The rough island surfaces once again make height determination impractical. The notable difference between room temperature and 400 K exposures is the island density. With the 400 K exposure the island density decreases from 2.4×10^{-4} islands/nm² to 6.0×10^{-5} islands/nm², close to an order of magnitude decrease. This decrease is significant when compared to the smaller decrease, 2.2×10^{-4} islands/nm² to 1.3×10^{-4} islands/nm², seen at 300 K. This slight temperature elevation could be causing a loss of dysprosium oxide from the surface, accounting for the large island density decrease. There is no additional decoration of the step edges, as shown in Figure A4.2(c).

Figures

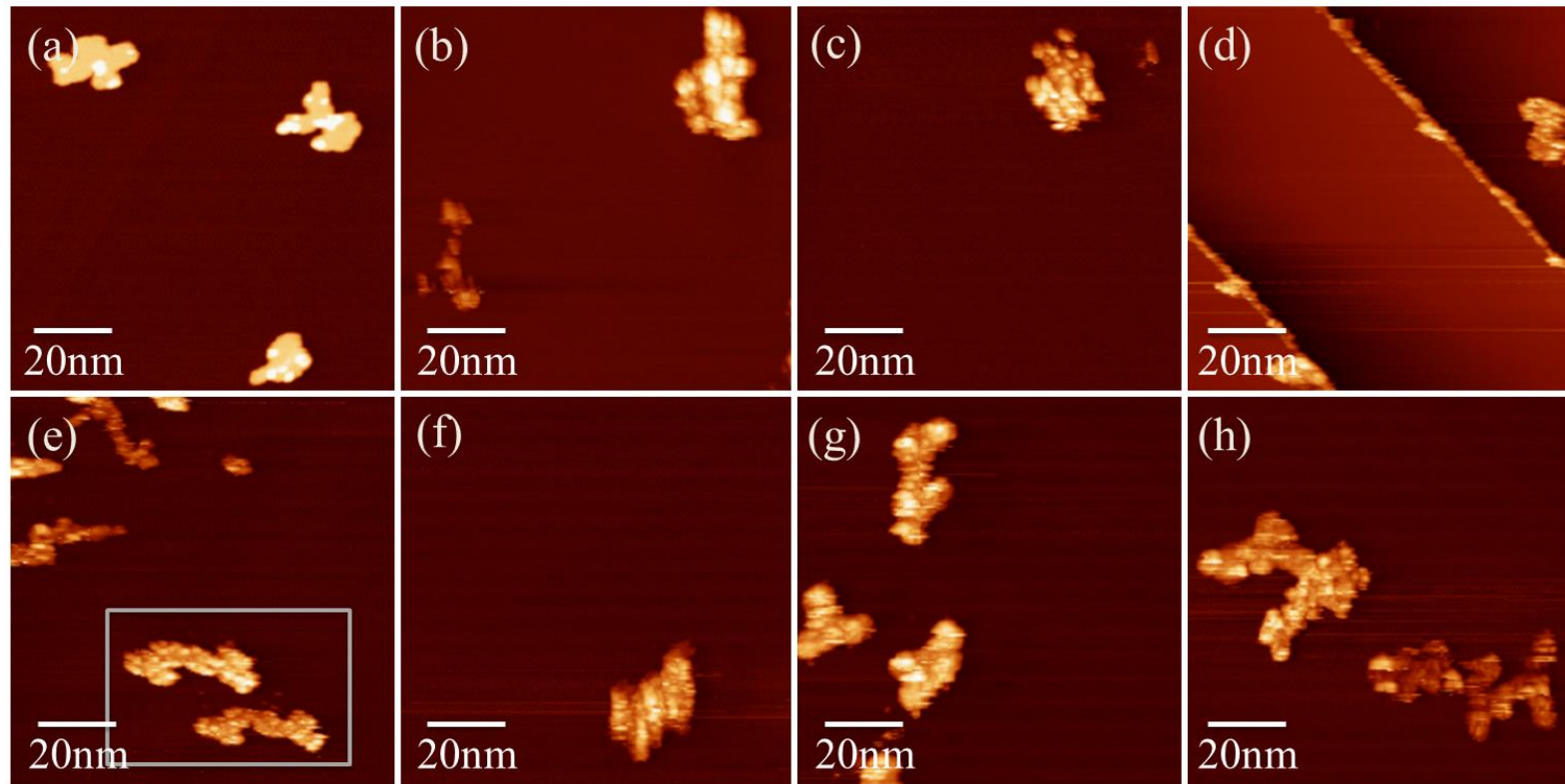


Figure A4.1. STM images illustrating the effects of oxygen exposure on a graphite sample without ion damage defects with adsorbed Dy islands. (a) Post-Dy deposition. (b)-(h) After 20 L O₂ exposure. The gray box in (e) highlights an example of double tip effect. All images 100 nm x 100 nm. Scanning parameters without oxygen 0.21 nA, -1.0 V; with oxygen 0.22 nA to 0.26 nA, -3.2 V to -3.8 V.

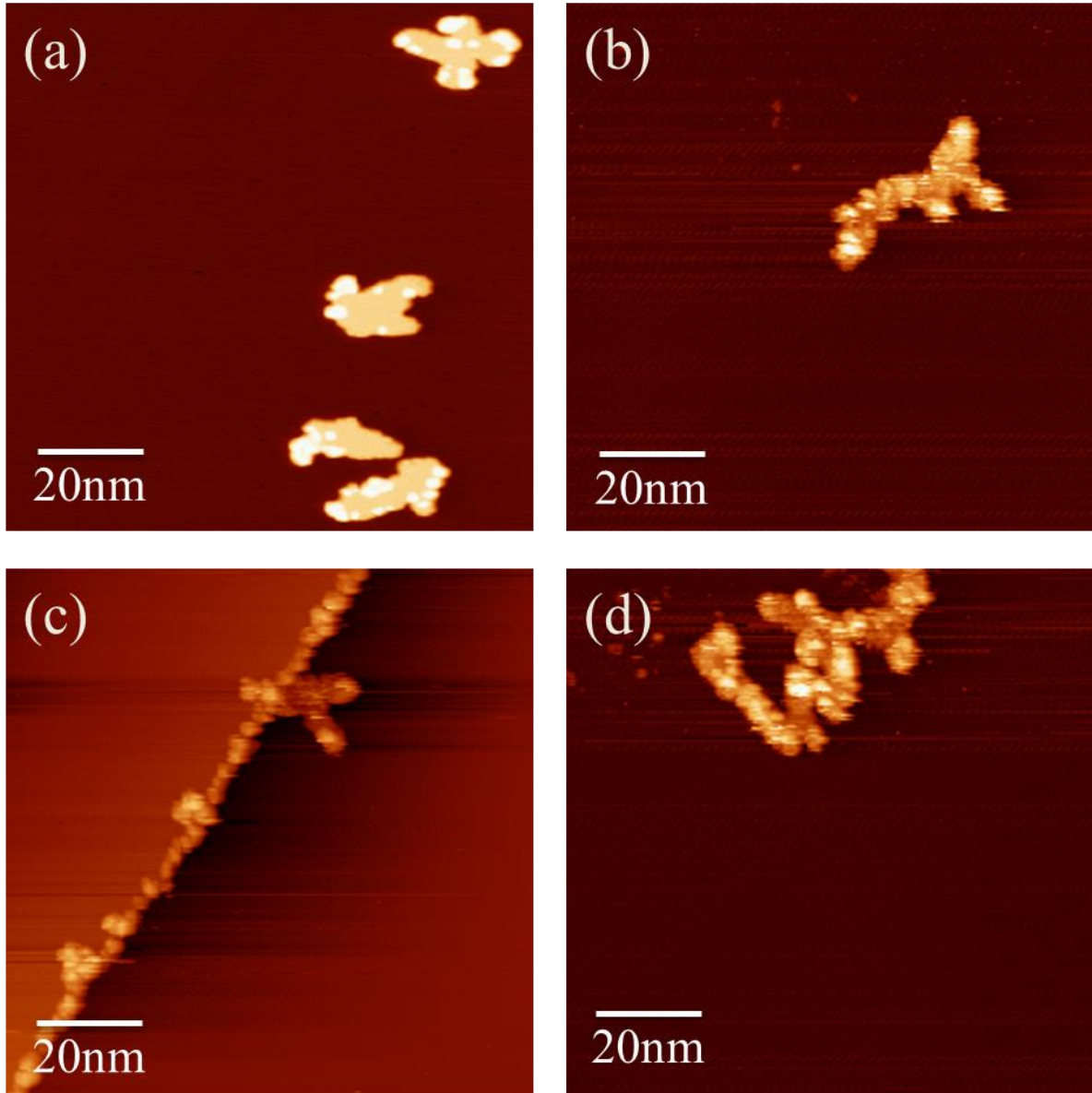


Figure A4.2. STM images illustrating the effects of oxygen exposure on a graphite sample without ion damage defects with adsorbed Dy islands held at 400 K during exposure. (a) Post-Dy deposition. (b)-(d) After 20 L O₂ exposure with graphite at 400 K. All images 100 nm x 100 nm. Scanning parameters without oxygen 0.19 nA, -1.0 V; with oxygen 0.20 nA, -3.3 V.

References

- ¹C. Vo-Van, Z. Kassir-Bodon, H. Yang, J. Coraux, J. Vogel, S. Pizzini, P. Bayle-Guillemaud, M. Chshiev, L. Ranno, V. Guisset, P. David, V. Salvador and O. Fruchart, "Ultrathin epitaxial cobalt films on graphene for spintronic investigations and applications," *New Journal of Physics* **12**, 103040 (2010).
- ²B. Uchoa, T. G. Rappoport and A. H. Castro Neto, "Kondo Quantum Criticality of Magnetic Adatoms in Graphene," *Physical Review Letters* **106**, 016801 (2011).
- ³H. Sevinçli, M. Topsakal, E. Durgun and S. Ciraci, "Electronic and magnetic properties of 3d transition-metal atom adsorbed graphene and graphene nanoribbons," *Physical Review B* **77**, 195434 (2008).
- ⁴S. M. Binz, M. Hupalo, X. Liu, C. Z. Wang, W.-C. Lu, P. A. Thiel, K. M. Ho, E. H. Conrad and M. C. Tringides, "High island densities and long range repulsive interactions: Fe on epitaxial graphene," *Physical Review Letters* **109**, 026103/1 (2012).
- ⁵A. N. Rudenko, F. J. Keil, M. I. Katsnelson and A. I. Lichtenstein, "Adsorption of cobalt on graphene: Electron correlation effects from a quantum chemical perspective," *Physical Review B* **86**, 075422 (2012).
- ⁶X. Liu, Y. Han, J. W. Evans, A. K. Engstfeld, R. J. Behm, M. C. Tringides, M. Hupalo, H.-Q. Lin, L. Huang, K.-M. Ho, D. Appy, P. A. Thiel and C.-Z. Wang, "Growth morphology and properties of metals on graphene," *Progress in Surface Science* **90**, 397 (2015).
- ⁷M. T. Hershberger, M. Hupalo, P. A. Thiel and M. C. Tringides, "Growth of fcc(111) Dy multi-height islands on 6H-SiC(0001) graphene," *Journal of Physics: Condensed Matter* **25**, (2013).
- ⁸M. Hupalo, X. Liu, C.-Z. Wang, W.-C. Lu, Y.-X. Yao, K.-M. Ho and M. C. Tringides, "Metal Nanostructure Formation on Graphene: Weak versus Strong Bonding," *Advanced Materials* **23**, 2082 (2011).
- ⁹X. Liu, C. Z. Wang, M. Hupalo, W. C. Lu, M. C. Tringides, Y. X. Yao and K. M. Ho, "Metals on graphene: correlation between adatom adsorption behavior and growth morphology," *Physical Chemistry Chemical Physics* **14**, 9157 (2012).
- ¹⁰S. A. Gorovikov, A. M. Shikin, G. V. Prudnikova, V. K. Adamchuk, S. L. Molodtsov, C. Laubschat and A. M. Ionov, "Formation of surface intercalation compounds at Gd(Dy)/graphite interfaces under thermal annealing," *Surface Science* **474**, 98 (2001).
- ¹¹G.-Y. Adachi, N. Imanaka and F. Zhang, "Chapter 99 Rare earth carbides" in *Handbook on the Physics and Chemistry of Rare Earths* (Elsevier, 1991), Volume 15, pp. 61.
- ¹²D. Appy, H. Lei, Y. Han, C.-Z. Wang, M. C. Tringides, D. Shao, E. J. Kwolek, J. W. Evans and P. A. Thiel, "Determining whether metals nucleate homogeneously on graphite: A case study with copper," *Physical Review B* **90**, 195406 (2014).

- ¹³G. Kresse and J. Furthmüller, "Efficiency of ab-initio total energy calculations for metals and semiconductors using a plane-wave basis set," *Computational Materials Science* **6**, 15 (1996).
- ¹⁴J. P. Perdew, K. Burke and M. Ernzerhof, "Generalized gradient approximation made simple," *Physical Review Letters* **77**, 3865 (1996).
- ¹⁵J. Klimeš, D. R. Bowler and A. Michaelides, "Van der Waals density functionals applied to solids," *Physical Review B* **83**, 195131 (2011).
- ¹⁶J. Klimeš, D. R. Bowler and A. Michaelides, "Chemical accuracy for the van der Waals density functional," *Journal of Physics: Condensed Matter* **22**, 022201 (2010).
- ¹⁷G. Graziano, J. Klimeš, F. Fernandez-Alonso and A. Michaelides, "Improved description of soft layered materials with van der Waals density functional theory," *Journal of Physics: Condensed Matter* **24**, 424216 (2012).
- ¹⁸P. E. Blöchl, "Projector augmented-wave method," *Physical Review B* **50**, 17953 (1994).
- ¹⁹D. Appy, H. Lei, C.-Z. Wang, M. C. Tringides, D.-J. Liu, J. W. Evans and P. A. Thiel, "Transition metals on the (0001) surface of graphite: Fundamental aspects of adsorption, diffusion, and morphology," *Progress in Surface Science* **89**, 219 (2014).
- ²⁰C. Kittel, *Introduction to Solid State Physics*, 8th ed. (John Wiley & Sons, USA, 2004).
- ²¹X. Liu, M. Hupalo, C.-Z. Wang, W.-C. Lu, P. A. Thiel, K.-M. Ho and M. C. Tringides, "Growth morphology and thermal stability of metal islands on graphene," *Physical Review B* **86**, 081414 (2012).
- ²²J. W. Evans, P. A. Thiel and M. C. Bartelt, "Morphological evolution during epitaxial thin film growth: Formation of 2D islands and 3D mounds," *Surface Science Reports* **61**, 1 (2006).
- ²³Y. Han, "Unpublished point island simulation results," (2015).
- ²⁴M. C. Bartelt, S. Günther, E. Kopatzki, R. J. Behm and J. W. Evans, "Island-size distributions in submonolayer epitaxial growth: Influence of the mobility of small clusters," *Physical Review B* **53**, 4099 (1996).
- ²⁵C. R. Stoldt, C. J. Jenks, P. A. Thiel, A. M. Cadilhe and J. W. Evans, "Smoluchowski ripening of Ag islands on Ag(100)," *The Journal of Chemical Physics* **111**, 5157 (1999).
- ²⁶P. I. Cohen, G. S. Petrich, P. R. Pukite, G. J. Whaley and A. S. Arrott, "Birth-death models of epitaxy," *Surface Science* **216**, 222 (1989).
- ²⁷W. C. Elliott, P. F. Miceli, T. Tse and P. W. Stephens, *Kinetic Roughening During Ag Homoepitaxy*, 1 ed. (Plenum, New York, 1997), Vol. 360, Nato Science Series B.

- ²⁸V. Fournée, A. R. Ross, T. A. Lograsso, J. W. Evans and P. A. Thiel, "Growth of Ag thin films on complex surfaces of quasicrystals and approximant phases," *Surface Science* **537**, 5 (2003).
- ²⁹Z. Luo, L. A. Somers, Y. Dan, T. Ly, N. J. Kybert, E. J. Mele and A. T. C. Johnson, "Size-Selective Nanoparticle Growth on Few-Layer Graphene Films," *Nano Letters* **10**, 777 (2010).
- ³⁰J. A. Venables, "Nucleation and growth of thin films," *Reports on Progress in Physics* **47**, 399 (1984).
- ³¹J. Zhang, M. Brehm, M. Grydlik and O. G. Schmidt, "Evolution of epitaxial semiconductor nanodots and nanowires from supersaturated wetting layers," *Chemical Society Reviews* **44**, 26 (2015).
- ³²Y. Kuo, P. Yen, W. Chen, S. Chen and S. Yau, "In situ scanning tunneling microscopy study of cobalt thin film electrodeposited on Pt(111) electrode," *Electrochimica Acta* **112**, 831 (2013).
- ³³E. Lundgren, B. Stanka, M. Schmid and P. Varga, "Thin films of Co on Pt(111): Strain relaxation and growth," *Physical Review B* **62**, 2843 (2000).
- ³⁴P. Allongue, L. Cagnon, C. Gomes, A. Gündel and V. Costa, "Electrodeposition of Co and Ni/Au(111) ultrathin layers. Part I: nucleation and growth mechanisms from in situ STM," *Surface Science* **557**, 41 (2004).
- ³⁵B. Voigtländer, G. Meyer and N. M. Amer, "Epitaxial growth of thin magnetic cobalt films on Au(111) studied by scanning tunneling microscopy," *Physical Review B* **44**, 10354 (1991).

CHAPTER 3
THE (111) SURFACE OF NaAu_2 : STRUCTURE, COMPOSITION, AND
STABILITY

A paper published in *Inorganic Chemistry*

Emma J. Kwolek¹, Roland Widmer², Oliver Gröning², Okan Deniz², Holly Walen¹, Chad D. Yuen^{1,5}, Wenyu Huang¹, Deborah L. Schlage³, Mark Wallingford³, Patricia A. Thiel^{1,3,4}

¹Department of Chemistry, Iowa State University, Ames, Iowa 50011 USA

²nanotech@surfaces Laboratory, EMPA, Swiss Federal Laboratories for Materials Science and Technology, Ueberlandstrasse 129, 8600 Duebendorf, Switzerland

³The Ames Laboratory, Ames, Iowa 50011 USA

⁴Department of Materials Science & Engineering, Iowa State University, Ames, Iowa 50011
USA

⁵Present address: Department of Chemistry and Biochemistry, Augstana College, Rock Island, Illinois 61201 USA

Abstract

The (111) surface of single-crystal NaAu_2 is a model for catalytically-active, powdered NaAu_2 . We prepare and characterize this surface with a broad suite of techniques. Preparation in ultrahigh vacuum consists of the traditional approach of ion bombardment (to remove impurities) and thermal annealing (to restore surface order). Both of these steps, however, cause loss of Na, and repeated treatments eventually trigger conversion of the

surface and near-surface region to crystalline Au. The bulk has a limited ability to repopulate the surface Na. Under conditions where Na depletion is minimized, electron diffraction patterns are consistent with the bulk-terminated structure, and STM reveals mesa-like features with lateral dimensions of a few tens of nanometers. The tops of the mesas do not possess fine structure characteristic of a periodic lattice, suggesting that the surface layer is disordered under the conditions of these experiments.

1. Introduction

Intermetallics are used commercially in a variety of applications, from structural components in the aerospace and automotive industries, to energy storage devices, heating elements, and electronic materials.¹ In recent years, they have also come into consideration as possible alternatives to precious metal catalysts for certain reactions, notably steam reforming of methanol² and selective dehydrogenation of alkynes.^{3,4} Independently, there has been great interest in Au—in the form of nanoparticles—as an effective low temperature catalyst, especially for the benchmark reaction of CO oxidation.⁵⁻⁷ These two trains of thought naturally intersect at the possibility that intermetallics containing Au might show interesting catalytic properties. John Corbett pioneered the use of Au to create diverse intermetallic compounds, and so this topic is a fitting vehicle to pay homage to his achievements.

Recently, a simple Au-rich intermetallic, NaAu₂, was found to have high catalytic activity for CO oxidation at relatively low temperature ($T < 400$ K), in powdered form.⁸ An explanation was proposed, on the basis of density functional theory (DFT). The theoretical work showed that the (111) surface is most stable among the low-index faces, and that it is

nearly bulk-terminated in its clean state. For the oxidation reaction mechanism, DFT revealed a pathway in which molecular oxygen triggers a Na atom to 'pop out' toward the surface, then reacts with CO to form an OOCO intermediate, with subsequent dissociation to CO₂ as the rate-limiting step. However, experimental determination of the clean surface structure and composition—especially their relation to the bulk structure and composition—has not been undertaken. This would test the DFT model for the catalytic surface. Thermal stability of any surface state is also an open question. The purpose of this work is to address these issues. We use a single-crystal sample to investigate the structure, composition, and stability of NaAu₂ (111) in ultrahigh vacuum. Single crystals are advantageous because their surfaces usually exhibit a terrace-step morphology, in which the atomic arrangement on the terraces and the step heights can be compared with bulk structure.⁹

No surfaces of bulk NaAu₂ have been characterized before, although a closely-related system has been investigated. Barth et al. studied Na films deposited on Au(111). They found that Na and Au react to form films and multilayers of NaAu₂, exhibiting a (111) surface orientation commensurate with the underlying Au, after heating samples (with sufficiently high Na coverages) to temperatures ranging from 300 to 600 K.^{10,11}

NaAu₂ has a cubic unit cell with 24 atoms and lattice parameter 0.795 nm.^{12,13} It is a diamond lattice in which 4 of the Na atoms fill tetrahedral holes. The (111) surface has a hexagonal arrangement of Au atoms in which 1/4 of the Au atoms are missing, with a Na atom below each Au vacancy. It is represented schematically in Figure 1. The surface lattice parameter of NaAu₂(111) is 0.550 nm, slightly less than twice the value of 0.288 nm for Au(111). Bulk NaAu₂ melts congruently at 1275 K.¹³

2. Experimental Details

Single-crystal samples of NaAu_2 were grown at the Materials Preparation Center of the Ames Laboratory via the Bridgman technique. Special precautions were necessary to handle Na because of its sensitivity to air and moisture, and its inability to be arc melted. Special techniques were also needed to extract, cut, and polish a sample after growth, because the intermetallic was brittle, and it had become bonded to the Ta crucible which also became brittle during growth. To our knowledge, this is the first growth of a macroscopic single crystal of this material. The sample was oriented by back reflection Laue and the surface prepared by normal metallographic techniques, since the Na was passivated once alloyed.

UHV experiments were conducted on 4 different samples (A, B, C, D), cut from 2 ingots prepared in separate growths (A from one growth, B-D from the other). The areal dimensions of the samples ranged from 2.5 to 3.5 mm wide, and 5.5 to 9.5 mm long. Different sets of experiments were carried out on different samples, with some overlap. Two of the samples were re-polished during the course of experiments, and this was considered to produce a totally fresh surface of NaAu_2 , based on data presented in Section 3.1. From this combined and extensive dataset, certain trends emerged, which are reported in Section 3.

Experiments were conducted both at EMPA in Dübendorf, Switzerland, and at the Ames Laboratory in Ames, Iowa, USA. All of the X-ray photoelectron diffraction (XPD), and low-energy electron diffraction (LEED) experiments were carried out at EMPA, together with the majority of the scanning tunneling microscopy (STM) and X-ray photoelectron spectroscopy (XPS) work. Some STM and XPS, plus all of the temperature-programmed

desorption (TPD) and X-ray diffraction (XRD) work was done at the Ames Laboratory.

Details relevant to the EMPA work¹⁴ and to the Ames work¹⁵ are available elsewhere.

All experiments (except XRD and TPD) were done in UHV with base pressure below 1.0×10^{-10} mbar. TPD was carried out in UHV with a base pressure of 7×10^{-10} mbar. XRD was conducted in air. All data were acquired with the sample at room temperature, except of course in TPD.

After introduction to UHV, and between each experiment, each sample was sputtered and annealed. Typically, sputtering was done with 0.75 keV Ar^+ for 5 minutes at normal incidence and with the sample at 300 K. Annealing temperatures of 435 K to 850 K were investigated, and the most common annealing condition was 20 minutes at 500 K.

In XPS and XPD, an Al K_{α} source was used. XPS data were analyzed using CASA software.¹⁶ Sensitivity factors for Na and Au were 8.52 and 17.1, respectively. In XRD, θ/θ scans were measured using Co K_{α} radiation (1.79 Å), and a PANalytical X'Pert Pro system. The XRD data were used purely for phase analysis.

3. Experimental Results

3.1. Composition from XPS and XRD

Figure 2 shows the Na:Au composition ratio, R , as a function of the number of sputter-anneal treatments, for two samples. (Between each treatment, an experiment such as XPD or STM was conducted.) Both samples showed ratios close to that expected from the bulk stoichiometry, $R = 0.5$, up to the point marked by the vertical line. For treatments to the right of the line, R dropped below 0.4 and never recovered.

The sample in (a) was annealed at temperatures (T_{ann}) of 430-600 K up until treatment 4 (just to the right of the vertical line), where it was annealed at $T_{ann} = 650$ K. This sequence, involving some treatments at relatively high T_{ann} , apparently triggered a permanent depletion of Na. The sample in (b) was kept at lower $T_{ann} = 500$ K. Nonetheless, its composition changed permanently after treatment 15. When R dropped below 0.4, no subsequent treatment could cause it to increase again, including long anneals at low $T_{ann} = 430$ -500 K, or short anneals at high $T_{ann} = 770$ -850 K. Together, these results show that irreversible Na depletion in the surface and near-surface region occurs quickly at high T_{ann} (600-650 K), or slowly as a result of sputter-annealing cycles at lower T_{ann} (500 K). In other words, not only temperature but also cumulative history is important. In the end, our preferred UHV treatment consisted of sputtering for 5 minutes and annealing at 500 K for 20 minutes. Samples could be subjected to 12-15 of these treatments before showing surface compositional change, and other signs of irreversible Na depletion outlined in Section 3.3.

Sample deterioration, resulting from repeated sputter-anneal treatments in UHV, is confirmed by XRD of samples before or after use in UHV. Figure 3(a) is a powder pattern from part of a ground NaAu_2 crystal; only lines associated with NaAu_2 are visible. Figure 3(b) and Figure 3(c) are post-mortem XRD patterns of single crystals that had shown signs of Na depletion. In Figure 3(b), signatures of Au and NaAu_2 co-exist, whereas in Figure 3(c) only Au is evident. Clearly, Na depletion in UHV causes conversion to bulk Au, and this conversion is more complete in (c) than (b). Further, given that XRD is sensitive to a depth of at least 1 μm , Figure 3(c)—showing only crystalline Au—indicates that Na depletion can penetrate to at least this depth. Figure 3(d) represents a single crystal that was re-polished after Na depletion, whereby 0.24 mm of material was removed from the surface. Only peaks

from NaAu_2 appear. Therefore Na depletion is limited to the region adjacent to the surface, and a sample can be regenerated by removing this region.

In the following two sections, we first present data acquired under conditions where samples exhibited a surface composition close to that of the bulk, i.e. before irreversible Na depletion. We then return to the issue of Na depletion and its effect on surface properties.

3.2. Surface characterization *before* Na depletion

LEED Figure 4(a) shows LEED patterns that are typical of an undepleted sample. There is good agreement with the patterns expected for a bulk-terminated surface, shown in Figure 4(b). Furthermore, we derive a surface lattice constant of 0.54 ± 0.02 from the LEED data, in agreement with the literature value of 0.550 nm. Thus, LEED is consistent with a bulk termination. However, the level of background intensity in the measured patterns suggests some degree of disorder.

XPD The XPD data are illustrated in Figure 5(a), for the Na 1s and Au 4f lines. Corresponding single-scattering calculations are shown in Figure 5(b). For both Na and Au, the symmetries and positions of features in the pattern agree well between experiment and simulation, although the level of anisotropy (differences in amplitude between bright and dark features) for the Na 1s does not. Note that the simulation for unreconstructed Au(111) is very similar to that for bulk-terminated NaAu_2 , so the Au 4f pattern cannot be used to distinguish between the two types of surfaces. The similarity between simulations for the two Au models is reasonable, since the surface plane of $\text{NaAu}_2(111)$ can nearly be considered an Au(111) plane in which some Au atoms are missing.

STM Figure 6 shows that undepleted surfaces typically do not exhibit the terrace-step morphology that is characteristic of single-crystal surfaces. Rather, they show individual mesa-like features with maximum diameters of about 60 nm. The images in Figure 6 are highly representative of the undepleted $\text{NaAu}_2(111)$ surfaces. The mesas have flat tops with a peak-to-peak roughness below 0.20 nm. Despite extensive efforts, no atomic-scale features could be resolved atop the mesas. Also, there is no systematic trend in the differences between heights of mesas, which range from 0.1 to 8 nm. The fact that good LEED and XPD patterns can be obtained from such a surface indicates that the mesas are atomically ordered and orientationally aligned. The partial disorder reflected in LEED and XPD may result, at least in part, from the interfaces and valleys between mesas.

3.3. Surface characterization *after* Na depletion

STM Figure 7 shows images of a surface that is deficient in Na. The majority of the surface is rough and featureless, like the image in Figure 7(a). Small parts can be found, however, that exhibit the well-known herringbone reconstruction of $\text{Au}(111)$, as shown in Figure 7(b). This herringbone-decorated terrace is bordered by a step bunch in which step heights are 0.25 ± 0.01 nm. This value agrees with the bulk separation between (111) planes in Au, 0.243 nm. (Note that the measured step heights have been calibrated against known step heights on a (111) surface of an Au single crystal.) Similar step bunches and herringbone-decorated terraces are not uncommon on surfaces with $R \leq 0.4$.

3.4. Evidence regarding mechanisms of Na depletion

Each sputter-anneal treatment has the potential to remove Na in two ways: Preferential evaporation of Na during annealing, and preferential removal of Na by sputtering. Our data indicate that both processes contribute.

TPD In Figure 8, the partial pressure of Na in the gas phase (proportional to the desorption rate) is shown as a function of increasing temperature, for three different heating rates. Thermally-activated desorption of Na is first detected at about 450 K. These experimental data became available after we observed Na depletion using other techniques, and after we developed the protocol for sputter-annealing that involved heating to 500 K. Thus, during the standard annealing treatment, there is continual evaporation of Na but at a moderately low rate. This explains the observation (Section 3.1) that heating a sample to temperatures of 600 K or above causes rapid deterioration, while heating to 500 K causes gradual deterioration.

In the TPD curves, the highest rate of desorption of Na at a given temperature is associated with the lowest heating rate. This observation can be explained if the rate of Na desorption is affected by the rate of Na transport from the bulk to the surface. For slow heating rates, the surface and bulk remain close to equilibrium and the surface is constantly replenished, while at high heating rates, the surface Na cannot be repopulated quickly enough and desorption slows.

Preferential sputtering Preferential sputtering in alloys and intermetallics is a well-known phenomenon. In NaAu₂, Ar⁺ ion sputtering reduces the Na concentration to very low levels. Data from a representative experiment are given in Table 1, for the same sample as in Figure 2(b). The sample was initially prepared by sputtering for 5 minutes and annealing at

500 K, corresponding to treatment 22 in Figure 2(b). After sputtering again for 5 minutes without subsequent annealing, R dropped to 14% of its initial value, indicating selective removal of Na.

Preferential sputtering can be attributed, in this case, to the better mass match of Ar^+ (40 amu) with Na (23 amu), than with Au (197 amu), resulting in more effective momentum transfer from the incident ion to Na than to Au. We conclude that Ar^+ ion sputtering contributes to overall Na depletion in NaAu_2 .

Table 1 Effect of sputtering (alone) on composition of sample B. The initial condition corresponds to treatment 22 in Figure 2(b). After the initial measurement of R , the sample was sputtered again for 5 minutes with 0.75 keV Ar^+ ions, but it was not annealed. Then the second value of R was obtained.

	atom% Na	atom% Au	R
Initial condition	27.0	73.0	0.37
After sputtering	4.7	95.3	0.05

4. Discussion

This work shows that the nature of the (111) surface of bulk NaAu_2 depends strongly on the conditions of its preparation in UHV.

If the sample is not heated too high ($T_{ann} \leq 500 \text{ K}$), nor subjected to excessive sputter-anneal cycles, its surface exhibits characteristics consistent with bulk termination. This is based upon both LEED and XPD, where the measured patterns are very close to simulations based on the bulk structure. In particular, the surface lattice constant calculated from the LEED data agrees well with the value for the bulk-terminated unit cell, and the LEED pattern

contains no extra diffraction spots that might indicate surface reconstruction. However, in both techniques, some disorder is suggested by the moderately high background in the patterns.

The STM data are unusual, because they do not display the anticipated terrace-step structure, but rather an array of mesa-like features with diameters on the order of a few tens of nm. These mesas give rise to the good LEED and XRD patterns, yet no regular atomic-scale structure can be discerned on the flat (to within 0.2 nm) tops. One possible explanation is that the top atomic layer is disordered, and the LEED and XRD patterns originate mainly from deeper layers. Perhaps the disorder is a static remnant of the dynamic Na desorption which occurs at temperatures above the observation temperature of 300 K. However, Barth et al. observed good atomic-scale order on surfaces of NaAu₂ films grown on Au(111) and heated to temperatures of 300-600 K.^{10,11} The reason for the contradictory result is unclear, although there are certain differences between the two systems and these may be significant. For instance, in the work of Barth et al., NaAu₂ was in the form of a thin surface layer with significant strain, and excess Au existed in the subsurface region (the Au substrate).

It is interesting that the mesas produce good LEED and XRD patterns. This means that the mesas must be atomically ordered and orientationally aligned, i.e. their orientation is fixed by the bulk lattice. Although the STM images in Figure 6 may give the impression that the mesas are independent mounds, they are more correctly regarded as terrace-like features separated by irregular valleys and crevasses. The reason for this unusual morphology warrants further investigation.

If the sample is heated to higher temperatures ($T_{ann} \geq 600$ K), and/or subjected to many sputter-anneal treatments at $T_{ann} \leq 500$ K, it loses Na and eventually decomposes into

elemental Au at the surface and in the adjacent bulk region. Evidence for this comes from the irreversible drop in R in XPS and the emergence of bulk Au in XRD. Because a NaAu_2 surface can be regenerated by polishing, Na depletion must be limited to the near-surface region. In a Na-depleted sample, there are small areas which have the herringbone reconstruction of Au(111), as well as cascades of steps each having the height of an Au(111) step. Such regions are in the minority, however, and most of the Na-depleted surface simply appears rough and featureless in STM.

We have determined that two mechanisms contribute to Na depletion. Thermally-activated desorption begins around 450 K. Preferential sputtering also contributes. Our model is that when surface and near-surface depletion becomes too extensive, the bulk can no longer replenish the surface effectively, and the surface transforms to Au. In fact, the importance of surface Na repopulation is evident from the inverse correlation between Na desorption rate and heating rate (at fixed temperature) in TPD.

Returning to the original motivation for this work, we can comment on the plausibility of $\text{NaAu}_2(111)$ as a model for the catalytically-active surface. In powder form, NaAu_2 showed good catalytic activity for CO oxidation at temperatures of 300 to 350 K.⁸ A reaction mechanism was proposed, based upon the nearly-bulk-terminated (111) surface. The present work does not *prove* that a (111)-like surface exists under reaction conditions, but this work is *compatible* with this model for the catalyst operating in this temperature range. The present work also predicts massive compositional changes in the intermetallic catalyst, starting at reaction temperatures of about 450 K.

5. Conclusion

We have found that the (111) surface of NaAu₂ can be prepared in a state where orientationally-aligned, mesa-like features predominate. This state produces good diffraction patterns in LEED and XPD, which are matched well by simulations based on a bulk-terminated structure. However, there is no regular fine structure atop the mesas, possibly indicating disorder in the topmost surface layer. The sample can lose Na both by thermal evaporation (onset at 450 K) and by Ar⁺ ion bombardment. Repeated sputter-annealing treatments under the conditions described here leads to precipitation of pure Au at the surface and near-surface region.

Acknowledgements The Ames portion of this work was supported by the John D. Corbett Endowment of Iowa State University, and the work was performed at the Ames Laboratory, which is supported by the Office of Science, Basic Energy Sciences, Materials Sciences and Engineering Division of the US Department of Energy (USDOE), under Contract No. DE-AC02-07CH11358 with the US Department of Energy. The EMPA portion of this work was supported by the Swiss National Science Foundation (Contract 200021-129511). We thank Dr. Lin-Lin Wang and Prof. Gordon Miller for many useful discussions.

Figures

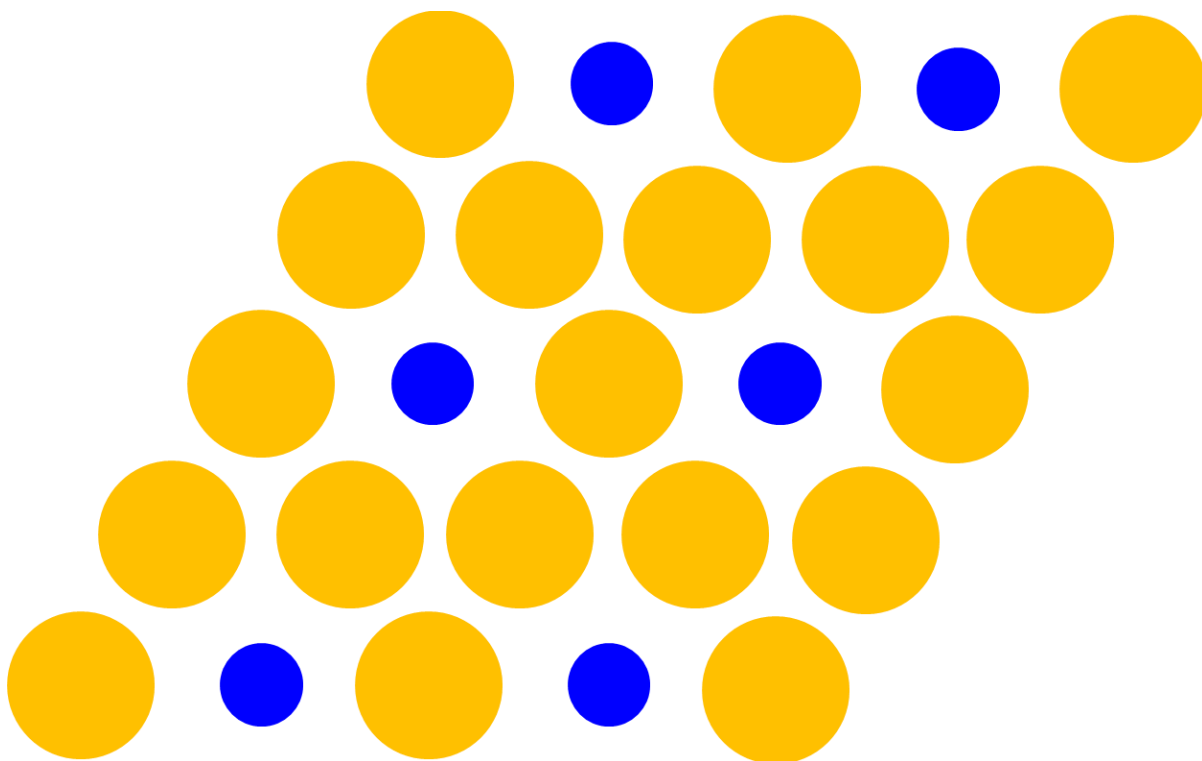


Figure 1. Schematic of the (111) plane of NaAu₂. Large (gold) circles represent in-plane Au atoms. Small (blue) circles represent Na atoms slightly below the surface plane. The rhombus shows the surface unit cell.

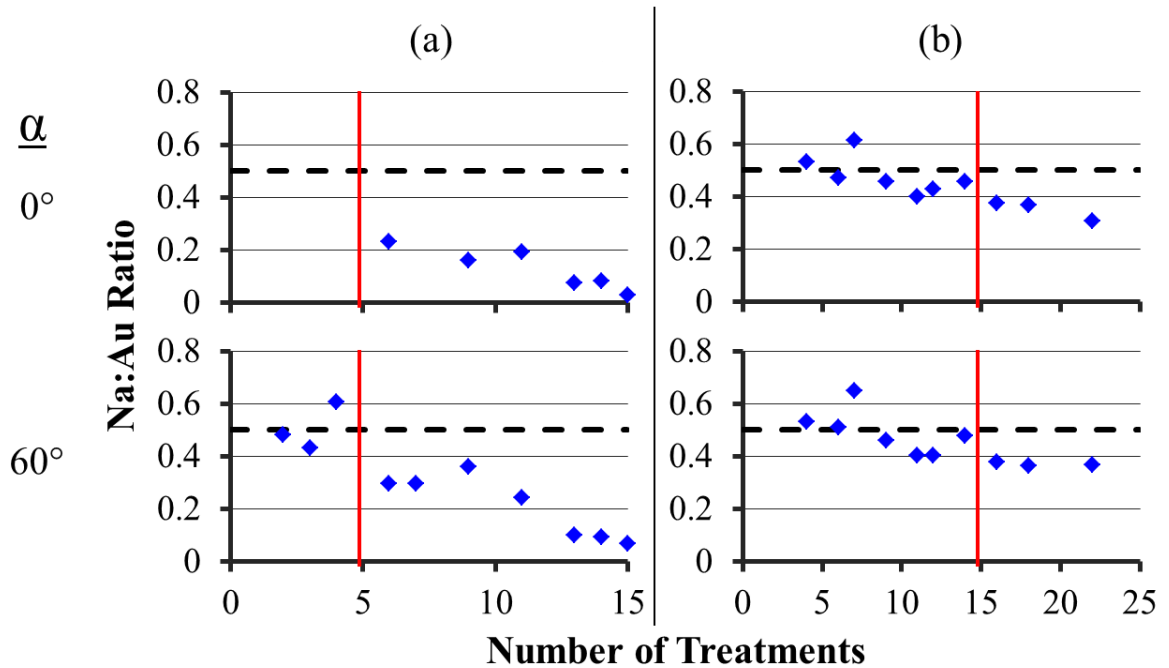


Figure 2. Na: Au composition ratio, from XPS, as a function of treatment in UHV. XPS data were not acquired after every treatment, so the number of data points is less than the number of treatments. The compositions are derived from the relative intensities of the Na 1s and Au 4f lines in XPS, as described in Section 2. (a) Evolution of Sample A. This sequence encompassed a wide variety of T_{ann} from 430 to 770 K. Prior to Na depletion, the treatments included 2 at $T_{ann} = 600$ K and 1 at $T_{ann} = 650$ K. (b) Evolution of Sample B. Each treatment included annealing at 500 K for 20 minutes. The top two panels show results for normal emission ($\alpha = 0^\circ$) while the bottom two panels show grazing emission ($\alpha = 60^\circ$).

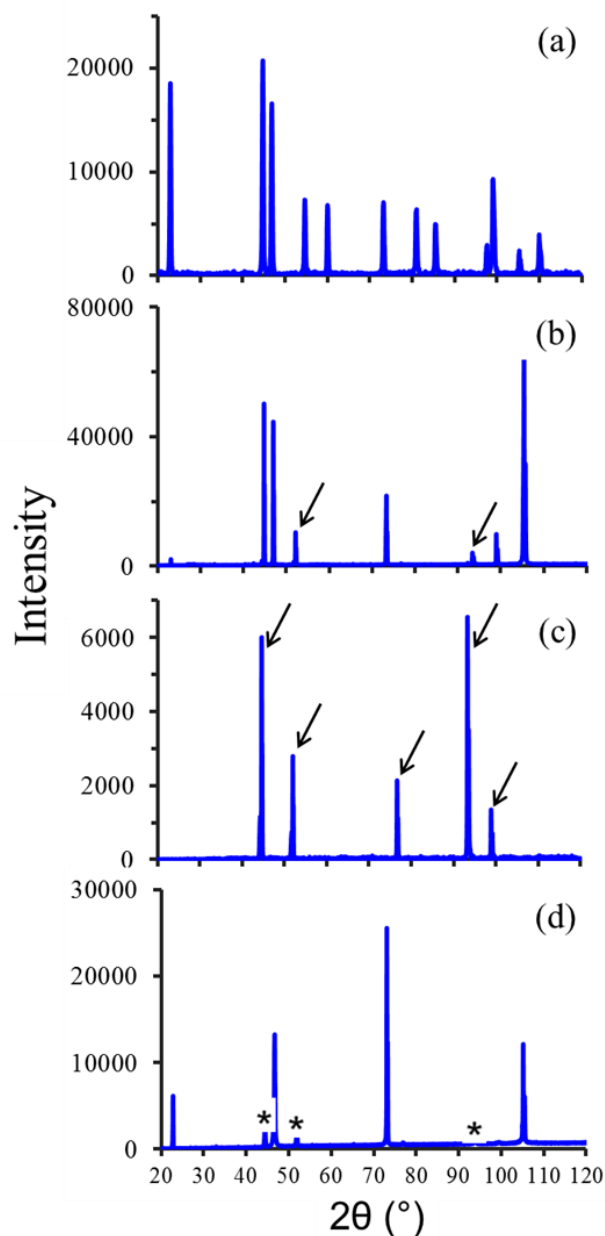


Figure 3. XRD patterns of NaAu_2 samples. (a) Powder pattern from a portion of the Sample D ingot that was crushed and ground. All peaks are attributed to NaAu_2 . (b) Sample A single crystal after heating from 400 K to 850 K in 50 K increments with 3 minutes of sputtering before each heating. The Na: Au composition ratio was not measured, but these conditions are expected to produce a Na-depleted surface. The pattern is a mixture of peaks assigned to NaAu_2 and Au, the latter denoted by arrows. (c) Sample D single crystal after 11 treatments that included flashing or annealing at 775 K and 825 K. These conditions are expected to produce a Na-depleted surface, confirmed by $R = 0.09$ in XPS at $\alpha=0^\circ$. The major XRD peaks can all be assigned to Au, denoted by arrows. (d) Sample D single crystal after re-polishing which removed 0.24 mm from the surface. All peaks are attributed to NaAu_2 , except the small features marked by asterisks, which are from the stainless steel sample holder. These features also make very small contributions in panels (b) and (c).

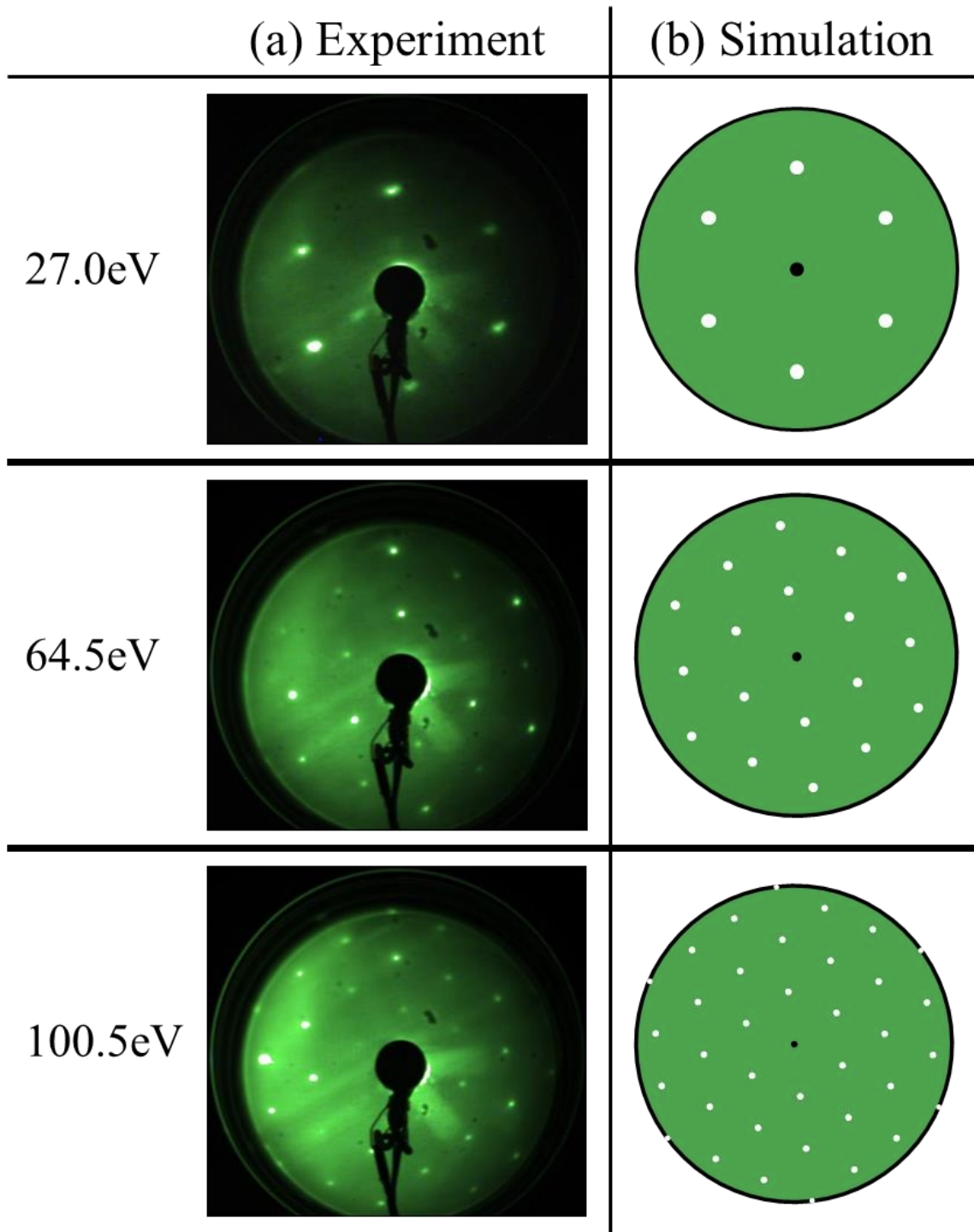


Figure 4. LEED patterns at 3 incident electron energies and normal incidence. (a) Sample C, after 13 sputter-anneal treatments, resulting in a cumulative history of 3 hours of sputtering, and 18 hours of annealing at temperatures not exceeding 530 K. $R = 0.55$ ($\alpha = 60^\circ$). (b) LEED pattern expected for the $\text{NaAu}_2(111)$ bulk-terminated surface (Figure 1).

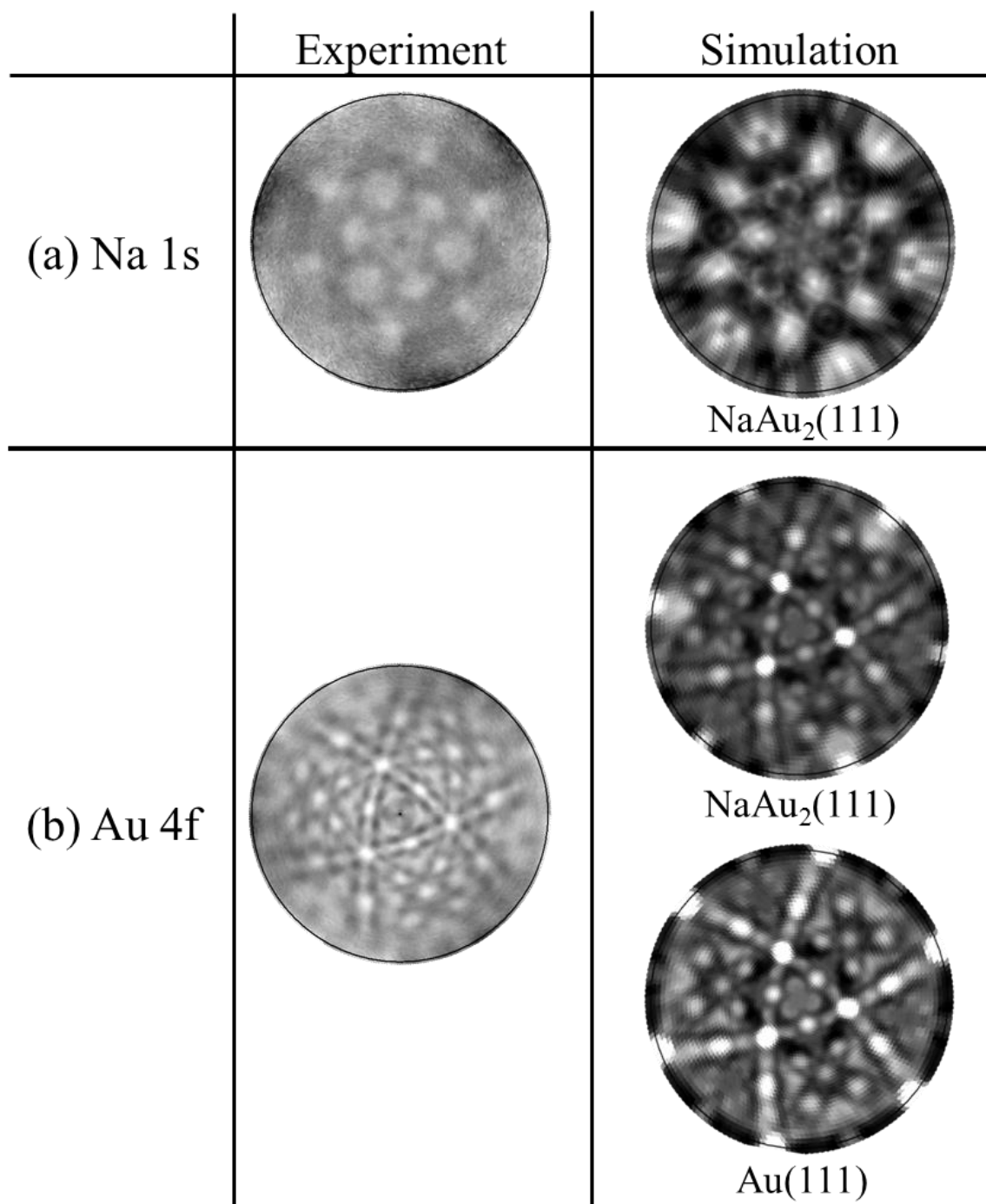


Figure 5. Comparison of experimental XPD patterns from Sample B with single-scattering calculations. Before XPD measurements, the sample underwent a total of 5 sputter-anneal treatments at $T_{ann} = 500$ K, which resulted in $R = 0.53$ ($\alpha = 60^\circ$). The sample was scanned at $\alpha = 0$ to 90° , in 1° steps. (a) Na 1s. (b) Au 4f.

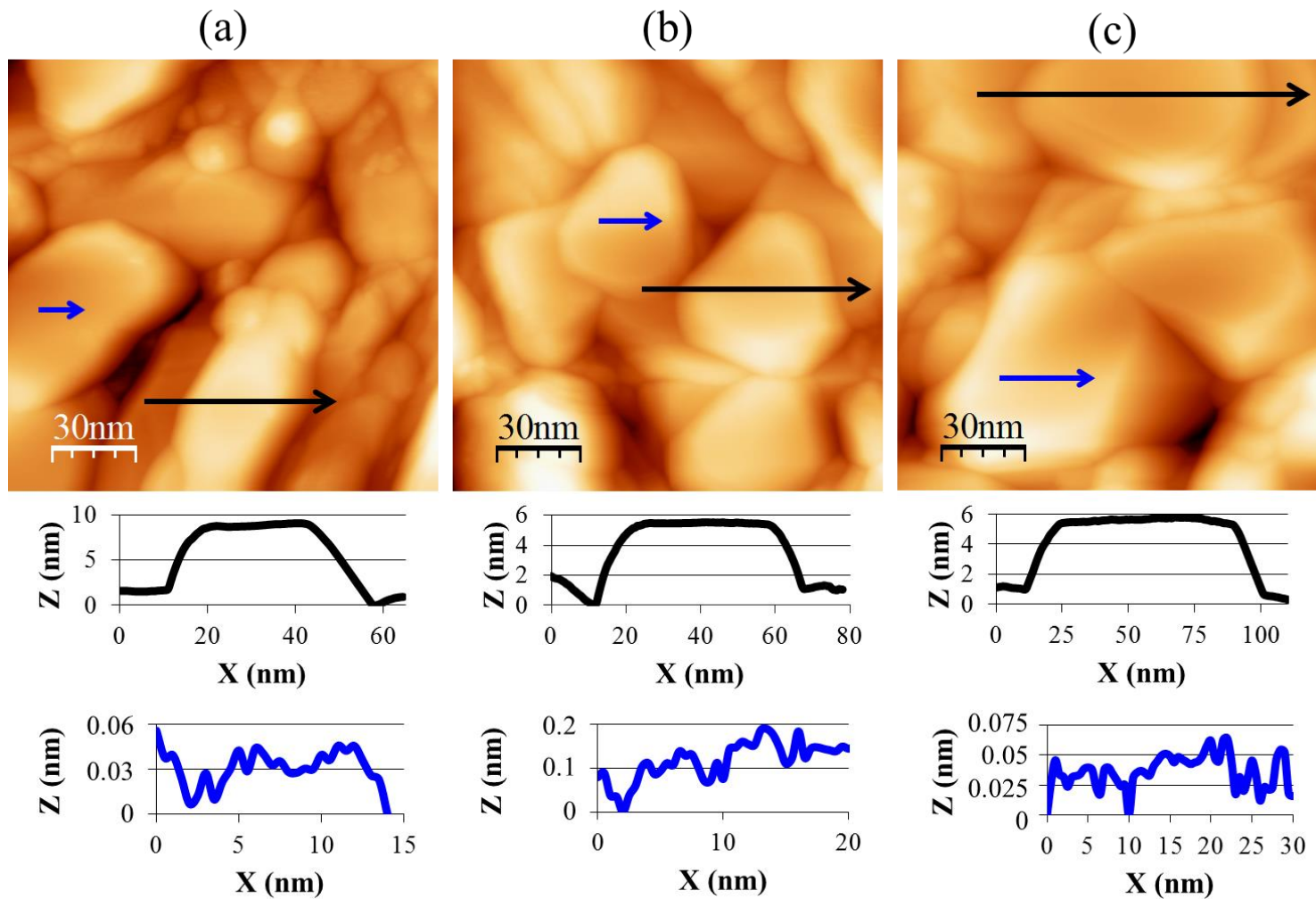


Figure 6. STM images and line profiles of Sample C. The sample started with a history of 8 sputter-anneal treatments at $T_{ann} = 425\text{-}480$ K. Between each pair of images, it was sputtered once and annealed for 20 minutes at 480-515 K. Values of R were measured at $\alpha = 60^\circ$. Tunneling parameters ranged from +1.1 to +1.6 V at the tip, and 0.1 to 0.3 nA. (a) $R = 0.48$. (b) $R = 0.47$, (c) $R = 0.44$.

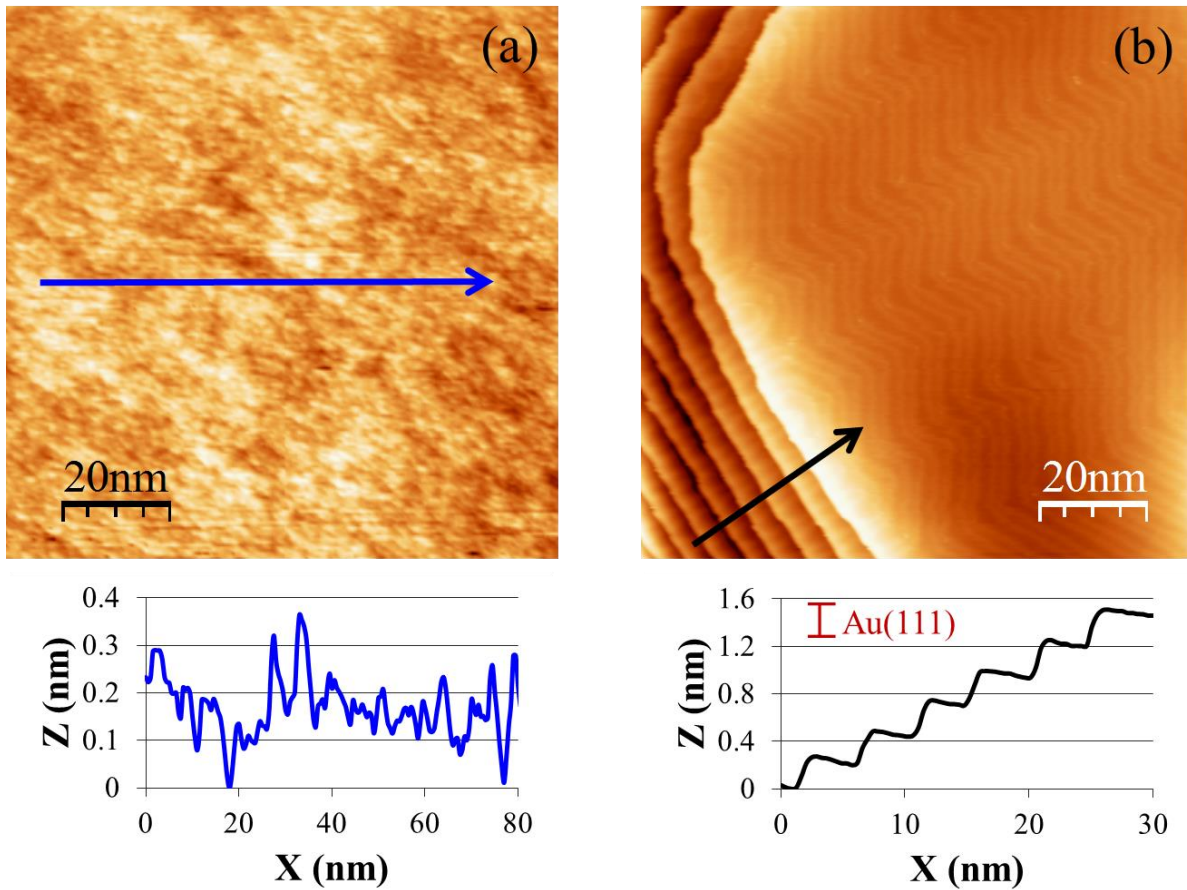


Figure 7. STM images of sample A after Na depletion, $R = 0.24$ ($\alpha = 60^\circ$). The sample started with a history of 10 sputter-anneal treatments at $T_{ann} = 430-750$ K. Between images, it was sputtered and annealed for 20 minutes at 770 K. (a) Typical surface image at +0.82 V, 0.08 nA. (b) Isolated region showing the herringbone reconstruction and step height associated with Au(111), at -1.4 V and 0.08 nA. The average step height is 0.25 ± 0.01 nm.

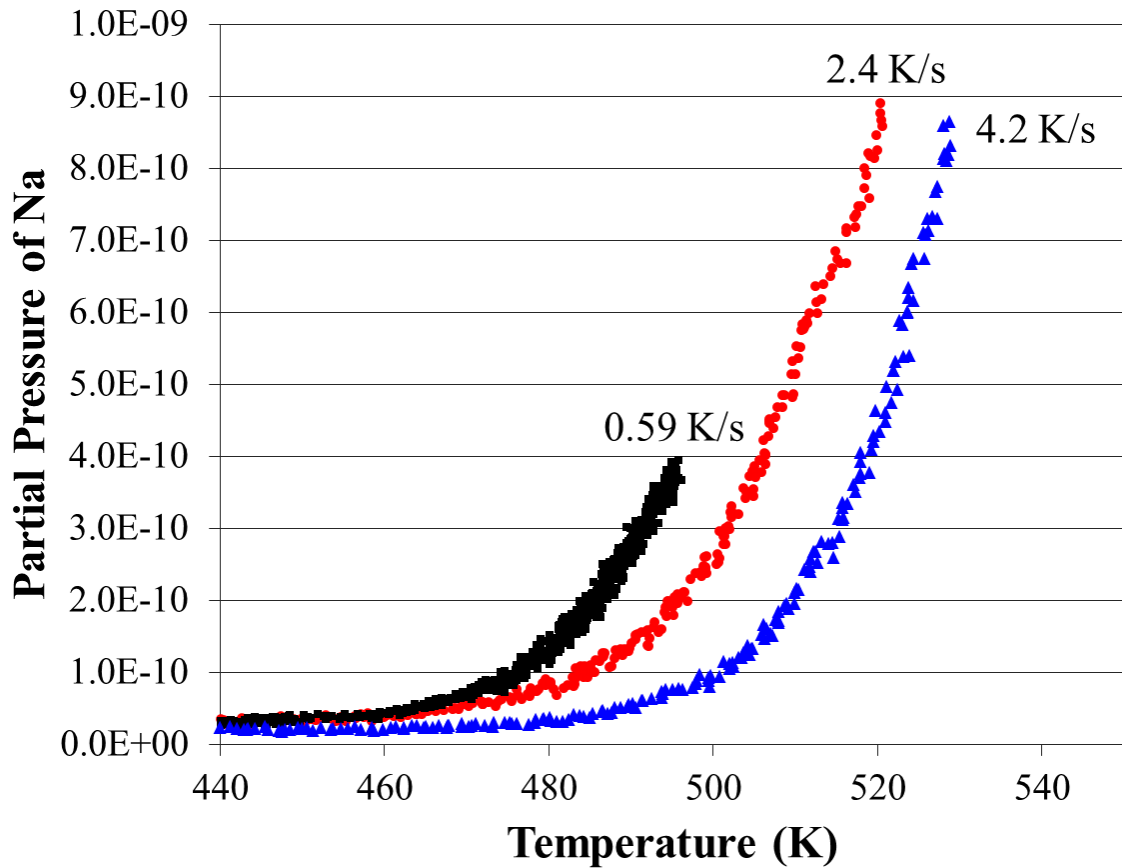


Figure 8. TPD spectra from Sample D showing the partial pressure of Na (mass-to-charge ratio of 23) versus temperature. Three different heating rates were used: 0.59 K/s, 2.4 K/s and 4.2 K/s.

Appendix. Surface Morphology

1. Incremental anneals

Many metals, both single element and mixed element, form step-terrace features on the surface following specific sputter-anneal cycles tailored for each. In order to find the specific sputter-anneal cycle combination for NaAu₂, we conducted a series of incremental anneals on NaAu₂ Sample A at the Ames Laboratory in March 2014. A sputter-anneal cycle consisted of a three minute sputter at 1 keV with Ar⁺ ions followed by a two minute anneal at the desired temperature. A controlled annealing ramp rate of 0.04 A/min was used. The sample cooled for 10-15 minutes before STM imaging. The annealing temperatures ranged from 400 K to 850 K, in 50 K increments. We repeated the 400 K anneal twice before moving on to higher temperatures. Figure A1.1 shows a compilation of STM images taken after the ten different temperature anneals. As annealing temperature increases the surface becomes rougher and small clusters appear. The large features, seen at all temperatures, range in height from less than 3 nm to 15 nm tall. The small clusters, seen at temperatures above 600 K, are 5 nm or less in width. Figure A1.2 shows STM images with line profiles highlighting these feature heights and widths. We found no features indicative of step-terrace morphology.

2. High temperature (>700 K) anneals

We conducted high temperature anneals on Samples A and D at EMPA. Sample A was not re-polished between the previous incremental anneals at the Ames Laboratory and the following high temperature anneals. Sample A was sputtered with Ar⁺ ions at 750 eV for 30 minutes followed by a 750 K anneal for 40 minutes. As shown in Figure A1.3(a)-(b), the

resulting surface is flat and covered with small clusters. No step-terrace formation is seen, so Sample A was sputtered again for 30 minutes followed by a 770 K anneal for 40 minutes. This resulted in a flatter, smoother surface with regions of step-terraces; see Figure A1.3(c)-(d). We determined these step-terrace regions to be that of Au(111) (cf. Section 3.3).

Sample D, a previously unused sample, also underwent high temperature anneal experiments. This sample was prepared and scanned in a separate chamber containing a low temperature STM (LT-STM). Here the sample was subjected to four cycles of sputtering for 10 minutes followed by flash heating to 775 K. The resulting surface morphology consisted of rolling mounds covered with the small clusters; see Figure A1.4(a)-(b). Sample D was then subjected to four cycles of sputtering for 10 minutes followed by 10 minute anneals at 825 K. The surface presented with what appear to be many steps with small terraces surrounded by large rough areas, as shown in Figure A1.4(c)-(d). The final conclusion is that high temperature anneals do not form the desired step-terrace morphology and in fact, deplete the surface of Na.

3. Scanning electron microscopy

We conducted a scanning electron microscopy (SEM) study on Samples A and C to image the surface area on a larger scale than STM could provide. The samples were removed from the UHV chamber and transported in air to a nearby SEM system within the building. Dr. Juan-Ramon Sanchez performed all SEM imaging.

Sample A was imaged after the >700 K anneals and additional sputter-anneal cycles at lower temperatures including at 16 hour anneal at 430 K. The R value of 0.07 indicates the surface is Na-depleted. Secondary electron images (topographic) show a rough surface

comprised of small clusters, Figure A1.5(a)-(c). The backscattered electron image (a combination of both topographic features and density), Figure A1.5(d), shows a lack of contrast on the surface suggesting there is only one element present. An element with a higher atomic number and thus higher atomic mass backscatters more electrons and appears brighter in the image. The large difference in mass between Au and Na (196 amu and 23 amu, respectively) means there would be a distinct contrast difference if both Au and Na are present. An energy-dispersive X-ray diffraction (EDX) mapping of the surface composition shows only Au is present. The typical EDX detection limit is 0.1 weight%, so if Na is present it is only in trace amounts.

Sample C was imaged after several sputter-anneal cycles around 500 K. The R value of 0.58 indicates the surface is not Na-depleted and actually close to the ideal value of 0.50. Secondary electron images show a rough surface comprised of small clusters, Figure A1.6(a)-(b). The backscattered electron image, Figure A1.6(c), shows a two-tone surface suggesting the presence of two elements, one with a higher density (i.e. Au) and one with a lower density (i.e. Na). An EDX map of the surface composition shows the surface is 30% Na and 70% Au, which is the ideal ratio for an undepleted sample.

4. Triangles

Unique triangular shaped features were found on Samples A and D of $\text{NaAu}_2(111)$. The first triangles were found in July 2012 on Sample A. The sample had undergone 10 sputter-anneal cycles consisting of Ar^+ ion sputtering at 1 keV for 15 minutes followed by a 450 K anneal for 30 minutes. These features were an anomaly on the surface as they were only seen in a small region. Figure A1.7(a) shows a group of these triangles clustered on a

step-terrace formation. The average island size, measured from peak to base, is $2.8 \text{ nm} \pm 0.2 \text{ nm}$ and the average island height is $0.26 \text{ nm} \pm 0.2 \text{ nm}$. The second set of triangles was found in April 2014 on Sample C. The sample had undergone ~ 16 sputter-anneal cycles consisting of Ar^+ ion sputtering at 1 keV for 5 - 15 minutes followed by 400 - 500 K anneals for 10 - 40 minutes. These features were again an anomaly on the surface as they were only seen on the tops of a few mesas. Figure A1.7(b) shows a group of triangles clustered on the top of a mesa. The average island size, measured from peak to base, is $1.3 \text{ nm} \pm 0.1 \text{ nm}$ and the average island height is $0.07 \text{ nm} \pm 0.01 \text{ nm}$. The difference in height of the triangles could be due to the variation in the tunneling conditions. We speculate that these may be Au islands that have nucleated on the NaAu_2 mesa.

5. Mesas

The typical surface morphology of an undepleted $\text{NaAu}_2(111)$ surface has mesa-like features. When present on the surface, these mesas are found on the entirety of the sample. Analyses of these mesas show they have a maximum width of 60 nm, range in height from 0.1 nm to 8 nm and exhibit an average peak-to-peak roughness of $0.18 \text{ nm} \pm 0.09 \text{ nm}$ ($N = 124$). The distribution for peak-to-peak roughness for six separate analyses is summarized in Figure A1.8. The plot is broken down into two groups. Group 1, containing experiments with fewer sputter-anneal cycles (<10), has an average peak-to-peak roughness of $0.15 \text{ nm} \pm 0.07 \text{ nm}$ ($N = 85$) while Group 2, containing experiments with more sputter-anneal cycles (>10), has an average peak-to-peak roughness of $0.25 \text{ nm} \pm 0.11 \text{ nm}$ ($N = 39$). This result in itself should not be unexpected. We know more sputter-anneal cycles leads to a deterioration of the surface via depletion of Na and thus a possible increase in overall roughness.

The overall shape of the mesas is similar. An analysis of clean surface images from 2014 and 2015 give the angle between the top of the mesas and the sloping sides as an average of $155^\circ \pm 7^\circ$. Figure A1.9 shows examples of this trend over various sized mounds. The “step” distance between the tops of different mesas ranges from 0.1 nm to 8.4 nm, with most “step” heights between 1 nm and 3 nm (N = 132); see Figure A1.10. The wide variation between “step” heights suggests there is no trend in this aspect of the growth morphology.

6. Round top mounds

There are exceptions to the clean surface mesas. Round top mounds are another feature that appears on the surface. These mounds are present on the surface for the first three to four sputter-anneal cycles on an unused or freshly re-polished sample. After five sputter-anneal cycles the mesas appear and the round top mounds are rarely seen on the surface. These round top mounds have a maximum width of 75 nm and range in height from 2 nm to 12 nm. Examples of these round top mesas are shown in Figure A1.11. It is possible these round top mounds are precursors for the mesas that form on the surface.

7. Controlled annealing rate

We conducted another endeavor to create a step-terrace formation on the NaAu₂(111) surface at EMPA in 2015. Sample C was re-polished and used for these experiments. A controlled ramping rate was used for heating and cooling the sample. It is known that Na depletion occurs with sustained sputtering in addition to annealing above 475 K, so the chosen base sputter-anneal cycle for the sample was sputtering with Ar⁺ ions at 750 eV for 3 minutes followed by annealing at 475 K for 20 minutes. Sample C was first annealed to 475

K using a heating rate of 0.1 A/min (~4.5 K/min) and cooled to room temperature at a rate of 0.1 A/min. The resulting surface structure was similar to that of the previously seen mesas, but with more separation between mesas and an underlying step-terrace morphology. Figure A1.12 shows examples of this surface. The average step height shown in Figure A1.12(e) is $0.47 \text{ nm} \pm 0.02 \text{ nm}$ ($N = 6$). It is known that the bulk structure gives a layer separation of 0.45 nm for $\text{NaAu}_2(111)$ measuring from one “Au1” layer to the next “Au1” layer,^{12,13} shown in Figure A1.13. It is plausible that these step-terraces are that of $\text{NaAu}_2(111)$.

A second sputter-anneal cycle was done with a heating rate of 0.1 A/min and a cooling rate of 0.05 A/min. The resulting surface structure is similar to that of the previously seen mesas. The step-terraces are still present, but are more infrequently seen. Figure A1.14 shows examples of this surface. The average step height shown in Figure A1.14(e) is $0.49 \text{ nm} \pm 0.01 \text{ nm}$ ($N = 9$). This height again is similar to the layer separation seen with the bulk structure and could again plausibly be $\text{NaAu}_2(111)$ step-terraces.

The parameters used in the second sputter-anneal cycle were repeated for another attempt at a step-terrace formation. The resulting surface resembled that of the typical mesas (cf. Figure 6) and small step-terrace areas were scarce. Figure A1.15 shows examples of this surface. The average step height shown in Figure A1.15(e) is $0.58 \text{ nm} \pm 0.03 \text{ nm}$ ($N = 6$). The height of these steps has increased by 0.10 nm indicating they may no longer be that of NaAu_2 .

After conducting these controlled annealing rate experiments, we determined that it is not easily possible to obtain a step-terrace morphology on the $\text{NaAu}_2(111)$ surface. It took only three mild sputter-anneal cycles before the underlying step-terrace morphology

disappeared and the typical mesa morphology appeared. The controlled cooling ramp rate had only short-term benefit in generating step-terrace morphology.

Figures

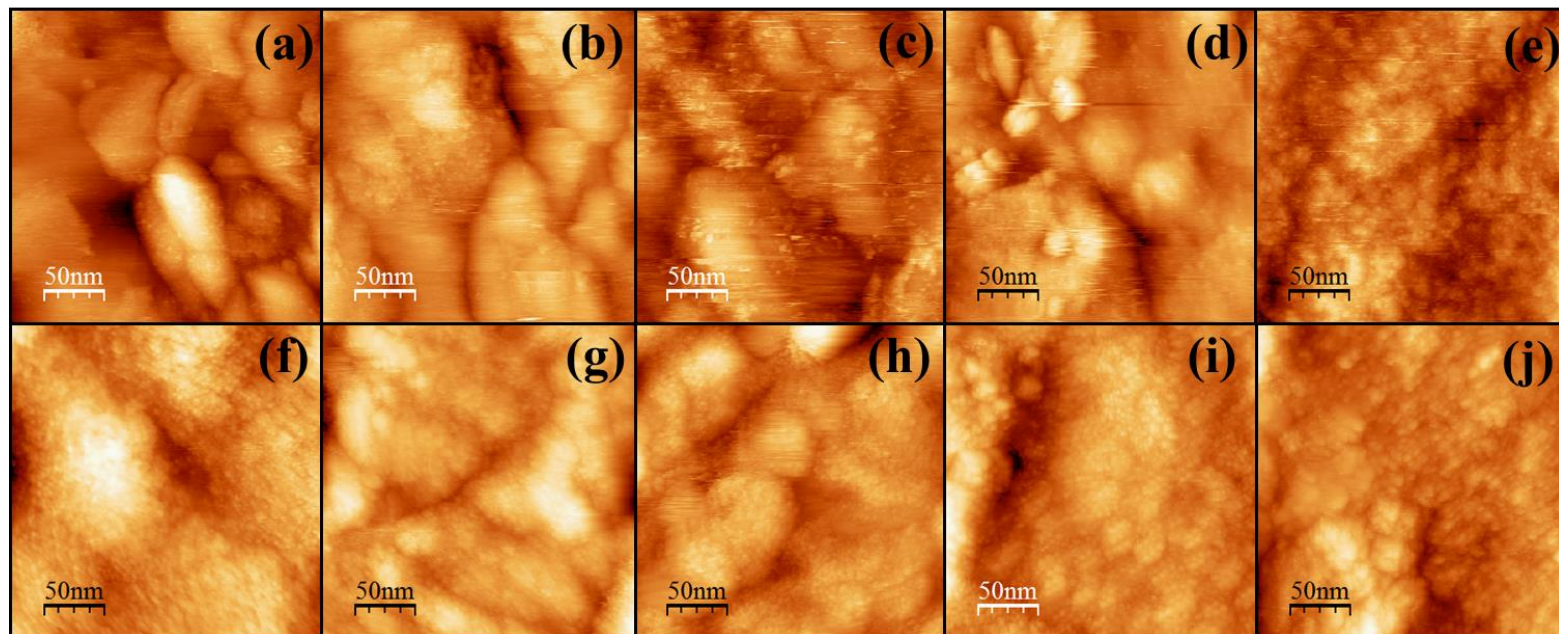


Figure A1.1. STM images of the NaAu₂(111) surface following ten incremental anneals ranging from 400 K to 850 K, in 50 K increments. (a) 400 K; (b) 450 K; (c) 500 K; (d) 550 K; (e) 600 K; (f) 650 K; (g) 700 K; (h) 750 K; (i) 800 K; (j) 850 K. All images are 250 nm x 250 nm. Scanning parameters 0.4 nA to 0.5 nA, -2.2 V to -3.5 V.

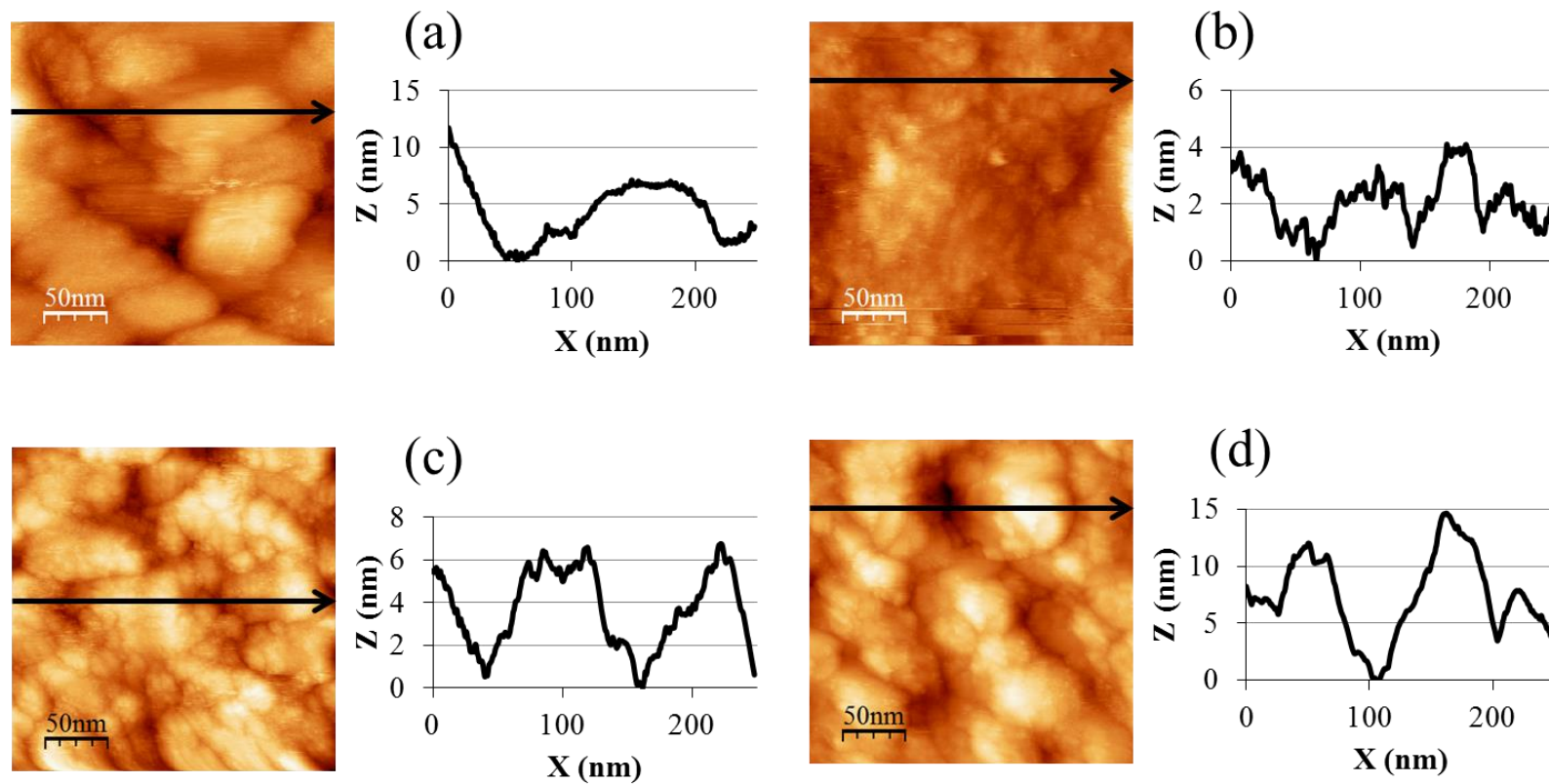


Figure A1.2. STM images and line profiles of the $\text{NaAu}_2(111)$ surface showing feature heights for various incremental anneals. (a) 400 K; (b) 550 K; (c) 700 K; (d) 850 K. All images are 250 nm x 250 nm. Scanning parameters 0.4 nA to 0.5 nA, -2.2 V to -3.5 V.

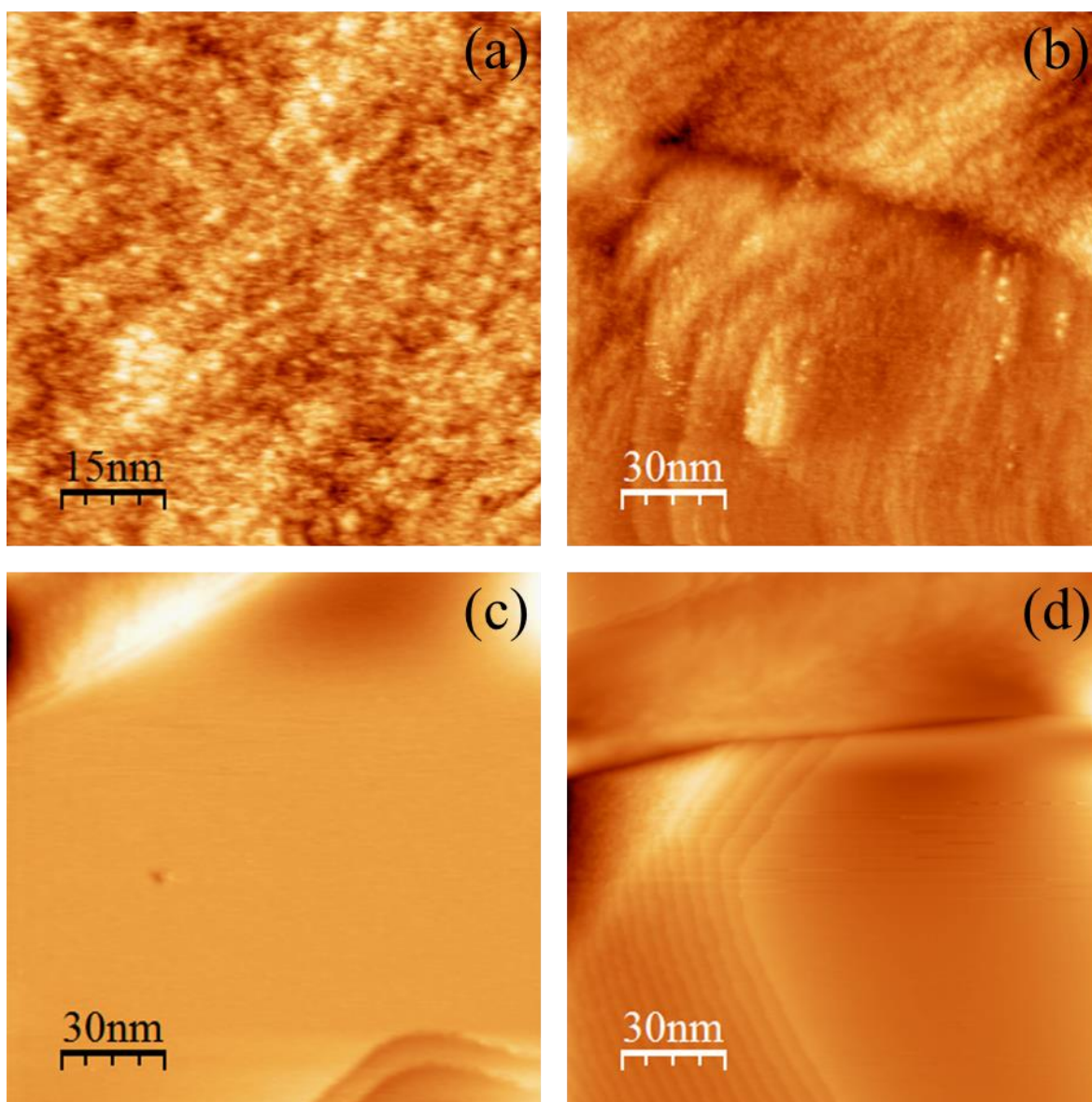


Figure A1.3. STM images of the $\text{NaAu}_2(111)$ surface of Sample A following two different high temperature sputter-anneal cycles. (a)-(b) 750 K; (c)-(d) 770 K. Step-terrace formations are seen in (c) and (d), (a) is 75 nm x 75 nm, (b)-(d) are 150 nm x 150 nm. Scanning parameters (a)-(b) 0.03 nA to 0.08 nA, +0.57 V to 1.2 V; (c)-(d) 0.06 nA to 0.08 nA, -1.65 V.

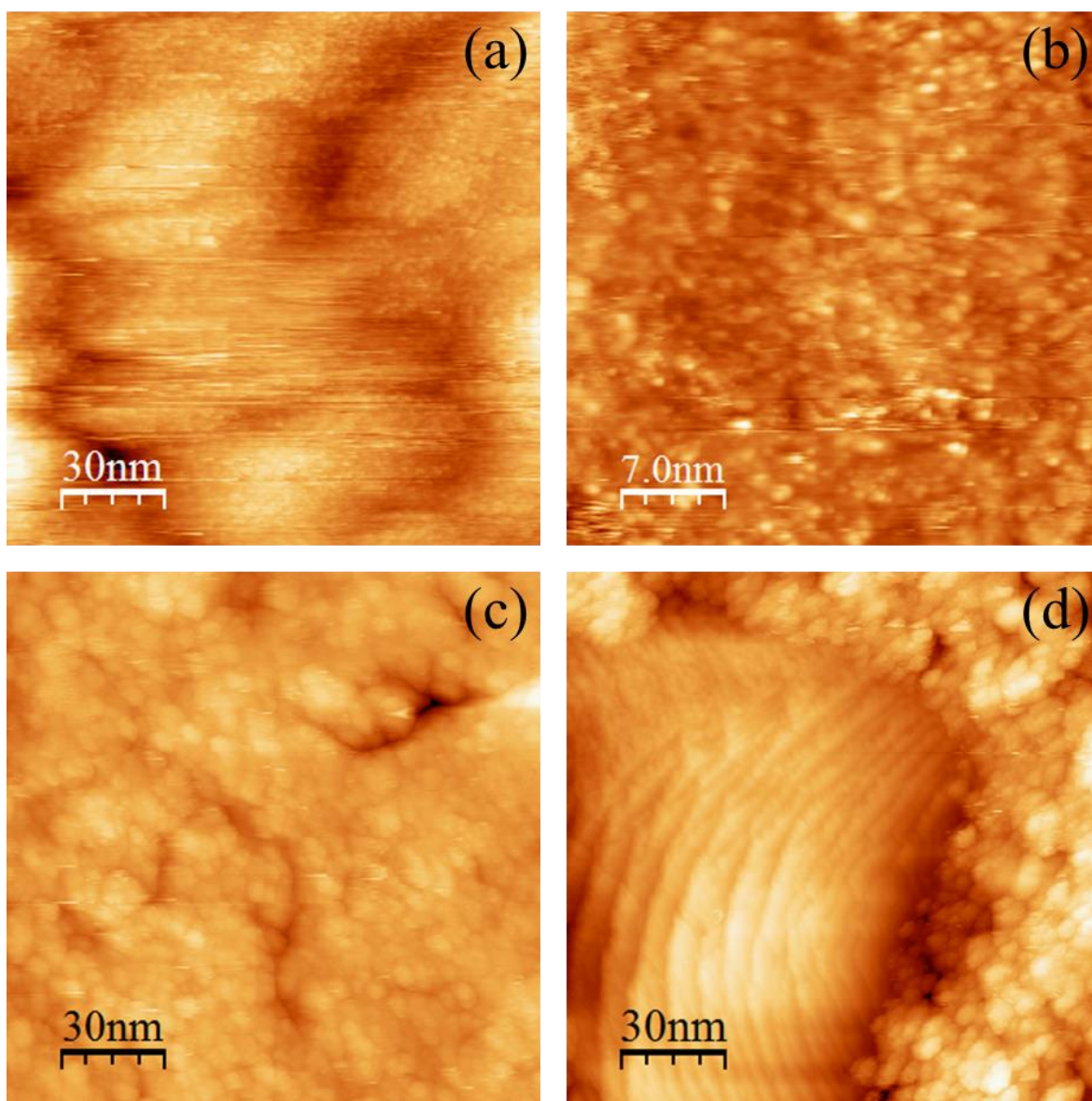


Figure A1.4. STM images of the $\text{NaAu}_2(111)$ surface of Sample D following two different high temperature sputter-anneal cycles. (a)-(b) 775 K; (c)-(d) 825 K. (a),(c)-(d) are 150 nm x 150 nm, (b) is 35 nm x 35 nm. Scanning parameters 0.1 nA, 0.8 V to 1.2 V.

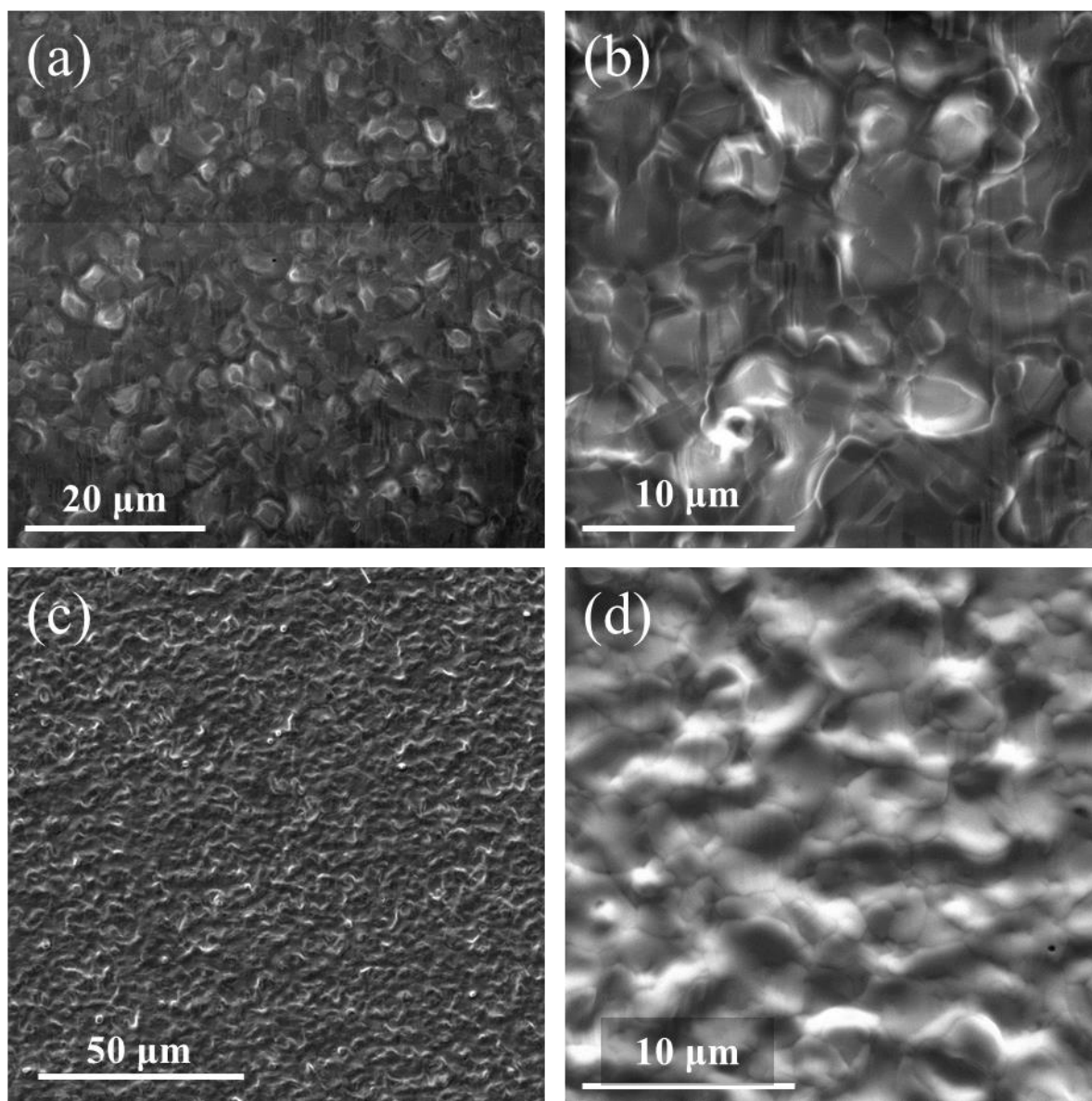


Figure A1.5. SEM images of the $\text{NaAu}_2(111)$ surface of Sample A. $R = 0.07$. Secondary electron images are (a)-(c), backscatter electron image is (d). (a) $70 \mu\text{m} \times 70 \mu\text{m}$; (b) $25 \mu\text{m} \times 25 \mu\text{m}$; (c) $150 \mu\text{m} \times 150 \mu\text{m}$; (d) $25 \mu\text{m} \times 25 \mu\text{m}$

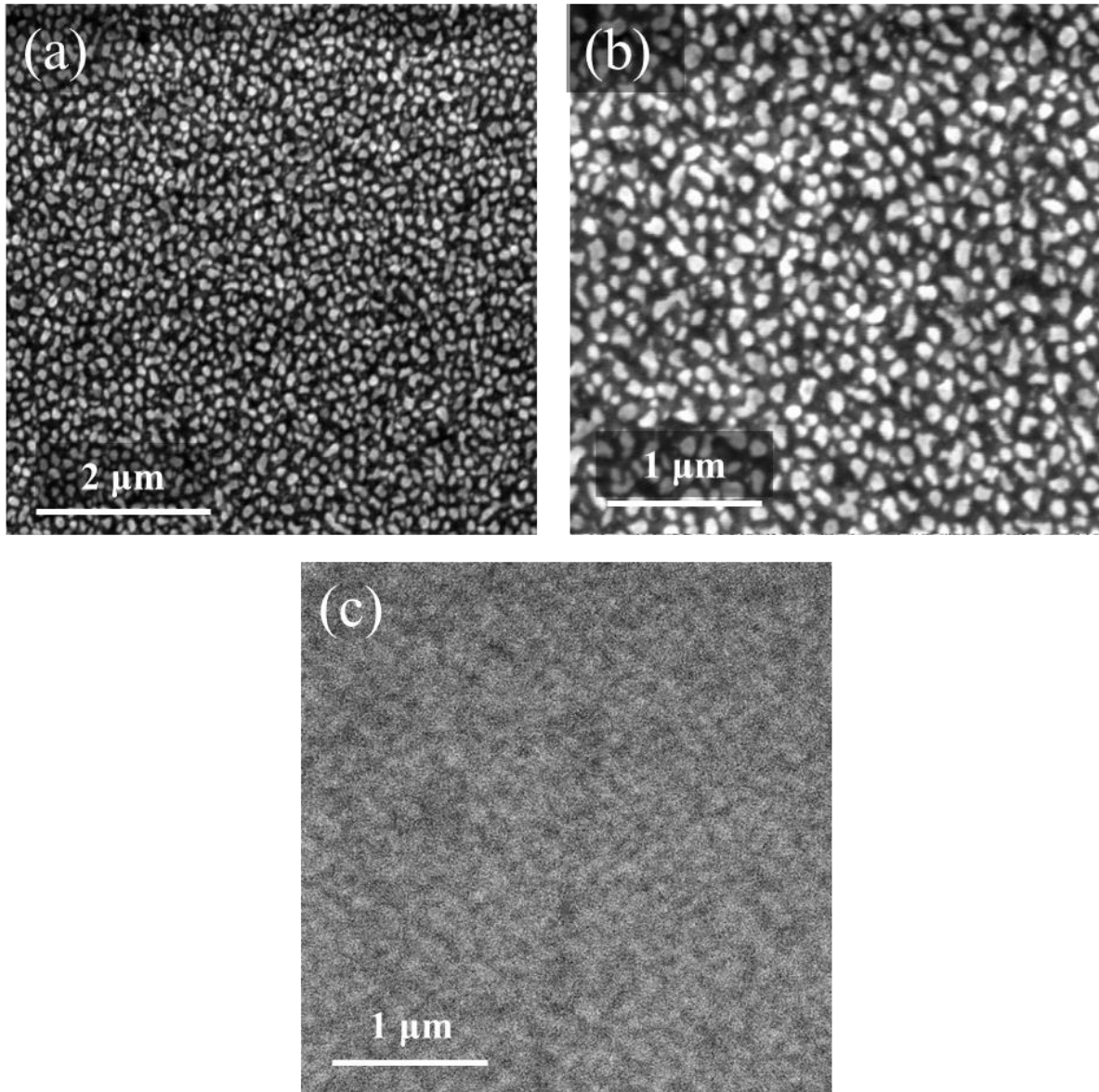


Figure A1.6. SEM images of the $\text{NaAu}_2(111)$ surface of Sample C. $R = 0.58$. Secondary electron images are (a)-(b), backscatter electron image is (c). (a) $7 \mu\text{m} \times 7 \mu\text{m}$; (b) $5 \mu\text{m} \times 5 \mu\text{m}$; (c) $5 \mu\text{m} \times 5 \mu\text{m}$

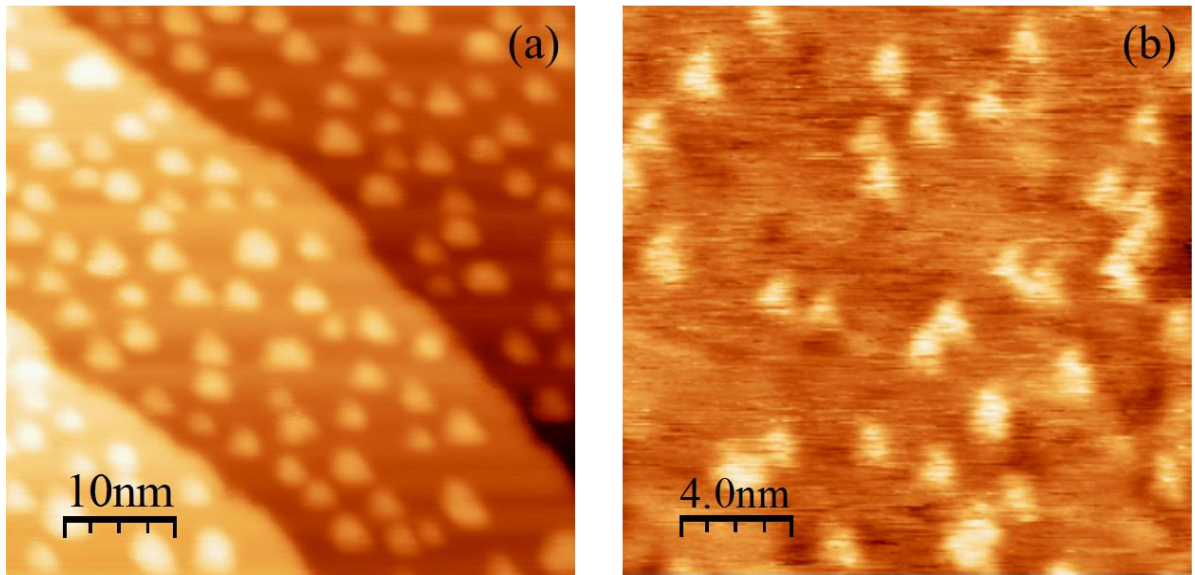


Figure A1.7. STM images of Samples A and C showing triangular features seen on the NaAu₂(111) surface. (a) Sample A, 50 nm x 50 nm; (b) Sample C, 20 nm x 20 nm. Scanning parameters (a) 0.5 nA, -2.5 V; (b) 0.09 nA, 0.5 V.

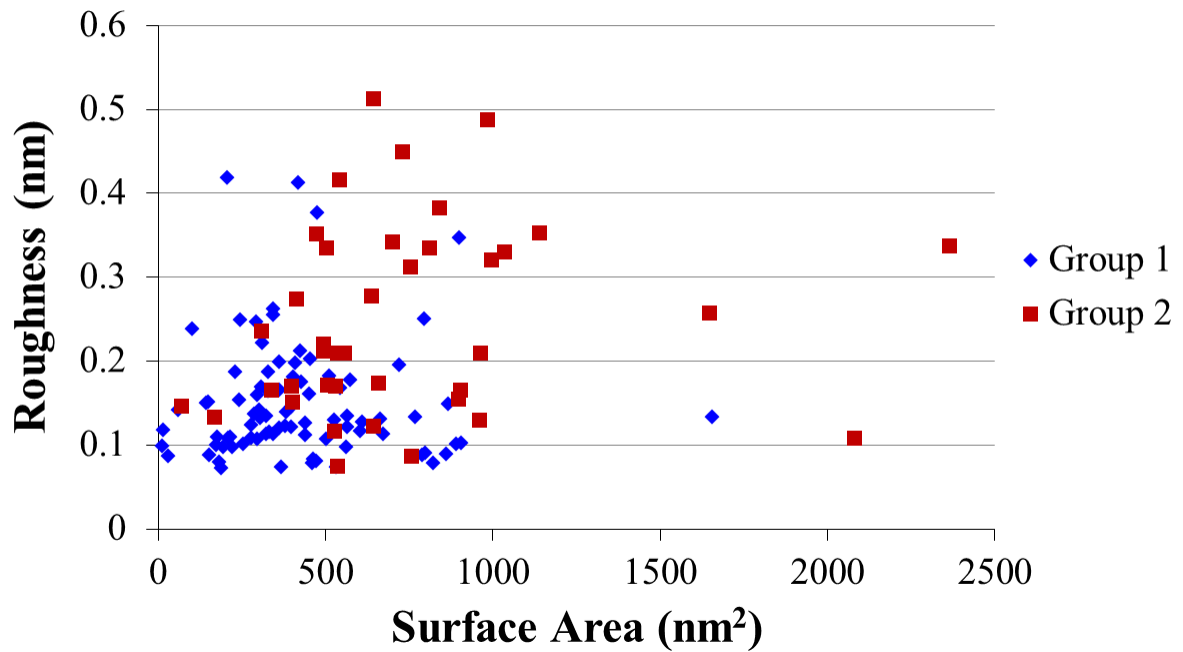


Figure A1.8. Plot of peak-to-peak roughness of mesa tops with respect to surface area for six separate experiments. Group 1 contains experiments with less than 10 total cleaning cycles while Group 2 contains experiments with more than 10 total cleaning cycles. Group 1 average peak-to-peak roughness is $0.15 \text{ nm} \pm 0.07 \text{ nm}$, Group 2 average peak-to-peak roughness is $0.25 \text{ nm} \pm 0.11 \text{ nm}$ with an overall peak-to-peak roughness of $0.18 \text{ nm} \pm 0.09 \text{ nm}$.

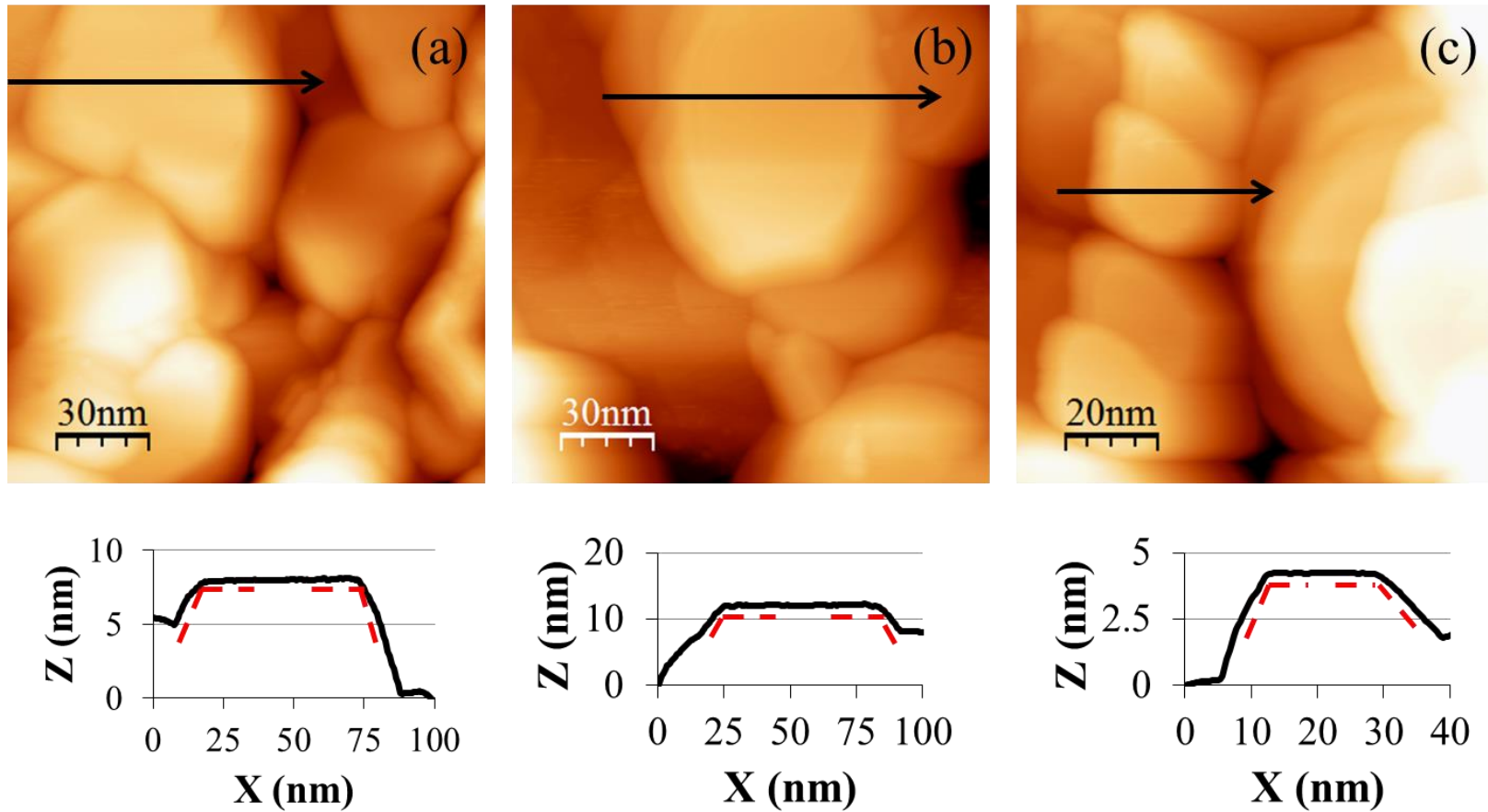
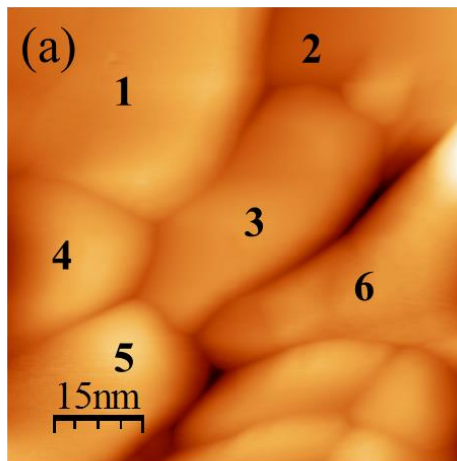
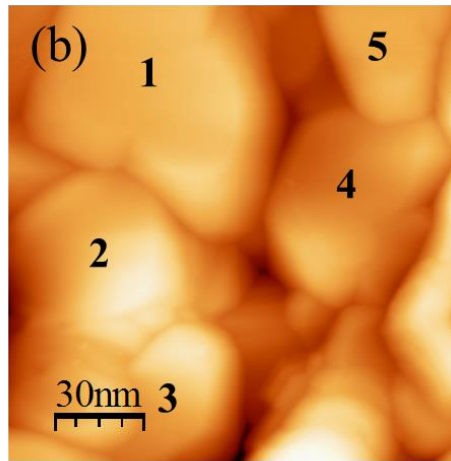


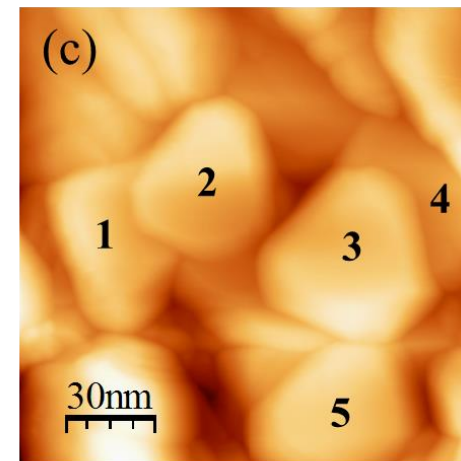
Figure A1.9. STM images and line profiles showing the angle between the top of the mesas and the slope of the sides. The average angle is $155^\circ \pm 7^\circ$. The red dotted lines represent the angles measured. (a)-(b) are 150 nm x 150 nm. (c) is 100 nm x 100 nm. Scanning parameters 0.1 nA to 0.2 nA, 1.0 V to 1.7 V.



Mesa 1:	Mesa 2:	“Step” Height (nm):
1	2	5.0
1	3	4.6
1	4	1.4
2	3	1.2
3	4	3.4
3	5	3.3
3	6	1.9
4	5	0.03
5	6	5.2



Mesa 1:	Mesa 2:	“Step” Height (nm):
1	2	1.6
1	4	4.6
2	3	6.8
4	5	1.3



Mesa 1:	Mesa 2:	“Step” Height (nm):
1	2	0.9
2	3	5.9
3	4	3.2
3	5	0.4

Figure A1.10. STM images of “step” heights between mesas. Each mesa is assigned a number within the image. The “step” height difference between two mesas is listed in the corresponding table below each image. (a) 75 nm x 75 nm, (b)-(c) 150 nm x 150 nm. Scanning parameters 0.15 nA to 0.5 nA, 1.2 V to 1.7 V.

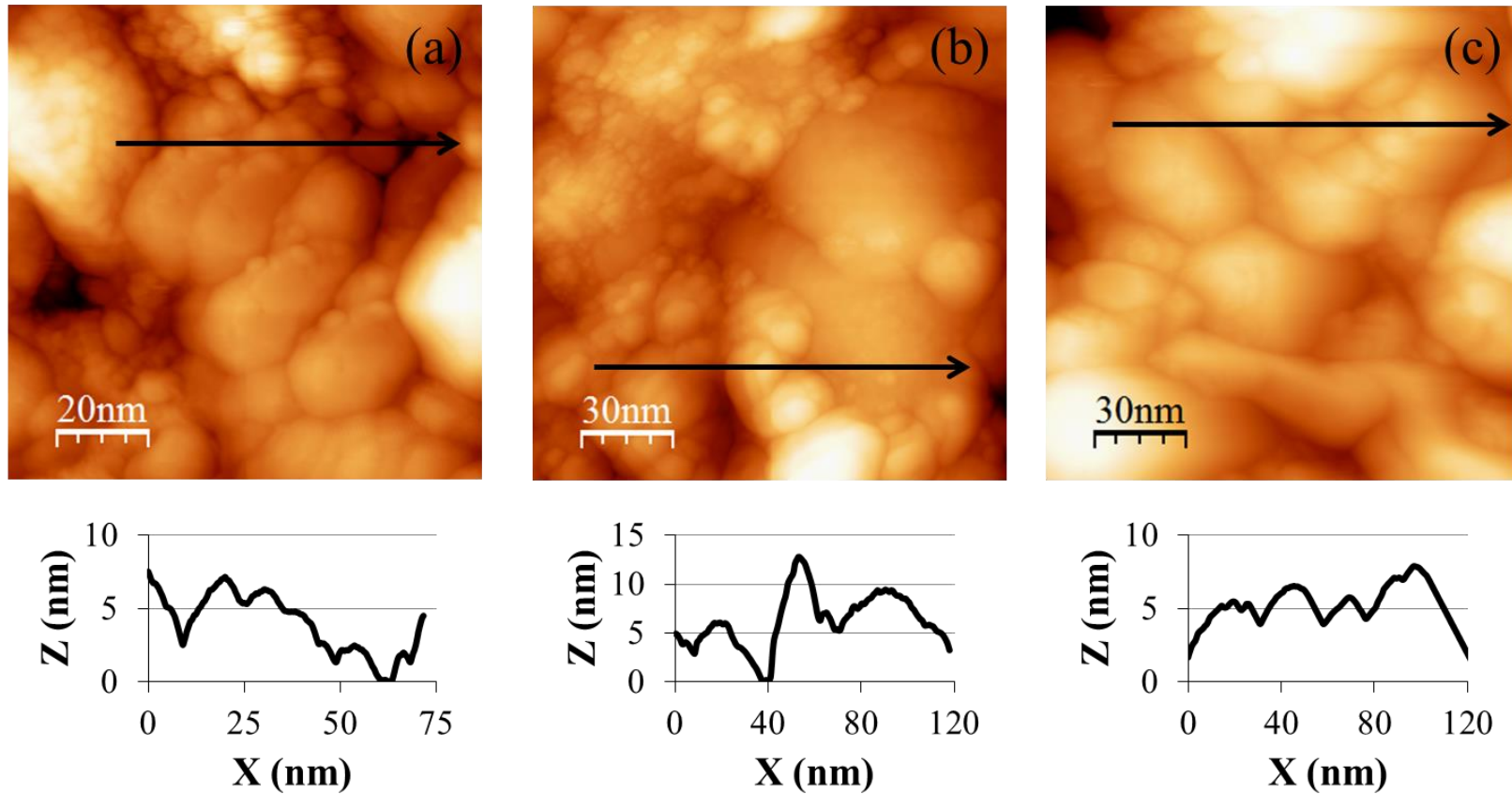


Figure A1.11. STM images and line profiles of the $\text{NaAu}_2(111)$ surface showing the round top mesas. (a) 100 nm x 100 nm (b)-(c) 150 nm x 150 nm. Scanning parameters (a)-(b) 0.2 nA to 0.4 nA, -2.0 V (c) 0.1 nA, 1.2 V.

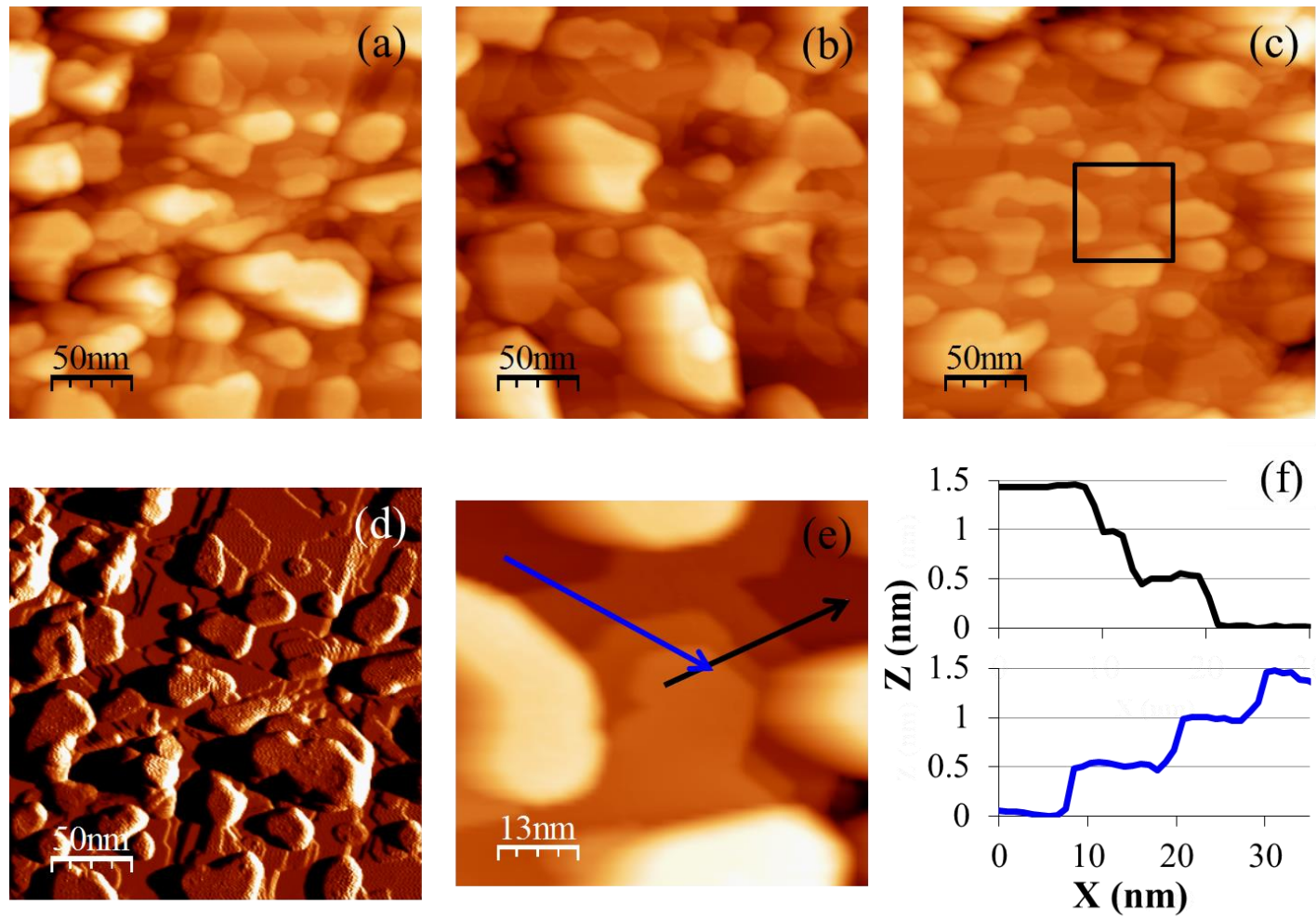


Figure A1.12. STM images of the transformed mesa structure with underlying step-terrace morphology. (a)-(c) are images of the typical sample surface after controlled cooling rate of 0.1 A/min. (d) the derivative of (a) to enhance the underlying step-terrace morphology. (e) a zoom of step-terrace in (c) indicated by the black box (f) Line profiles of the step edges in (e). Average step height seen in (e)-(f) is $0.47 \text{ nm} \pm 0.02 \text{ nm}$. (a)-(d) 250 nm x 250 nm (e) 66 nm x 62 nm. Scanning parameters 0.1 nA, 1.3 V.

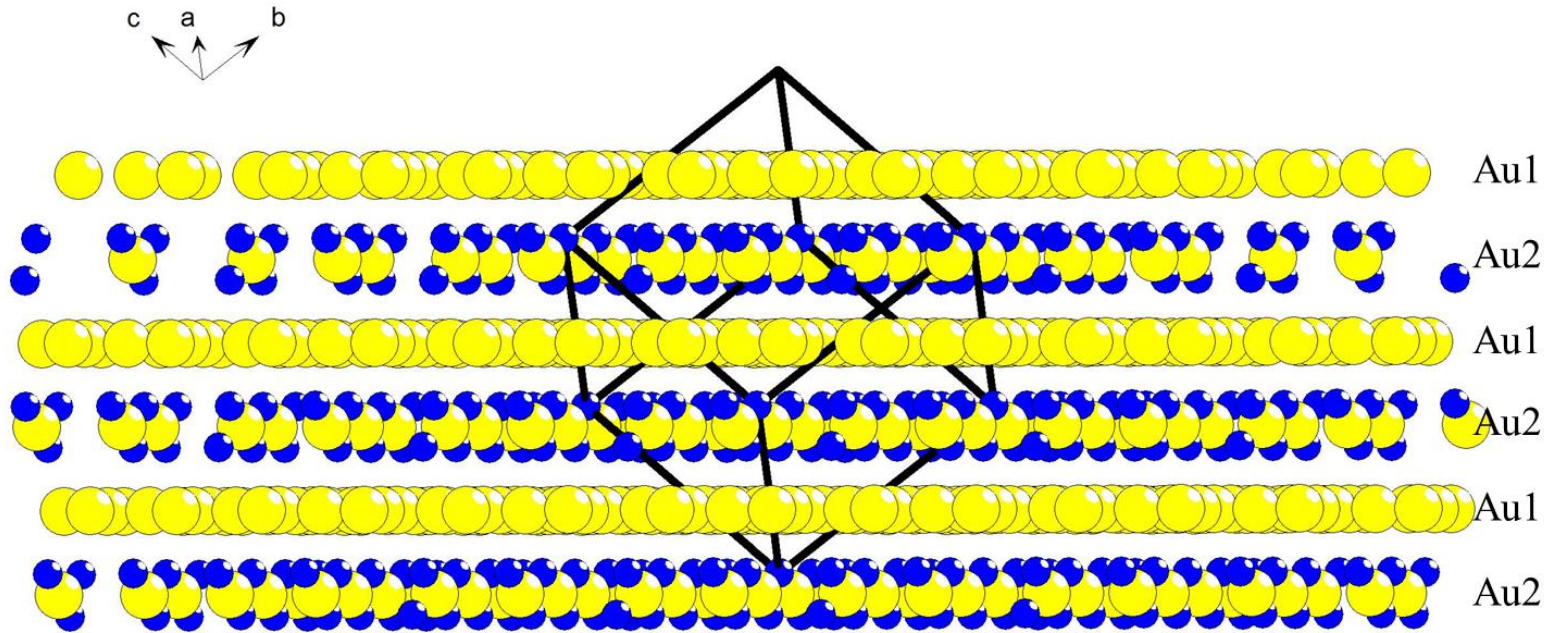


Figure A1.13. Schematic of NaAu₂ with view perpendicular to the (111) axis. Au atoms are yellow, Na atoms are blue. The black box shows the bulk unit cell. The separation between Au1 and Au1 is 0.45 nm. The separation between Au1 and Au2 is 0.23 nm. Figure provided by Professor Gordon J. Miller.

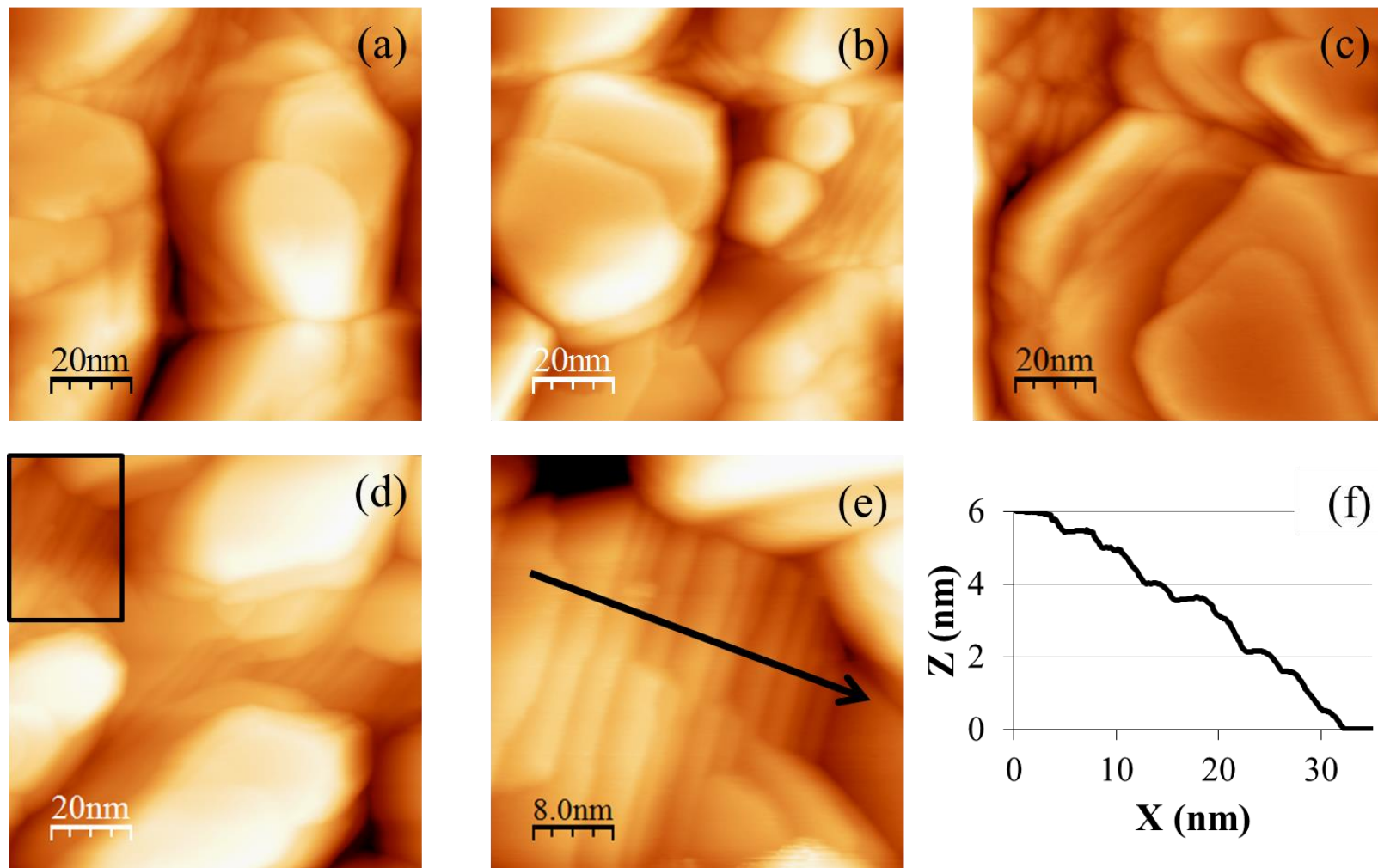


Figure A1.14. STM images of the mesa structure with infrequent step-terrace morphology after a second controlled cooling rate experiment. (a)-(d) are images of the typical sample surface after controlled cooling rate of 0.05 A/min. (e) a zoom of step-terrace in (d) indicated by the black box. (f) Line profile of the step edges in (e). Average step height seen in (e)-(f) is $0.49 \text{ nm} \pm 0.01 \text{ nm}$. (a)-(d) 100 nm x 100 nm (e) 40 nm x 40 nm. Scanning parameters 0.08 nA to 0.4 nA, 0.7 V to 0.9 V.

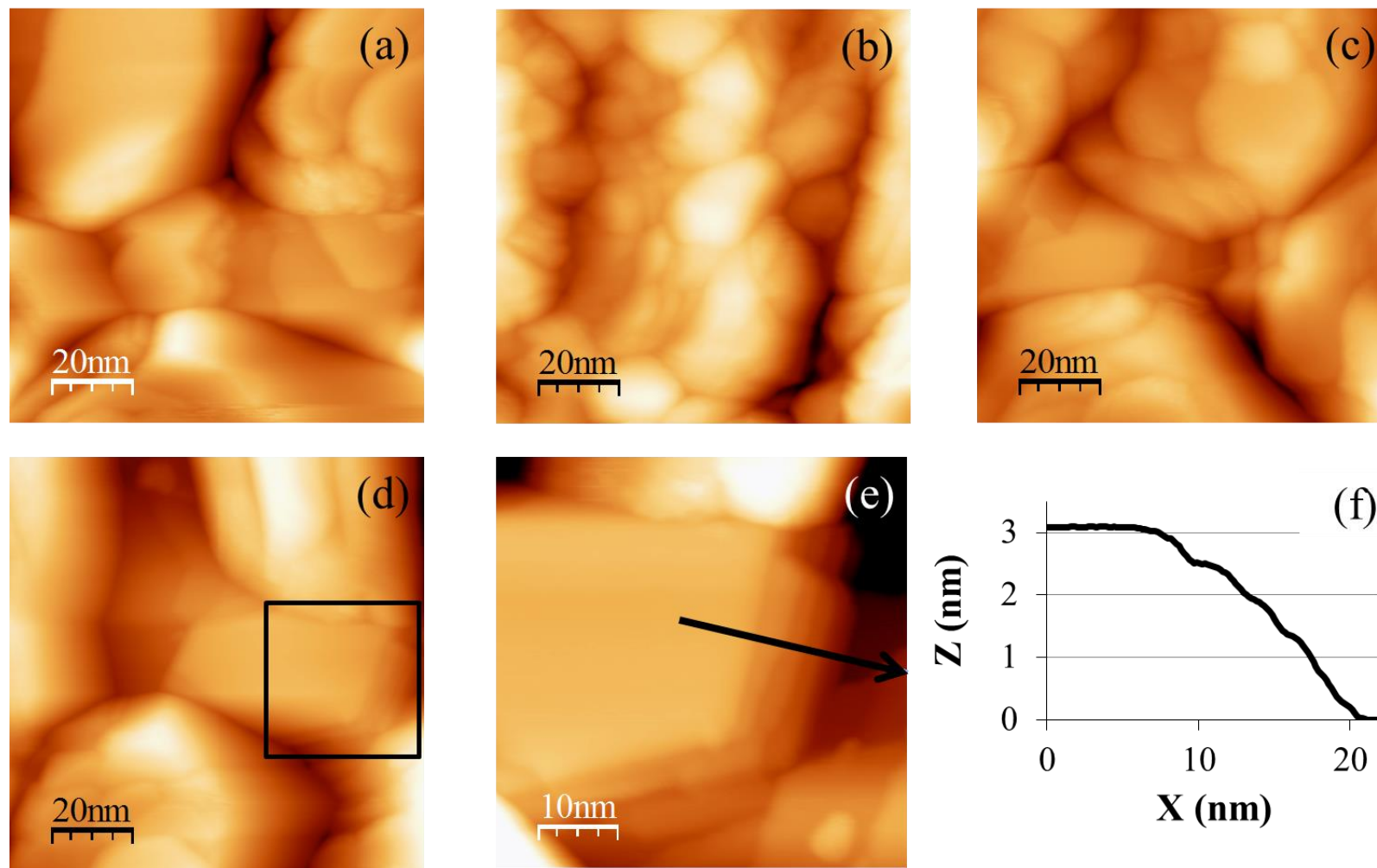


Figure A1.15. STM images of the mesa structure after a third controlled cooling rate experiment. (a)-(d) are images of the typical sample surface after controlled cooling rate of 0.05 A/min. (e) a zoom of step-terrace in (d) indicated by the black box. (f) Line profile of the step edges in (e). Average step height seen in (e)-(f) is $0.49 \text{ nm} \pm 0.01 \text{ nm}$. (a)-(d) 100 nm x 100 nm (e) 50 nm x 50 nm. Scanning parameters 0.1 nA, 0.7 V.

References

- ¹N. S. Stoloff, C. T. Liu and S. C. Deevi, "Emerging applications of intermetallics," *Intermetallics* **8**, 1313 (2000).
- ²A. P. Tsai and M. Yoshimura, "Highly active quasicrystalline Al-Cu-Fe catalyst for steam reforming of methanol," *Applied Catalysis A: General* **214**, 237 (2001).
- ³K. Kovnir, M. Armbrüster, D. Teschner, T. V. Venkov, F. C. Jentoft, A. Knop-Gericke, Y. Grin and R. Schlögl, "A new approach to well-defined, stable and site-isolated catalysts," *Science and Technology of Advanced Materials* **8**, 420 (2007).
- ⁴M. Armbrüster, K. Kovnir, M. Friedrich, D. Teschner, G. Wowsnick, M. Hahne, P. Gille, L. Szentmiklosi, B. Feuerbacher, M. Heggen, F. Girgsdies, D. Rosenthal, R. Schlögl and Y. Grin, "Al₁₃Fe₄ as a low-cost alternative for palladium in heterogeneous hydrogenation," *Nature Materials* **11**, 690 (2012).
- ⁵M. Haruta, T. Kobayashi, H. Sano and N. Yamada, "Novel Gold Catalysts for the Oxidation of Carbon Monoxide at a Temperature far Below 0°C," *Chemistry Letters* **16**, 405 (1987).
- ⁶A. S. K. Hashmi and G. J. Hutchings, "Gold Catalysis," *Angewandte Chemie International Edition* **45**, 7896 (2006).
- ⁷B. K. Min and C. M. Friend, "Heterogeneous gold-based catalysis for green chemistry: low-temperature CO oxidation and propene oxidation," *Chemical Reviews* **107**, 2709 (2007).
- ⁸C. Xiao, L.-L. Wang, R. V. Maligal-Ganesh, V. Smetana, H. Walen, P. A. Thiel, G. J. Miller, D. D. Johnson and W. Huang, "Intermetallic NaAu₂ as a Heterogeneous Catalyst for Low-Temperature CO Oxidation," *Journal of the American Chemical Society* **135**, 9592 (2013).
- ⁹P. A. Thiel and R. McGrath, "Surfaces of quasicrystals and complex metallic alloys" in *Properties of Composite Surfaces*, edited by K. Wandelt (Wiley, 2013), 3, pp. 349.
- ¹⁰J. V. Barth, H. Brune, R. Schuster, G. Ertl and R. J. Behm, "Intermixing and two-dimensional alloy formation in the Na/Au(111) system," *Surface Science* **292**, L769 (1993).
- ¹¹J. V. Barth, R. J. Behm and G. Ertl, "Adsorption, surface restructuring and alloy formation in the NaAu(111) system," *Surface Science* **341**, 62 (1995).
- ¹²K. Lieser and H. White, "Untersuchungen in den ternären Systemen Magnesium-Kupfer-Zinc, Magnesium-Nickel-Zinc und Magnesium-Kupfer-Nickel," *Zeitschrift für Metallkunde* **43**, 396 (1952).
- ¹³A. D. Pelton, "The Au-Na (Gold-Sodium) system," *Bulletin of Alloy Phase Diagrams* **7**, 228 (1986).

¹⁴D. Rosenthal, R. Widmer, R. Wagner, P. Gille, M. Armbrüster, Y. Grin, R. Schlögl and O. Gröning, "Surface Investigation of Intermetallic PdGa($\bar{1}\bar{1}\bar{1}$)," *Langmuir* **28**, 6848 (2012).

¹⁵C. D. Yuen, G. J. Miller, H. Lei, C.-Z. Wang and P. A. Thiel, "Structure of the clean Gd₅Ge₄(010) surface," *Journal of Physics: Condensed Matter* **25**, 485002 (2013).

¹⁶CasaXPS: Processing Software for XPS, AES, SIMS and More; www.CasaXPS.com, (October 19, 2014).

CHAPTER 4

INTERACTION OF OXYGEN WITH THE (111) SURFACE OF NaAu_2

A paper published in *Surface Science*

Emma J. Kwolek¹, Roland Widmer², Oliver Gröning², Okan Deniz², Holly Walen¹, Chad D. Yuen^{1,6}, Wenyu Huang¹, Deborah L. Schlager³, Mark Wallingford³, C. R. Brundle⁴, Patricia A. Thiel^{1,3,5}

¹Department of Chemistry, Iowa State University, Ames, Iowa 50011, USA

²nanotech@surfaces Laboratory, EMPA, Swiss Federal Laboratories for Materials Science and Technology, Ueberlandstrasse 129, 8600 Duebendorf, Switzerland

³The Ames Laboratory, Ames, Iowa 50011, USA

⁴C.R. Brundle & Associates, 4215 Fairway Drive, Soquel, California 95073, USA

⁵Department of Materials Science & Engineering, Iowa State University, Ames, Iowa 50011, USA

⁶Present address: Department of Chemistry and Biochemistry, Augustana College, Rock Island, Illinois 61201, USA

Abstract

NaAu_2 , in powder form, is known to be an active catalyst for CO oxidation. The goal of the present study is to elucidate the interaction of one reactant, molecular oxygen, with a single-crystal surface of this material, $\text{NaAu}_2(111)$. Exposing the clean surface to gas-phase molecular oxygen produces three types of oxygen on the surface. One type is bound in

spurious carbonate that forms during exposure. The second is adsorbed atomic oxygen that interacts both with Na and Au. The third type is atomic oxygen that interacts mainly or only with Na. We propose that the last species is an oxide of Na distributed throughout the surface and near-surface region. Its formation is accompanied by surface segregation of Na.

1. Introduction

Intermetallics are potential alternatives to precious metal catalysts for certain reactions.¹ For instance, quasicrystalline AlCuFe shows good activity and stability in steam reforming of methanol,² and both Pd-Ga compounds and Al₁₃X₄ (X = Fe, Co) intermetallics show promise for selective hydrogenation of alkynes.^{3,4} Independently, there has been great interest in Au—especially as supported nanoparticles⁵⁻⁸ and as nanoporous solids^{9,10}—as an effective low temperature catalyst for oxidation reactions.¹¹ The reasons for the intriguing catalytic properties of both classes of catalyst are diverse, and remain under active investigation.

The possibility of finding new catalysts at the nexus of these two types of materials—intermetallics and nano-structured Au—led to a recent investigation of the catalytic properties of an Au-rich intermetallic, NaAu₂.¹² The CO oxidation reaction was chosen because it is important, and also it is a benchmark indicator of the oxidative activity of Au in its various forms.¹³ Powders of this material showed excellent activity for CO oxidation, in a range of relatively low temperatures (T) between 300 K and 400 K.¹² In the model developed for this reaction, molecular oxygen adsorbs at a site involving multiple Au and Na atoms, including 1 Na atom that moves above the surface plane, i.e. it ‘pops out’. The molecule can react directly with CO_{ad} to form an intermediate OOCO_{ad}, and ultimately CO_{2,g} and O_{ad}.

Motivated by this report, we characterized the clean (111) surface of single-crystal NaAu₂ in ultrahigh vacuum (UHV), to determine its stability relative to the bulk, and hence the suitability of the (111) termination as a model for the active catalyst surface.¹⁴ We found that the surface could exist in one of two conditions. In one, both low-energy electron diffraction (LEED) and X-ray photoelectron diffraction (XPD) were consistent with expectations from bulk structure, with some evidence of disorder. Furthermore, STM showed mesa-like features whose flat tops likely exhibited bulk-termination—though atomic order could not be resolved. The regions separating the mesas must be regarded as significant defect regions. To provide a more graphic review, Figure 1 shows STM images and line profiles, together with diffraction data, for this state of the clean surface. In this paper, we present a re-analysis of the surface composition in this state using XPS and Auger electron spectroscopy (AES), showing that the surface is Na-enriched.

In the second condition, the surface was Na-depleted/Au-enriched. Na depletion was attributed both to preferential sputtering and desorption at elevated temperature. Based on temperature programmed desorption (TPD), Na desorption began at about 450 K. Since both processes (sputtering and heating) were employed repeatedly as part of the normal cleaning process between experiments, the samples could be used only for a limited number of experiments before pure, crystalline Au precipitated irreversibly. Prior to this point, surface Na could apparently be replenished from the near-surface reservoir.

With this as background, we now investigate the interaction of oxygen with the NaAu₂(111) surface. From energetics calculated previously,¹² certain predictions can be made. First, the residence time of molecular oxygen is so low that it should be unobservable under our experimental conditions. For the calculated adsorption energy, E_{ad} , of -0.38 eV, the

residence time at room temperature is of order 10^{-7} to 10^{-5} s, assuming a pre-exponential desorption rate factor of $10^{12\pm 1}$ s⁻¹. Measurements take place over several hours following oxygen exposure. Low temperatures would be necessary to stabilize it on an appropriate time-scale, as is true in general for molecular oxygen on surfaces, e.g.¹⁵⁻¹⁷. Second, the barrier to dissociation of adsorbed molecular O₂ is 1 eV, so irrespective of residence time, it would not dissociate at room temperature. Of course, both predictions apply to the ideal flat surface and, as noted above, the real surface is morphologically irregular. Our goal here is to determine whether atomic oxygen adsorbs and if so, whether its chemical state can be related to the surface composition and/or structure.

We first present analysis of XPS and AES data for the nominally-clean surface. We then describe standard oxygen adsorption experiments, which show that oxygen does adsorb, giving rise to two well-separated O 1s peaks in XPS. From these results, we develop a hypothesis that is tested with tailored experiments.

2. Experimental Details

Single-crystal samples of NaAu₂ were grown at the Materials Preparation Center of the Ames Laboratory via the Bridgman technique. All of the XPS experiments were carried out at EMPA in Dübendorf, Switzerland. All of the TPD experiments took place at the Ames Laboratory in Ames, Iowa, USA. Many aspects of the UHV instrumentation and experimental conditions for both sites have been described as part of our previous study of clean NaAu₂(111).¹⁴ Details unique to the oxygen adsorption experiments follow.

XPS experiments were conducted on the sample denoted B,¹⁴ which was re-polished for these oxygen experiments. Between each experiment, the sample was cleaned with two

cycles of sputter-annealing. Each cycle consisted of Ar⁺ ion bombardment at 1 keV for 3 minutes at 300 K, then annealing at 475 K for 15 minutes. For XPS, the sample was exposed to O_{2,g} by back-filling the chamber to a pressure of 1.0 x 10⁻⁸ to 1.0 x 10⁻⁷ mbar. Exposures are reported in units of Langmuir (L), where 1 L = 1.33 x 10⁻⁶ mbar-s. In cases where the sample was annealed after exposure to O_{2,g}, it was held at temperature for 20 minutes.

The XPS instrument was part of an Omicron ESCA UHV system, and consisted of a VSW 125 HR electron analyzer and a twin anode (Mg and Al) X-ray source. Spectra were acquired at emission (take-off) angles, θ , of 0°, 60°, and 80°, defined with respect to the surface normal. Unless noted otherwise the energy step was 0.1 eV and $\theta = 60^\circ$ in the figures. Spectra at $\theta = 60^\circ$ were used for quantitative analyses because signal-to-noise was optimal. The pass energy was constant at 80 eV. The energy scale was calibrated with an Au(111) sample, using Au lines from the 5d_{5/2} to the 4s_{1/2}. XPS data were analyzed using CasaXPS software.¹⁸ The purity of the oxygen used in the XPS experiments was checked on a separate UHV chamber, and no impurities were found. The detection limit for CO_{2,g} in the O_{2,g} was estimated at 0.5 vol%.

TPD experiments were conducted on Sample D,¹⁴ which was also freshly re-polished for these experiments. Between each run, Sample D was cleaned by sputtering with Ar⁺ at 1 keV for 3 minutes, and annealing at 420 K for 20 minutes. The sample was exposed to O_{2,g} through a doser with a design similar to that of Winkler and Yates,¹⁹ but with a single-aperture metal cap replacing the microchannel array. Based on our geometry, and the cosine distribution provided by such a doser, the pressure at the sample surface relative to the background pressure was enhanced by a factor of 7 ± 2 .²⁰ During O_{2,g} exposure the background pressure in the TPD chamber rose to 3 x 10⁻⁹ mbar, meaning that pressure at the

sample was $(2.1 \pm 0.6) \times 10^{-8}$ Torr. In TPD, original software created within the LabView framework controlled the thermal program and also was interfaced with a mass spectrometer for multiplexing.

In two experiments, the NaAu₂(111) surface was deliberately depleted of Na. In one case, moderate depletion was achieved with a two-cycle regimen: Ar⁺ bombardment at 300 K for 10 and 20 minutes, followed by heating at 525 K and 700 K for 10 and 20 minutes, respectively. In the other case, severe depletion was achieved with a three-cycle sequence of Ar⁺ bombardment at 300 K for 20, 45, and 3 minutes, followed by heating at 700 K, 750 K, and 475 K for 30, 20, and 10 minutes, respectively.

3. Experimental Results and Interpretation

3.1. Composition of the initial surface

Previously,¹⁴ we defined a quantity R as the ratio of integrated intensities for Na 1s and Au 4f peaks (cf. Figure 2(a)), corrected for the (Scofield) cross-section for each photoionization event.²¹ R was not corrected for photoelectron attenuation or instrumental parameters. The correction for attenuation would be particularly large, since the inelastic mean free path (IMFP) of Na 1s electrons is only one-third that of Au 4f electrons (in bulk Au), i.e. 0.5 and 1.5 nm, respectively.²² Therefore R , as previously defined, is not an accurate measure of the Na: Au composition, but it is used in this paper partly to facilitate comparisons with prior work, and partly because it reflects compositional trends with high signal-to-noise.

While the difference in sampling depth for the strong Na 1s and Au 4f XPS signals is large, this is not the case for the weaker Na 2s and Au 5p_{3/2} pair. Because these differ by only 6 eV in binding energy (BE), they have essentially identical IMFP values. Hence they are

more suitable for quantitative analysis, but precision is lower. Using these and correcting for the known cross-sections,²¹ a set of values from 9 separate surface preparations results in a Na: Au composition ratio of 0.6 ± 0.1 , or $\text{Na}_{1.2}\text{Au}_2$, suggesting an excess of Na in the near surface region. (See Supplementary Material.)

Other evidence supports Na enrichment. Even though the Na 1s: Au 4f ratio, R , should greatly underestimate the Na content for a homogeneous distribution, owing to the smaller sampling depth for Na, values of R are roughly stoichiometric.¹⁴ This indicates substantial excess Na within the small sampling depth of the Na 1s. Another indication is found in the peak/step background ratios for the Na signals compared to the Au signals. From Figure 2(a), it is obvious that the inelastically-scattered background steps after the Na Auger signals (on the higher BE side) are substantially weaker than those after the Au signals. This is clear evidence that, within the depth probed, the Na is distributed closer to the surface, so that there is less inelastic scattering of the exiting Na photoelectrons.

Assuming, for simplicity, that the excess Na is segregated to the top atomic layer, and beyond that the composition is stoichiometric, the excess amount can be estimated from the standard Beer-Lambert attenuation law. Using an Effective Attenuation Length, EAL, of 1.25 nm (to account for a 15 to 20% elastic scattering effect correction to the IMFP²³), and an atomic layer defined as 0.3 nm thick, a composition of $\text{Na}_{1.5}\text{Au}_2$ accounts for the observed Na 2s: Au 5p_{3/2} ratio of 0.6. We do not, however, suggest that there is a homogeneous layer of this composition at the surface, which has a substantial fraction not representative of the bulk terminated structure (Figure 1). The excess Na could be located on mesa edges, in the valleys, or distributed in random sites on top of the mesas, which according to the LEED and XPD results do have the bulk terminated structure. We also note that the Na 1s: Au 4f ratio

measurements on the 9 prepared surfaces exhibit a range of values, indicating a genuine variation in composition.

After cleaning, surfaces of NaAu₂ show a small residual peak at $E_b = 531.2 \pm 0.3$ eV, which falls in the range expected for the O 1s BE.²⁴ See Figure 2(c). The KL₁L_{2,3} Auger line of Na also appears in this range with an Al K α source, nominally at 532 eV.^{24,25} The Auger line does not fall in this region with a Mg K α source. In our experiments, the small feature is present with both X-ray sources, so it must originate at least in part from an oxygen species. Based on an analysis of relative intensities of Auger peaks with Mg and Al sources (see Supplementary Material), the Na Auger transition typically contributes 20 to 40% of the total residual intensity, with the Al source (number of data sets, N, of 4).

The nominally-clean surfaces also exhibit intensity in the C 1s region. As shown in Figure 2(d), there are two peaks. The larger, at 284-285 eV, is in the range associated with C-C bonded species, and the smaller, at 289-290 eV, is associated with C-O double bonds. The large negative heat of formation of sodium carbonate, -1130 kJ/mol,²⁶ makes carbonate a likely assignment for the latter. For comparison, the C 1s position falls at 289.0 eV for carbonate on Ni(111),²⁷ and at 289.3 eV for bulk Na₂CO₃.²⁸ The carbonate peak is convolved with the KL₁L_{2,3} Na Auger line for a Mg K α source, but not for Al.²⁵ It is notable that although the carbonate C 1s peak is small, it correlates with a much stronger O 1s peak, partly because of the 3:1 stoichiometry, and partly because the photoionization cross-section of O 1s is 2.9 times that of C 1s,²¹ leading to intensity amplification by a factor of 8.7. Throughout this paper, we assume that the 289-290 eV peak is carbonate, and use the factor of 8.7 to deduce the fraction of associated O 1s intensity. For the initial surface, carbonate then accounts for 20-30% of the oxygen-derived (non-Auger) O 1s signal (N = 2). The

remainder is reasonably attributed to oxygen dissolved in the bulk, supported by data in Section 3.3 below.

3.2. Oxygen exposure at 300 K

Focusing first on the O 1s spectral region, exposure to oxygen causes the residual peak to intensify. It also produces peaks at 1 or 2 new positions in the O 1s region, depending on the X-ray source, as shown in Figure 3. The 3 peaks are labeled A, B, C in order of decreasing (apparent) BE. Their areas and positions are determined via deconvolution, as illustrated in Figure 3(a) and Figure 3(d). Arguments for individual assignments follow.

Peak A, at 535 ± 0.2 eV, is observed only with the Al source, and must therefore be the Na $KL_1L_{2,3}$ Auger peak. It apparently shifts upward from the residual position upon oxygen exposure (cf. Section 3.1). This is substantiated by shifts observed for other Na Auger lines. For example, in Figure 2(b) the $KL_{2,3}L_{2,3}$ line moves upward by about 3 eV after 50 L O_2 exposure. The intensification of Peak A with increasing oxygen exposure, evident in Figure 3(b), reflects increasing Na surface concentration as will be discussed in the following material.

Peaks B and C, at 531.5 ± 0.4 eV and 527.9 ± 0.2 eV respectively, represent oxygen species that grow with increasing oxygen exposure, developing roughly in parallel as shown by Figure 3(c) and Figure 3(f). Close inspection reveals a difference, however: Peak C reaches a plateau at 10 L, whereas Peak B continues to grow steadily beyond this exposure. This different evolution indicates that these two peaks do not have a common origin. The BE of Peak B is compatible with carbonate and, as shown below, carbonate contributes a substantial fraction of its total intensity but not all. The BE of Peak C is much lower than

normally observed for atomic oxygen adsorbed on transition metal surfaces, suggesting an electron-rich oxygen atom in an ionic bond; sodium oxide is an obvious candidate. For comparison, the O 1s BE for an oxidized surface of bulk Na falls at 529.6 eV.²⁵

Angle-resolved XPS is not generally informative in this system. Most often, trends as a function of θ are small and irreproducible. This may be due to the intrinsic roughness of the surface, illustrated in the STM images of Figure 1. However, there is one trend that is reproducible and relatively strong. Figure 4 shows the relative contributions of Peaks B and C to the total O 1s intensity, after 50 L exposure at 300 K, at $\theta = 0^\circ$, 60° , and 80° with a Mg source. Two separate experiments are shown, to illustrate the degree of consistency. Peak B contributes a greater fraction of the total O 1s intensity as the emission angle becomes more shallow (more surface-sensitive). From this, we conclude that Peak B represents species that are more localized at the surface, whereas Peak C has contributions from deeper in the bulk.

Oxygen adsorption is accompanied by changes in the Na, Au, and C signals. Figure 5 shows that the Na 1s line intensifies, while the Au 4f line weakens. (Neither has any overlap with lines of other elements in the system.) These changes are also represented as a strong increase in R , shown in Figure 5(c). After exposure to 50 L O_{2,g} at 300 K, R increases by an average factor of 2.6 ± 0.6 ($N = 8$). This means that Na becomes much more abundant, concurrent with oxygen adsorption. At the same time, the carbonate peak grows as shown in Figure 5(d). At 50 L, carbonate accounts for half of the oxygen species represented by Peak B in the experiment of Figure 2(a)-(c).

The intensity of Peak B depends on the conditions of exposure, being reduced by 1/3 if exposure is carried out in a single step rather than sequentially. This is almost entirely due to a reduction in the quantity of carbonate-oxygen. Possible sources of carbon for carbonate

include contamination from the X-ray anode, adventitious carbon represented by the C 1s peak at 284-285 eV, and diffusion of carbon from the bulk sample in concert with Na. We do not consider CO_g or CO_{2,g} as likely candidates, since they were undetectable in the O_{2,g}. Consistently, the amount of adventitious carbon declines upon oxygen exposure, indicating that this may indeed contribute, although there is not a quantitative correlation between the magnitude of this decrease and carbonate increase. But also, the fact that carbonate is higher in the sequential experiments could indicate an origin in contamination from the X-ray source. In short, we are unable at present to determine the carbonate's source(s).

Finally, in Figure 6 we show the XPD patterns observed after 50 L O_{2,g} exposure at 300 K. The structure in the Na 1s pattern for the initial surface (Figure 1(c)) is gone, replaced by a diffuse background exhibiting broad three-fold symmetry. The O 1s XPD is similar. The Au 4f pattern is still evident, but with higher background. The Au structure is probed more deeply than Na due to its larger IMFP (cf. Section 3.1), so these XPD data likely mean that the top few layers become disordered, while the bulk structure is retained deeper below the surface.

3.3. Effects of heating to temperatures below and above the Na desorption onset

Experiments in which the surface is exposed to 50 L O_{2,g} at 300 K, then annealed at 425 K and 475 K, are informative. These two temperatures are chosen because they are slightly below and slightly above the onset of Na desorption, respectively.¹⁴ Peaks B and C respond differently to this thermal treatment, as illustrated in Figure 7(a) and Figure 7(b).

We have considered the possibility that Peak B (at higher BE) represents molecular oxygen, and the other peak represents atomic oxygen. However, if Peak B were molecular

oxygen, its intensity would decrease with heating, due to dissociation. (Desorption can be ruled out based on TPD data presented below.) Its behavior rules out this assignment.

Heating also affects the intensities of the Au 4f and Na 1s peaks, and consequently affects the value of R . The Na 1s spectra, and R , are shown in Figure 7(c) and Figure 7(d). (The Au 4f spectra are omitted, since only their intensity changes measurably, and this change is captured in R .) Between 300 K and 425 K, the Na content increases slightly, but between 425 K and 475 K, it decreases. We attribute these changes in Na and Au concentration to activated diffusion of Na from the bulk toward the surface at 425 K, followed by loss of Na due to desorption at 475 K. At the same time, the intensity of the carbonate C 1s signal (not shown) is unaffected by heating, indicating that carbonate does not contribute to the observed changes. Anhydrous sodium carbonate is reportedly stable in air up to 800 K.²⁹

TPD adds more insight. Figure 8(a) illustrates the intensity of the signal at a mass-to-charge ratio of $m/e = 23$, corresponding to the apparent partial pressure of Na, as a function of temperature. The curves overlap, i.e. oxygen has no effect on Na desorption. At this heating rate, 6.0 K/s, Na begins to desorb at about 480 K. However, there would certainly be significant desorption if the sample were held at 475 K for extended periods, like the 20 minute anneals in the experiments of Figure 7. Figure 8(b) demonstrates that the partial pressures of $m/e = 32$ and $m/e = 39$, corresponding to O_2 and NaO, respectively, are invariant with temperature in the same temperature range. In other words, there is no evidence for desorption of O_2 or NaO. This means that as the sample is heated, the loss of oxygen indicated in XPS must be due to bulk dissolution, hence explaining part of the residual peak on the as-prepared surface.

All of this information forms a basis for the following model. Peak C originates from oxygen bonded only or mainly to Na, located in the surface and near-surface region. At 300 K, it grows in a self-limiting process, leading to saturation of Peak C as a function of oxygen exposure. If this sample is heated to 425 K, the reaction can proceed a little further; more Na moves upward (toward the surface), causing R to increase slightly. However, this process must result purely from equilibration, since no new oxygen is available from adsorption during this experiment. At 475 K, the sample loses some Na via desorption, causing a decrease in R , and a further decrease in Peak C intensity. On the other hand, Peak B originates partly from carbonate, and partly from adsorbed atomic oxygen in an environment that is influenced by both Na and Au. We do not associate Peak B with oxygen interacting only with Au atoms, since oxygen is not stable on macroscopic, pure Au surfaces.³⁰⁻³³

If this model is correct, then two predictions can be made. First, oxygen exposure at 425 K should favor Peak C over Peak B, by allowing the O-Na reaction to occur more effectively *during* oxygen adsorption. This should be accompanied by a stronger increase in R than the 2.6-fold increase upon simply heating from 300 K to 425 K. Secondly, a Na-depleted surface should ad/absorb less total oxygen, and Peak C should be especially attenuated. We therefore test the model by performing these specific experiments.

3.4. Oxygen adsorption at 425 K

Exposing the surface to 100 L O_{2,g} at 425 K yields the O 1s spectrum shown in Figure 9(a). Compared to exposure at 300 K (Figure 3), the intensities of Peaks B and C are reversed, i.e. Peak C is more intense than Peak B. Furthermore, R increases from 0.48 for the initial clean surface, to 4.4 after oxygen exposure—almost a 10-fold change, much higher

than the factor of 2.6 at 300 K. This indicates much stronger surface segregation of Na when the sample is exposed to $O_{2,g}$ at 425 K than at 300 K. Both of these changes are consistent with predictions from Section 3.3.

3.5. Oxygen adsorption on Na-depleted surfaces at 300 K

As described in Section 2, we deliberately removed Na from the surface via extended ion bombardment at 300 K, followed by annealing at temperatures as high as 750 K. In this way, surfaces with initial values $R_0 = 0.30$ and $R_0 = 0.09$ were generated. ($R_0 \leq 0.4$ indicates that an irreversible transformation to crystalline Au has begun in the surface and near-surface region.¹⁴) Subsequent exposure to 50 L $O_{2,g}$ in a single step produced the results shown in Figure 10. Under these conditions, there is no trace of Peak C (even in deconvoluted spectra). This validates the expectation that Peak C is more strongly dependent on Na concentration than Peak B.

The total amount of adsorbed oxygen decreases with decreasing R_0 (decreasing initial Na content), as shown by comparing Figure 10(a) with Figure 10(b). To illustrate this further, the O 1s area is plotted vs. R_0 in Figure 11. The data point at far left represents a normal $NaAu_2$ surface. Comparing this point with the two from Na-depleted surfaces (farther right), shows a steady decrease and ultimately a ten-fold reduction in the total amount of adsorbed oxygen. This is also in agreement with the prediction.

Another feature is that oxygen adsorption on depleted surfaces produces only small changes in R . For the marginally depleted surface, R increases from 0.30 to 0.48, a factor of 1.6. For the heavily depleted surface, R increases from 0.09 to 0.12, a factor of 1.3. These are much smaller than the factors of 2.6 and 10 for non-depleted surfaces at 300 K and 425 K,

respectively. This result is reasonable since, on the depleted surfaces, there is less Na available in the near-surface region to segregate upward in response to oxygen adsorption.

4. Discussion

The data show that there are two main O 1s lines associated with adsorbed oxygen. The one at low BE, Peak C, represents a sodium oxide(-like) species that is distributed in the surface and near-surface region. The one at higher BE, Peak B, has contributions from carbonate and from a type of adsorbed oxygen that interacts both with Na and Au.

The XPD patterns show that these species cannot be interpreted in terms of the bulk termination. Nonetheless, earlier calculations for atomic oxygen adsorbed on such a surface¹² are informative. Relevant adsorption sites are shown in Figure 12. Two of these are most favorable for atomic oxygen, with equal adsorption energies of $E_{ad} = -0.60$ eV. The first site is labeled fcc-Na. Here the oxygen adatom interacts with three Au atoms in the top layer and one Na atom beneath. If every such site is filled, then oxygen coverage in atomic monolayers (ML) is 1/3, where unity means one O atom per Au atom in the surface layer. The stabilization imparted by underlying Na is clear from comparison with the hcp-Au site, for which $E_{ad} = -0.18$ eV. The second site is the Na-bridge site (Figure 12), where oxygen bridges 2 Au atoms and also interacts with a pop-out Na. If all such sites are filled the coverage is again 1/3 ML. Therefore, DFT points to the importance of mixed Na-Au sites for oxygen adsorption, which agrees with experiment.

It is possible to estimate the amount of oxygen present in Peak B, as follows. The XPS intensity, I_d , originating from a depth, d , is given by

$$I_d = I_0 (1 - e^{-d/(EAL \cos \theta)}) \quad (1)$$

Here I_0 is the integrated intensity from infinite depth, i.e. from the bulk material. To calculate the fraction of Au signal originating from the top atomic layer of the clean surface, an EAL of 1.25 nm is used (as justified in Section 3.1, for a Mg anode) and an atomic layer thickness of 0.3 nm is assumed. The emission angle θ is 60° . Substituting in the equation above gives an I_d of 0.37, that is, 37% of the Au signal originates from the outermost layer of Au. The oxygen coverage then is simply the observed O 1s intensity after adsorption, relative to 37% of the observed Au signal of the clean surface, after correcting both intensities for their relative photoionization cross-sections. (An underlying assumption is that all oxygen in Peak B is at the surface, as supported by the angle-resolved XPS.) The experimental ratio of O 1s:Au 4f intensities with the Mg anode, for sequential exposures to 50 L, is 0.085 ($N = 2$). Correcting for the known relative cross-sections of 2.85 and 17.5, respectively,²¹ the ratio becomes 0.52, so the oxygen coverage is $0.52/0.37 = 1.4$ ML. Half of this is carbonate per Section 3.2, leaving 0.7 ML of Peak B as oxygen adsorbed at Na-Au sites. This is twice the coverage predicted for an ideal NaAu_2 surface. The disordering that accompanies oxygen adsorption may be a restructuring that optimizes local Na-Au-oxygen bonding, producing higher oxygen coverage than could be achieved on the ideal surface.

Turning now to the oxygen in Peak C, its development is accompanied by diffusion of Na from the bulk toward the surface. This diffusion is more facile at 425 K than at 300 K, leading to a deeper and more extensive sodium oxide. (Inward diffusion of oxygen may also be important.) This oxide is greatly suppressed when the initial surface is Na-depleted. Given the structural heterogeneity of the initial surface (Figure 1), we postulate that nucleation of the oxide is also heterogeneous, probably forming initially in troughs and at edges of mesas. A schematic is shown in Figure 13, summarizing our observations and interpretation.

Formation of sodium oxide is reasonable from a thermodynamic perspective. The formation enthalpy of NaAu_2 is -99 kJ/mol from experiment,³⁴ whereas the corresponding values for oxides of sodium are much more negative:²⁶ -263 for NaO_2 , -409 for Na_2O , and -505 for Na_2O_2 , all in kJ/mol. The surface oxide may well be a mixture or a progression of these, depending upon relative availability of Na and O.

Finally, we consider some implications for understanding the catalytic activity of powdered or dispersed NaAu_2 . Our data show that oxygen disrupts the surface structure of $\text{NaAu}_2(111)$, implying that the bulk termination is not a good model for the majority of a real surface, at least not under reaction conditions where oxygen can accumulate. Second, the data show that sodium oxide—and sodium carbonate—form readily in oxygen-rich environments, and so may influence catalytic reactions. Third, there is evidence for an atomic oxygen species that is stabilized by interaction both with Na and Au, consistent with the stability of atomic oxygen at such mixed sites in Ref. 12. It is possible that the formation of sodium oxide and carbonate, entails the production of under-coordinated Au sites on the surface. It has been shown, both experimentally and theoretically, that under-coordinated Au sites can greatly increase the catalytic activity of gold surfaces.^{35,36}

5. Conclusions

XPS and AES analysis of the as-prepared surface reveals enrichment in Na. The excess Na is probably distributed heterogeneously on the surface, in light of the structural heterogeneity. XPS also reveals residual oxygen and carbon. After oxygen exposure, there are two oxygen-derived XPS peaks. From angle-resolved data, the one at higher BE represents a species that is surface-localized, whereas the other is distributed through the

surface and near-surface region. The surface-localized state is a combination of adventitious carbonate, and atomic oxygen at a mixed Na-Au site (about 0.7 ML). While it could be appealing to associate the mixed Na-Au sites with the bulk-terminated surface regions, XPD shows that oxygen disrupts the first few $\text{NaAu}_2(111)$ layers. The other state is sodium oxide, associated with surface segregation of Na. Formation of sodium oxide is strongly enhanced when adsorption occurs at 425 K because diffusion of sodium is facilitated. At higher temperature, loss of Na in XPS is due to desorption, and loss of oxygen is due to bulk dissolution. On surfaces that are initially Na-depleted, the oxide is suppressed preferentially and oxygen adsorption is suppressed overall. This is because depleted surfaces progressively revert to pure Au, where oxygen is not stable. The reasons for good catalytic activity of powdered NaAu_2 in CO oxidation may be more complex than envisioned initially.

Acknowledgements This work was a collaboration between EMPA in Dübendorf, Switzerland, and Iowa State University in Ames, Iowa. Accordingly, this work was supported from two sources: the Swiss National Science Foundation (contract number (Contract 200021-129511), and the John D. Corbett Endowment of Iowa State University.

Figures

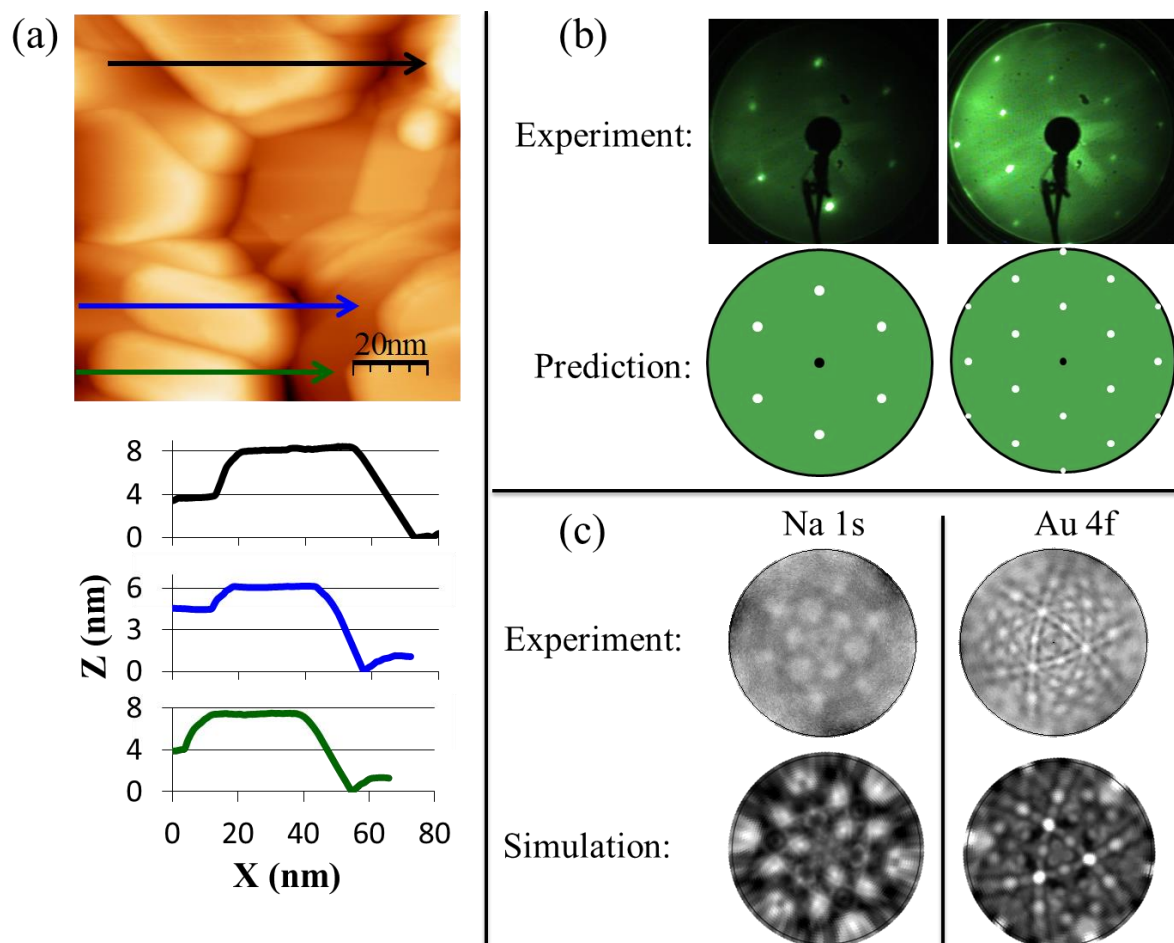


Figure 1. STM and diffraction data for the clean surface of NaAu_2 . (a) Typical STM image (top) and line profiles (bottom), showing the mesa-like structure. (b) Low-energy electron diffraction patterns. Top two patterns show images measured at 27.0 eV (left) and 45.0 eV (right). Lower two patterns show images predicted for a bulk-terminated surface at these energies. (c) X-ray photoelectron diffraction patterns using Na 1s and Au 4f photoelectrons, both measured with an Al $K\alpha$ source (top) and simulated (bottom).

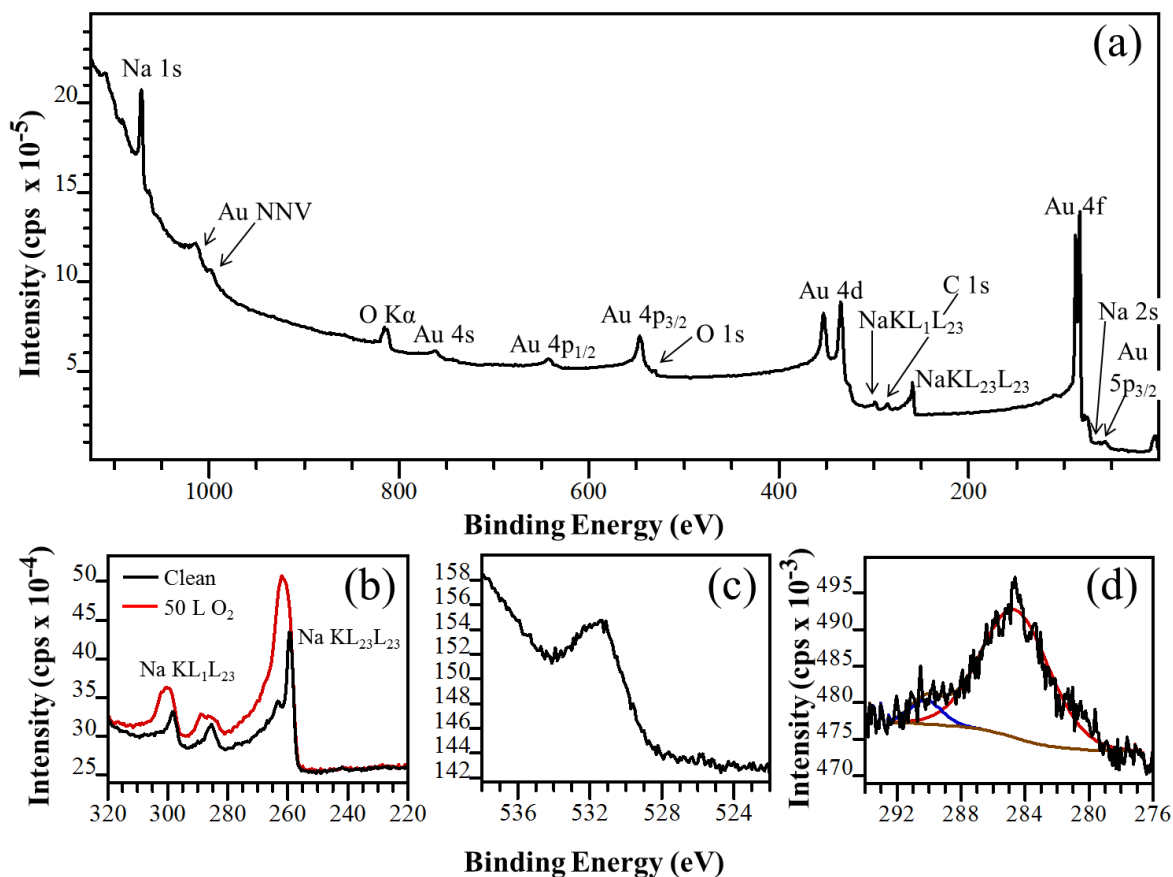


Figure 2. Photoelectron spectra for the NaAu₂ clean surface. Panels (a)-(c) are acquired with a Mg anode, panel (d) with Al in a separate experiment. (a) Entire spectral range, 0-1125 eV, measured in 0.5 eV steps. (b) Spectral range including Na KL_{2,3}L_{2,3} (ca. 260 eV) and Na KL₁L_{2,3} (ca. 300 eV) lines, measured in 0.5 eV steps. Black: Cleaned surface. Red: Surface after 50 L O₂ exposure at 300 K. (c) O 1s region, cleaned surface. (d) C 1s spectrum, cleaned surface. The Al anode is chosen in (d) to circumvent overlap with a Na Auger peak.

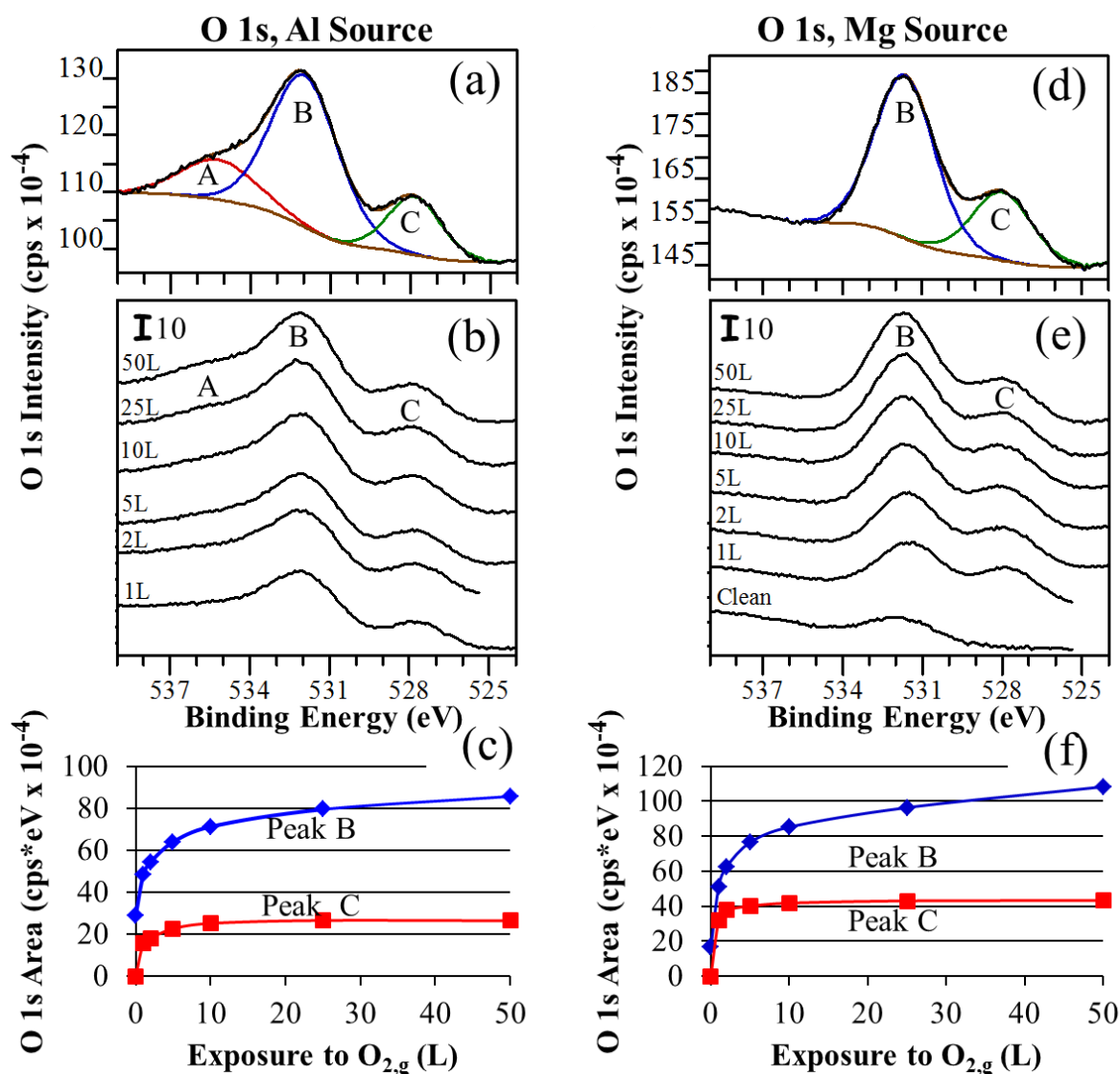


Figure 3. Photoelectron spectra in the O 1s region, for two sequences of oxygen exposures at 300 K. Data in (a), (b), and (c) were acquired with an Al $K\alpha$ X-ray source. Data in (d), (e), and (f) were acquired with a Mg $K\alpha$ X-ray source in an entirely separate experiment. In (b) and (e), the curves are displaced vertically to minimize overlap. The intensity, in units of $\text{cps} \times 10^{-4}$, can be derived using the scale bar. (a) Spectrum obtained after 50 L exposure, deconvoluted into three peaks. (b) Sequence of spectra following exposures to 1 L to 50 L (c) Integrated areas of Peaks B and C as a function of exposure. (d) Spectrum obtained after 50 L exposure, deconvoluted into two peaks. (e) Sequence of spectra following exposures to 1 L to 50 L (f) Integrated areas of Peaks B and C as a function of exposure. Y-axis “cps” units are defined as counts per second.

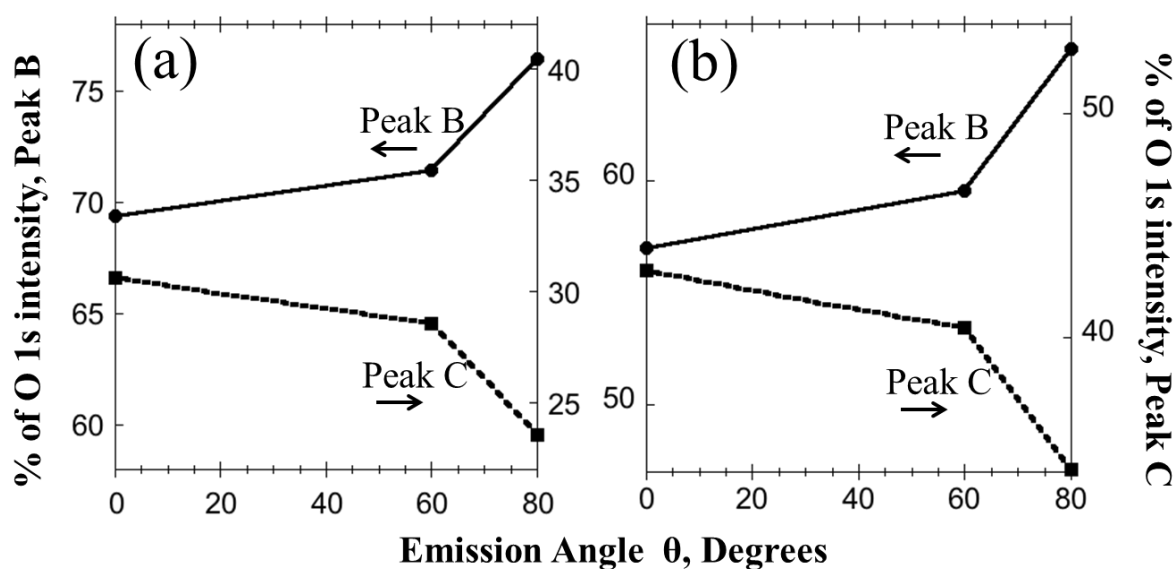


Figure 4. Percent of total O 1s intensity for Peaks B and C, as a function of emission angle, following a 50 L exposure at 300 K. The X-ray source is Mg $K\alpha$. Each vertical axis spans 20%. (a) and (b) represent two separate experiments, and are shown to indicate reproducibility.

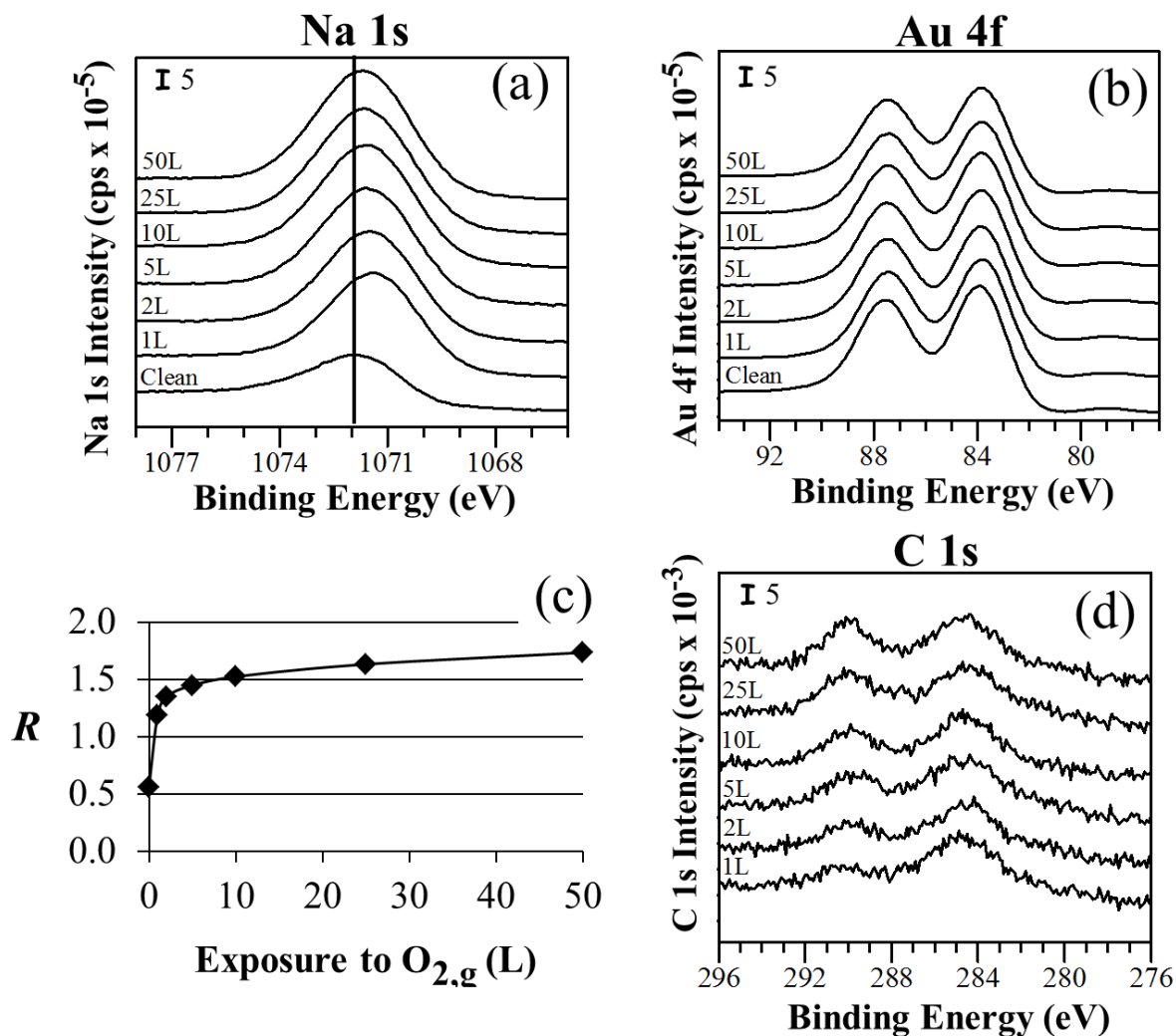


Figure 5. Na 1s, Au 4f, and C 1s photoelectron peaks for experiments in which the surface was exposed to oxygen sequentially from 1 to 50 L at 300 K. The X-ray anode is Mg in the experiment of panels (a)-(c), and Al in the experiment of panel (d). In (a), (b), and (d), the curves are displaced vertically to minimize overlap. The intensity, in units of $\text{cps} \times 10^{-5}$ or $\text{cps} \times 10^{-3}$ can be derived using the scale bar. (a) Na 1s. (b) Au 4f. (c) R vs. oxygen exposure. (d) C 1s.

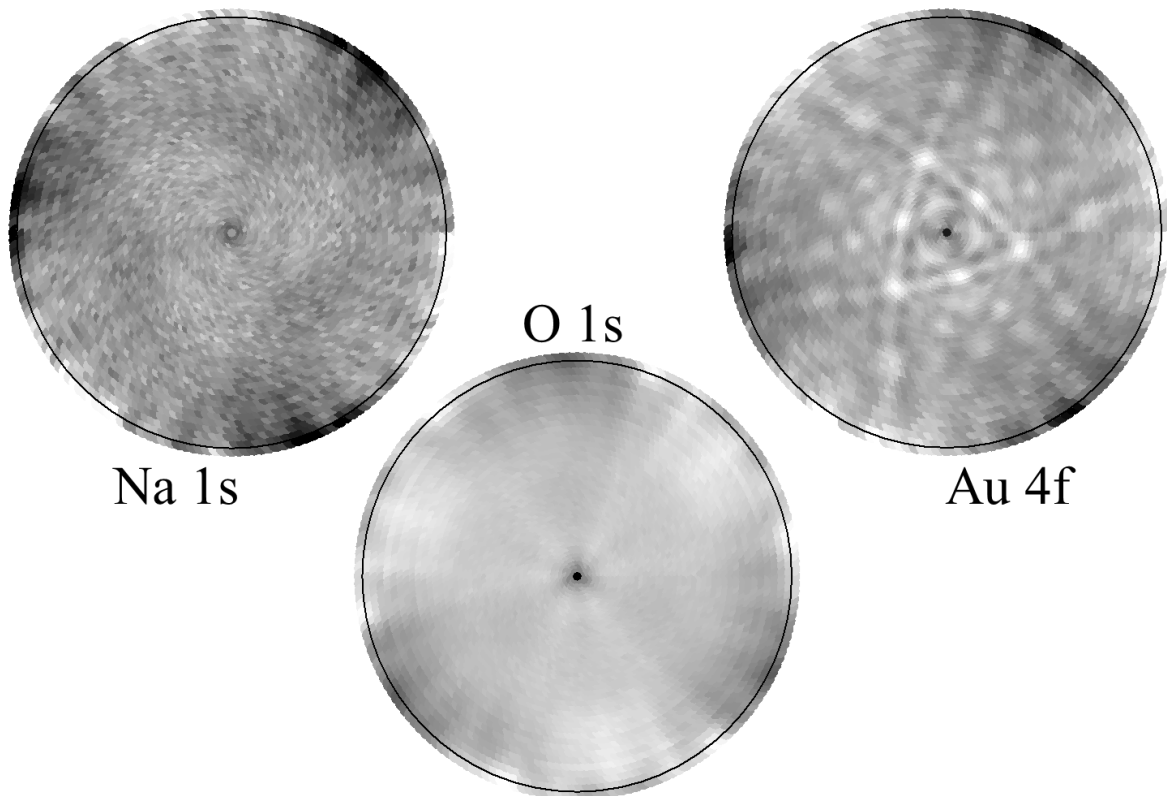


Figure 6. XPD patterns after 50 L exposure at 300 K.

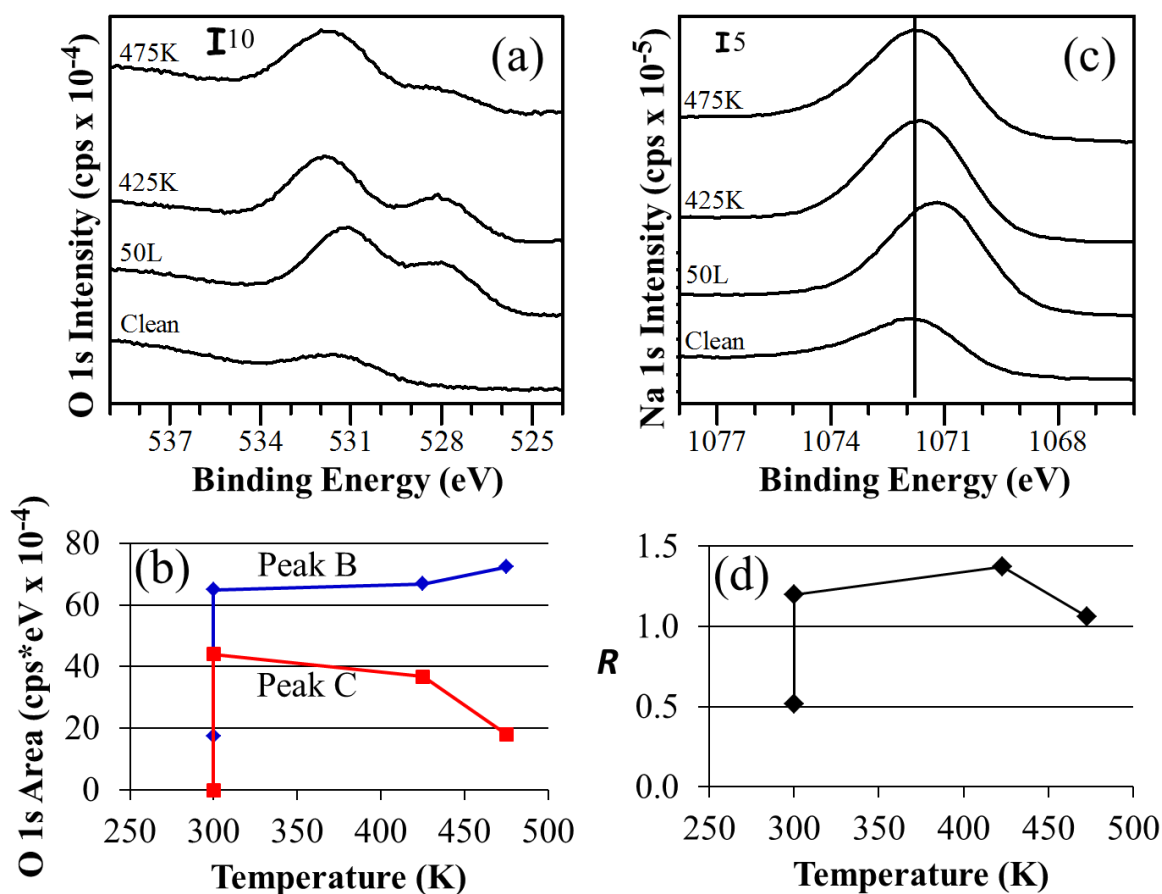


Figure 7. Result of exposing a surface to 50 L O_{2,g} at 300 K, then annealing sequentially to 425 K and 475 K. The X-ray source is Mg K α . In (a) and (c), the curves are displaced vertically to minimize overlap. The intensity, in units of cps x 10⁻⁴ or 10⁻⁵, can be derived using the scale bar. (a) O 1s spectral region. (b) Integrated areas of Peaks B and C. In each case, the lower point at 300 K represents the clean surface, and the upper point is obtained after 50 L exposure to oxygen. (c) Na 1s spectra for the same sequence as in panel (a). (d) R vs temperature. The lower point at 300 K represents the clean surface, and the upper point is obtained after 50 L exposure to oxygen.

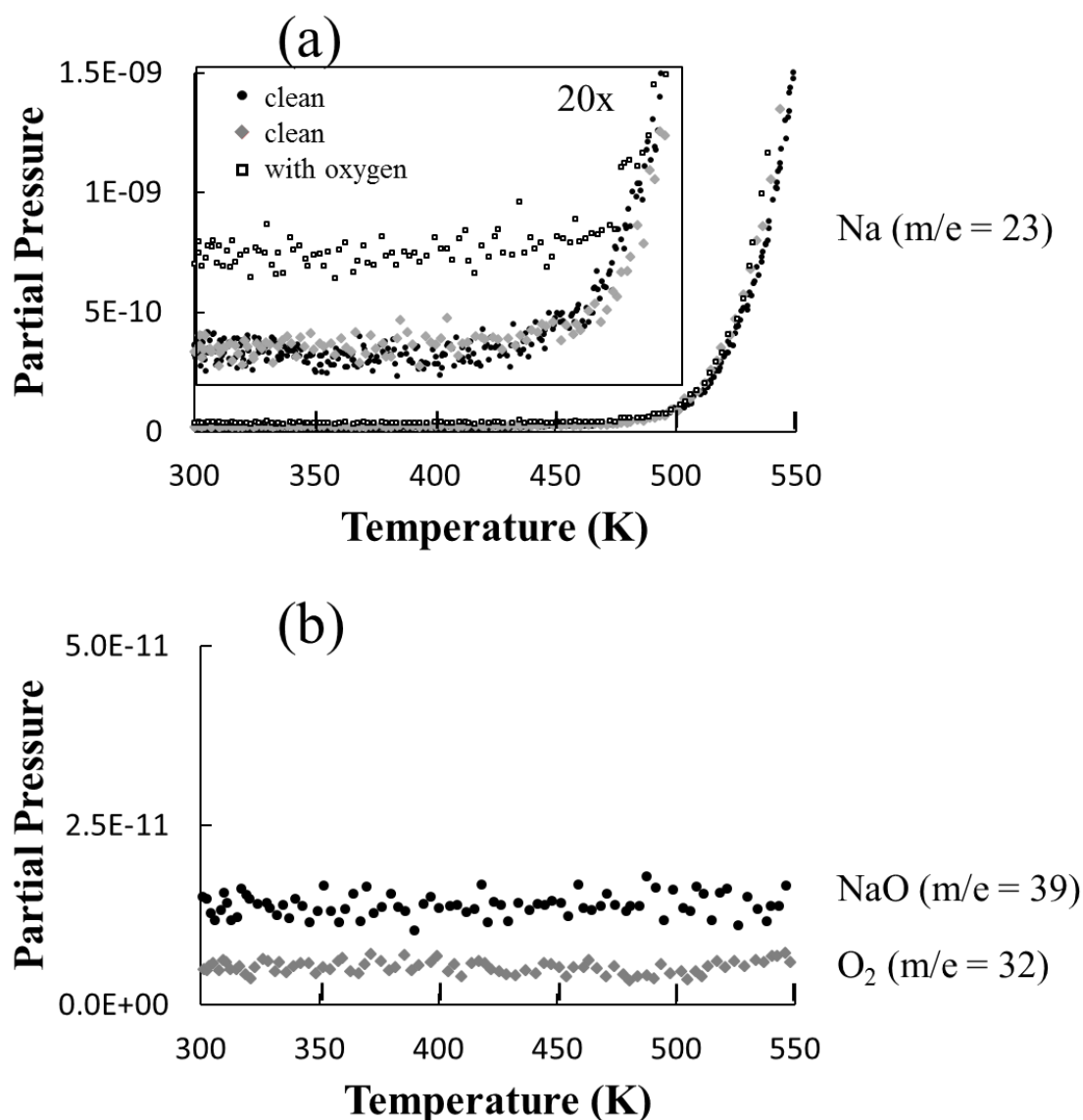


Figure 8. Results of temperature programmed desorption (TPD) for clean surfaces and a 25 L $O_{2,g}$ exposures at 300 K. Heating ramp rate was 6.0 K/s and was highly linear starting at 350 K. (a) Sodium desorption ($m/e = 32$) from sample clean surfaces and an oxygen exposure. (b) NaO ($m/e = 39$) and O_2 ($m/e = 32$) desorption after oxygen exposure.

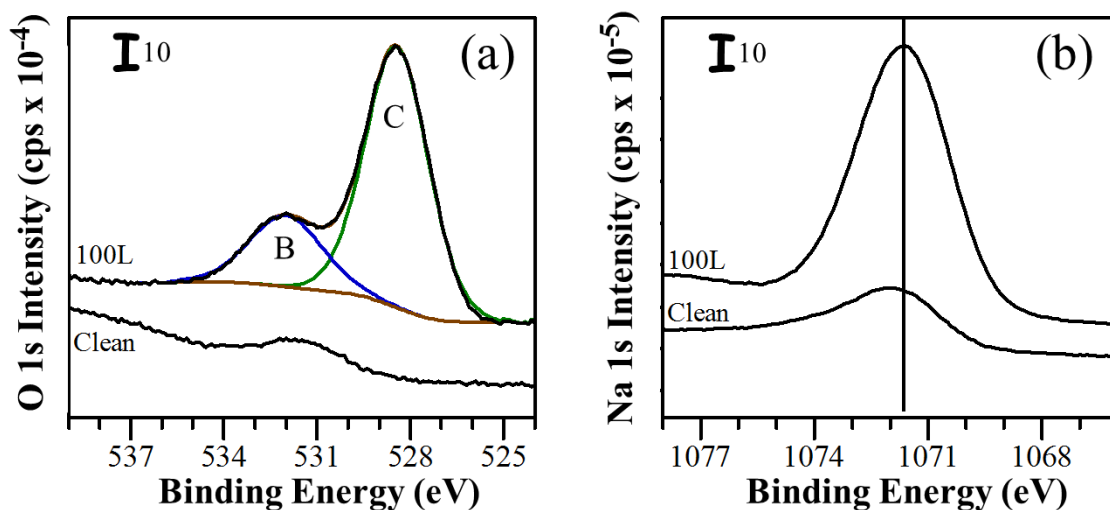


Figure 9. Result of exposing a surface to 100 L O_{2,g} at 425 K. The X-ray source is Mg K α . The curves are displaced vertically to minimize overlap. The intensity, in units of cps x 10⁻⁴, can be derived using the scale bar. (a) O 1s spectral region, with clean surface for reference and 100 L exposure deconvoluted into two peaks. (b) Na 1s spectral region for the same sequence as in panel (a).

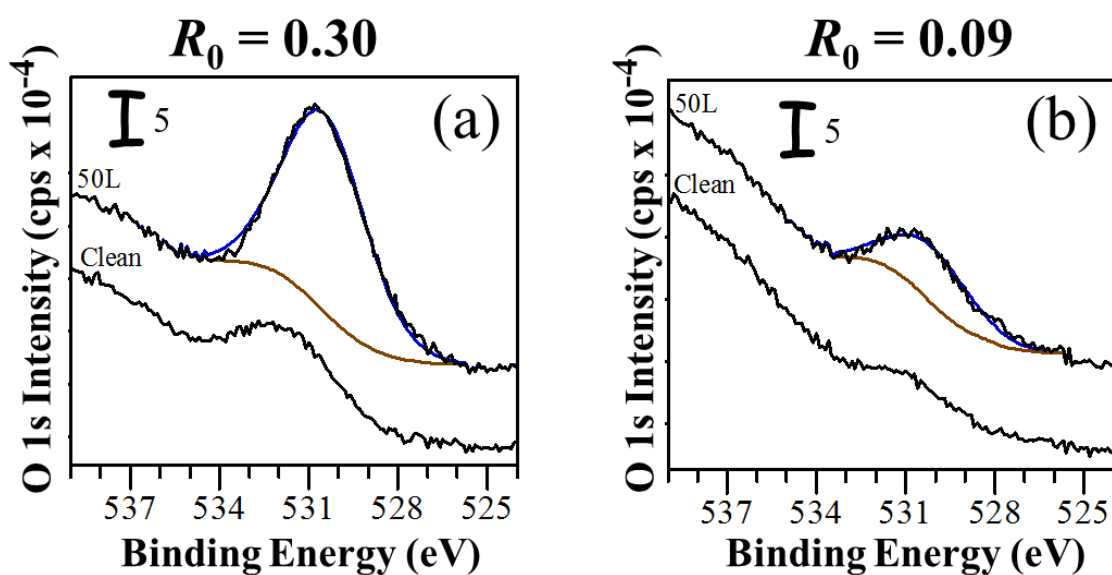


Figure 10. Results of exposing two sodium-depleted surfaces to 50 L $O_{2,g}$ in a single step at 300 K. The X-ray source is Mg $K\alpha$. The curves are displaced vertically to minimize overlap. The intensity, in units of $\text{cps} \times 10^{-4}$, can be derived using the scale bar. (a) $R_0 = 0.30$. O 1s spectral region. Bottom and top curves are before and after exposure, respectively. (b) $R_0 = 0.09$. O 1s spectral region. Bottom and top curves are before and after exposure, respectively.

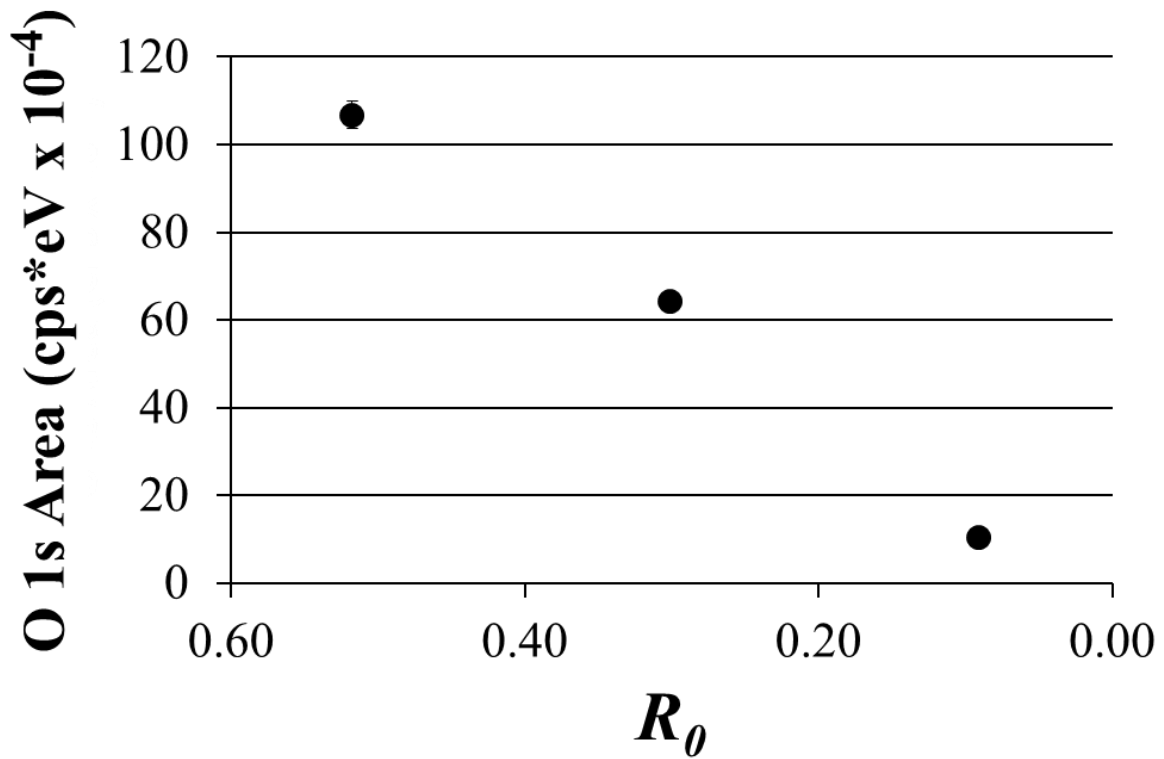


Figure 11. O 1s integrated areas vs. R_0 values after exposing a surface to 50 L O_{2,g}. The point at 0.52 R_0 is an average of two one-step exposures with the Mg anode. Error bars are barely larger than the data symbol. The remaining points are each one exposure with the Mg anode, corresponding to Figure 9.

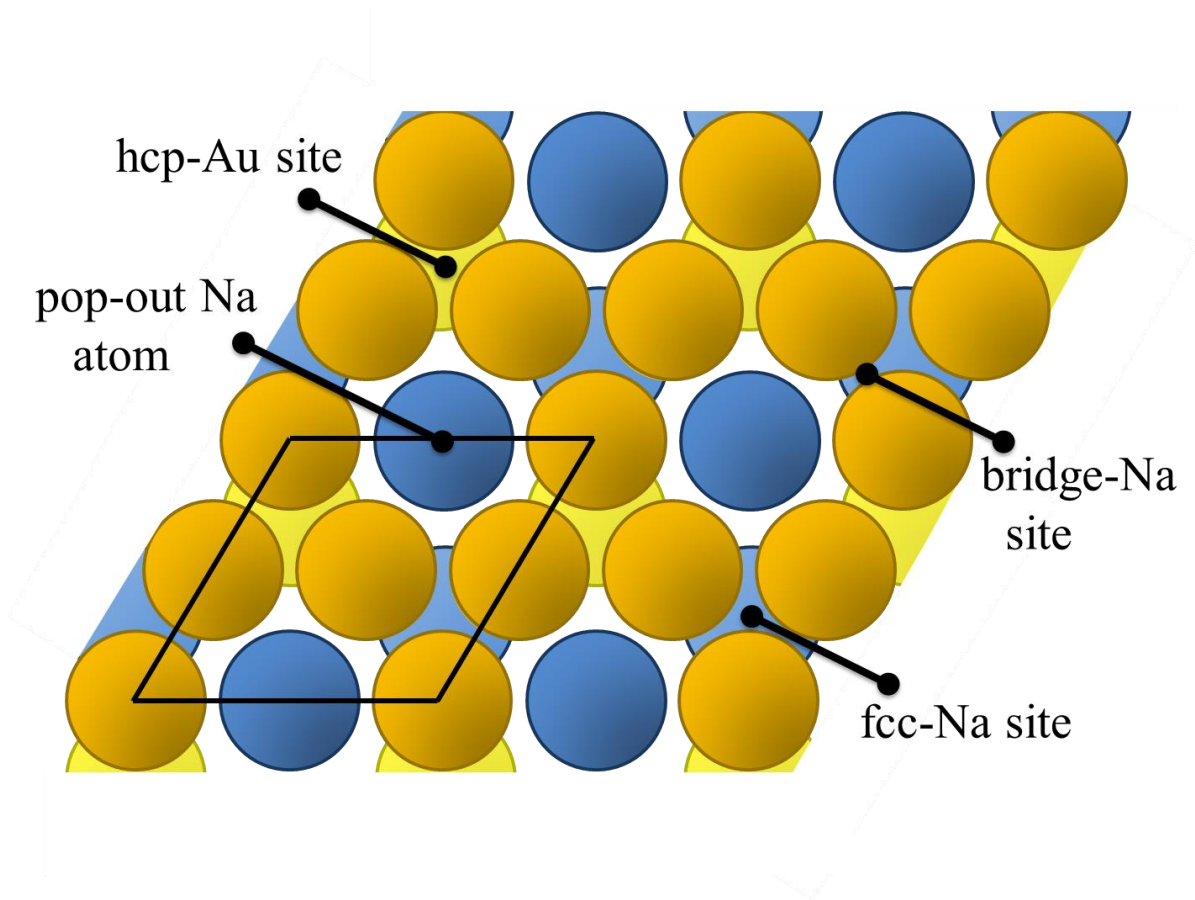


Figure 12. Top four planes of atoms in $\text{NaAu}_2(111)$. Planes and atoms in planes are identified as follows, with the z -axis defined perpendicular to the surface plane: Dark yellow, Au atoms at $z = 0$; dark blue, Na at $z = -0.143$ nm; yellow, Au at $z = -0.225$ nm; and light blue, Na at $z = -0.307$ nm.

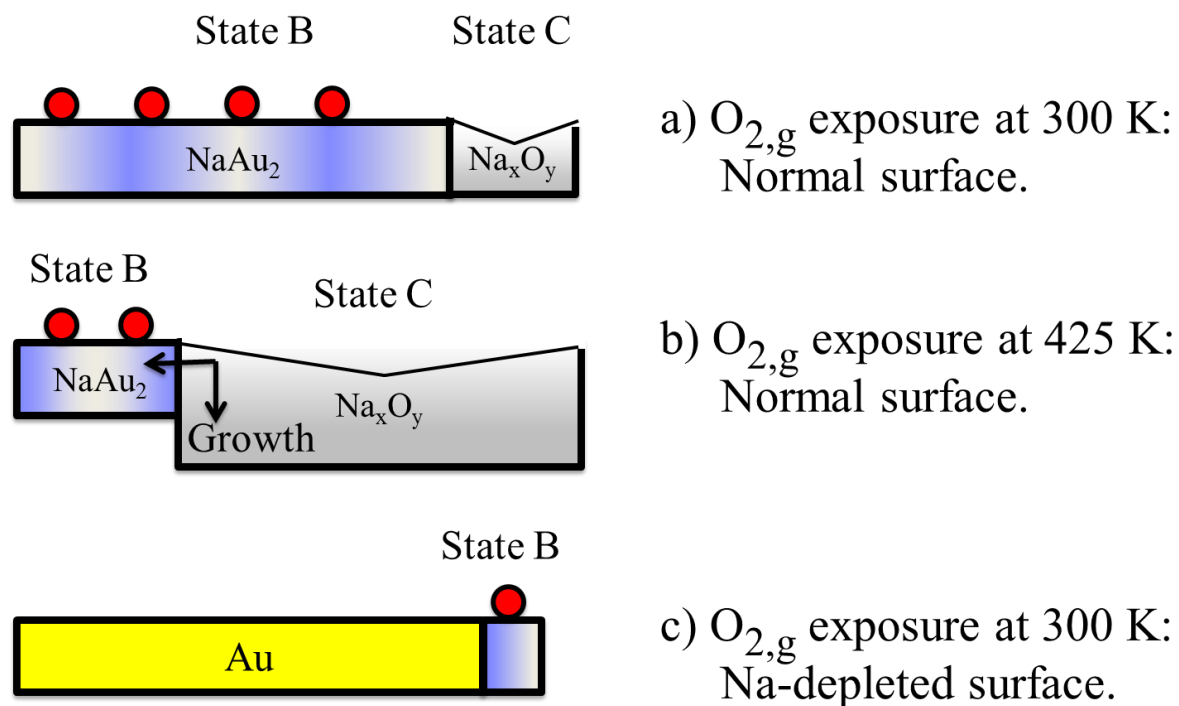


Figure 13. Model of sample surface depicting oxygen adsorption at various surface compositions and temperatures, where State B represents $NaAu_2$ and State C represents Na_xO_y . The angled shape associated with Na_xO_y is meant to suggest that the oxide may preferentially form at troughs and edges of mesas. (a) Normal surface composition with $O_{2,g}$ exposure at 300 K. (b) Normal surface composition with $O_{2,g}$ exposure at 425 K. (c) Na-depleted surface composition with $O_{2,g}$ exposure at 300 K.

Appendix 1. Supplementary Information

1. Calculation of Na: Au composition ratio using Na 2s and Au 5p_{3/2} lines

Na 2s (62.9 eV) and Au 5p_{3/2} (56.6 eV) peaks were used to give a more accurate value of the Na: Au atomic ratio. These two lines were chosen because they are close in energy and hence, their IMFP values are essentially identical. The peaks themselves overlap in the spectrum, so they must be deconvoluted to give respective areas. Satellite peaks of the Au 4f peak were also present at lower binding energies and intensities as a result of non-monochromatized Mg K α X-rays and Al K α X-rays.³⁷ Some of the Au 4f satellite peaks fall within the Na 2s and Au 5p_{3/2} region and must also be deconvoluted. The following method was used to do that.

Deconvolution regions were set for each spectrum and a linear background was used. A linear fit was used to subtract a spectrum background which included the peak tail of the Au 4f K α ₄ satellite peaks at ~78-72 eV. Each region was then fitted for the Na 2s, Au 5p_{3/2} and additional Au 4f_{7/2} K α ₅ satellite peak. The Au 4f_{7/2} K α ₅ satellite peak appears at ~66.5 eV for the Mg source and ~64.5 eV for the Al source.³⁷ Figure A1(a)-(b) show an example of the deconvolution for the Mg source spectra, with the Au 4f_{7/2} K α ₅ satellite peak clearly visible at ~66.5 eV. Figure A1(c)-(d) shows an example of the deconvolution for the Al source spectra. In this case, the Au 4f_{7/2} K α ₅ satellite peak was within the same range as the Na 2s peak and had to be deconvoluted using a different method. A clean Au(111) spectrum from the same instrument was used to determine the ratio between the Au 5p_{3/2} peak area and the Au 4f_{7/2} K α ₅ satellite peak area (which is visible without sodium present). See Eq. A.1a.

$$R_{\text{Au}} = \text{Au } 5p_{3/2} : \text{Au } 4f_{7/2} K\alpha_5 \text{ ratio} = \frac{\text{Au } 5p_{3/2} \text{ Area Au(111)}}{\text{Au } 4f_{7/2} K\alpha_5 \text{ Area Au(111)}} \quad (\text{Eq. A.1a})$$

This ratio, denoted as R_{Au} , gave a value of 0.06. To correct the Na 2s peak area in the NaAu₂ spectrum, the area of the Au 5p_{3/2} peak was multiplied by 0.06 and the resulting value subtracted from the Na 2s peak area as shown in Eq. A.1b.

$$\text{Corrected Na 2s Area} = \text{Na 2s Area} - (\text{Au 5p}_{3/2} \text{ Area} * R_{Au}) \quad (\text{Eq. A.1b})$$

Known Scofield cross-sections (δ) given for Na 2s and Au 5p_{3/2} in Table A.1, were then applied to each corrected peak area, respective to the X-ray source.²¹ These cross-sections give the probability of an electron being emitted from specific elemental orbitals and are used to normalize elemental intensities.

Table A.1. Scofield Cross-Sections (δ)

X-ray Source	Scofield Cross-Section (δ)	
	Na 2s	Au 5p _{3/2}
Al Anode	0.422	1.10
Mg Anode	0.390	0.877

This corrected Na 2s area was then divided by the corrected Au 5p_{3/2} area to calculate the composition ratio, as shown in Eq. A.1c.

$$\text{Na:Au composition ratio} = \frac{\text{Corrected Na 2s Area} / \delta_{Na\ 2s}}{\text{Corrected Au 5p}_{3/2} \text{ Area} / \delta_{Au\ 5p_{3/2}}} \quad (\text{Eq. A.1c})$$

2. Determination of the Na KL₁L_{2,3} contribution on cleaned surfaces of NaAu₂

In the XPS spectrum for NaAu₂, the O 1s peak (531.2 eV \pm 0.3 eV) and Na KL₁L_{2,3} (532 eV) peak fall within the same range with an Al K α X-ray source. To determine the

percentage of the O 1s peak that is Na KL₁L_{2,3} on the cleaned surface, the following method was used.

The ratio of the oxidized peak area to the cleaned surface peak area for the Na KL₁L_{2,3} line should be equivalent for the two X-ray sources used. See Eq. A.2.

$$X_1/Y_2 = X_2/Y_1 \quad (\text{Eq. A.2a})$$

For this method the variables were defined as:

X_1 = Na KL₁L_{2,3} oxidized peak area with Mg source

X_2 = Na KL₁L_{2,3} oxidized peak area with Al source

Y_1 = Na KL₁L_{2,3} cleaned surface peak area with Mg source

Y_2 = Na KL₁L_{2,3} cleaned surface peak area with Al source

The Na KL₁L_{2,3} cleaned surface peak area with Al source, Y_2 , was the desired variable to be determined. Values for variables X_1 , Y_1 , and X_2 were found by integrating the area under each respective peak. Figure A2(a)-(c) show examples of each integrated peak area. Next, the X_1/Y_1 ratios for the Mg source experiments for cleaned surface peak area (Y_1) and oxidized peak area (X_1) from four experiments were calculated and averaged. Then the Al source experiment values for the oxidized peak areas (X_2) were compiled and values for Y_2 were determined. As seen in Figure A2(d), the Na KL₁L_{2,3} cleaned peak is only part of the total O 1s cleaned surface peak, so to calculate the percent it comprises, Y_2 was divided by the total O 1s cleaned surface peak area and multiplied by 100% (see Eq. A.2b).

$$\% \text{ Na KL}_1\text{L}_{2,3} \text{ (cleaned)} = \left(\frac{Y_2}{O \text{ 1s Area (cleaned)}} \right) \times 100\% \quad (\text{Eq. A.2b})$$

Figures

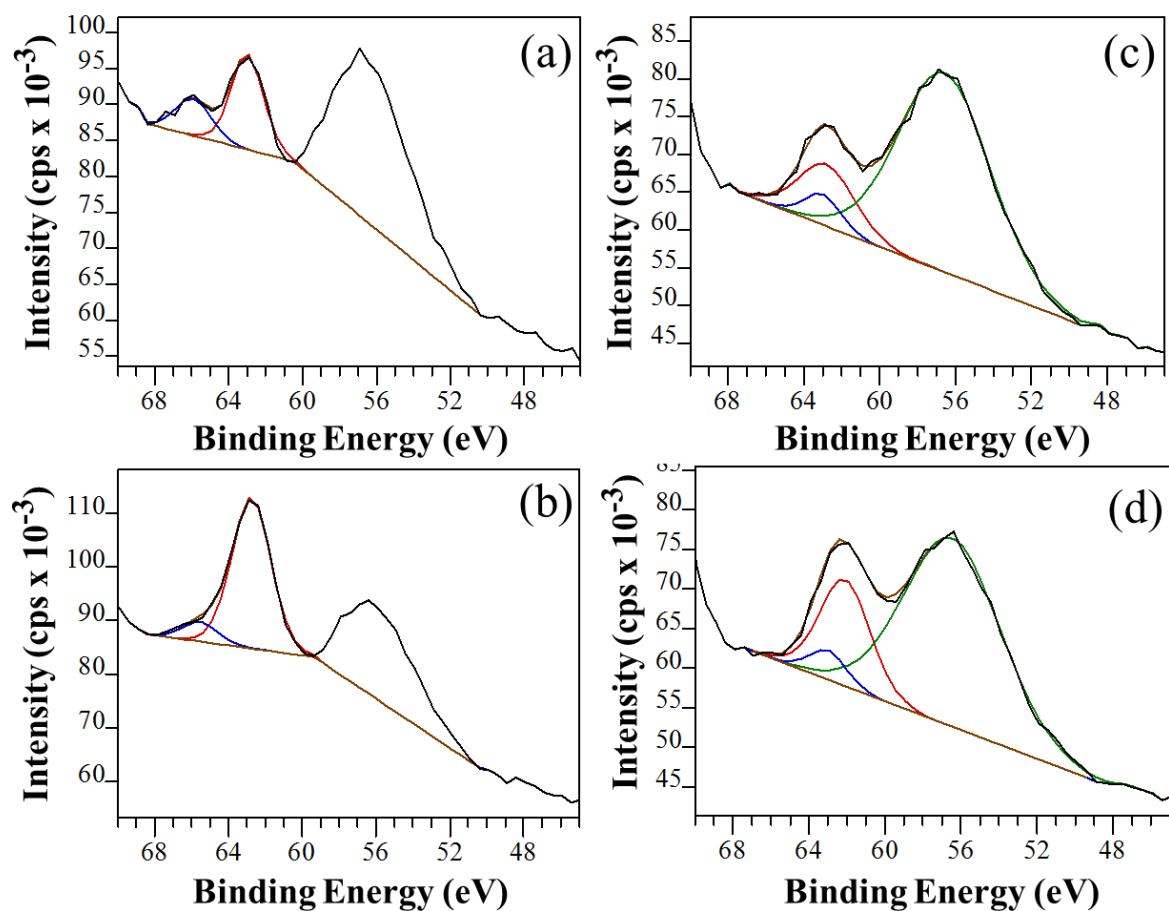


Figure A1.1. Photoelectron spectra regions for the Na 2s and Au 5p_{3/2} peaks, which have been integrated using a linear background. Panels (a) and (b) are acquired with a Mg anode and panels (c) and (d) with an Al anode. (a) clean surface (b) 50 L O₂ exposure (c) clean surface (d) 50 L O₂ exposure Blue: Au 4f_{7/2} Kα₅ satellite Red: Na 2s Green: Au 5p_{3/2}

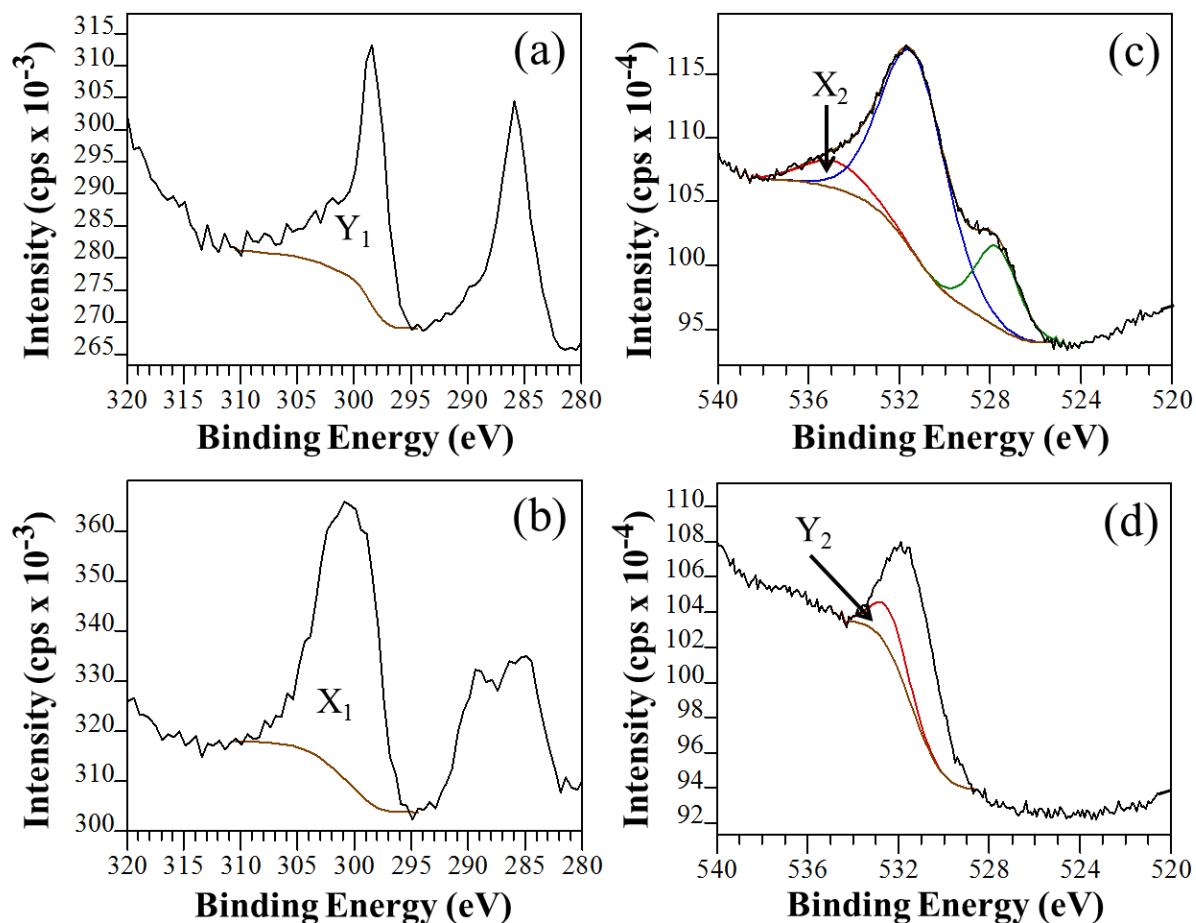


Figure A1.2. Photoelectron spectra regions for the Na $KL_1L_{2,3}$ Auger line, which have been integrated using a Shirley background. Panels (a) and (b) are acquired with a Mg anode and panels (c) and (d) with an Al anode. (a) clean surface (b) 50 L O_2 exposure (c) 50 L O_2 exposure (d) clean surface

Appendix 2. Experimental Parameters

1. Cleaning protocol

Typical gas exposure experiment procedures carried out at EMPA followed a cleaning and analysis routine that extended over two separate days for each experiment, both in 2014 and 2015. The sample underwent cleaning cycles, typically two cycles, on Day 1. The sample was then left in the chamber overnight. The following morning, Day 2, we implemented the experimental portion. We used this protocol due to the extended time period required to carry out a gas exposure experiment. A typical cleaning cycle required 2.5 hours and a typical gas exposure experiment required 10 hours.

2. Experimental hardware

A button heater was used to anneal all samples in the ESCA chamber. The heater was connected to a power supply which allowed the user to set amperage (A) and voltage (V) to obtain the desired power (W). An Optris infrared laser pyrometer was used to measure temperature of the sample via line of sight through a chamber window. The pyrometer had a limited measurable temperature range of 420 K to 900 K.

The XPS electronics were replaced with new electronics in November 2014. They had become increasingly unstable within the last few months before replacement.

Appendix 3. Oxygen Adsorbed on NaAu₂(111)

1. Low-energy electron diffraction (LEED)

We conducted LEED experiments on Sample B after exposure to 50 L of O_{2,g} at 300 K. Figure A3.1(d)-(f) shows LEED patterns of the O_{2,g} exposed surface. These are compared

to those of a clean surface with R value of 0.55, Figure A3.1(a)-(c). The LEED pattern is gone after oxygen exposure. LEED probes up to 1 nm beneath the surface roughly equivalent to 4-5 atomic layers. The lack of a pattern combined with the probing depth of LEED tells us that after oxygen exposure the top few layers of surface become disordered. This result also correlates with the XPD results (cf. Section 3.2). After a 50 L $O_{2,g}$ exposure at 300 K, the structure in the Na 1s XPD pattern for the cleaned surface (Figure 1(c)) is gone. Present now is a pattern with a diffuse background exhibiting broad three-fold symmetry (Figure 6). The O 1s XPD is similar. The Au 4f pattern is still present after $O_{2,g}$ exposure, but with higher background. The Au structure is probed more deeply than Na due to its larger IMFP (cf. Section 3.1), so these XPD data likely mean that the top few layers become disordered.

2. Extended time dependence

As a test of the stability of the surface after oxygen exposure, we exposed Sample B to $O_{2,g}$ on two separate occasions (once in 2014 and again in 2015) and left it *in vacuo*. The sample was re-polished between 2014 and 2015. We acquired XPS spectra immediately after exposure and then the sample remained *in vacuo* for 14-16 hours. We again acquired XPS spectra to determine whether the surface changed measurably. All atom% values come from spectra acquired at an emission angle of 60° (with respect to surface normal).

We conducted a sequential set of $O_{2,g}$ exposures resulting in a total exposure of 100 L in 2014. The sample remained *in vacuo* for 14 hours until the second XPS measurement. The Al source was used for these spectra. Table A3.1 gives a summary of the atom% concentration variations seen in the three main peaks, Na 1s, Au 4f, and O 1s with the additional breakdown of the three convoluted peaks in the O 1s region. C 1s is absent as only

overview spectra are available.

Table A3.1. Atom% concentrations before and after 14 hour *in vacuo* period

	atom% Na	atom% Au	atom% O	atom% O Peak A	atom% O Peak B	atom% O Peak C
100 L O _{2,g}	45.7	28.8	26.1	2.8	20.1	3.2
100 L O _{2,g} plus 14 hours <i>in vacuo</i>	47.3	27.1	25.5	2.9	19.9	2.7
Δ atom%	+1.6	-1.7	-0.6	+0.1	-0.2	-0.5

Uncertainty values for XPS spectra range from 0.1 atom% to 1 atom% dependent on the XPS system.^{38,39} We assume that the ESCA system has an uncertainty of 1 atom%. With this uncertainty in mind, we see there is little to no change in atom% of the three main peaks. This suggests that the sample was inert during the 14 hours, as no measurable reactions occurred. It is possible some additional Na diffused slowly to the sample surface, reacting further with the pre-existent oxygen during that time, which accounts for the slight 1.6 atom% increase (a factor of 1.03). It is reasonable to conclude that the oxygen-covered sample is stable in vacuum under these conditions.

In 2015, we exposed the sample to 50 L O_{2,g}. The sample then remained *in vacuo* for 16 hours until the second XPS measurement. The Mg source was used for these spectra. Table A3.2 gives a summary of the atom% concentration variations in the four main peaks, Na 1s, Au 4f, O 1s, and C 1s with the additional breakdown of the two convoluted peaks for both the O 1s region and C 1s region.

Table A3.2. Atom% concentrations before and after 16 hour *in vacuo* period

	atom % Na	atom % Au	atom % O	atom % C	atom% O Peak B	atom% O Peak C	atom% C Peak A	atom% C Peak B
50 L O _{2,g}	46.7	38.1	15.2	15.3	9.7	5.5	5.9	9.4
50 L O _{2,g} plus 16 hours <i>in vacuo</i>	49.3	36.1	14.6	16.1	8.1	6.5	4.5	11.6
Δ atom%	+2.6	-2.0	-0.6	+0.8	-1.6	+1.0	-1.4	+2.2

We again assume that ESCA system has an uncertainty of 1 atom%. With this uncertainty in mind, we see there is little to no change in atom% of the main four peaks. This suggests no measureable reactions occurred during the 16 hours with oxygen present on the surface. It is possible that some Na diffused slowly to the sample surface due to the presence of oxygen, which accounts for the slight 2.6 atom% increase (a factor of 1.09) in Na. The atom% changes in the deconvoluted Peaks B and C for the O 1s region suggest some conversion from the adsorbed atomic oxygen at mixed Au-Na sites to Na-rich sites. This possible conversion from mixed Au-Na sites to Na-rich sites could also partially account for the increase in atom% of Na as more Na diffuses toward the surface. The atom% decrease in the deconvoluted Peaks A and increase in B for the C 1s region suggest some conversion from carbonate to adventitious carbon on the surface. However, it is still reasonable to conclude that the surface is stable for the first 16 hours after O_{2,g} exposure.

3. Additional annealing with O₂

We conducted the first anneal of a NaAu₂(111) surface, with adsorbed oxygen, in 2014 at EMPA. We exposed Sample B to 100 L O_{2,g} and then annealed to three different temperatures with respective powers of 0.5 W, 0.85 W and 2.6 W. XPS spectra were

acquired with the Al source before and after $O_{2,g}$ exposure and after each subsequent anneal. The Optris pyrometer cannot measure temperatures below 420 K, so at the time the temperature was not known for all data points, specifically 0.5 W and 0.85W. To get an estimate of these values, we created a plot of temperature vs. power after experiments were completed, Figure A3.2. We compiled temperature and power data from $NaAu_2$ anneals to create the plot. An estimated curve was fit with a power function to account for temperatures below 420 K. The curve was forced through the point 0, 300 to account for a temperature of 300 K (room temperature) at 0 watts. From this curve we estimate that 0.5 W is ~320 K and 0.85 W is ~340 K. We also estimate from this curve that 2.6 W is 430 K, which is very close to the actual temperature of 425 K.

The temperatures for this experiment were all below that of Na desorption at 450 K. Peaks B and C in the O 1s region respond differently to this thermal treatment, as seen in Figure A3.3(a) and A3.3(b). Peak A is omitted from Figure A3.3(b) as it is the Na $KL_1L_{2,3}$ peak. We know the Peak B represents atomic oxygen at Au-Na sites while Peak C represents atomic oxygen at Na-rich sites. We see that as the sample is annealed at increasing temperatures Peak B decreases while Peak C increases. This suggests the possibility that atomic oxygen is moving from mixed Au-Na sites to Na-rich sites, or converting Au-Na regions to Na-rich regions.

The intensities of the Au 4f and Na 1s peaks also change upon heating which in turn alters the value of R . Figure A3.3(c) and (d) give the Na 1s spectra and R , respectively. Any change in Au 4f is reflected in the plot of R , so Au 4f spectra are omitted. All anneals cause the amount of Na on the surface to increase. This suggests diffusion of Na from the bulk to the surface. The increase in the Na content could also contribute to the increase in Peak C

and decrease in Peak B. As more Na is available, the atomic oxygen migrates to Na-rich sites. This result is analogous to the 425 K anneal after O_{2,g} exposure in 2015 (cf. Section 3.3). Here, the Na content also increases slightly after annealing to 425 K, which we attributed to activated diffusion of Na from the bulk toward the surface.

Figures

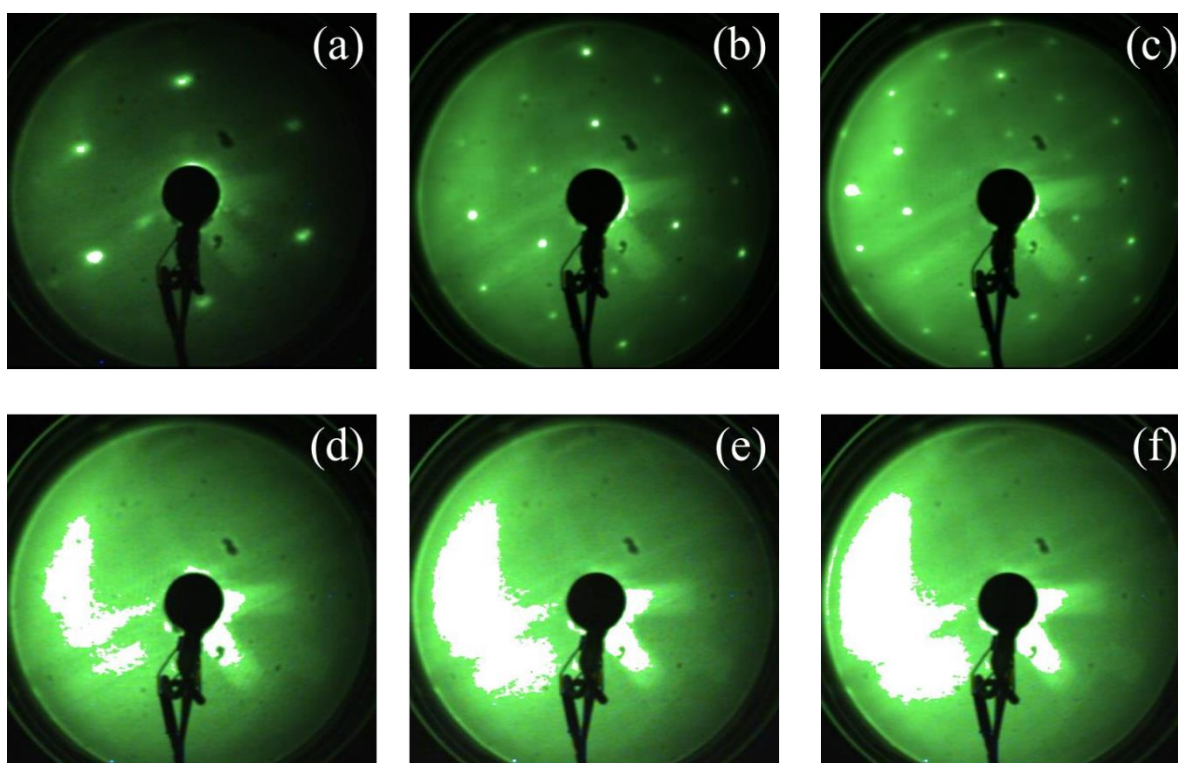


Figure A3.1. Low-energy electron diffraction (LEED) patterns. (a)-(c) show patterns of a clean surface with $R = 0.55$. (d)-(f) show patterns of a surface after 50 L $O_{2,g}$ exposure at 300 K. (a)&(d) 27.0 eV (b)&(e) 64.5 eV (c)&(f) 100.5 eV.

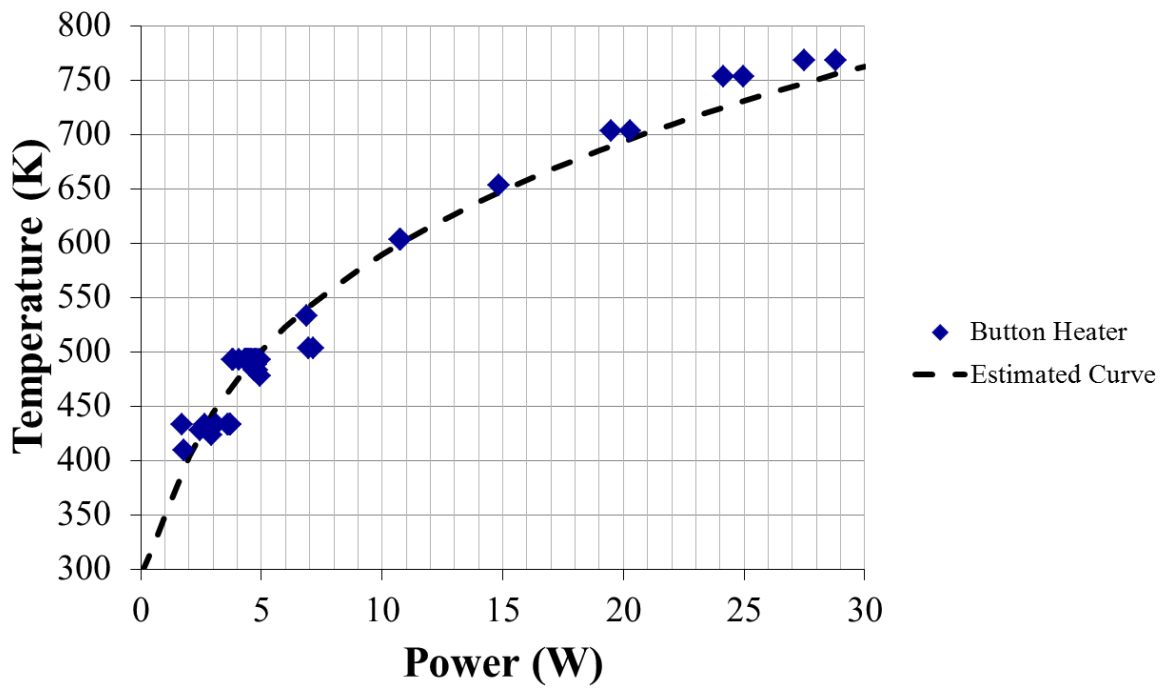


Figure A3.2. Plot of temperature vs. power for the button heater used for annealing at EMPA.

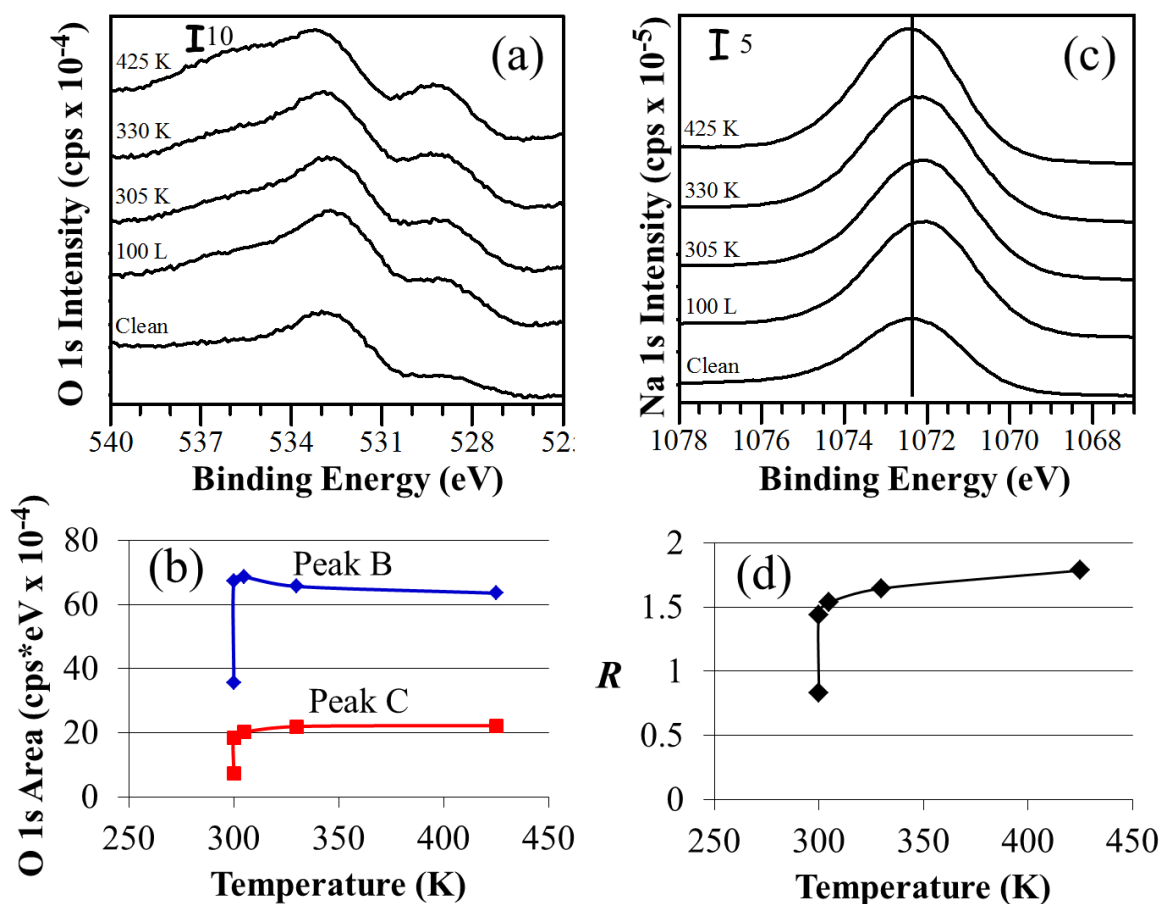


Figure A3.3. Result of exposing a surface to 100 L $O_{2,g}$ at 300 K, ten annealing sequentially to 305 K, 330 K and 425 K. The X-ray source is Al K α . In (a) and (c), the curves are displaced vertically to minimize overlap. The intensity, in units of cps $\times 10^{-4}$ or 10^{-5} , can be derived using the scale bar. (a) O 1s spectral region. (b) Integrated areas of Peaks B and C. In each case, the lower point at 300 K represents the clean surface, and the upper point is obtained after 100 L exposure to oxygen. (c) Na 1s spectra for the same sequence as in panel (a). (d) R vs temperature. The lower point at 300 K represents the clean surface, and the upper point is obtained after 100 L exposure to oxygen.

References

- ¹M. Armbrüster, R. Schlögl and Y. Grin, "Intermetallic compounds in heterogeneous catalysis—a quickly developing field," *Science and Technology of Advanced Materials* **15**, 034803 (2014).
- ²A. P. Tsai and M. Yoshimura, "Highly active quasicrystalline Al-Cu-Fe catalyst for steam reforming of methanol," *Applied Catalysis A: General* **214**, 237 (2001).
- ³K. Kovnir, M. Ambrüster, D. Teschner, T. V. Venkov, F. C. Jentoft, A. Knop-Gericke, Y. Grin and R. Schlögl, "A new approach to well-defined, stable and site-isolated catalysts," *Science and Technology of Advanced Materials* **8**, 420 (2007).
- ⁴M. Armbrüster, K. Kovnir, M. Friedrich, D. Teschner, G. Wowsnick, M. Hahne, P. Gille, L. Szentmiklosi, B. Feuerbacher, M. Heggen, F. Girgsdies, D. Rosenthal, R. Schlögl and Y. Grin, "Al₁₃Fe₄ as a low-cost alternative for palladium in heterogeneous hydrogenation," *Nature Materials* **11**, 690 (2012).
- ⁵A. Sanchez, S. Abbet, U. Heiz, W.-D. Schneider, H. Häkkinen, R. N. Barnett and U. Landman, "When gold is not noble: Nanoscale gold catalysts," *The Journal of Physical Chemistry A* **103**, 9573 (1999).
- ⁶A. S. K. Hashmi and G. J. Hutchings, "Gold catalysis," *Angewandte Chemie International Edition* **45**, 7896 (2006).
- ⁷M. Haruta and M. Date, "Advances in the catalysis of Au nanoparticles," *Applied Catalysis A: General* **222**, 427 (2001).
- ⁸B. Hvolbæk, T. V. W. Janssens, B. S. Clausen, H. Falsig, C. H. Christensen and J. K. Nørskov, "Catalytic activity of Au nanoparticles," *Nano Today* **2**, 14 (2007).
- ⁹A. Wittstock, V. Zielasek, J. Biener, C. M. Friend and M. Baeumer, "Nanoporous gold catalysts for selective gas-phase oxidative coupling of methanol at low temperature," *Science* **327**, 319 (2010).
- ¹⁰L.-C. Wang, K. J. Stowers, B. Zugic, M. M. Biener, J. Biener, C. M. Friend and R. J. Madix, "Methyl ester synthesis catalyzed by nanoporous gold: from 10⁻⁹ Torr to 1 atm," *Catalysis Science & Technology* **5**, 1299 (2015).
- ¹¹R. Meyer, C. Lemire, S. K. Shaikhutdinov and H. J. Freund, "Surface chemistry of catalysis by gold," *Gold Bulletin* **37**, 72 (2004).
- ¹²C. Xiao, L.-L. Wang, R. V. Maligal-Ganesh, V. Smetana, H. Walen, P. A. Thiel, G. J. Miller, D. D. Johnson and W. Huang, "Intermetallic NaAu₂ as a Heterogeneous Catalyst for Low-Temperature CO Oxidation," *Journal of the American Chemical Society* **135**, 9592 (2013).

- ¹³M. Haruta, T. Kobayashi, H. Sano and N. Yamada, "Novel Gold Catalysts for the Oxidation of Carbon Monoxide at a Temperature far Below 0°C," *Chemistry Letters* **16**, 405 (1987).
- ¹⁴E. J. Kwolek, R. Widmer, O. Gröning, O. Deniz, H. Walen, C. D. Yuen, W. Huang, D. L. Schlagel, M. Wallingford and P. A. Thiel, "The (111) Surface of NaAu₂: Structure, Composition, and Stability," *Inorganic Chemistry* **54**, 1159 (2015).
- ¹⁵K. C. Prince, G. Paolucci and A. M. Bradshaw, "Oxygen-adsorption on silver (110) - dispersion, bonding and precursor state," *Surface Science* **175**, 101 (1986).
- ¹⁶K. Sakamoto, H. M. Zhang and R. I. G. Uhrberg, "Adsorption and reaction processes of physisorbed molecular oxygen on Si(111)-(7x7)," *Physical Review B* **72**, 075346 (2005).
- ¹⁷K. W. Kolasinski, *Surface Science: Foundations of Catalysis and Nanoscience*, (John Wiley & Sons Ltd, Chichester, West Sussex, England, 2002).
- ¹⁸CasaXPS: Processing Software for XPS, AES, SIMS and More; www.CasaXPS.com, (October 19, 2014).
- ¹⁹A. Winkler and J. T. Yates Jr., "Capillary array dosing and angular desorption distribution measurements: a general formalism," *Journal of Vacuum Science & Technology A* **6**, 2929 (1988).
- ²⁰C. T. Campbell and S. M. Valone, "Design considerations for simple gas dosers in surface science applications," *Journal of Vacuum Science & Technology A* **3**, 408 (1985).
- ²¹J. H. Scofield, "Hartree-Slater subshell photoionization cross-sections at 1254 and 1487 eV," *Journal of Electron Spectroscopy and Related Phenomena* **8**, 129 (1976).
- ²²S. Tanuma, C. J. Powell and D. R. Penn, "Calculations of electron inelastic mean free paths. IX. Data for 41 elemental solids over the 50 eV to 30 keV range," *Surface and Interface Analysis* **43**, 689 (2011).
- ²³A. Jablonski and C. J. Powell, "Information depth and the mean escape depth in Auger electron spectroscopy and X-ray photoelectron spectroscopy," *Journal of Vacuum Science & Technology A* **21**, 274 (2003).
- ²⁴J. F. Moulder, W. F. Stickle, P. E. Sobol and K. D. Bomben, *Handbook of X-ray Photoelectron Spectroscopy: a reference book of standard spectra for identification and interpretation of XPS data*, (Perkin-Elmer Corporation, Physical Electronics Division, Eden Prairie, Minnesota, 1992).
- ²⁵A. Barrie and F. J. Street, "An Auger and X-ray photoelectron spectroscopic study of sodium metal and sodium oxide," *Journal of Electron Spectroscopy and Related Phenomena* **7**, 1 (1975).

- ²⁶D. D. Wagman, W. H. Evans, V. B. Parker, R. H. Schumm, I. Halow, S. M. Bailey, K. L. Churney and R. L. Nuttall, "The NBS tables of chemical and thermodynamic properties," *Journal of Physical and Chemical Reference Data* **11**, Suppl. 2 (1982).
- ²⁷R. J. Behm and C. R. Brundle, "On the formation and bonding of a surface carbonate on Ni(100)," *Surface Science* **255**, 327 (1991).
- ²⁸A. V. Shchukarev and D. V. Korolkov, "XPS study of group IA carbonates," *Central European Journal of Chemistry* **2**, 347 (2004).
- ²⁹K. Motzfeldt, "The thermal decomposition of sodium carbonate by the effusion method," *The Journal of Physical Chemistry* **59**, 139 (1955).
- ³⁰J. J. Pireaux, M. Chtaib, J. P. Delrue, P. A. Thiry, M. Liehr and R. Caudano, "Electron spectroscopic characterization of oxygen adsorption on gold surfaces: I. Substrate impurity effects on molecular oxygen adsorption in ultra high vacuum," *Surface Science* **141**, 211 (1984).
- ³¹N. D. S. Canning, D. Outka and R. J. Madix, "The adsorption of oxygen on gold," *Surface Science* **141**, 240 (1984).
- ³²T. Visart de Bocarme, T. D. Chau, F. Tielens, J. Andres, P. Gaspard, R. L. C. Wang, H. J. Kreuzer and N. Kruse, "Oxygen adsorption on gold nanofacets and model clusters," *The Journal of Chemical Physics* **125**, 054703 (2006).
- ³³S. A. C. Carabineiro and B. E. Nieuwenhuys, "Adsorption of small molecules on gold single crystal surfaces," *Gold Bulletin* **42**, 288 (2009).
- ³⁴H. Qiao, T. Nohira and Y. Ito, "Electrochemical formation of Au₂Na alloy and the characteristics of (Au₂Na+Au) reference electrode in a LiF–NaF–KF eutectic melt," *Electrochimica Acta* **47**, 4543 (2002).
- ³⁵B. K. Min, A. R. Alemozafar, M. M. Biener, J. Biener and C. M. Friend, "Reaction of Au(111) with Sulfur and Oxygen: Scanning Tunneling Microscopic Study," *Topics in Catalysis* **36**, 77 (2005).
- ³⁶J. A. Rodriguez, M. Pérez, T. Jirsak, J. Evans, J. Hrbek and L. González, "Activation of Au nanoparticles on oxide surfaces: reaction of SO₂ with Au/MgO(100)," *Chemical Physics Letters* **378**, 526 (2003).
- ³⁷C. Klauber, "Refinement of magnesium and aluminium K α X-ray source functions," *Surface and Interface Analysis* **20**, 703 (1993).
- ³⁸K. Harrison and L. B. Hazell, "The determination of uncertainties in quantitative XPS/AES and its impact on data acquisition strategy," *Surface and Interface Analysis* **18**, 368 (1992).
- ³⁹M. P. Seah, "Ultrathin SiO₂ on Si. VI. Evaluation of uncertainties in thickness measurement using XPS," *Surface and Interface Analysis* **37**, 300 (2005).

CHAPTER 5

INTERACTION OF WATER, CARBON MONOXIDE AND CARBON DIOXIDE
WITH THE (111) SURFACE OF NaAu_2

Emma J. Kwolek^a, Roland Widmer^b, Oliver Gröning^b, Okan Deniz^b, Deborah L. Schlage^c,
Mark Wallingford^c, Patricia A. Thiel^{a,c,e}

^aDepartment of Chemistry, Iowa State University, Ames, Iowa 50011, USA

^bnanotech@surfaces Laboratory, EMPA, Swiss Federal Laboratories for Materials Science
and Technology, Ueberlandstrasse 129, 8600 Dübendorf, Switzerland

^cThe Ames Laboratory, Ames, Iowa 50011, USA

^eDepartment of Materials Science & Engineering, Iowa State University, Ames, Iowa 50011,
USA

Abstract

In this study we observe and report the interaction of three small molecules, water, carbon monoxide and carbon dioxide, with the (111) surface of single-crystal NaAu_2 . Gaseous water exposure produces two types of oxygen-species on the surface. The first is spurious carbonate that forms during exposure. The second is hydroxyl which adsorbs at Na sites. Exposure to CO_g does not result in adsorption or interaction with the $\text{NaAu}_2(111)$ surface. Exposure to $\text{CO}_{2,g}$ does not result in adsorption on the surface, but does result in the formation of a small amount of carbonate.

1. Introduction

Starting with the discovery of low temperature catalytic gold nanoparticles by Haruta and co-workers in 1987,¹ there has been great interest in using gold catalysts for oxidation reactions. Since that time, low temperature reactions have been successful using a variety of supported gold nanoparticles²⁻⁴ as well as nanoporous solids.^{5,6} There has also been growing interest in replacing precious metals with intermetallics for specific catalytic reactions.⁷ Intermetallic NiGa is a catalyst in the hydrogenation of CO₂ to methanol⁸ and quasicrystalline Ti₇₀Zr₁₀Co₂₀ is a catalyst for the oxidation of cyclohexane.⁹ Investigations into the catalytic properties of both gold catalysts and intermetallics are ongoing.

Xiao and co-workers conducted a recent investigation on the catalytic properties of NaAu₂, an Au-rich intermetallic.¹⁰ NaAu₂ combines both the properties of an intermetallic and nano-structured Au, potentially leading to a new catalyst that encompasses the catalytic properties of both. Xiao et al. chose the oxidation of CO as the reaction to investigate because it is a benchmark for oxidative activity for various forms of Au¹ and because it is an important reaction. Powdered NaAu₂ shows high activity for CO oxidation at low temperatures ranging from 300 K to 400 K.¹⁰ In the model developed earlier for this reaction,^{10,11} oxygen adsorbs at a site involving multiple Au and Na atoms, including 1 Na atom that moves above the surface plane, i.e. it 'pops out'. The model predicts that CO weakly adsorbs on an Au site, while CO₂ does not bind to the surface. The model oxidation reaction involves a CO_{ad} molecule that reacts with an adsorbed O₂ molecule to form an intermediate OOCO_{ad}, and ultimately CO_{2,g} and O_{ad}.

Motivated by this investigation, we characterized the clean (111) surface of single-crystal NaAu₂ in ultrahigh vacuum (UHV). The goal was to determine the stability of the

surface relative to the bulk, which led to the determination of the suitability of the (111) termination as a model for the catalyst surface.¹² We discovered that the surface exists in one of two states. In the first, low-energy electron diffraction (LEED) and X-ray photoelectron diffraction (XPD) were consistent with the expected bulk structure with some evidence of surface disorder. STM showed mesa-like features with flat tops that likely were bulk-terminated. Atomic order could not be resolved on these features. The regions between the mesas are regarded as defect regions. Figure 1 illustrates the surface of this clean state, both with STM images and line profiles as well as with diffraction data. In the second state, the surface was Na-depleted/Au-enriched. We attributed both preferential sputtering and desorption at elevated temperature to Na depletion. Temperature programmed desorption (TPD) results showed that Na desorption began at around 450 K. Both processes were used for the normal cleaning cycles between experiments. Thus, samples could only be used for a limited number of experiments before pure, crystalline Au precipitated irreversibly. Before this stage was reached, the Na could be replenished from the near-surface reservoir.

Previously, we investigated the effects of oxygen exposure on the $\text{NaAu}_2(111)$ surface.¹³ Our results determined that oxygen readily adsorbs on the surface and causes Na segregation at the surface. O_2 dissociates into atomic oxygen, which adsorbs on the surface at two different sites. The first adsorption site is a Na-site, which is sodium oxide, and the second site is a mixed Au-Na site. Our investigation also found that oxygen migrates into the bulk upon annealing, resulting in residual oxygen on the cleaned surface and also reacts to form carbonate on the surface.

With this background, we now examine the effects of water, carbon monoxide and carbon dioxide exposure on the $\text{NaAu}_2(111)$ surface. We can make certain predications based

on previously calculated energetics.^{10,11} First, the residence time of water is so low that at our experimental conditions it should be unobservable. Using the calculated adsorption energy, E_{ad} , of -0.49 eV, the residence time at room temperature is of order 10^{-5} to 10^{-3} s (assuming a pre-exponential desorption rate factor of $10^{12\pm 1}$ s⁻¹). Second, the residence time of carbon monoxide is also so low that it should be unobservable. Using an E_{ad} of -0.35 eV, the residence time at room temperature is of order 10^{-8} to 10^{-6} s (assuming the same pre-exponential factor as used above). Finally, the residence time of carbon dioxide is so low that it should not be observable either. An E_{ad} of +0.04 eV gives a residence time at room temperature of order 10^{-14} to 10^{-12} s. The positive E_{ad} value also indicates there should be no adsorption of CO₂ on the surface. All of our gas exposure measurements take place over several hours, so low temperatures would be necessary to stabilize molecules on an appropriate time-scale. All of these predications apply to the ideal flat surface and, as noted above, the real surface is morphologically irregular. Our goal is to determine whether water, either as water or a water-derived species, carbon monoxide, or carbon dioxide adsorb and if so, whether their chemical states can be related to the surface composition and/or structure.

We first present analysis of water adsorption experiments, which shows a water-derived species does adsorb, giving one O 1s peak in XPS. We then present analysis of carbon monoxide and carbon dioxide adsorption experiments. From this data we develop a hypothesis about the interactions of these gases on the NaAu₂(111) surface.

2. Experimental Details

Single-crystal samples of NaAu₂ were grown at the Materials Preparation Center of the Ames Laboratory via the Bridgman technique. All of the XPS and LEED experiments

were carried out at EMPA in Dübendorf, Switzerland. All of the TPD experiments took place at the Ames Laboratory in Ames, Iowa, USA. Aspects of the UHV instrumentation and experimental conditions for both locations have been described as part of our previous studies of clean $\text{NaAu}_2(111)$ ¹² and oxygen exposed surface of $\text{NaAu}_2(111)$.¹³ Details unique to the water, carbon monoxide and carbon dioxide adsorption experiments are as follows. The pyrometer used for temperature measurements is described in Appendix 1.

XPS experiments were conducted on the samples denoted B and C,¹² which were re-polished for the water and carbon dioxide experiments. Between each experiment, the sample was cleaned with two cycles of sputter-annealing. The cycles for carbon monoxide and some of the water experiments consisted of Ar^+ ion bombardment at 1 keV for 5 minutes at 300 K, then annealing at 500 K for 20 minutes. The cycles for carbon dioxide and some of the water experiments consisted of Ar^+ ion bombardment at 1 keV for 3 minutes at 300 K, then annealing at 475 K for 15 minutes. Samples B and C were exposed to CO_g and $\text{CO}_{2,g}$, respectively, by back-filling the UHV chamber to a pressure of 1.0×10^{-8} to 1.0×10^{-7} mbar. Sample B was exposed to H_2O_g by back-filling the fast entry load lock (to prevent contaminating the chamber) with water vapor to a pressure of 1.0×10^{-6} to 7.0×10^{-6} mbar. Exposures are reported in units of Langmuir (L), where $1 \text{ L} = 1.33 \times 10^{-6}$ mbar-s. In cases where the sample was annealed after exposure to H_2O_g , it was held at temperature for 20 minutes. Details on XPS instrumentation are given in a previous publication.¹³ XPS data was analyzed using CasaXPS software.¹⁴ LEED experiments were conducted on the cleaned surfaces of samples B and C as well as after gas exposures of water and carbon monoxide.

TPD experiments were conducted on Sample D,¹² which was re-polished for these experiments. Between each experimental run, Sample D was cleaned by sputtering with Ar^+

ion bombardment at 1 keV for 3 minutes followed by annealing at 420 K for 20 minutes. The sample was exposed to CO_g by back-filling the chamber to a pressure of 1.0 x 10⁻⁷ Torr. The sample was exposed to O_{2,g} via a doser with a design similar to that of Winkler and Yates,¹⁵ described elsewhere.¹³ Original software created within the LabView framework controlled the thermal program and interfaced with a mass spectrometer for multiplexing.

3. Experimental Results and Interpretation

3.1. Cleaned surface composition

In previous work,^{12,13} we defined a quantity, R , as the ratio of integrated intensities for Na 1s and Au 4f peaks. R was corrected for the (Scofield) cross-section for each photoionization event,¹⁶ but not corrected for photoelectron attenuation or instrumental parameters. The correction for attenuation is particularly large, since the inelastic mean free path (IMFP) of Au 4f electrons (in bulk Au) is only one-third that of Na 1s electrons, i.e. 0.5 and 1.5 nm, respectively.¹⁷ Consequently R , as previously defined, is not an accurate measure of the Na:Au composition. We use it in this paper to facilitate comparisons with prior work, and because it reflects compositional *trends* with high signal-to-noise.

Cleaned surfaces of NaAu₂ show a small residual peak in XPS spectra at $E_b = 531.3 \pm 0.2$ eV. This peak falls within the expected BE region for the O 1s peak,¹⁸ as shown in Figure 2(a). The Na KL₁L_{2,3} (¹P) Auger line is also present in this BE region with an Al K α source, typically at 532 eV.^{18,19} The Auger line is absent in this region with a Mg K α source. This small residual peak occurs with both X-ray sources, indicating it is partially comprised of an oxygen species. Calculations, based on the analysis of relative intensities of Auger peaks with Mg and Al sources (described elsewhere¹³), show that the Na Auger line

contributes 30 to 40% of the total residual peak intensity (number of data sets with Al source, $N = 2$).

Cleaned surfaces also show peaks in the C 1s region, illustrated in Figure 2(b). The larger peak, positioned at 285-286 eV, is in the range of C-C bonds, while the smaller, positioned at 289-290 eV, is in the range of C-O double bonds. Sodium carbonate has a large negative heat of formation, -1130 kJ/mol ,²⁰ which makes a carbonate the likely assignment for the C-O bond. The carbonate peak in bulk Na_2CO_3 falls at 289.3 eV,²¹ supporting our assignment. The small C 1s carbonate peak is associated with a large O 1s peak, because of the 3:1 stoichiometry together with the photoionization cross-section ratio of 2.9:1.¹⁶ The resulting amplification factor is 8.7, which can be used to calculate the fraction of the O 1s peak intensity associated with the carbonate. For a cleaned surface, the carbonate comprises 20 to 30% of the non-Auger O 1s intensity ($N = 2$).

3.2. Water exposure at 300 K

Beginning with the O 1s spectral region, exposure to water causes the residual clean surface peak to increase. A second peak also occurs in the O 1s region, dependent on the X-ray source (as shown in Figure 3). These two peaks are labeled A and B in order of decreasing (apparent) BE. Areas and positions for both peaks are determined by deconvolution, shown in Figure 3(a) and 3(d). Assignments for each peak are as follows.

Peak A ($536.8 \pm 0.2 \text{ eV}$), is observed only with the Al $K\alpha$ source and thus must be the Na $\text{KL}_1\text{L}_{2,3}$ (^1P) Auger peak. Upon exposure to water, the peak shifts upward $\sim 4 \text{ eV}$ from the initial residual clean surface position. This shift is also observed for other Na Auger lines, one of which can be seen in Figure 2(c). Peak A intensifies with increasing water exposure,

shown in Figure 3(b), indicating an increase in the amount of Na on the surface, which is discussed later.

Peak B (531.5 ± 0.2 eV) represents a water-derived species, probably hydroxyl or atomic oxygen, which grows with increasing water exposure. A XPS study of sodium by Barrie and Street exhibits an oxide peak at 529.6 eV and a hydroxide peak at 532.7 eV.¹⁹ The chemical shift between these two peaks is 3.1 eV. Applying this shift to our oxide peak energy, found at 527.9 eV after oxygen exposure¹³, results in a hydroxide peak position of 531 eV. This is close to the Peak B position of 531.5 eV, indicating the possible presence of hydroxyl. Sodium hydroxide has a large negative heat of formation, -456 kJ/mol,²⁰ making it a suitable candidate for Peak B. Several studies have found that the pre-adsorption of alkali metals on a nickel surface promotes the dissociation of $\text{H}_2\text{O}_{\text{ad}}$ into OH_{ad} .²²⁻²⁴ The sodium present in our sample is likely dissociating the water into hydroxyl. The position of Peak B also coincides with the position of the Au-Na site atomic oxygen seen after oxygen exposure.¹³ Sodium readily reacts with water to form sodium hydroxide, so the presence of molecular water is not likely. Peak B continues to grow in intensity until 500 L, where it plateaus, implying surface saturation. The BE of Peak B falls within the same range as carbonate, suggesting carbonate contributes to part of the total peak intensity, as discussed below.

The intensities of the Na 1s, Au 4f and C 1s peaks also change upon exposure to water. Figure 4 shows that the Na 1s peak increases in intensity while the Au 4f peak decreases in intensity. These changes correlate with an increase in R , seen in Figure 4(c). Exposures of 250 L H_2O_g at 300 K lead to an increase in R by a factor of 3.2 ± 0.4 ($N = 3$). This shows that as water adsorption proceeds, the surface and sub-surface becomes enriched

in Na. The carbonate peak also grows as shown in Figure 4(d). Above 200 L, carbonate accounts for one-third of the oxygen species represented by Peak B.

As with oxygen,¹³ the intensity of Peak B is dependent on water exposure conditions. When water exposure is done in one single step, the intensity is reduced by 1/3 compared to a sequential exposure. This intensity difference can be attributed to a reduction in the quantity of carbonate on the surface. Currently, we are unable to determine the source(s) of the carbonate, but there are several possibilities. These sources include, but are not limited to, contamination from the X-ray anodes, adventitious carbon present on the surface (C 1s peak at 285-286 eV) and diffusion of carbon from the bulk to the surface.

LEED was performed after a H₂O_g exposure. Compared to the cleaned surface, there was a significant change as the spots can no longer be distinguished, suggesting that a water-derived species adsorbed and disrupted the atomic positions, Figure 5(a)-(c).

3.3. Effects of heating to temperatures below and above the Na desorption onset

An experiment in which the surface is exposed to 250 L H₂O_g at 300 K and then annealed at 425 K and 475 K is informative. We chose 425 K because it is slightly below the onset of Na desorption and 475 K because it is slightly above the onset.¹²

Annealing the sample affects the peak intensities of Au 4f and Na 1s, which in turn affects the value of *R*. These effects are shown in Figure 6(c) and Figure 6(d) (the Au 4f spectra are absent as the intensity change is reflected in *R*). After annealing to 425 K, the Na intensity has decreased slightly and after annealing to 475 K, the intensity decreases further. Both of these changes are attributed to the loss of Na via desorption. The intensity of O 1s Peak B decreases after both the 425 K and 475 K anneals, suggesting there is a loss of O

from the surface as well. The loss of O is likely due to desorption of NaOH from the surface and/or the recombination of two OH_{ad} , (cf. Section 4.1). This recombination reaction results in $\text{H}_2\text{O}_{\text{g}}$ and O_{ad} . The remaining O_{ad} partly explains the presence of the residual O 1s peak on the cleaned surface. An increase occurs for the Au-Na site atomic oxygen intensity after annealing with oxygen exposures.¹³ This contradicts the observation after annealing with water exposures, suggesting there is a different adsorbate with water. The intensity of the carbonate C 1s peak (not shown) also remains unchanged after annealing, suggesting the carbonate is not involved in the observed changes. Anhydrous sodium carbonate is reportedly stable in air up to 800 K.²⁵

This information leads us to believe that Peak B originates partly from carbonate and partly from hydroxyl bonded to Na. Due to the lack of the sodium oxide peak that was present at 527.9 eV in the oxygen adsorption experiments,¹³ we know that the adsorbed species is not an atomic oxygen bonded to Na. Atomic oxygen bound to Au-Na sites is also not present as indicated by the annealing after water exposures. The large segregation of Na to the surface indicates there is a strong sodium-oxygen species interaction occurring, which is presumably sodium hydroxide.

3.4. Carbon monoxide exposures at 300 K and 500 K

Next, we studied carbon monoxide on the $\text{NaAu}_2(111)$ surface. The O 1s region for the cleaned surface once again shows the residual peak, with carbonate comprising 20-30% of it. Only the Al K α X-ray source was used and as previously stated (cf. Section 3.1) the Na $\text{KL}_1\text{L}_{2,3}$ (^1P) Auger peak comprises 30-40% of this peak. Upon exposure to carbon monoxide at 300 K, the C 1s intensity increases by a factor of 1.08 (from 10.8 atom% to 11.2 atom%)

and the O 1s intensity increases by a factor of 1.25 (from 5.1 atom% to 7.2 atom%). The atom% is calculated by taking the respective peak area divided by the sum of the Na 1s, Au 4f, O 1s and C 1s peak areas (each element area was corrected with its respective Scofield cross-section). Uncertainties for XPS spectra range from 0.1 atom% to 1 atom% dependent on the XPS system.^{26,27} Assuming that the XPS system has an uncertainty of 1 atom%, there is very little, if any, CO_g adsorbed on the surface.

We also investigated carbon monoxide at elevated temperature. In this experiment, the sample was held at 500 K, while exposed to 100 L of CO. The C 1s intensity decreases by a factor of 0.8 (from 13.8 atom% to 11.1 atom%), while the O 1s intensity increases by a factor of 1.25 (from 5.2 atom% to 6.5 atom%). As with the 300 K exposure, there appears to be very little, if any, CO_g adsorption on the sample surface.

LEED patterns were acquired after CO exposure. Compared to the cleaned surface, there is little change in the spot positions and intensity, suggesting no CO adsorption on the surface; see Figure 5(d). TPD experiments confirm the absence of CO on the surface as well. Figure 7(a) shows the partial pressure of CO, as a function of temperature from 280 K to 540 K. The result is a flat line, indicating no CO desorption from the surface.

3.5. Carbon dioxide exposure at 300 K

Finally, we studied carbon dioxide on the NaAu₂(111) surface. The residual peak located in the O 1s region is present again with 20-30% being carbonate. Only the Mg K α X-ray source was used. The Na KL₁L_{2,3} (³P) Auger line is also present in the C 1s BE region with an Mg K α source, typically at 286 eV.¹⁹ This coincides with the location of the carbonate peak. Calculations, based on the analysis of relative intensities of the Na KL₁L_{2,3}

(^1P) and (^3P) lines for the cleaned and CO_2 exposed surface, show that the Na $\text{KL}_1\text{L}_{2,3}$ (^3P) line contributes 60% to 70% of the total carbonate peak intensity ($N = 4$). This percent contribution has been accounted for in all following calculations. Upon exposure to carbon dioxide, the C 1s intensity increases by a factor of 1.20 (from 16.3 atom% to 17.9 atom%) and the O 1s intensity increases by a factor of 4.5 (from 1.8 atom% to 9.0 atom%). The C 1s increase is seen in the carbonate peak, suggesting the increase in both O 1s and C 1s is from carbonate formation. Applying the uncertainty of 1 atom%, there is very little $\text{CO}_{2,g}$ adsorbing on the surface.

We conducted TPD experiments focusing on the formation of $\text{CO}_{2,g}$, since powdered NaAu_2 is reportedly a good catalyst for this reaction.¹⁰ The sample was first exposed to $\text{O}_{2,g}$ and then heated to 350 K. Concurrent with heating, the sample was exposed to CO_g . The increase in the partial pressure of CO_g starting at 150 minutes in Figure 7(b) is due to an increase in CO exposure pressure intentionally done during the run. Figure 7(b) shows the partial pressures of O_2 ($m/e = 32$), CO ($m/e = 28$) and CO_2 ($m/e = 44$) as a function of time. The partial pressures of O_2 , CO , and CO_2 are all invariant indicating there is no desorption of any from (or formation of CO_2 by) the surface.

4. Discussion

The $\text{NaAu}_2(111)$ surface layer is similar to that of hexagonal $\text{Au}(111)$, with the difference being $\frac{1}{4}$ of the Au atoms are missing and a Na atom lies below each vacancy, as shown in Figure 8.¹² The lattice parameter of $\text{NaAu}_2(111)$ is 0.550 nm, about twice as large as that of $\text{Au}(111)$ at 0.288 nm.

4.1. Water

The data show that there is one main O 1s peak related to an adsorbed water-derived species after water exposure. This peak is comprised of both carbonate and adsorbed hydroxyl interacting with Na. This interaction causes the segregation of Na to the surface. We discussed earlier the possibility that the adsorbate is a water-derived species or an oxygen species. The possible adsorbates are water, atomic oxygen or hydroxyl. Previous studies of water adsorption on Au(111) reveal there is no adsorption of H₂O_g on pristine Au(111) at room temperature.^{28,29} Sodium readily reacts with water to form sodium hydroxide, reducing the possibility the adsorbate is molecular water. This effectively rules out the possibility of the adsorbed species being water. The next possibility is that of an adsorbed oxygen species. The oxygen adsorbs at either Na atoms or both Na and Au atoms on the surface. The lack of the oxide peak as seen with the oxygen exposures,¹³ rules out an Na-rich environment. An oxygen atom adsorbed on an Au-Na site shows stability (consistent with slightly increasing peak intensity) after annealing at both 425 K and 475 K.¹³ This conflicts with the results for annealing after water exposure which show an evident decrease in O 1s intensity. The C 1s carbonate intensity does not change indicating there is no change in its intensity contribution to Peak B O 1s. Thus the change in Peak B O 1s cannot be atomic oxygen adsorbed at an Au-Na site. The final possibility is the adsorbed water-derived species, hydroxyl. A +3.6 eV shift from our oxide peak at 527.9 eV¹³ to our hydroxyl peak at 531.5 eV correlates with the +3.1 eV shift Barrie and Street reported for sodium oxide to sodium hydroxyl.¹⁹ The presence of Na likely promotes the dissociation of water into hydroxyl. Previous studies show that the presence of alkali metals promotes the dissociation of water, which is likely occurring on our sample.²²⁻²⁴ The large negative heat of formation for sodium hydroxide (-456 kJ/mol)

indicates a stable compound. The loss of O from the surface after annealing at both 425 K and 475 K is due to desorption of NaOH from the surface and/or the recombination of two OH_{ad} . We have not conducted TPD experiments studying desorption after water exposure, but it is possible that the NaOH desorbs at ~ 450 K, similar to Na.¹² Researchers have reported that pre-adsorption of alkali metals on nickel surfaces promotes the dissociation of $\text{H}_2\text{O}_{\text{ad}}$ to OH_{ad} with the OH_{ad} binding to the alkali metal.²²⁻²⁴ Kuch and co-workers reported that the hydroxyl species on K/Ni(111) does not appreciably desorb until potassium atoms begin to desorb.²³ It is likely that some of the OH on our NaAu_2 is desorbing with or at the same temperature as Na. The recombination of hydroxyl on metal surfaces is well studied. Researchers have found disproportionation of hydroxyl occurs on a wide variety of single crystal metals including Ni(110),^{30,31} Pd(100),^{32,33} Pt(111),³² Cu(110),³⁴ and Ag(110).³⁵ The temperature range in which disproportionation occurs for those metals is between 220 K and 350 K.³⁰⁻³⁵ Comparing these temperatures to the lower annealing temperature (425 K) utilized for NaAu_2 , it is reasonable to assume that the hydroxyl present on our NaAu_2 surface is recombining. The products of this disproportionation reaction are $\text{H}_2\text{O}_{\text{g}}$ and O_{ad} . The remaining O_{ad} is likely the residual O 1s peak, at 531.3 eV, that is present on the cleaned surface (cf. Section 3.1). The segregation of Na to the surface suggests that the hydroxyls are adsorbing to Na. Additionally, two distinct peaks were seen after oxygen exposure, corresponding to atomic oxygen adsorbing at an Au-Na site and a Na site. The presence of only one peak in the O 1s region after water exposure leads us to the conclusion there is one adsorption site for the hydroxyls. From this data, we conclude that the adsorbed water-derived species on the surface is hydroxyl adsorbed at a Na site. Confirmation of adsorption is seen in the LEED patterns after exposure. The clean surface pattern is absent suggesting

adsorption and possible surface disruption. This experimental information contradicts the DFT theory of a water adsorption site involving both Na and Au atoms. DFT also predicts an undissociated water molecule, while experiment shows a hydroxyl. The presence of the Na atoms could play a role in the Na-site preference, dissociation of water and strong adsorption of hydroxyl.

4.2. Carbon monoxide

The data show that there is little, if any, adsorption of carbon monoxide on the surface. XPS peak intensity increases for both C 1s and O 1s are less than 3 ± 1 atom% at both room temperature and elevated temperature. CO exposed surface LEED patterns are comparable to those of the cleaned surface and TPD results indicate no evidence of CO_g desorption. This all leads to the conclusion that CO does not adsorb on NaAu₂(111) at room temperature. Previous studies for carbon monoxide adsorption on Au surfaces at room temperature (300 K) reveal there is no adsorption of CO on pristine Au(111) at exposure pressures below 0.01 mbar.^{36,37} These findings coincide with those of DFT which predicted little to no CO adsorption on the surface.

4.3. Carbon dioxide

The data show that there is little adsorption of carbon dioxide on the surface. XPS peak intensity increases for C 1s are about 2 ± 1 atom% at room temperature, with this increase seen only in the carbonate peak. TPD results indicate no evidence of CO_{2,g} desorption or formation. This all leads to the conclusion that CO_{2,g} does not adsorb on NaAu₂(111) at room temperature. Previous studies of carbon dioxide adsorption on Au

surfaces reveal there is no adsorption of $\text{CO}_{2,g}$ on Au films at room temperature.³⁸⁻⁴⁰ $\text{CO}_{2,g}$ adsorption on Au(110) and Au films does occur at low temperatures (<110 K), but the gas completely desorbs upon warming to room temperature.³⁸⁻⁴⁰ Reports also state Na atoms pre-adsorbed on Au substrates activate the surface and upon $\text{CO}_{2,g}$ exposure catalyze a reaction to form $\text{CO}_{3,ad}$.^{38,39} The potential source of oxygen needed to react with CO_2 to form the carbonate is likely the residual oxygen that is present on the cleaned surface. Experimental results combined with the previous Au(111) studies indicate our theory of similar behavior for $\text{NaAu}_2(111)$ and Au(111) is correct. The experimental findings of an increase in the amount of carbonate after CO_2 exposure match with reported findings on Au substrates and suggest the Na does indeed activate the surface.

5. Conclusions

XPS and LEED analysis show there is adsorption of a water-derived species on, and disruption of, the surface after water exposure. The water molecule dissociates leaving hydroxyl on the surface. The oxygen-derived peak is a combination of adventitious carbonate and hydroxyl at Na sites. XPS, LEED and TPD analysis show that neither CO_g nor $\text{CO}_{2,g}$ adsorb on the surface upon exposure. Any $\text{CO}_{2,g}$ that does adsorb on the surface reacts and becomes a carbonate, present in small amounts. TPD also reveals that exposing CO_g to an oxygen saturated surface does not produce $\text{CO}_{2,g}$ in measureable amounts. The reasons for good catalytic activity of powdered NaAu_2 for CO oxidation appear to be more complex than initially envisioned.

Acknowledgements This work was a collaboration between EMPA in Dübendorf, Switzerland, and Iowa State University in Ames, Iowa. Accordingly, this work was supported from two sources: the Swiss National Science Foundation (Contract 200021-129511), and the John D. Corbett Endowment of Iowa State University.

Figures

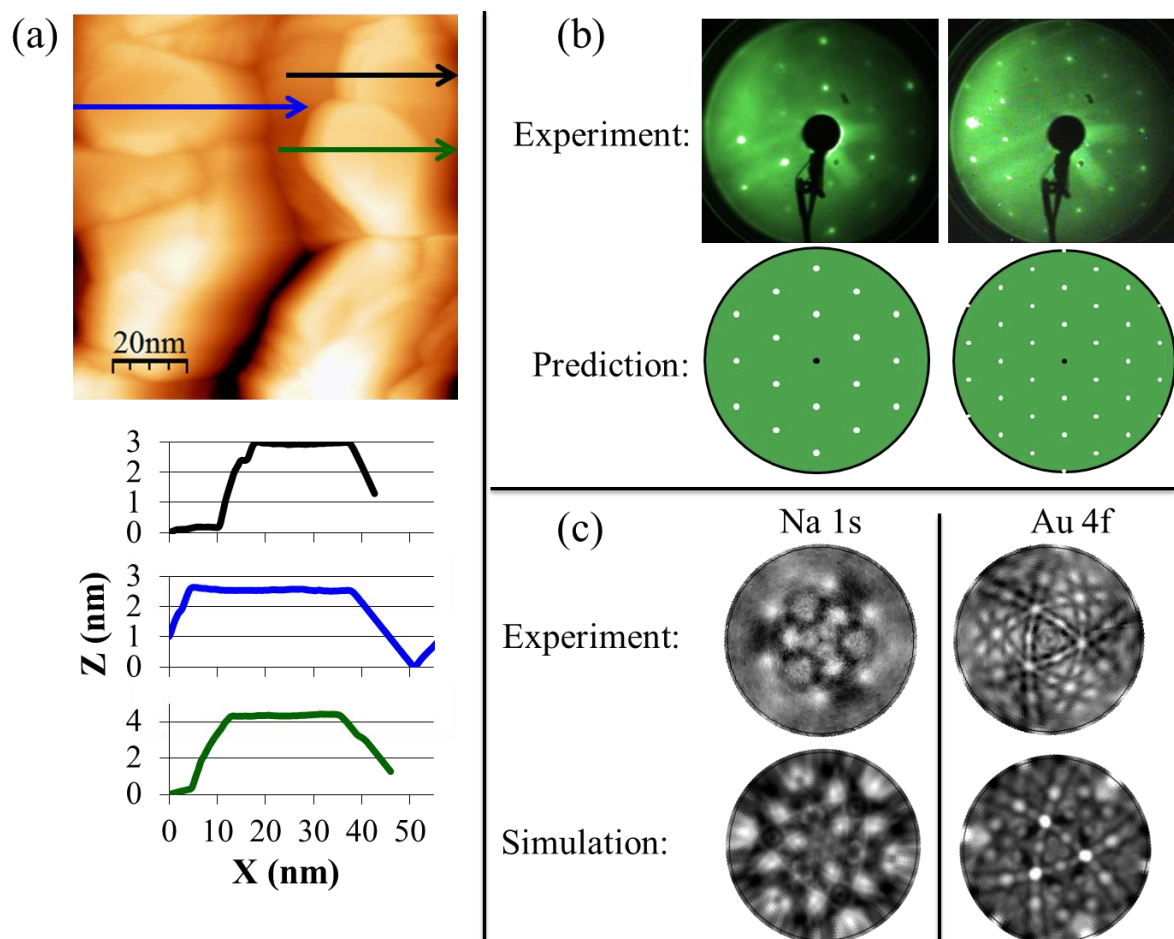


Figure 1. STM and diffraction data for the clean surface of NaAu₂(111). (a) Typical STM image (top) and line profiles (bottom), showing mesa-like features. (b) Low-energy electron diffraction patterns. Top two patterns show images measured at 64.5 eV (left) and 100.5 eV (right). Lower two patterns show images predicted for a bulk-terminated surface at these energies. (c) X-ray photoelectron diffraction patterns using Na 1s and Au 4f photoelectrons, both measured with an Al K α source (top) and simulated (bottom).

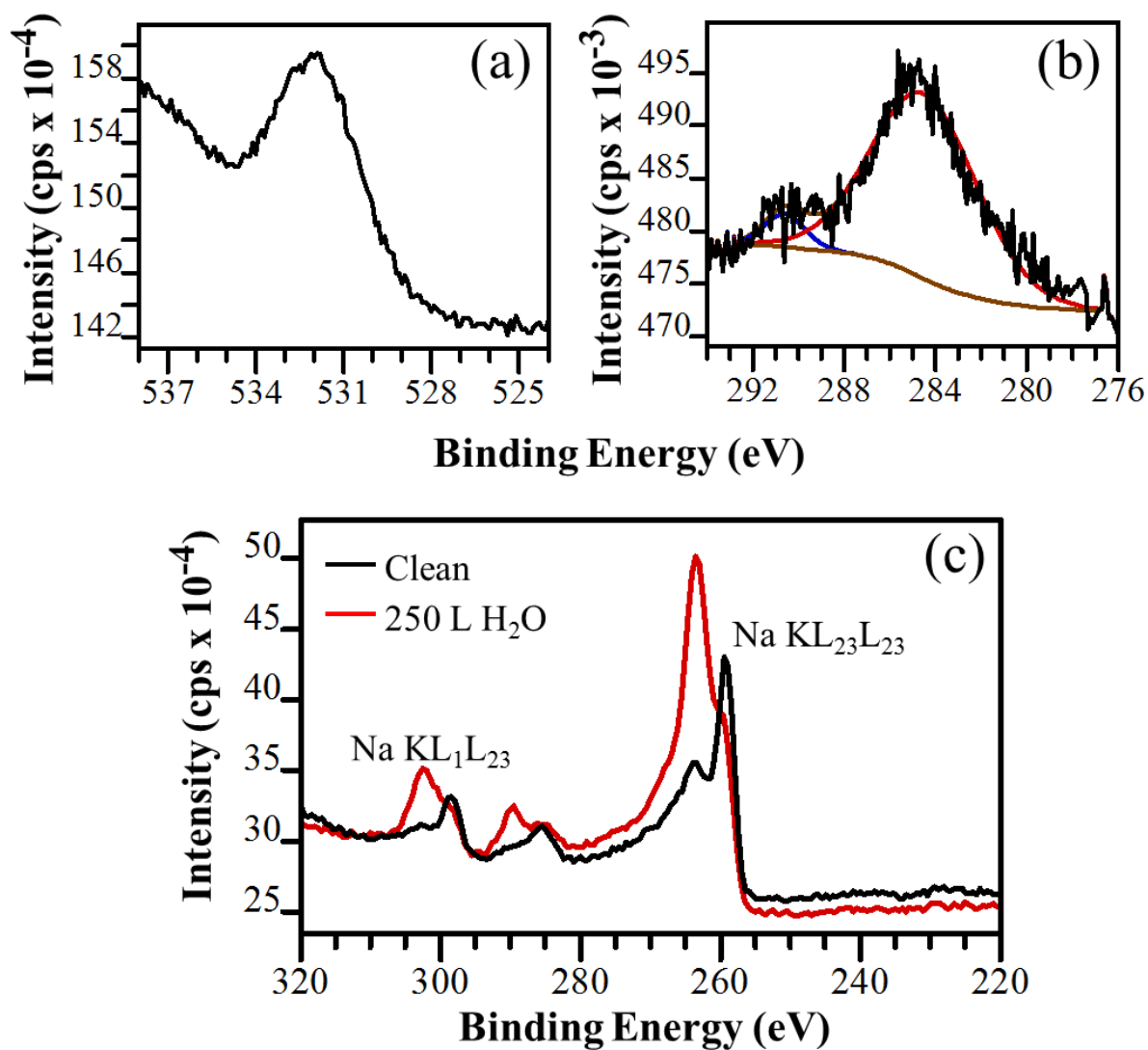


Figure 2. Photoelectron spectra for the NaAu₂ cleaned surface. Panels (a)&(c) are acquired with a Mg K α source, panel (b) with an Al K α source. (a) O 1s region, cleaned surface. (b) C 1s region, cleaned surface. The Al K α source is chosen in (b) to circumvent overlap with a Na Auger peak. (c) Spectral region including both Na KL_{2,3}L_{2,3} (ca. 260 eV) and Na KL₁L_{2,3} (ca. 300 eV) lines, measured in 0.5 eV steps. Black: Cleaned surface. Red: Surface after 250 L H₂O exposure at 300 K.

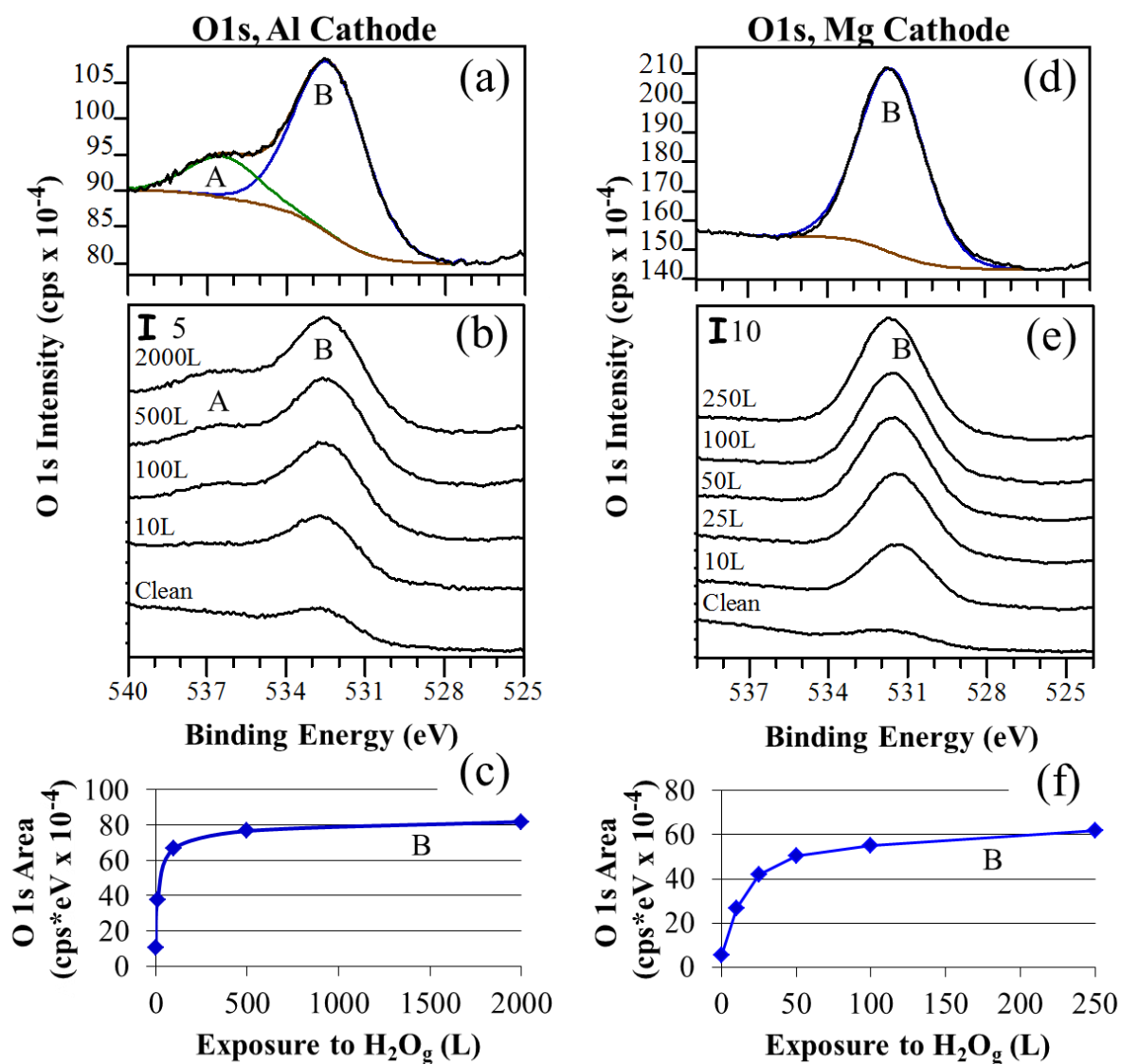


Figure 3. X-ray photoelectron spectra for the O 1s region. Two separate sequences of water exposures at 300 K, (a)-(c) are a Mg K α source, (d)-(f) are an Al K α source. Curves in (b) and (e) are displaced vertically to minimize overlap. The intensity, in units of cps $\times 10^{-4}$, can be derived using the scale bar. (a) Spectrum after 2000 L exposure, deconvoluted into two peaks. (b) Sequence of spectra for exposures from 10 L to 2000 L. (c) Integrated area of Peak B as a function of exposure. (d) Spectrum after 250 L exposure, deconvoluted into one peak. (e) Sequence of spectra for exposures from 10 L to 250 L. (f) Integrated area of Peak B as a function of exposure. Y-axis “cps” units are defined as counts per second.

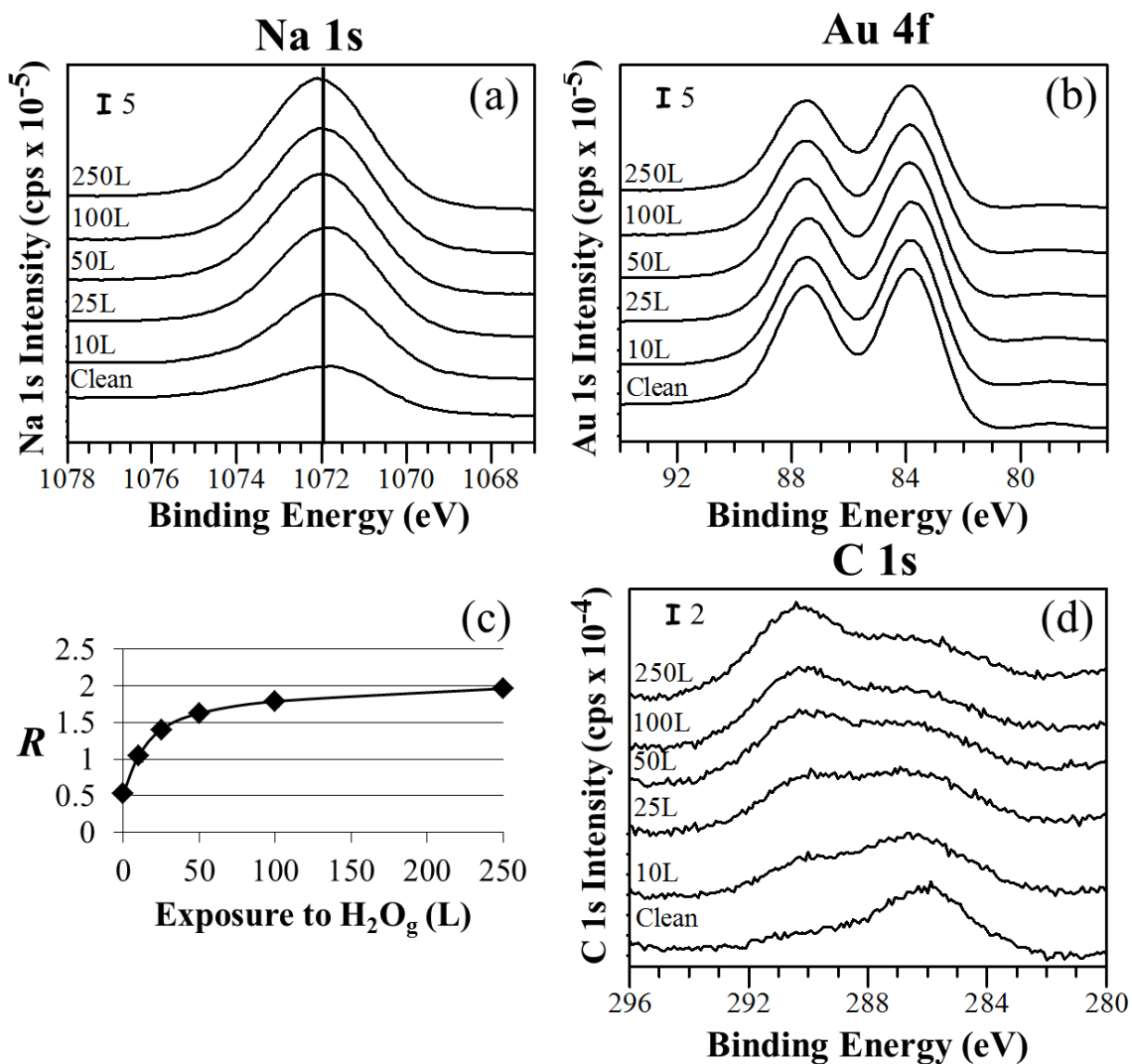


Figure 4. Na 1s, Au 4f, and C 1s X-ray photoelectron peaks for experiments where the surface was exposed to water sequentially from 10 L to 250 L at 300 K. The source is Mg K α for all panels. Curves in (a), (b), (d) are displaced vertically to minimize overlap. The intensity, in units of cps $\times 10^{-5}$ or $\times 10^{-4}$ can be derived using the respective scale bars. (a) Na 1s. (b) Au 4f. (c) R vs. water exposure. (d) C 1s. A Na Auger peak is present in the ~ 290 eV range affectedly increasing the C 1s peak intensity.

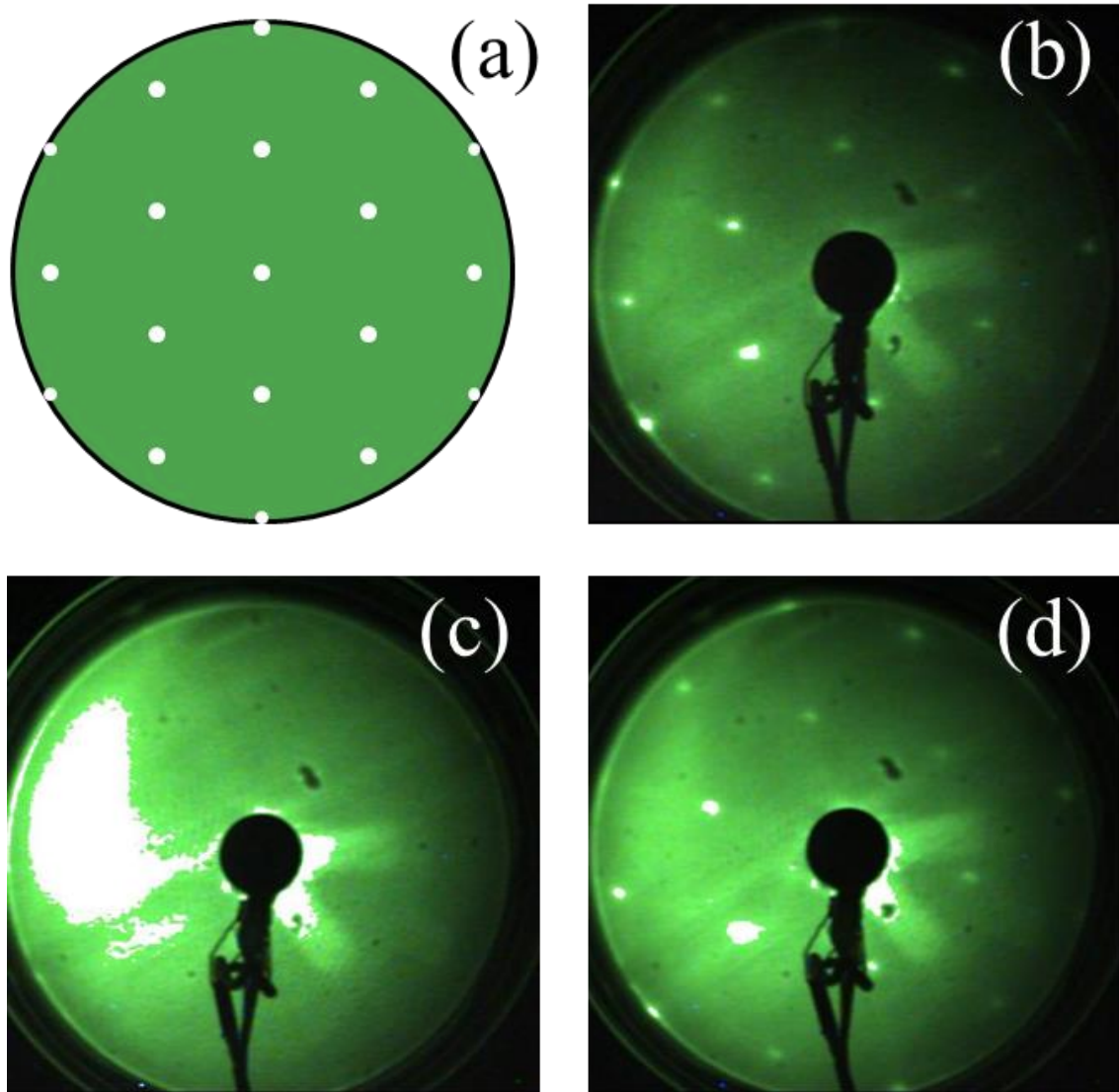


Figure 5. Low-energy electron diffraction (LEED) patterns at 45.0 eV before and after gas exposure. (a) Expected. (b) Clean. (c) 2000 L H₂O. (d) 150 L CO

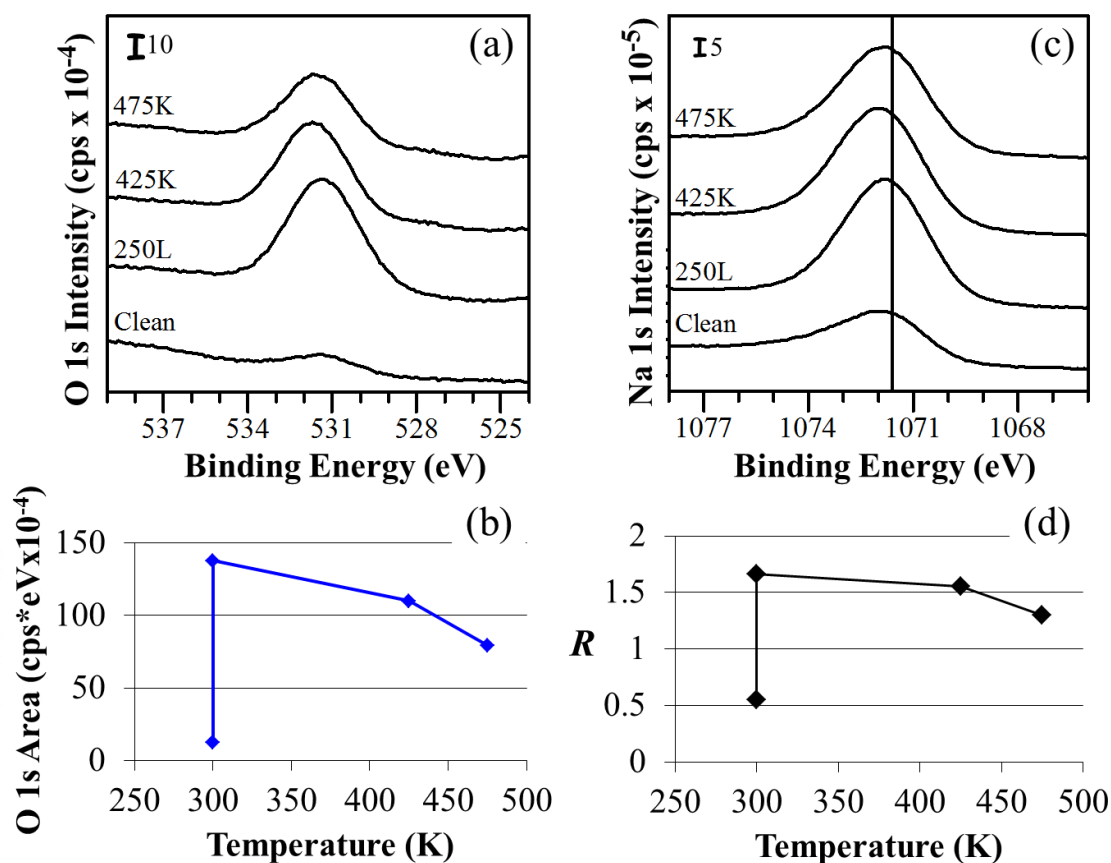


Figure 6. Result of exposing a surface to 250 L H₂O_g at 300 K, then annealing sequentially to 425 K and 475 K. The X-ray source is Mg K α . In (a) and (c), the curves are displaced vertically to minimize overlap. The intensity, in units of cps x 10⁻⁴ or 10⁻⁵, can be derived using the respective scale bars. (a) O 1s spectral region. (b) Integrated area of Peak B. In this case, the lower point at 300 K represents the clean surface, and the upper point is obtained after 250 L exposure to water. (c) Na 1s spectra for the same sequence as in panel (a). (d) *R* vs temperature. The lower point at 300 K represents the clean surface, and the upper point is obtained after 250 L exposure to water.

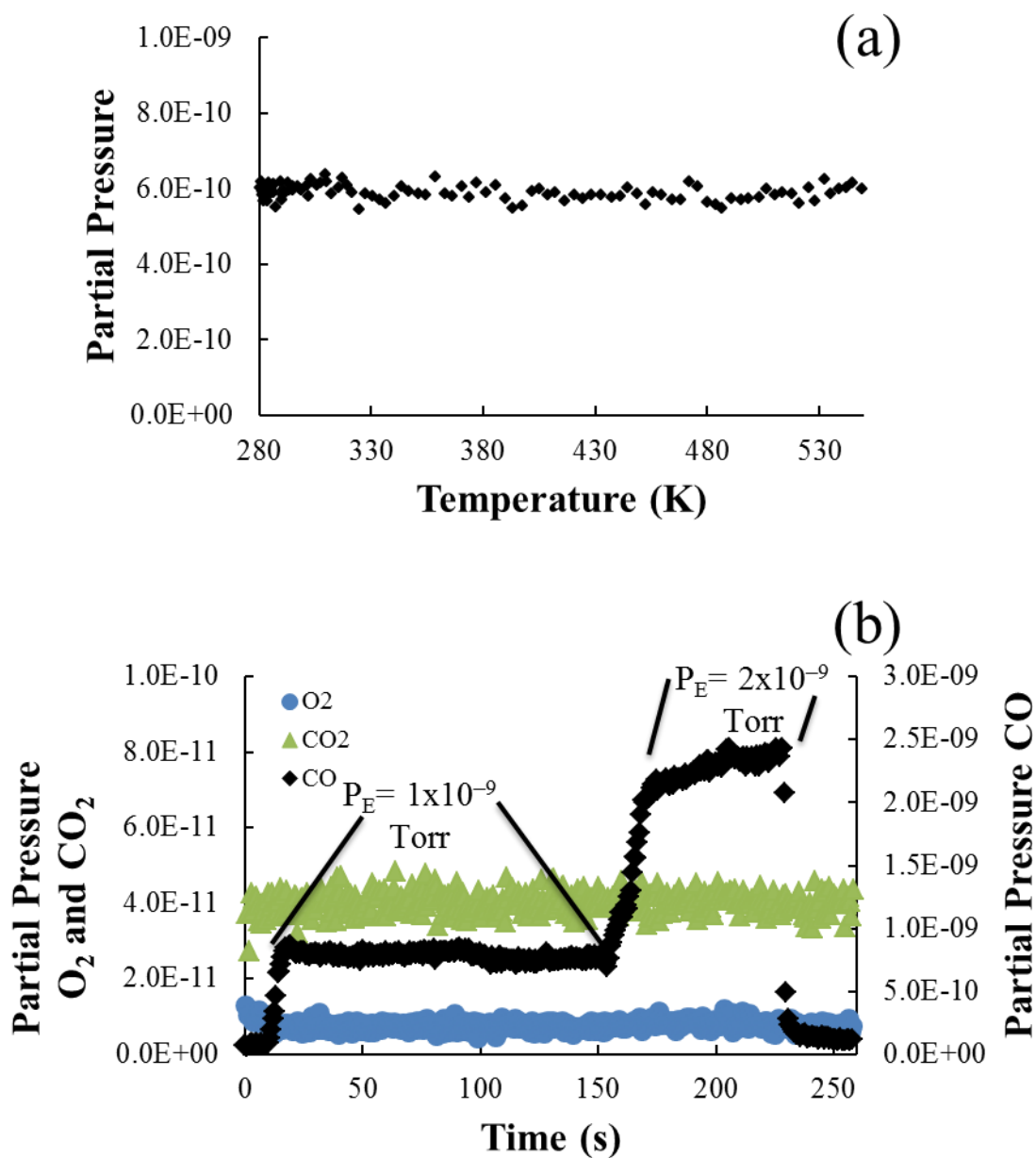


Figure 7. Results of temperature programmed desorption (TPD) gas exposures. Heating rate was 6.0 K/s and was highly linear starting at 350 K. (a) CO desorption ($m/e = 28$) after CO exposure. (b) CO ($m/e = 28$), CO₂ ($m/e = 44$) and O₂ ($m/e = 32$) desorption after oxygen exposure and while exposed to CO at 350 K. P_E denotes the exposure pressure of CO.

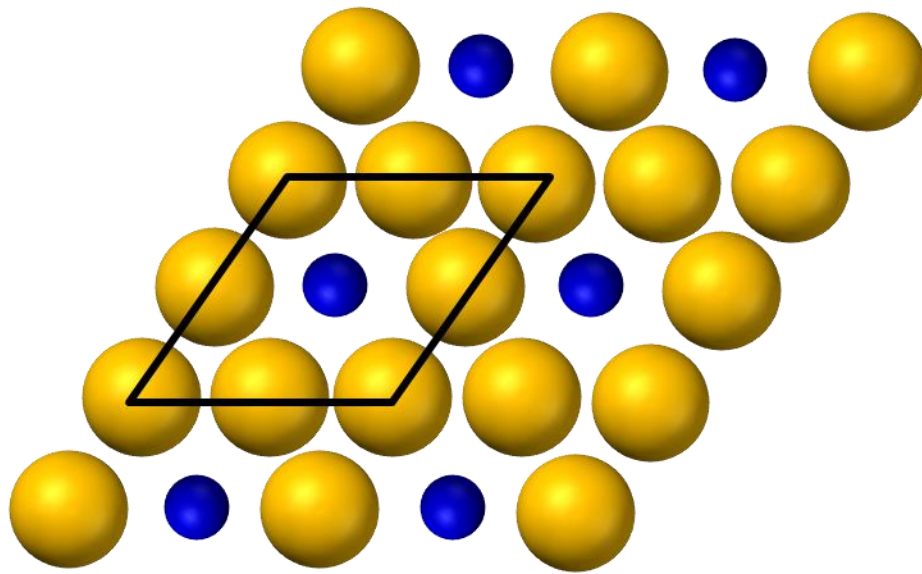


Figure 8. The $\text{NaAu}_2(111)$ surface plane structure. Large (gold) spheres are Au atoms. Small (blue) spheres are Na atoms. The rhombus shows the surface unit cell.

Appendix. Experimental Parameters

1. Cleaning protocol

Typical gas exposure experiment procedures carried out at EMPA followed a cleaning and analysis routine that extended over two separate days for each experiment, both in 2014 and 2015. The sample underwent cleaning cycles, typically two cycles, on Day 1. The sample was then left in the chamber overnight. The following morning, Day 2, we implemented the experimental portion. We used this protocol due to the extended time period required to carry out a gas exposure experiment. A typical cleaning cycle required 2.5 hours and a typical gas exposure experiment required 10 hours.

2. Experimental hardware

A button heater was used to anneal all samples in the ESCA chamber. The heater was connected to a power supply which allowed the user to set amperage (A) and voltage (V) to obtain the desired power (W). An Optris infrared laser pyrometer was used to measure temperature of the sample via line of sight through a chamber window. The pyrometer had a limited measurable temperature range of 420 K to 900 K.

The XPS electronics were replaced with new electronics in November 2014. They had become increasingly unstable within the last few months before replacement.

References

¹M. Haruta, T. Kobayashi, H. Sano and N. Yamada, "Novel Gold Catalysts for the Oxidation of Carbon Monoxide at a Temperature far Below 0°C," *Chemistry Letters* **16**, 405 (1987).

²A. Sanchez, S. Abbet, U. Heiz, W.-D. Schneider, H. Häkkinen, R. N. Barnett and U. Landman, "When gold is not noble: Nanoscale gold catalysts," *The Journal of Physical Chemistry A* **103**, 9573 (1999).

- ³A. S. K. Hashmi and G. J. Hutchings, "Gold catalysis," *Angewandte Chemie International Edition* **45**, 7896 (2006).
- ⁴B. Hvolbæk, T. V. W. Janssens, B. S. Clausen, H. Falsig, C. H. Christensen and J. K. Nørskov, "Catalytic activity of Au nanoparticles," *Nano Today* **2**, 14 (2007).
- ⁵A. Wittstock, V. Zielasek, J. Biener, C. M. Friend and M. Baeumer, "Nanoporous gold catalysts for selective gas-phase oxidative coupling of methanol at low temperature," *Science* **327**, 319 (2010).
- ⁶L.-C. Wang, K. J. Stowers, B. Zugic, M. M. Biener, J. Biener, C. M. Friend and R. J. Madix, "Methyl ester synthesis catalyzed by nanoporous gold: from 10^{-9} Torr to 1 atm," *Catalysis Science & Technology* **5**, 1299 (2015).
- ⁷M. Armbrüster, R. Schlögl and Y. Grin, "Intermetallic compounds in heterogeneous catalysis—a quickly developing field," *Science and Technology of Advanced Materials* **15**, 034803 (2014).
- ⁸I. Sharafutdinov, C. F. Elkjær, H. W. Pereira de Carvalho, D. Gardini, G. L. Chiarello, C. D. Damsgaard, J. B. Wagner, J.-D. Grunwaldt, S. Dahl and I. Chorkendorff, "Intermetallic compounds of Ni and Ga as catalysts for the synthesis of methanol," *Journal of Catalysis* **320**, 77 (2014).
- ⁹J. Hao, J. Wang, Q. Wang, Y. Yu, S. Cai and F. Zhao, "Catalytic oxidation of cyclohexane over Ti–Zr–Co catalysts," *Applied Catalysis A: General* **368**, 29 (2009).
- ¹⁰C. Xiao, L.-L. Wang, R. V. Maligal-Ganesh, V. Smetana, H. Walen, P. A. Thiel, G. J. Miller, D. D. Johnson and W. Huang, "Intermetallic NaAu₂ as a Heterogeneous Catalyst for Low-Temperature CO Oxidation," *Journal of the American Chemical Society* **135**, 9592 (2013).
- ¹¹L.-L. Wang, "Personal Communcation", 2014-2016.
- ¹²E. J. Kwolek, R. Widmer, O. Gröning, O. Deniz, H. Walen, C. D. Yuen, W. Huang, D. L. Schlagel, M. Wallingford and P. A. Thiel, "The (111) Surface of NaAu₂: Structure, Composition, and Stability," *Inorganic Chemistry* **54**, 1159 (2015).
- ¹³E. J. Kwolek, R. Widmer, O. Gröning, O. Deniz, H. Walen, C. D. Yuen, W. Huang, D. L. Schlagel, M. Wallingford, C. R. Brundle and P. A. Thiel, "Interaction of oxygen with the (111) surface of NaAu₂," *Surface Science* (2016).
- ¹⁴CasaXPS: Processing Software for XPS, AES, SIMS and More; www.CasaXPS.com, (October 19, 2014).
- ¹⁵A. Winkler and J. T. Yates Jr., "Capillary array dosing and angular desorption distribution measurements: a general formalism," *Journal of Vacuum Science & Technology A* **6**, 2929 (1988).

- ¹⁶J. H. Scofield, "Hartree-Slater subshell photoionization cross-sections at 1254 and 1487 eV," *Journal of Electron Spectroscopy and Related Phenomena* **8**, 129 (1976).
- ¹⁷S. Tanuma, C. J. Powell and D. R. Penn, "Calculations of electron inelastic mean free paths. IX. Data for 41 elemental solids over the 50 eV to 30 keV range," *Surface and Interface Analysis* **43**, 689 (2011).
- ¹⁸J. F. Moulder, W. F. Stickle, P. E. Sobol and K. D. Bomben, *Handbook of X-ray Photoelectron Spectroscopy: a reference book of standard spectra for identification and interpretation of XPS data*, (Perkin-Elmer Corporation, Physical Electronics Division, Eden Prairie, Minnesota, 1992).
- ¹⁹A. Barrie and F. J. Street, "An Auger and X-ray photoelectron spectroscopic study of sodium metal and sodium oxide," *Journal of Electron Spectroscopy and Related Phenomena* **7**, 1 (1975).
- ²⁰D. D. Wagman, W. H. Evans, V. B. Parker, R. H. Schumm, I. Halow, S. M. Bailey, K. L. Churney and R. L. Nuttall, "The NBS tables of chemical and thermodynamic properties," *Journal of Physical and Chemical Reference Data* **11**, Suppl. 2 (1982).
- ²¹A. V. Shchukarev and D. V. Korolkov, "XPS study of group IA carbonates," *Central European Journal of Chemistry* **2**, 347 (2004).
- ²²T. Bornemann, H. P. Steinrück, W. Huber, K. Eberle, M. Glanz and D. Menzel, "The adsorption of H₂O on K precovered Ni(111) studied by ARUPS and TPD," *Surface Science* **254**, 105 (1991).
- ²³W. Kuch, W. Schnurnberger, M. Schulze and K. Bolwin, "Equilibrium determination of H₂O desorption kinetic parameters of H₂O/K/Ni(111)," *The Journal of Chemical Physics* **101**, 1687 (1994).
- ²⁴C. Mundt and C. Benndorf, "H₂O adsorption on alkali (Li, Na and K) precovered Ni(775)," *Surface Science* **405**, 121 (1998).
- ²⁵K. Motzfeldt, "The thermal decomposition of sodium carbonate by the effusion method," *The Journal of Physical Chemistry* **59**, 139 (1955).
- ²⁶K. Harrison and L. B. Hazell, "The determination of uncertainties in quantitative XPS/AES and its impact on data acquisition strategy," *Surface and Interface Analysis* **18**, 368 (1992).
- ²⁷M. P. Seah, "Ultrathin SiO₂ on Si. VI. Evaluation of uncertainties in thickness measurement using XPS," *Surface and Interface Analysis* **37**, 300 (2005).
- ²⁸B. D. Kay, K. R. Lykke, J. R. Creighton and S. J. Ward, "The influence of adsorbate-adsorbate hydrogen bonding in molecular chemisorption: NH₃, HF, and H₂O on Au(111)," *The Journal of Chemical Physics* **91**, 5120 (1989).

- ²⁹N. Ikemiya and A. A. Gewirth, "Initial Stages of Water Adsorption on Au Surfaces," *Journal of the American Chemical Society* **119**, 9919 (1997).
- ³⁰G. Benndorf, C. Nöbl and T. E. Madey, "H₂O adsorption on oxygen-dosed Ni(110): Formation and orientation of OH(ad)," *Surface Science* **138**, 292 (1984).
- ³¹C. Benndorf and T. E. Madey, "Adsorption of H₂O on clean and oxygen-preposed Ni(110)," *Surface Science* **194**, 63 (1988).
- ³²E. M. Stuve, S. W. Jorgensen and R. J. Madix, "The adsorption of H₂O on clean and oxygen-covered Pd(100): Formation and reaction of OH groups," *Surface Science* **146**, 179 (1984).
- ³³C. Nyberg and C. G. Tengstål, "Adsorption and reaction of water, oxygen, and hydrogen on Pd(100): Identification of adsorbed hydroxyl and implications for the catalytic H₂-O₂ reaction," *The Journal of Chemical Physics* **80**, 3463 (1984).
- ³⁴W. D. Clendening, J. A. Rodriguez, J. M. Campbell and C. T. Campbell, "The chemisorption and coadsorption of water and oxygen on Cs-dosed Cu(110)," *Surface Science* **216**, 429 (1989).
- ³⁵M. Bowker, M. A. Barteau and R. J. Madix, "Oxygen induced adsorption and reaction of H₂, H₂O, CO and CO₂ on single crystal Ag(110)," *Surface Science* **92**, 528 (1980).
- ³⁶W.-L. Yim, T. Nowitzki, M. Necke, H. Schnars, P. Nickut, J. Biener, M. M. Biener, V. Zielasek, K. Al-Shamery, T. Klüner and M. Bäumer, "Universal Phenomena of CO Adsorption on Gold Surfaces with Low-Coordinated Sites," *The Journal of Physical Chemistry C* **111**, 445 (2007).
- ³⁷I. Nakamura, A. Takahashi and T. Fujitani, "Selective Dissociation of O₃ and Adsorption of CO on Various Au Single Crystal Surfaces," *Catalysis Letters* **129**, 400 (2009).
- ³⁸V. M. Browne, A. F. Carley, R. G. Copperthwaite, P. R. Davies, E. M. Moser and M. W. Roberts, "Activation of carbon dioxide at bismuth, gold and copper surfaces," *Applied Surface Science* **47**, 375 (1991).
- ³⁹H. J. Freund and M. W. Roberts, "Surface chemistry of carbon dioxide," *Surface Science Reports* **25**, 225 (1996).
- ⁴⁰C. R. Brundle and M. W. Roberts, "Some Observations on the Surface Sensitivity of Photoelectron Spectroscopy," *Proceedings of the Royal Society of London A* **331**, 383 (1972).

CHAPTER 6**PRINCIPLES OF ANALYZING X-RAY PHOTOELECTRON SPECTROSCOPY
DATA****Abstract**

XPS is a powerful technique used in sample analysis. It can lead to complicated spectra which require the correct information to analyze accurately. We have compiled a report on the basics of XPS acquisition and analysis and what a user needs to be aware of when evaluating a spectrum.

1. Introduction

The technique of X-ray Photoelectron Spectroscopy (XPS), also known as Electron Spectroscopy of Chemical Analysis (ESCA), was developed by Kai Siegbahn and his team at Uppsala, Sweden beginning in the early 1950s. The first recorded spectrum, cleaved NaCl, was acquired in 1954, but it was not until the mid-1960s that XPS became a recognized technique in the scientific community.^{1,2} A team at Hewlett-Packard, in collaboration with Siegbahn, developed the first commercial monochromatic XPS instrument and it was released in 1969. For his contributions and advancements in XPS, Siegbahn received the Nobel Prize in Physics in 1981.² Since that time, XPS has become a widely used and important technique in chemical analysis.

The complexity in both XPS acquisition and data analysis are illustrated well by the NaAu₂ study, discussed in Chapters 3, 4 and 5. In analyzing these data, complications arose

due to X-ray source selections, convoluted and additional peaks, and normalization of the spectrum.

The following text is designed to give a review of XPS and its analysis. To start, background about XPS and data acquisition is given. It is followed by the basics of XPS analysis including spectrum normalization, peak shifts and errant peaks. Finally an example analysis is shown which incorporates the information assembled in the preceding sections.

2. Spectrum Acquisition

2.1. X-ray photoelectron spectroscopy

X-ray Photoelectron Spectroscopy is a surface sensitive technique which can provide a quantitative and qualitative analysis of a sample surface. Figure 1 shows a schematic of a typical layout for an XPS setup. The instrumentation consists of an X-ray source, an electron analyzer, an electron multiplier and the detector system. This detector system is interfaced with a computer to display the acquired information in the form of a spectrum.

A thermionic electron source bombards the X-ray anode producing X-rays which irradiate the sample. These X-rays penetrate ~1 micron into the sample, but only electrons emitted in the top 10 nm (approximately) can escape from the sample. Electrons in the top layer, ~ 0.25 nm in depth, have the highest probability of escaping the material without inelastic collisions. This probability decreases with increasing depth below the surface. Below 10 nm in depth, the probability essentially becomes zero. An article by Jablonski and Powell describe this subject in more detail.³ X-rays adsorbed by an atom can knock out a core shell electron which leaves the sample as a photoelectron and travels toward the detector. Figure 2(a) illustrates this process. The electron analyzer is biased to only allow the

electrons with a specific kinetic energy (E_k), or pass energy, through to the detector. A concentric hemispherical analyzer (CHA) is commonly used with XPS.⁴ The outer plate of the hemispherical analyzer is biased negative to repel electrons and the inner plate is biased positive to attract electrons. This forces the electrons to follow an arc to reach the detector and only electrons with the specific pass energy can pass through the analyzer. Electrons with a higher energy (moving faster) crash into the outer plate while those with a lower energy (moving slower) crash into the inner plate. A sweep of an energy range is done by varying the retarding voltage, which results in a XPS spectrum.

A higher resolution is obtained by adjusting the pass energy of the analyzer. A lower pass energy corresponds to a higher resolution (sharper peaks) while a larger pass energy corresponds to a lower resolution (broader peaks). A lower pass energy also means fewer electrons pass through the analyzer to the detector, resulting in a smaller signal and higher noise.⁵ Resolution is also dependent on the size of the aperture (focuses the photoelectrons) located at the entrance of the analyzer. A smaller aperture size results in a higher resolution, but smaller signal to noise ratio. The signal size can be improved by increasing the number of sweeps over the energy range. Each sweep in the run can be added to the last to compound the number of counts and thus the overall spectrum signal. The energy of inbound electrons is also retarded, forcing them to have a constant energy as they arc through the analyzer. This constant energy allows the same resolution over the entire spectrum. A higher pass energy should be used for overview spectra (e.g. 1100 eV to 0 eV), while a lower pass energy should be used for specific peaks (e.g. 295 eV to 275 eV).

The X-ray sources, detailed below, emit X-rays at a specific energy, $h\nu$. Combined with the measured E_k from the detector, we can calculate the binding energy (E_b) of the

emitted electron. This is summarized in Equation 1, where Φ is the work function of the spectrometer.

$$h\nu = E_k + E_b - \Phi \quad (\text{Eqn. 1})$$

Each element has a characteristic E_b associated with its core shell electrons. This allows us to qualitatively determine what elements are present in the sample. Figure 3 shows an example of an XPS spectrum of NaAu_2 with labeled peaks. XPS peaks are labeled with their respective core shells (e.g. 1s) and Auger peaks are labeled with their respective electron shell locations (e.g. KLL). A further description of Auger is given in Section 2.3. The spectrum background is comprised of inelastic electrons, valence orbital electrons and Auger electrons. Inelastic electrons arise from electrons within the sample colliding with another atom which results in a loss of kinetic energy before being emitted. The emitted inelastic electron no longer has a characteristic E_b and becomes part of the background. A valence orbital electron is an electron emitted from an atom's outermost shell. The characteristic core shell energy E_b also provides information about the chemical state or environment of the atom. This includes but is not limited to oxidation, reduction and chemical environment, all detailed below.

Varying degrees of surface sensitivity are also possible when using XPS. A higher surface sensitivity is obtained by adjusting the take-off angle, TOA or θ . The TOA is defined as the angle between the surface and the detector. Figure 4 illustrates this concept. Figure 4(a) shows a large TOA which results in more electrons emitting from multiple layers. Figure 4(c) shows a smaller TOA which results in more electrons emitting from the surface region. The appearance of the spectrum can also be affected by changing the step width for the energy range sweep. A step width is defined as the increase in eV before the next signal point

is acquired. The smaller the step, the more spectrum points are taken and the sharper the peaks. A smaller step (e.g. 0.1 eV) should be used for specific peak sweeps while a larger step (e.g. 0.5 eV) can be used for overview sweeps to minimize scan time.

UHV is required for XPS analysis due to the length of the path the photoelectron must travel to get from sample to detector without colliding with another particle (e.g. electron, atom, or molecule). The mean free path, which is the average distance a particle travels before a collision, in air (pressure ~ 760 Torr) is $\sim 10^{-8}$ m whereas in UHV (pressure $\sim 10^{-10}$ Torr) it is $\sim 10^5$ m. UHV provides the ideal environment to eliminate this gas phase scattering.

2.2. X-ray sources

The two most common x-ray sources are the twin anode source and monochromatic Al source. The twin anode source is comprised of a magnesium (Mg) anode and an aluminum (Al) anode. Each anode emits an X-ray at a specific energy, 1253.6 eV for Mg and 1486.7 eV for Al. These X-rays directly irradiate the sample surface as previously shown in the schematic of Figure 1.

The configuration of a monochromatic Al source is almost identical to that of the twin anodes with the exception of an added quartz crystal. Figure 5 shows a schematic of this layout. The X-rays are emitted from the Al source and directed toward a quartz crystal. This crystal monochromatizes the X-ray beam (allowing only the X-ray energy of 1486 eV to pass through). Monochromatizing the X-ray beam has many advantages when compared to using a twin anode source. Unwanted X-rays which cause satellite and “ghost” peaks (cf. Section 3.4.2 and Section 3.4.3, respectively) are removed as well as high-energy Bremsstrahlung

(electromagnetic radiation) and thermal radiation from the source. The background decreases and the energy resolution increases, resulting in sharper peaks and a higher chemical selectivity.

Selecting the correct X-ray source is highly dependent on the sample being analyzed as will be discussed below.

2.3. Auger electron spectroscopy

Auger Electron Spectroscopy (Auger or AES) is another type of surface spectroscopy. It is used primarily to detect elements with a lower mass ($Z < 15$). Auger peaks can be convoluted with XPS peaks in a given spectrum, dependent on the elements present in the sample.

The appearance of Auger peaks in XPS spectra begins with the core hole created by the emitted photoelectron. An outer shell electron then relaxes and drops to the vacant core hole. The energy emitted by this relaxing electron is transferred to a second outer electron. A fraction of this transferred energy is used to overcome the binding energy of the outer electron while the remaining energy stays with the emitted Auger electron in the form of kinetic energy. This process is illustrated in Figure 2(b). Nomenclature for Auger is based on the locations of the electrons in the process. The core shell numbers (1, 2, 3,...) are replaced with letters (K, L, M,..., respectively). The first letter is the shell of the initial core hole, the second letter is the shell of the outer relaxing electron, and the final letter is the shell of the emitted Auger electron. An Auger electron that has a core hole in shell 1, a relaxing electron from shell 2 and an emitted electron from shell 2 is named a KLL Auger electron. Relaxing and emitted electrons located within shell 2 (or higher) can come from the s or p orbitals

which are at different levels within the orbital. This makes their energies unique and distinguishable in the spectrum. A subscript is added to the letters to denote the orbital angular momentum (e.g. $s = 1$; $p = 2,3$). If the previous KLL Auger electron had the relaxing electron come from the 2s orbital it is denoted as L_1 and if the emitting electron came from the 2p orbital it is denoted as $L_{2,3}$. This gives a final name of $KL_{1,L_{2,3}}$ for the Auger electron. Examples of Auger peaks can be seen in Figure 3.

Typical XPS spectra are plotted as signal with respect to E_b . XPS photoelectrons have a defined E_b due to the emission and detection of characteristic core level electrons. This means that XPS peaks have fixed binding energies and thus fixed positions in the binding energy spectrum regardless of the X-ray source. Auger electrons have a defined E_k . This means that Auger peaks have varied E_b and shift positions in the spectrum dependent upon the X-ray source. Thus, an XPS peak and Auger peak that are convoluted when using the Al source are not be convoluted when using the Mg source. Figure 6 illustrates this peak shift for the Na KLL peak when different X-ray sources are used. Selecting the correct source for data collection is very important especially when it comes to later data analysis.

3. Spectrum Analysis

3.1. Scofield cross-sections

All elements have a specific photoionization cross-section or probability that an electron will be emitted from an orbital. These cross-sections are also specific for each orbital subshell. In electron energy based techniques, it is important to apply the correct cross-sections in order to obtain accurate results. In the case of XPS, these probabilities need to be applied to all peaks during analysis in order to normalize peak intensities and calculate

sample composition. Photoionization cross-sections are source dependent as well. To account for these probabilities John H. Scofield calculated a series, now known as the Scofield cross-sections (δ), of these photoionization cross-sections for X-ray energies of 1487 eV (Al) and 1254 eV (Mg).⁶

The Scofield cross-section tables are typically provided within XPS analysis software. These values can be applied by the user if composition analysis is done within the software or the values can be ascertained from the software and applied to data spreadsheets by the user. In the case of CasaXPS software,⁷ the Scofield cross-sections are renamed “relative sensitivity factors” (RSF) values and must be applied externally via a spreadsheet. Scofield cross-sections are a large part of XPS analysis, so applying the correct cross-section is essential for accurate analysis.

3.2. Inelastic mean free path

Electron scattering is a common occurrence in spectroscopy and diffraction techniques. This scattering is either inelastic (measurable energy loss) or elastic (no energy loss). Inelastic scattering has a large effect on the surface sensitivity of XPS. The inelastic mean free path (IMFP) is a measure of how far an electron travels through a solid before losing energy (i.e. due to a collision). The IMFP is highly dependent on the kinetic energy of the electron. Figure 7, frequently called the Universal Curve, shows the mean free path (λ) of an electron dependent on the kinetic energy. The dashed line approximates this curve and is given by Equation 2.

$$\lambda \text{ (in } \text{\AA}) = 1430E_k^{-2} + 0.54\sqrt{E_k} \quad (\text{Eqn. 2})$$

The blue box indicates the typical energy range for XPS spectra. The curve shows that electrons with a lower kinetic energy have a shorter mean free path while electrons with a higher kinetic energy have a longer mean free path. A shorter mean free path length results in a smaller sampling depth because the majority of the signal comes from the surface layers. Peaks with similar kinetic energies should be used for sample composition values because they have similar IMFPs and thus similar sampling depths. IMFP sampling depths range from 3 Å to 50 Å, roughly 1 to 20 layers.⁸ Various tables and databases of IMFP data are available for the elements, due to the work of C. J. Powell and collaborators. The most useful and up-to-date one is published by NIST,⁹ and available on-line at <http://www.nist.gov/>.

Elastic scattering causes attenuation in the acquired spectrum. A correction to the XPS intensity to account for this attenuation and the IMFP can be applied using an Effective Attenuation Length (EAL). The XPS intensity, I_d , originating from a depth, d , is given by Equation 3.

$$I_d = I_0 (1 - e^{-d/(EAL \cdot \cos\theta)}) \quad (\text{Eqn. 3})$$

I_0 is the integrated intensity from infinite depth, i.e. the bulk, and θ is the emission angle.

Substituting in d , EAL and θ for the specific experiment gives a corrected XPS intensity.

Various tables and databases of EAL data are available for the elements, due to the work of C. J. Powell, A. Jablonski and collaborators. The most useful and up-to-date one is published by NIST,¹⁰ and available on-line at <http://www.nist.gov/>.

3.3. Chemical shifts

Peak shifts due to oxidation or reduction of the atoms, or the chemical environment surrounding the atoms, are detectable in XPS. These shifts typically range from 0.1 eV to 1 eV.¹¹ Oxidization of an atom or location in a highly electronegative environment shifts the corresponding peak to a higher E_b . In both cases, as electrons are removed and the atom becomes more positive, the remaining electrons bind more tightly to the nucleus requiring more energy to remove them from the atom which results in a higher E_b . These same trends are seen with the Auger peaks.

Peak shifts also occur with clusters and sample interfaces. Researchers have found a correlation between cluster size and E_b .^{12,13} As cluster size decreases, the size of the shift to a higher E_b increases. The overall shift is less than 1 eV. As the cluster gets smaller, the structure and electronic properties no longer resemble the bulk which results in a deviation from the bulk peak energy via a peak shift. A correlation between sample interfaces, most commonly studied for thin films on bulk oxides, was also found.¹⁴⁻¹⁶ Interface effects are similar to chemical environment effects. As a thin film layer increases in thickness the underlying support layer has a smaller interaction with the thin film. This results in a smaller peak position shift from the thin film's bulk properties. When the thin film is thick enough to negate any support interactions it resembles that of a bulk system. Most peak shifts caused by interface effects are to a higher E_b and are less than 1 eV.

3.4. Errant peaks

A typical XPS spectrum contains peaks from the sample, which are used to quantify and characterize the elements present. In some cases, even after taking into consideration the

peak locations due to the X-ray source and potential chemical shifts, there are additional peaks present which are not from the sample. These additional peaks can lead to a misinterpretation of the acquired spectrum and an inaccurate sample analysis. These peaks are separated into three classifications: sample plate peaks, satellite peaks, and “ghost” peaks. Each is discussed in detail below.

3.4.1. Sample plate peaks

A sample plate peak is an additional peak that appears in a XPS spectrum which originates from the sample holder. Sample plate peaks cause issues in data analysis if the plate contains an element present in the sample or if the sample plate peaks overlap with sample peaks. To eliminate these issues it is best to pick a plate without any similar elements and to center the sample so the detected signal comes only from the sample itself. In the case where a sample is very small, it is only possible to center the plate so that the detected sample plate peaks are at a minimum intensity. The most common sample plate materials are tantalum (Ta), molybdenum (Mo), and stainless steel (primarily composed of Fe, Cr, and Ni). The photoelectrons that reach the detector are dependent on two factors, the X-ray beam size and the analyzer aperture. In a system using a twin anode source, the X-ray beam cannot be focused and thus it irradiates the sample and sample plate. This results in photoelectron emission in many directions from the sample. To focus the photoelectrons emitted from the sample and to enhance energy resolution, an aperture is placed at the entrance of the analyzer. The sample itself should be centered under this aperture so the photoelectron beam is primarily that of the sample. Figure 8 shows an XPS spectrum which contains both sample and sample plate peaks.

3.4.2. Satellite peaks

A satellite peak is an additional unwanted peak that appears in the XPS spectrum due to higher kinetic energy $K\alpha$ X-rays emitted from the X-ray source. These higher energy X-rays reproduce the same spectrum but are shifted to lower E_b and have reduced peak intensities. The primary XPS peak is denoted as α_1 and assigned an amplitude of 100. The satellite XPS peaks, denoted $\alpha_2, \alpha_3, \dots, \alpha_n$, are scaled relative to the primary peak's amplitude. Table 1 lists the relative kinetic energy shifts and amplitudes for the most common satellite peaks for the twin anode Al and Mg sources. Figure 9 illustrates an example of satellite peaks for a Mg X-ray source.

Table 1. XPS Source Satellite Peaks^{17,18}

Line	ΔE_k (eV)	%Amplitude	Line	ΔE_k (eV)	%Amplitude
Mg $K\alpha_2$	-0.265	0.5	Al $K\alpha_2$	-0.415	0.5
Mg $K\alpha_1$	0	100	Al $K\alpha_1$	0	100
Mg $K\alpha_{\cdot}$	4.74	1.027	Al $K\alpha_{\cdot}$	5.452	0.8369
Mg $K\alpha_3$	8.21	6.797	Al $K\alpha_3$	9.526	6.514
Mg $K\alpha_{3'}$	8.487	3.469	Al $K\alpha_{3'}$	9.958	2.078
Mg $K\alpha_4$	10.095	4.905	Al $K\alpha_4$	11.701	3.081
Mg $K\alpha_5$	17.404	0.4268	Al $K\alpha_5$	20.072	0.2459
Mg $K\alpha_6$	20.43	0.3362	Al $K\alpha_6$	23.576	0.1828
Mg $K\beta$	48	2	Al $K\beta$	70	2

Satellite peaks which overlap with the peaks of other elements in the spectrum can be removed in two ways. The first is to use a monochromatized Al X-ray source. The quartz crystal monochromator in such a source only allows X-rays with energy 1487 eV to pass through and reach the sample, effectively removing the higher energy $K\alpha$ X-rays. In our laboratory, we do not have a quartz monochromator; our system is equipped with a dual anode source. The second method, appropriate for the twin anode source, is to calculate the intensity of the satellite peak based on its relative intensity to the primary peak and then

subtract that value from the total overlapping peak intensity. An example of this is illustrated in Figure 10. In the E_b region of 66 eV to 58 eV, the Au $4f_{7/2}$ $K\alpha_5$ satellite peak overlaps with the Na 2s peak with an Al source. To remove this satellite peak we would begin by integrating the area under the Au $4f_{7/2}$ primary peak. This integration is illustrated in Figure 10(a) and results in a value of 1.3×10^6 . Using Table 1, we would then determine the percent intensity of the $K\alpha_5$ satellite peak with respect to the Au $4f_{7/2}$ primary peak ($K\alpha_1$). In this case the $K\alpha_5$ satellite is 0.4268% the intensity of the $K\alpha_1$, which when applied to the integrated value gives us:

$$1.3 \times 10^6 * 0.004268 = 5548.4 = K\alpha_5 \text{ satellite}$$

In the E_b region of 66 eV to 50 eV, the Na 2s peak also overlaps with the Au $5p_{3/2}$ peak. This is illustrated in Figure 10(b). In order to obtain the correct integrated value for the Na 2s + $K\alpha_5$ satellite overlap, a deconvolution must be done to obtain accurate values for both peaks. See Section 4.2 for a detailed description of this type of peak deconvolution. The integrated value for the red curve (Na 2s + $K\alpha_5$ satellite) in Figure 10(b) gives a total value of 3.3×10^4 . Subtracting the $K\alpha_5$ satellite value from the total value gives us:

$$3.3 \times 10^4 - 5548.4 = 2.7 \times 10^4$$

Thus this gives us a corrected value for the intensity of the Na 2s peak of 2.7×10^4 .

3.4.3. "Ghost" peaks

A "ghost" peak is an additional unwanted peak that appears in the XPS spectrum due to contamination of, or impurities in, the primary X-ray source. These

contaminants/impurities are excited by the same thermionic electron source that bombards the primary X-ray source and emit their own $K\alpha$ or $L\alpha$ energy X-rays. These secondary X-rays create a superimposed spectrum that is shifted to a lower E_b and has reduced peak intensity. Typically the highest intensity peaks from the primary X-ray source spectrum are the reproduced “ghost” peaks resulting from the secondary X-ray source. Common secondary X-rays seen with the twin anode source are O $K\alpha$, due to oxidation of the primary X-ray sources, and from the respective Al and Mg X-ray sources themselves. Figure 11 illustrates an example of a “ghost” peak found in a $NaAu_2$ spectrum. In this case, the “ghost” peak occurs due to the oxidation of the Mg source. An Al monochromator prevents these secondary X-rays from reaching the sample as the quartz crystal only allows the X-ray energy of 1487 eV to pass through. Table 2 lists the kinetic energy shifts and relative amplitudes for the most common contaminants and impurities for the twin anode Al and Mg sources. These values come from a comprehensive list of X-ray wavelengths for elements from lithium to americium ($Z = 3$ to 95) compiled by J.A. Bearden.¹⁹

Table 2. Common XPS Source Contaminates and Impurities¹⁹

Line	ΔE_k (eV)	Energy Relative to Mg (eV)	Energy Relative to Al (eV)
Al $K\alpha$	1486.7	+233.1	---
Mg $K\alpha$	1253.6	---	-233.1
Cu $L\alpha$	929.7	-323.9	-557.0
Ni $L\alpha$	851.5	-402.1	-635.2
Co $L\alpha$	776.2	-477.4	-710.5
Fe $L\alpha$	705.0	-548.6	-781.7
Cr $L\alpha$	572.8	-680.8	-913.9
O $K\alpha$	524.9	-728.7	-961.8
Ti $L\alpha$	452.2	-801.4	-1034.5
Sc $L\alpha$	395.3	-858.3	-1091.4

4. Example Analysis

Acquiring a XPS spectrum using the correct X-ray source is crucial for accurate sample analysis. The first step is to identify the peak positions for the elements within the sample. There are many online databases^{20,21} and the Handbook of X-ray Photoelectron Spectroscopy¹¹ available for this. Next, if applicable, identify the peak positions for elements that will be added to the surface, e.g. via evaporator deposition, or gas exposure. XPS binding energies are fixed regardless of the X-ray source so any primary XPS peak overlap cannot be removed. Such overlapping (unresolved) peaks will require deconvolution to obtain accurate analysis. Finally, identify the Auger peak positions in the XPS spectrum for the elements in the sample. Compare the XPS peak positions with the Auger peak positions and determine if there is any peak position overlap. Select the X-ray source that has either no overlapping peaks or the fewest overlapping peaks. In some cases, an Auger peak shifts from overlapping one essential analysis peak (e.g. with an Al source) to overlapping another essential analysis peak (e.g. Mg source). In this case, either choose the source that overlaps the less essential analysis peak or take the spectrum with both sources. This issue is illustrated with an example in Figure 6. Panel (a) is a spectrum acquired with an Al K α source. The O 1s XPS peak and Na KL₁L_{2,3} Auger peak overlap with each other. The C 1s XPS peak does not overlap with another peak. Panel (b) is a spectrum acquired with a Mg K α source. Here, the Na KL₁L_{2,3} Auger peaks have shifted to a lower E_b. The O 1s XPS peak no longer overlaps with another peak. The C 1s XPS peak, however, now overlaps with the Na KL₁L_{2,3} Auger peak.

4.1. Single peak

A basic XPS analysis technique is taking the area under the curve of a single peak. To take the area under the curve, begin by opening the desired file in a XPS analysis software. CasaXPS software⁷ is used for this and all following examples. There are many background types that can be used in analysis, but the three most popular are Linear, Shirley^{22,23} and Tougaard.²⁴ It has been found that all three backgrounds give comparable results.^{25,26} Linear and Shirley are more commonly used when analyzing single peaks or small energy ranges, while Tougaard is useful for both small and large energy ranges.^{25,26} When performing a comparative analysis of several peaks in a spectrum is it best to use the same background type. In the following example, a Shirley type background is used. Figure 12 illustrates the steps to obtain the peak area. Figure 12(a) shows the peak as initially opened in CasaXPS. Set the desired background type and create a region which highlights the peak and adjust the range it integrates over; see Figure 12(b). Set the end points of the integration range to where the peak itself ends and the spectrum line becomes flat. The software automatically integrates the area under the peak for the set region and provide a corresponding value. CasaXPS provides this value in a “Quantification Parameters” window as shown in Figure 12(c). This technique can be applied to all single peaks in a XPS spectrum.

When integrating areas of a given peak obtained in different experiments for purposes of comparison—for instance, if the desired result is a plot of peak area vs. exposure, or peak area vs. temperature—it is very important to use the same integration limits for each spectrum. Changing integration limits can change intensities significantly and corrupt the data analysis.

4.2. Convolved peaks

It is not uncommon to have two peaks that overlap in a XPS spectrum. These peaks need to be deconvoluted to obtain accurate peak area values. As with the single peak analysis, choose the desired background type and create a range that encompasses the peaks to deconvolute. See Figure 13(a). Next insert two component peaks, as shown in Figure 13(b), which will be used to fit the designated peak area. To fit the peaks either click the “Fit Components” button, highlighted by the blue box in Figure 13(d) or manually fit by adjusting the peak components in the spectrum window. Figure 13(c) shows a set of deconvoluted peaks which have been fit using the “Fit Components” button. The corresponding areas are given in the “Quantification Parameter” window shown in Figure 13(d).

The convoluted peaks in Figure 13 also illustrate an example of a chemical shift as discussed in Section 3.3. This spectrum shows the O 1s region of a NaAu₂ sample. There are two peaks present, indicating oxygen species in different chemical environments. In Chapter 4, these peaks from higher to lower E_b were assigned to atomic oxygen interacting with an Au-Na site and atomic oxygen interacting only with a Na site, respectively. Recall that a higher E_b is indicative of an environment that is more electronegative. Electronegativity values for Au and Na are 2.54 and 0.93, respectively²⁷ and a larger value indicates a higher electronegativity. An Au-Na site should be more electronegative than a sole Na site, thus shifting the O 1s peak to a higher E_b , which is the case in Figure 13.

4.3. Atomic composition

XPS spectra are commonly used to determine the atomic composition of a sample. For this example, a sample of NaAu₂ acquired with a Mg K α is used. The peaks selected for

analysis are the Na 2s and Au 5p_{3/2}. These peaks were chosen due to their peak locations. They are only separated by 6 eV in the spectrum, giving them a similar IMFP value and thus a similar sampling depth. This provides a more accurate sample composition. Figure 14(a) shows a spectrum of the Na 2s and Au 5p_{3/2}. A Linear background type was used for this analysis. There is a third peak present to the left of the Na 2s peak which, after eliminating the possibility of a primary Au or Na peak, a “ghost” peak or a sample plate peak, must be a satellite peak. The primary Au 4f_{7/2} peak is positioned at 84.0 eV while the satellite peak is positioned at 66.5 eV. Subtracting the two gives the following:

$$\text{Primary peak} - \text{Satellite peak} = \Delta E_k$$

$$\text{Au } 4f_{7/2} \text{ peak} - \text{satellite peak} = 84.0 \text{ eV} - 66.5 \text{ eV} = 17.5 \text{ eV}$$

Using the Mg source columns in Table 1 (cf. Section 3.4.2), we see that our calculated ΔE_k of 17.5 eV correlates with the K α_5 satellite peak (typically a 17.4 eV difference). In order to obtain an accurate peak integration for Na 2s a deconvolution must be done. Figure 14(b) illustrates the deconvolution and integration of the K α_5 satellite and Na 2s peaks as well as the integration of the Au 5p_{3/2} peak. In order to get an accurate sample composition, the peaks must be normalized to the C 1s peak. Scofield cross-sections (δ) specific to each peak are applied by dividing the raw peak area by its respective δ . For this sample $\delta_{\text{Na } 2s} = 0.390$ and $\delta_{\text{Au } 5p_{3/2}} = 0.877$. Atomic composition is determined by summing the normalized peak areas and dividing each separate peak by the sum. The result is multiplied by 100% to obtain a percent value; see Equation 3.

$$\% \text{ Composition of Na} = \frac{\text{Norm. Na } 2s \text{ Area}}{(\text{Norm. Na } 2s \text{ Area} + \text{Norm. Au } 5p_{3/2} \text{ Area})} \times 100\% \quad (\text{Eqn. 3})$$

This analysis shows that the sample contains 37.0% Na and 63.0% Au. This is expected based on the formula of NaAu_2 with 1 Na (33.3%) for every 2 Au (66.7%).

5. Conclusions

The acquisition and analysis of XPS spectra can be complicated depending on both the X-ray source and the sample. X-ray sources produce Auger peaks in the spectrum which may overlap with XPS peaks. X-ray sources, specifically the twin anode source, also can produce unwanted satellite and “ghost” peaks in the spectrum. Accurate analysis depends on applying the correct Scofield cross-section and EAL to sample elements and identifying possible chemical shifts. The deconvolution of overlapping peaks is also pertinent to analysis especially regarding calculations of percent composition. If a user is aware of these complications before starting acquisition, the subsequent analysis can be made easier and more accurate.

Acknowledgements

The data shown as examples in this work was acquired in a collaboration between EMPA in Dübendorf, Switzerland, and Iowa State University in Ames, Iowa. Accordingly, this work was supported from two sources: the Swiss National Science Foundation (Contract 200021-129511), and the John D. Corbett Endowment of Iowa State University. We thank C.R. Brundle for many fruitful and informative discussions on XPS acquisition and spectrum analysis.

Figures

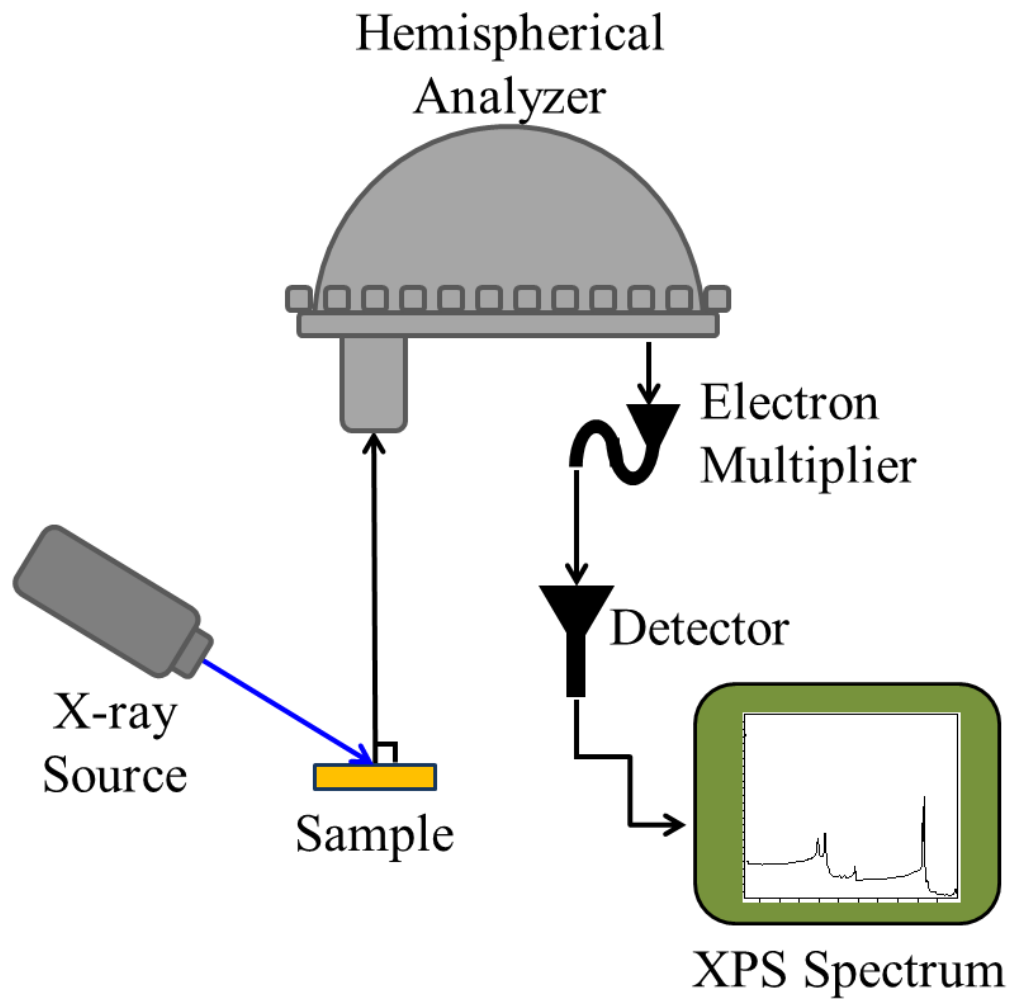


Figure 1. Schematic of a typical layout for an XPS setup. The schematic is not to scale.

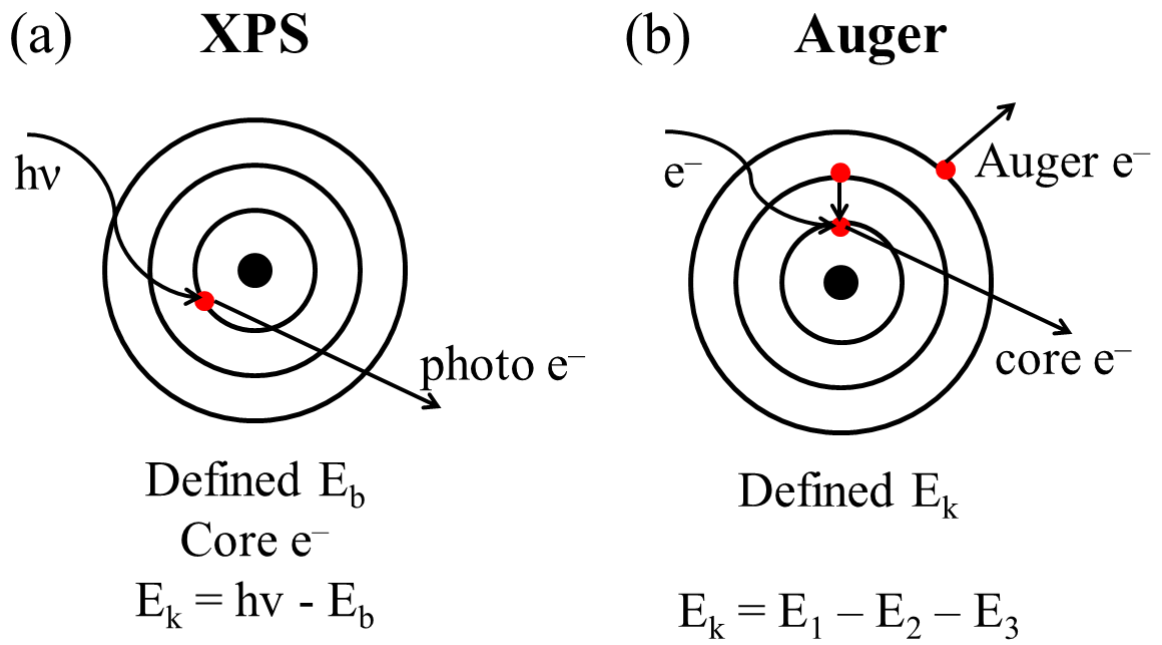


Figure 2. Schematic of processes which emit XPS photoelectrons and Auger electrons from atoms. (a) XPS. (b) Auger.

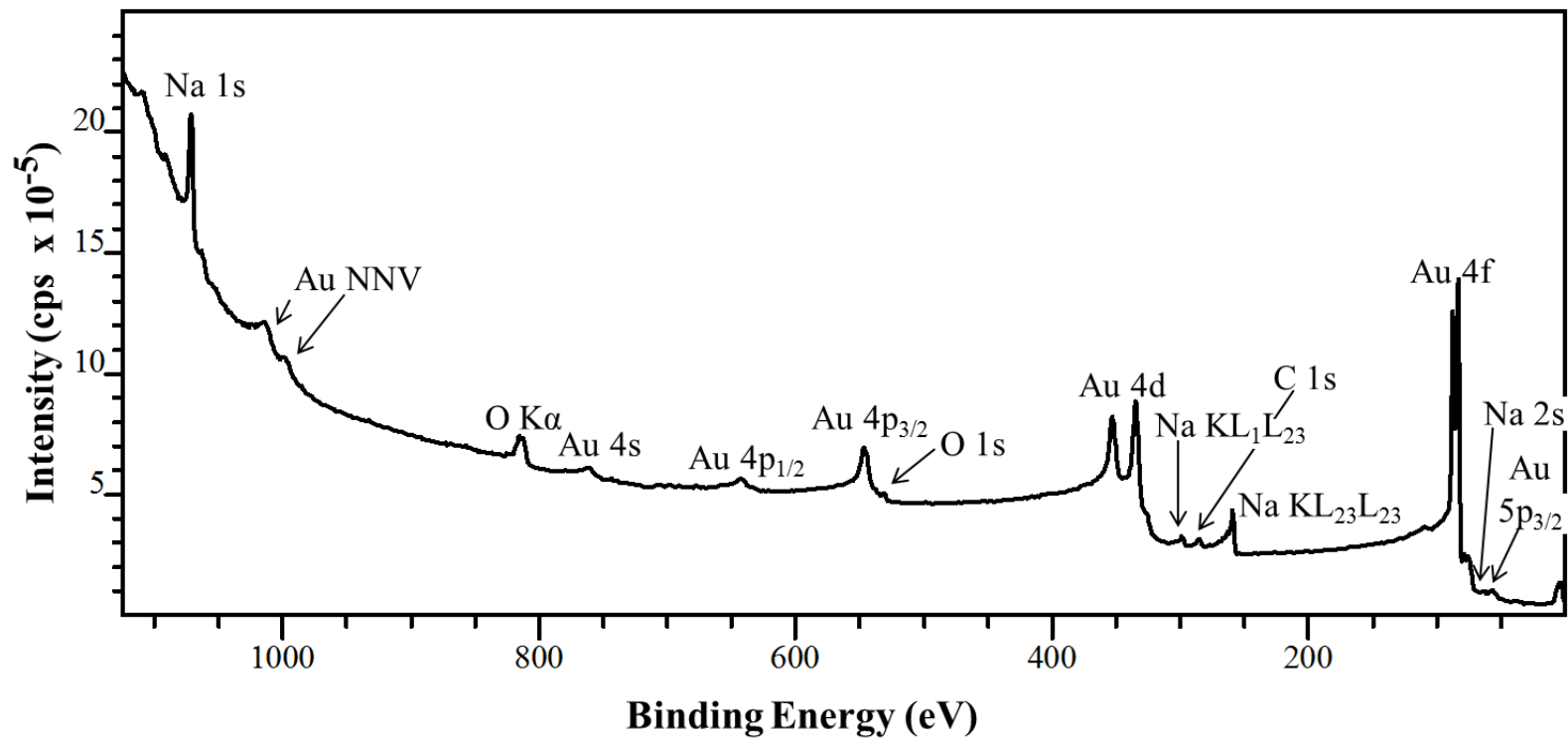


Figure 3. Example XPS spectrum of NaAu₂. The spectrum was acquired with a Mg K α source. The sample was taken with a take-off angle (TOA) of 60° with respect to the sample normal.

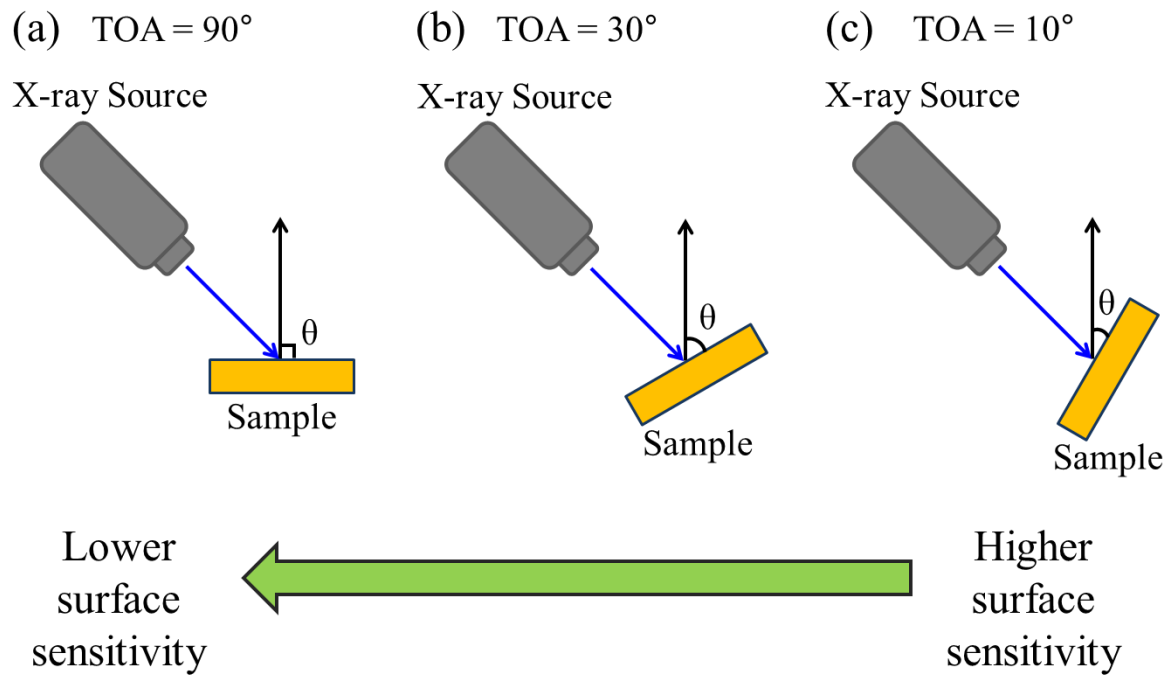


Figure 4. Schematic of surface sensitivity due to take-off angles (TOA). (a) TOA of 90°. (b) TOA of 30°. (c) TOA of 10°. Surface sensitivity increases with a decreasing TOA.

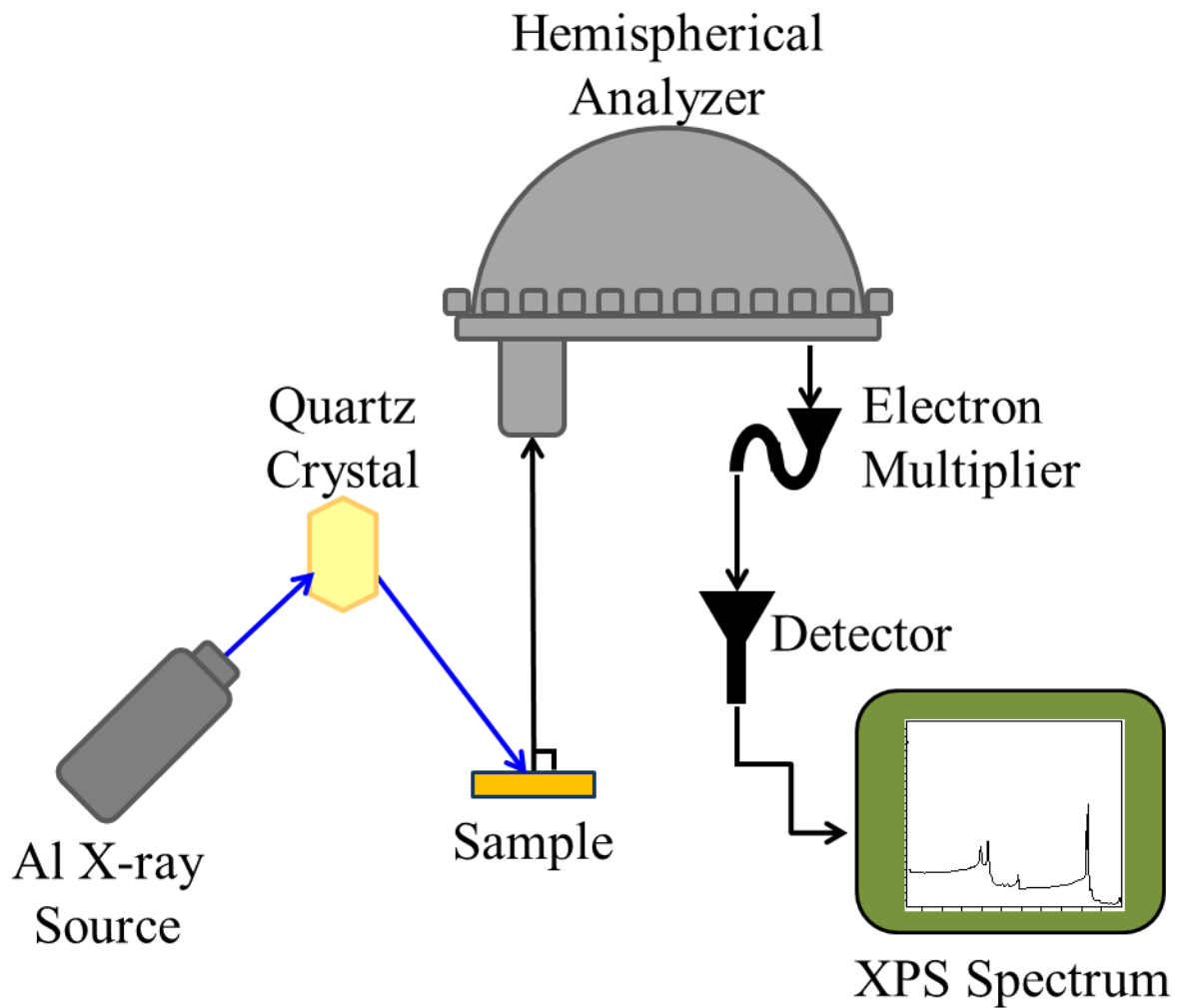


Figure 5. Schematic of a typical layout for an XPS setup with a monochromated Al source. The schematic is not to scale.

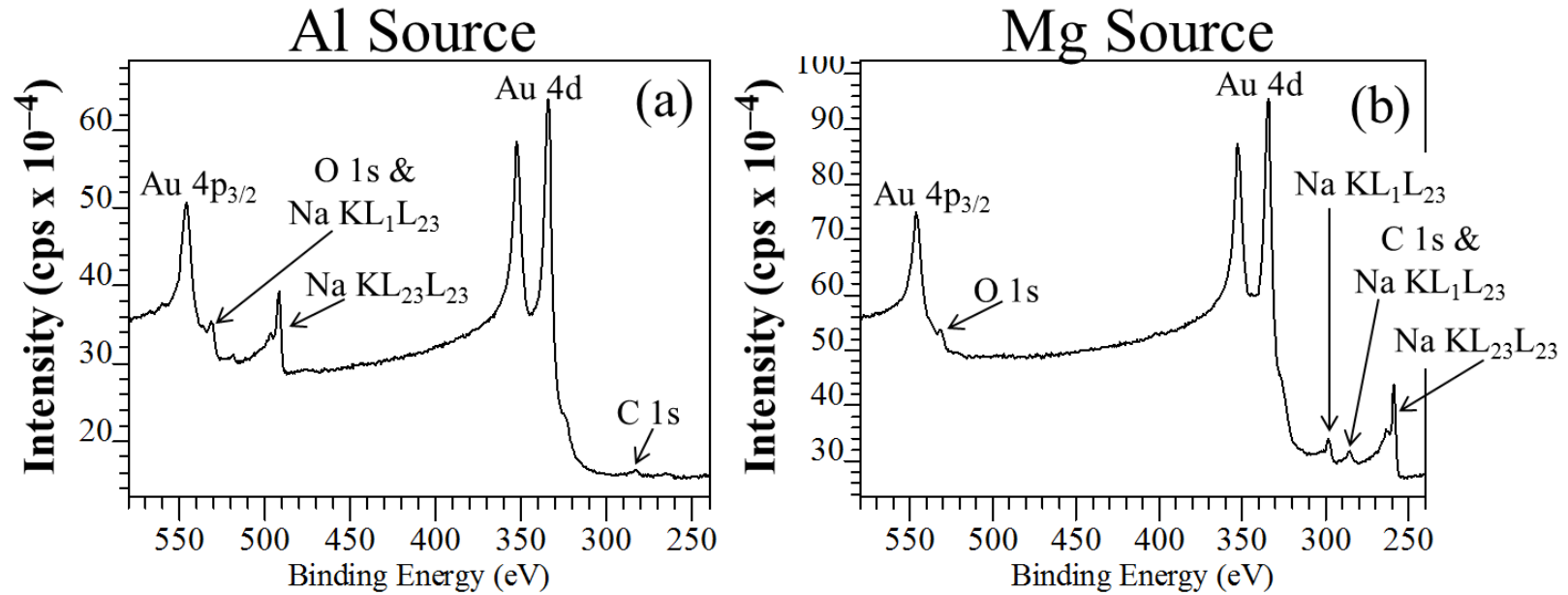


Figure 6. XPS spectra illustrating an Auger peak shift due to the X-ray source. (a) Al K α X-ray source; (b) Mg K α X-ray source; In panel (a) the Na KL₁L₂₃ Auger peak overlaps with the O 1s peak. In panel (b) the Na Auger peaks have shifted to a lower E_b and overlap with the C 1s peak.

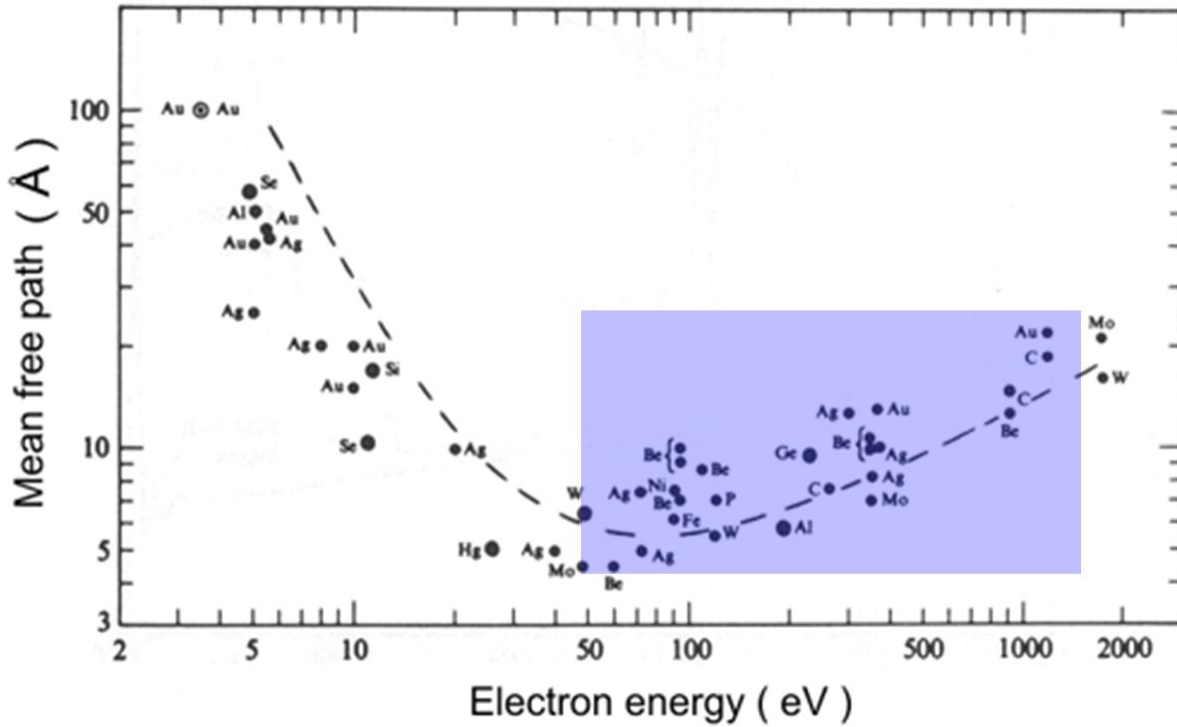


Figure 7. A plot of electron mean free path with respect to electron kinetic energy (eV). The blue box indicates the typical energy range for XPS analysis. Figure is reproduced from Reference [28].

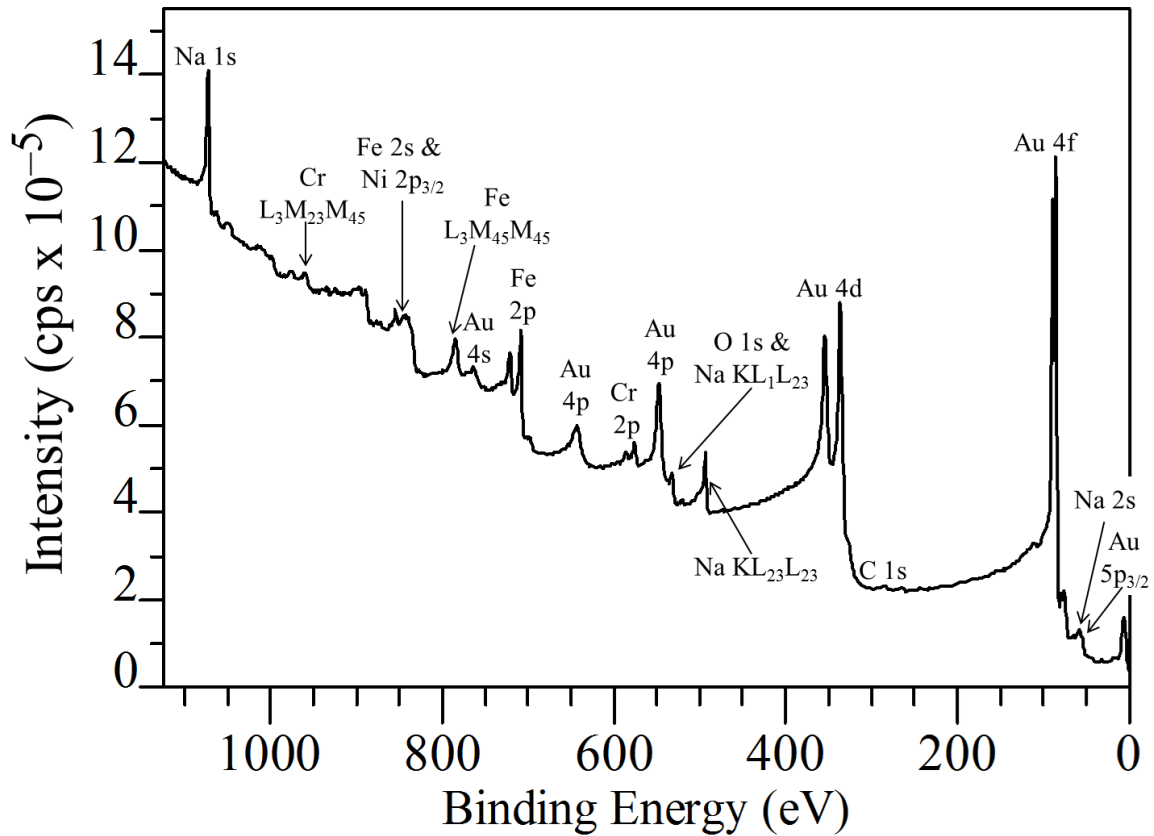


Figure 8. Example XPS spectrum of a NaAu_2 sample showing several sample plate peaks. The sample plate is composed of Fe, Ni and Cr. The spectrum was acquired with an Al K α source.

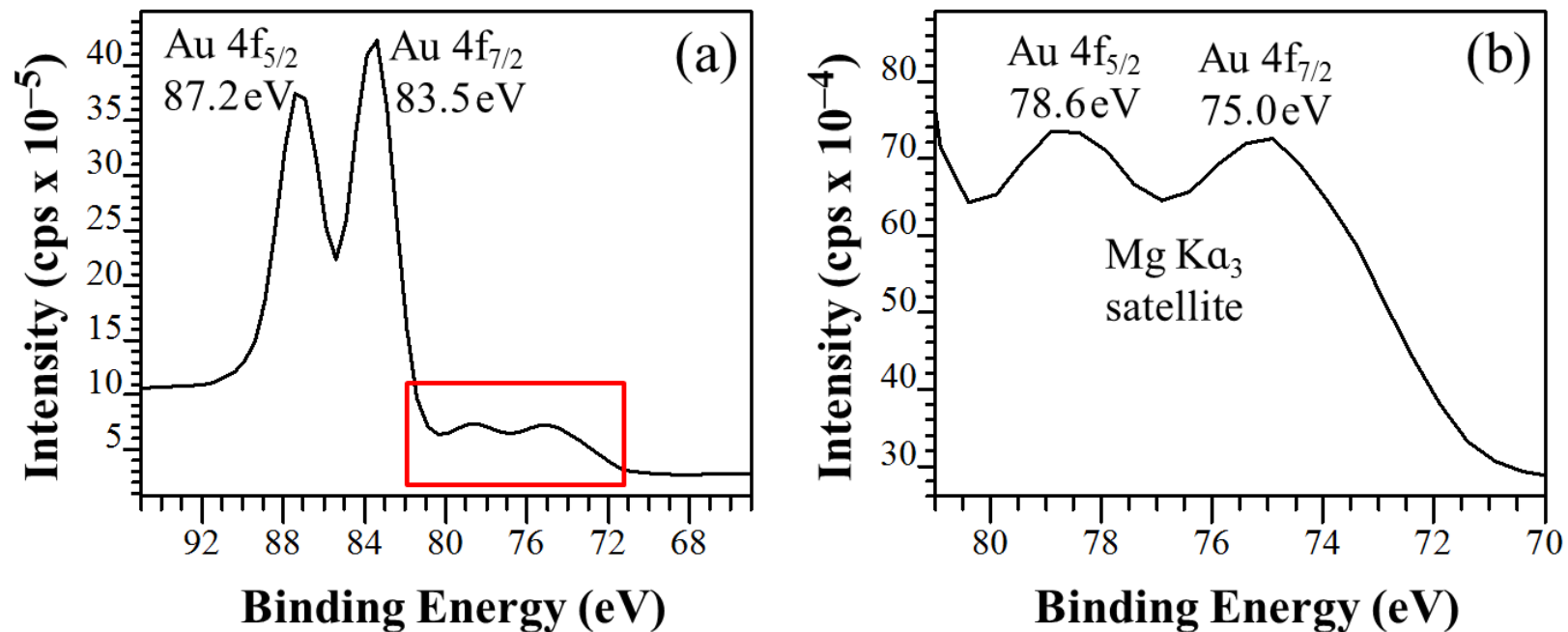


Figure 9. XPS spectra highlighting the presence of satellite peaks. The example peak is the Au 4f_{5/2} and Au 4f_{7/2} doublet. The spectrum was acquired with a Mg K α source. (a) Spectrum with Au 4f primary peak and satellite peak. (b) Satellite peak of Au 4f primary peak. The red box in (a) indicates the region in (b). The satellite peaks are shifted ~8.5 eV lower in E_b and are 7% of the primary peak area. This matches the energy shift for a K α_3 satellite peak listed in Table 1. Y-axis scale in is counts per second “cps”.

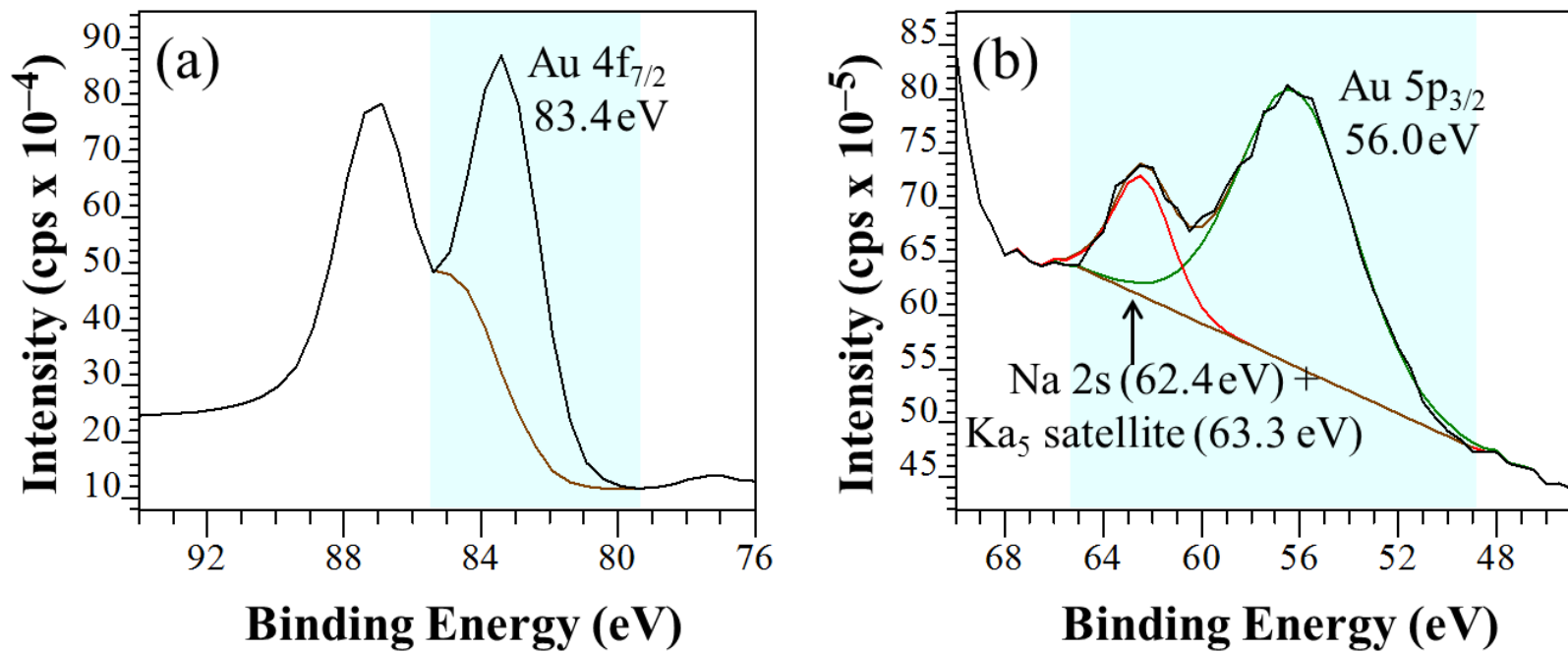


Figure 10. XPS spectra illustrating the process of calculating the intensity of and removing a convoluted satellite peak. The example is the Au 4f_{7/2} primary peak and Au 4f_{7/2} Ka₅. The spectrum was acquired with a Al Ka source. (a) Au 4f_{7/2} peak integrated area. (b) Na 2s peak overlapping with both the Au 4f_{7/2} Ka₅ satellite peak and Au 5p_{3/2} peak. Y-axis scale in is counts per second “cps”.

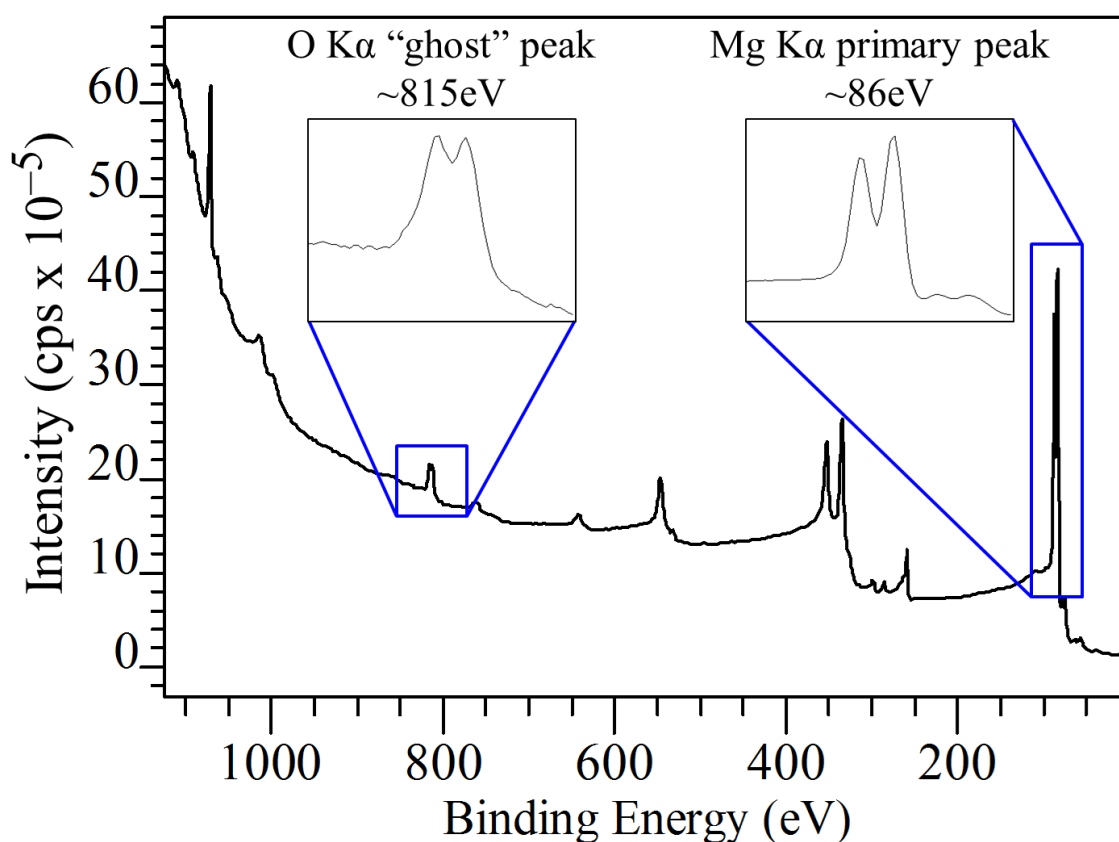


Figure 11. XPS overview spectrum highlighting the location of a “ghost” peak. In this case, the “ghost” peak occurs due to the oxidation of the Mg source. The highlighted peak is the Au 4f_{5/2} and Au 4f_{7/2} doublet. The spectrum was acquired with the Mg Kα source. The “ghost” peak is shifted ~729 eV higher in E_b which matches the energy shift for a O Kα peak listed in Table 2. The spectrum enlargements are over a 30 eV E_b range. Y-axis scale in is counts per second “cps”.

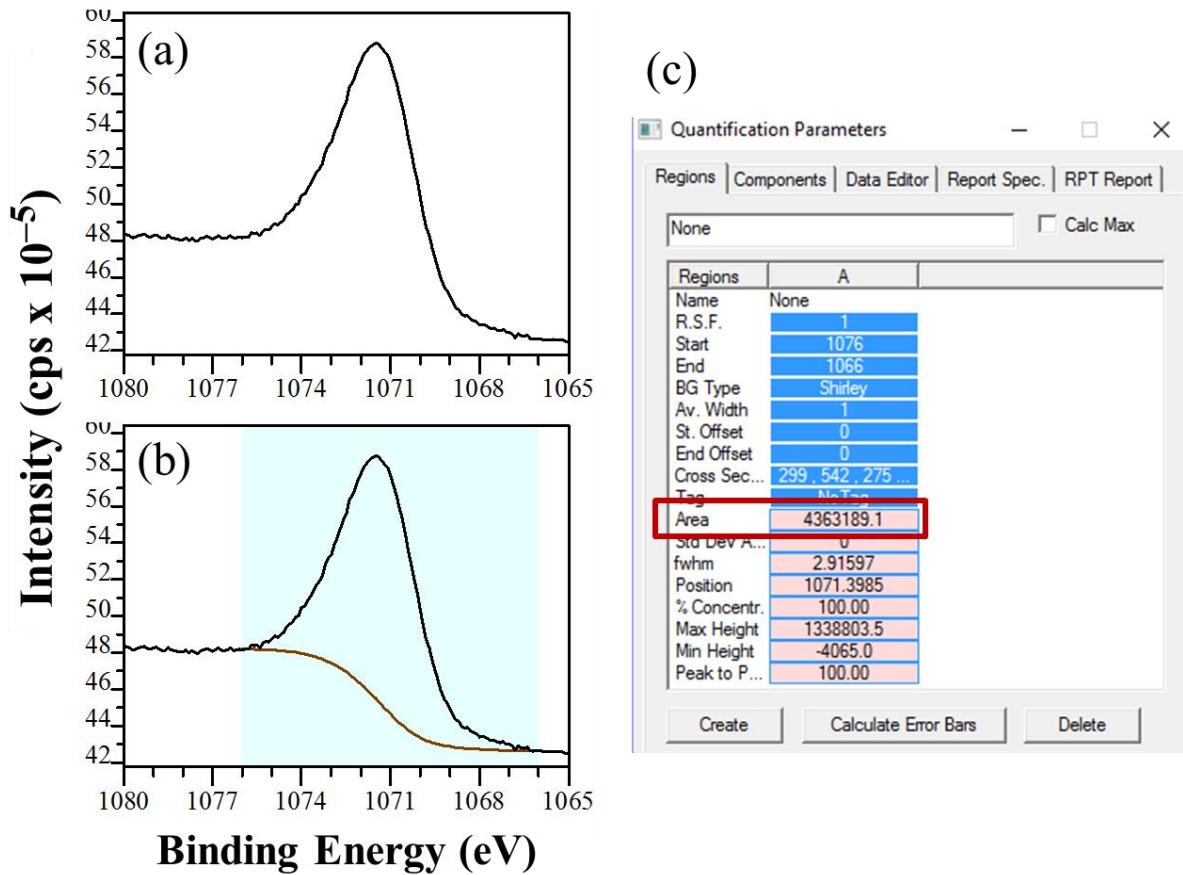


Figure 12. XPS spectra illustrating the process of determining the area under a peak. (a) Original XPS peak. (b) Integration range (denoted by blue box) for finding peak area. (c) CasaXPS “Quantification Parameters” window which gives the value for integrated area (highlighted by red box).

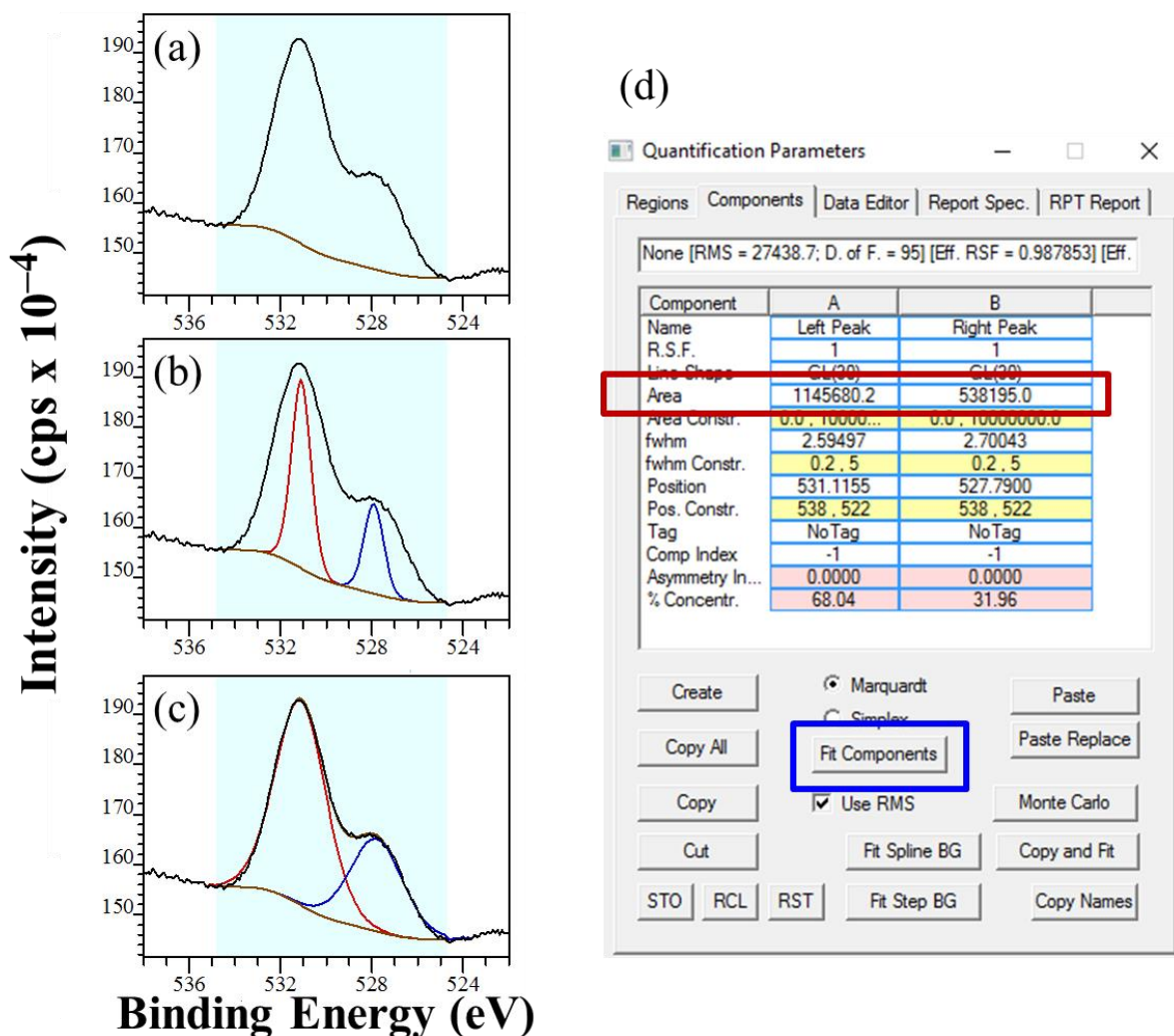
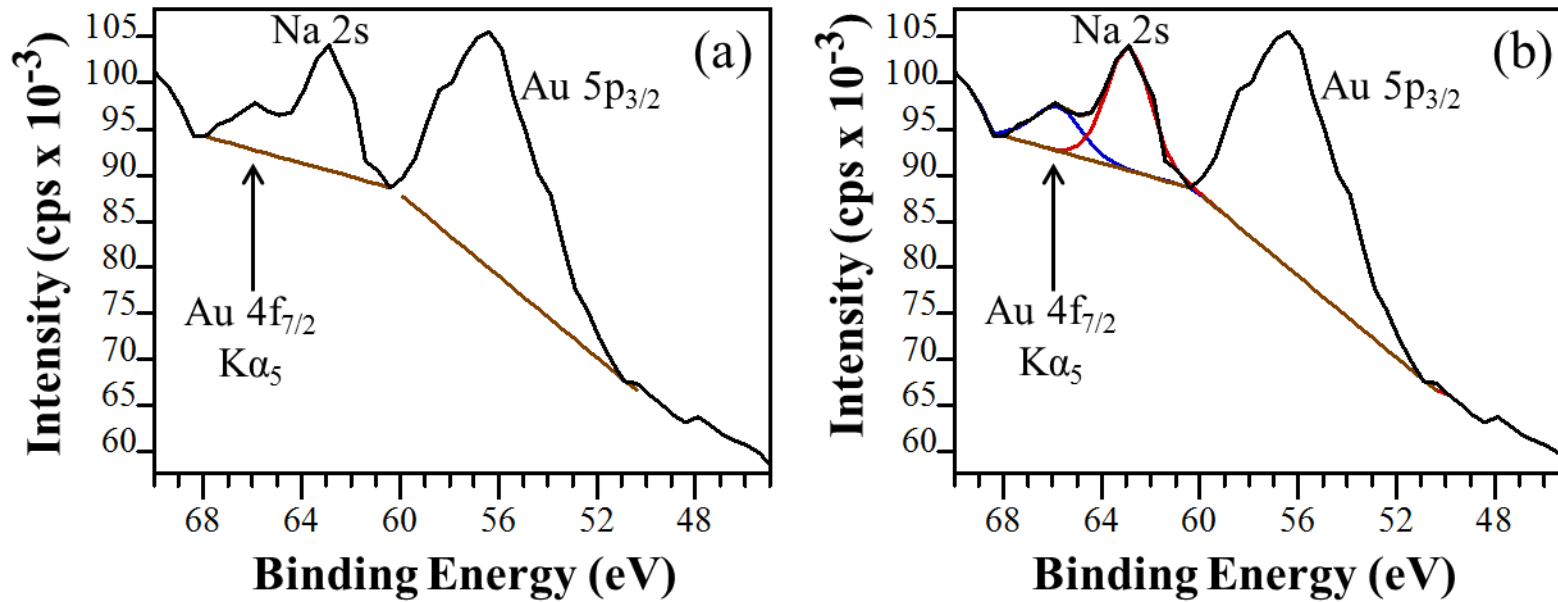


Figure 13. XPS spectra illustrating the process of deconvoluting two peaks. (a) Original convoluted XPS peak. (b) Component peaks that need to be fitted. (c) Fitted component peaks which deconvolute the overlapping peak into two separate peaks. (d) CasaXPS "Quantification Parameters" window which gives the values for the deconvoluted areas (highlighted by the red box).



(c)

	Raw Area	δ	Corrected Area	% Composition
Na 2s	30653	0.390	78597	37.0%
Au 5p _{3/2}	117693	0.877	134200	63.0%

Figure 14. XPS spectra illustrating a percent composition calculation. (a) Na 2s and Au 5p_{3/2} with additional satellite peak. (b) Deconvolution of satellite peak and Na 2s. (c) Table with representative area numbers for percent composition.

References

- ¹K. Siegbahn and K. Edvarson, " β -Ray spectroscopy in the precision range of 1:105," *Nuclear Physics* **1**, 137 (1956).
- ²K. Siegbahn, in *Nobel Lecture*, University of Uppsala, Sweden (1981).
- ³A. Jablonski and C. J. Powell, "The electron attenuation length revisited," *Surface Science Reports* **47**, 33 (2002).
- ⁴*Surface Analysis Methods in Materials Science*, 2 ed. (Springer-Verlag, Berlin, 2003), Springer Series in Surface Sciences, 23.
- ⁵J. Cazes, *Analytical Instrumentation Handbook, Third Edition*, (CRC Press, 2004).
- ⁶J. H. Scofield, "Hartree-Slater subshell photoionization cross-sections at 1254 and 1487 eV," *Journal of Electron Spectroscopy and Related Phenomena* **8**, 129 (1976).
- ⁷CasaXPS: Processing Software for XPS, AES, SIMS and More; www.CasaXPS.com, (October 19, 2014).
- ⁸C. J. Powell and A. Jablonski, "Evaluation of Calculated and Measured Electron Inelastic Mean Free Paths Near Solid Surfaces," *Journal of Physical and Chemical Reference Data* **28**, 19 (1999).
- ⁹C. J. Powell and A. Jablonski, *NIST Electron Inelastic-Mean-Free-Path Database - Version 1.2*, (National Institute of Standards and Technology, Gaithersburg, MD, 2010).
- ¹⁰C. J. Powell and A. Jablonski, *NIST Electron Effective-Absorption-Length Database - Version 1.3*, (National Institute of Standards and Technology, Gaithersburg, MD, 2011).
- ¹¹J. F. Moulder, W. F. Stickle, P. E. Sobol and K. D. Bomben, *Handbook of X-ray Photoelectron Spectroscopy: a reference book of standard spectra for identification and interpretation of XPS data*, (Perkin-Elmer Corporation, Physical Electronics Division, Eden Prairie, Minnesota, 1992).
- ¹²S. Peters, S. Peredkov, M. Neeb, W. Eberhardt and M. Al-Hada, "Size-dependent XPS spectra of small supported Au-clusters," *Surface Science* **608**, 129 (2013).
- ¹³D. Q. Yang and E. Sacher, "Initial- and final-state effects on metal cluster/substrate interactions, as determined by XPS: copper clusters on Dow Cyclotene and highly oriented pyrolytic graphite," *Applied Surface Science* **195**, 187 (2002).
- ¹⁴J. Morales, J. P. Espinos, A. Caballero, A. R. Gonzalez-Elipse and J. A. Mejias, "XPS Study of Interface and Ligand Effects in Supported Cu₂O and CuO Nanometric Particles," *The Journal of Physical Chemistry B* **109**, 7758 (2005).

- ¹⁵I. Preda, A. Gutiérrez, M. Abbate, F. Yubero, J. Méndez, L. Alvarez and L. Soriano, "Interface effects in the Ni 2*p* X-ray photoelectron spectra of NiO thin films grown on oxide substrates," *Physical Review B* **77**, 075411 (2008).
- ¹⁶J. P. Espinós, J. Morales, A. Barranco, A. Caballero, J. P. Holgado and A. R. González-Elipe, "Interface Effects for Cu, CuO, and Cu₂O Deposited on SiO₂ and ZrO₂. XPS Determination of the Valence State of Copper in Cu/SiO₂ and Cu/ZrO₂ Catalysts," *The Journal of Physical Chemistry B* **106**, 6921 (2002).
- ¹⁷C. Klauber, "Refinement of magnesium and aluminium K α X-ray source functions," *Surface and Interface Analysis* **20**, 703 (1993).
- ¹⁸T. Carlson, *Photoelectron and Auger Spectroscopy*, 1st ed. (Springer US, 1975), Modern Analytical Chemistry.
- ¹⁹J. A. Bearden, "X-Ray Wavelengths," *Reviews of Modern Physics* **39**, 78 (1967).
- ²⁰NIST X-ray Photoelectron Spectroscopy Database, Version 4.1 (National Institute of Standards and Technology, Gaithersburg, 2012); <http://srdata.nist.gov/xps/>
- ²¹XPS and AES Database (ThermoFisher Scientific: Thermo Electron France, 2016); <http://www.lasurface.com/accueil/index.php>
- ²²D. A. Shirley, "High-Resolution X-Ray Photoemission Spectrum of the Valence Bands of Gold," *Physical Review B* **5**, 4709 (1972).
- ²³A. Proctor and P. M. A. Sherwood, "Data analysis techniques in X-ray photoelectron spectroscopy," *Analytical Chemistry* **54**, 13 (1982).
- ²⁴S. Tougaard, "Practical algorithm for background subtraction," *Surface Science* **216**, 343 (1989).
- ²⁵M. Repoux, "Comparison of background removal methods for XPS," *Surface and Interface Analysis* **18**, 567 (1992).
- ²⁶T. Heizo, I. Naganori, N. Katsumi, K. Satoru and T. Takuei, "The Comparison of the Background Removal Methods in XPS Spectra," *Japanese Journal of Applied Physics* **29**, 2512 (1990).
- ²⁷*CRC Handbook of Chemistry and Physics*, 95th ed. (CRC Press, 2014).
- ²⁸How to investigate solid surface?;
http://users.uj.edu.pl/~ufpostaw/2_Pracownia/D1/jak_badac_powierzchnie_eng.htm
February 16, 2016.

APPENDIX A

ADSORPTION OF AU AND PT ON THE GRAPHITE (0001) SURFACE

The clean graphite surface was prepared by cleaving the sample using Scotch tape in air, followed by transfer into the UHV chamber where all experiments took place. Samples were heated in the manipulator, equipped with a pyrolytic boron nitride (PBN) heater, to 500 K for 60 minutes in UHV to remove contaminants and then transferred to the scanning tunneling microscopy (STM) stage for subsequent metal deposition and STM imaging. Samples were transferred from the STM stage to the manipulator for all anneals after deposition.

1. Au on Graphite

There have been numerous previous studies of Au deposited on graphite.¹⁻⁷ Wayman and co-workers conducted one of the first in-depth studies with Au deposition on graphite at room temperature, at lower sample temperatures and at elevated sample temperatures. Their results show that at and below room temperatures, deposition produces dendritic Au islands on the surface while above room temperature, it produces polygonal shapes, most commonly triangles and hexagons.¹ Several other researchers confirm a dendritic island shape at room temperature,^{3,5,6} and polygonal shapes (triangles and hexagons) at elevated temperature.^{2,4} Additionally, Ganz and co-workers reported that at room temperature, Au nucleates as small two-dimensional (2D) islands which precede the growth of three-dimensional (3D) clusters.^{7,8} An in-depth review of transition metals on the graphite (0001) surface gives additional information about Au on graphite.⁹ In the present research, experiments were

conducted to study island morphology after a room temperature deposition followed by sample annealing to above room temperature, detailed below.

We studied the adsorption of Au on the graphite (0001) surface at room temperature and after annealing to temperatures of 400 K to 900 K, in 100 K increments. We also conducted a 950 K anneal. Each anneal was for 15 minutes. Au was deposited via physical vapor deposition from a Mantis QUAD-EV-C Mini e-beam evaporator. All surfaces undergo ion damage from the e- beam evaporator, as previously discussed in Chapter 2, Appendix 2. STM tunneling parameters were in the range of 0.7 V to 1.0 V or -0.2 V to -1.1 V tip bias and 0.15 nA to 0.20 nA tunneling current.

Au tends to form triangular islands which cluster together, which has been reported previously.⁴⁻⁶ Figure A1 illustrates our Au coverage of 7.3 ML. Large triangular islands are distributed across the terraces. Smaller triangular islands are found on top of the large islands, on the terrace itself and preferentially at step edges. Gray arrows in Figure A1(c) indicate a step edge, with others visible in the other images. Base island heights range from 4 nm to 5 nm with growth on top of the islands having total heights from 7 nm to 15 nm above the graphite base. Triangle widths, measured triangle edge to opposing vertex, range from 30 nm to 80 nm with an average island width of 60 nm.

Annealing the graphite after Au deposition causes the Au to desorb or migrate to the step edges. Figure A2 shows how the Au islands change over the course of incremental annealing. The island shape morphology changes, shifting from triangular to hexagonal after the first anneal at 400 K. Figure A3 illustrates this morphology change.

2. Pt on Graphite

There have been several previous studies of Pt deposition on graphite.¹⁰⁻¹³ Howells and co-workers report that on a pristine graphite surface, deposited Pt forms dendritic islands. On Ar⁺ ion-damaged graphite surfaces, deposited Pt forms small, flat, circular clusters.¹⁰ Additional reports state that Pt forms small 2D islands and then 3D clusters with increasing coverage.^{11,12} An in-depth review of transition metals on the graphite (0001), noted above for Au on graphite, also gives additional information for Pt on graphite.⁹ As part of the present thesis research, experiments were conducted to study island morphology after a room temperature deposition followed by sample annealing above room temperature, detailed below.

We studied the adsorption of Pt on the graphite (0001) surface at room temperature and after annealing to temperatures of 400 K to 1300 K, in 100 K increments. Pt was deposited via physical vapor deposition from an Omicron EFM3 evaporator, using a pyrolytic boron nitride (PBN) lined crucible. The crucible was biased at +780 V with respect to the filament located above the crucible. All surfaces undergo ion damage from the evaporator, similar to that produced by the Mantis QUAD e-beam evaporator. STM tunneling parameters were in the range of -0.3 V to -0.5 V tip bias and 0.2 nA to 0.3 nA tunneling current.

Pt tends to form very small circular islands with an average height of $0.19 \text{ nm} \pm 0.02 \text{ nm}$ (~1 atom). The islands are distributed across the terraces and show no preferential growth on step edges. The average diameter of these islands is $5.9 \text{ nm} \pm 0.3 \text{ nm}$. Figure A4 illustrates these small circular islands. The average island density and coverage for a 20 minute, 64 W deposition are $(1.50 \pm 0.07) \times 10^{-3} \text{ islands/nm}^2$ and $0.041 \text{ ML} \pm 0.002 \text{ ML}$, respectively.

Figure A5 illustrates these values. The average island density and coverage for a 20 minute, 75 W deposition are $(2.0 \pm 0.5) \times 10^{-3}$ islands/nm² and $0.055 \text{ ML} \pm 0.008 \text{ ML}$, respectively. Figure A6 illustrates these values. For coverage estimates, we calculated the average island area using $A = \pi r^2$ and the average island diameter. This area was multiplied by the number of islands in an image to get an estimate of total island area. This total island area was then divided by the image area for an estimated coverage. We assumed for coverage calculations that the islands were one atomic layer tall.

Annealing the graphite after Pt deposition causes the Pt to possibly desorb or intercalate into the graphite. Figures A7 and A8 show the evolution of Pt islands on graphite after incremental annealing. The island density decreases by about half after the first anneal (400 K) and is steady at 1.0×10^{-3} islands/nm² following the other higher temperature anneals. There is no mass migration to the step edges, as illustrated in Figure A9. The island morphology remains circular and the heights and diameters are slightly smaller ($<0.02 \text{ nm}$ and $<0.3 \text{ nm}$, respectively) than Pt islands deposited at room temperature. The Pt is most likely desorbing or intercalation to account for the decrease in island density. The Pt islands are similar to what Howells and co-workers reported after deposition on an Ar⁺ ion-damaged graphite surface.¹⁰ This suggests the islands are nucleating at ion-damage defects on the surface. A new feature, a slight circular depression in the surface, appears after annealing to 900 K and higher. Figure A10 shows these depressions. The average depth of these depressions is $0.018 \text{ nm} \pm 0.004 \text{ nm}$, while the average diameter is $6.9 \text{ nm} \pm 0.5 \text{ nm}$. Some of the depressions have what appears to be a Pt island in the center. We have not determined the source of these depressions but speculate they are intercalated Pt atoms.

Figures

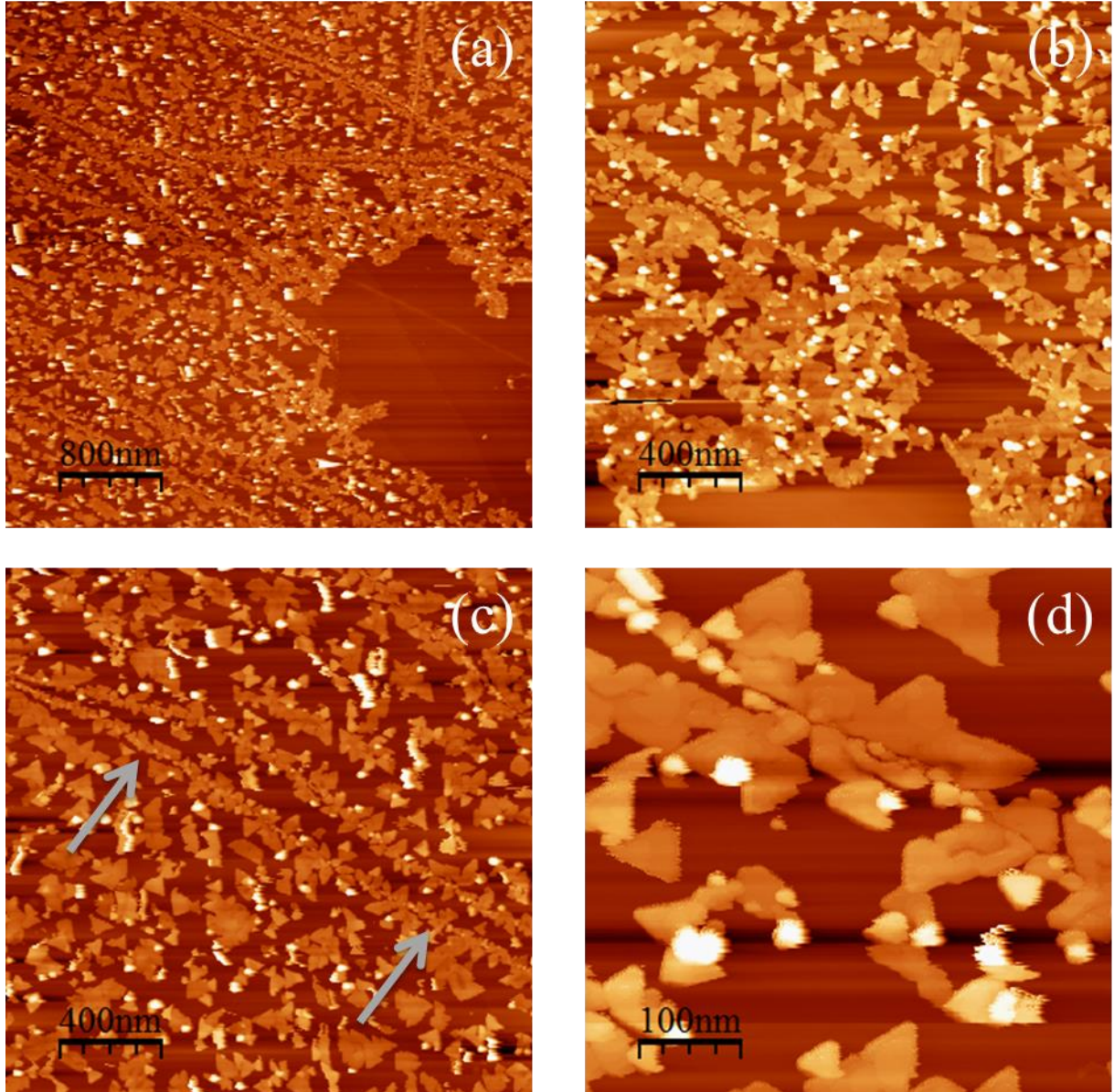


Figure A1. Au on graphite with a coverage of 7.3 ML. Islands are predominately triangular in shape and cover both terraces and step edges. Gray arrows in (c) indicate a step edge. (a) $4 \mu\text{m} \times 4 \mu\text{m}$ (b)-(c) $2 \mu\text{m} \times 2 \mu\text{m}$ (d) $500 \text{ nm} \times 500 \text{ nm}$.

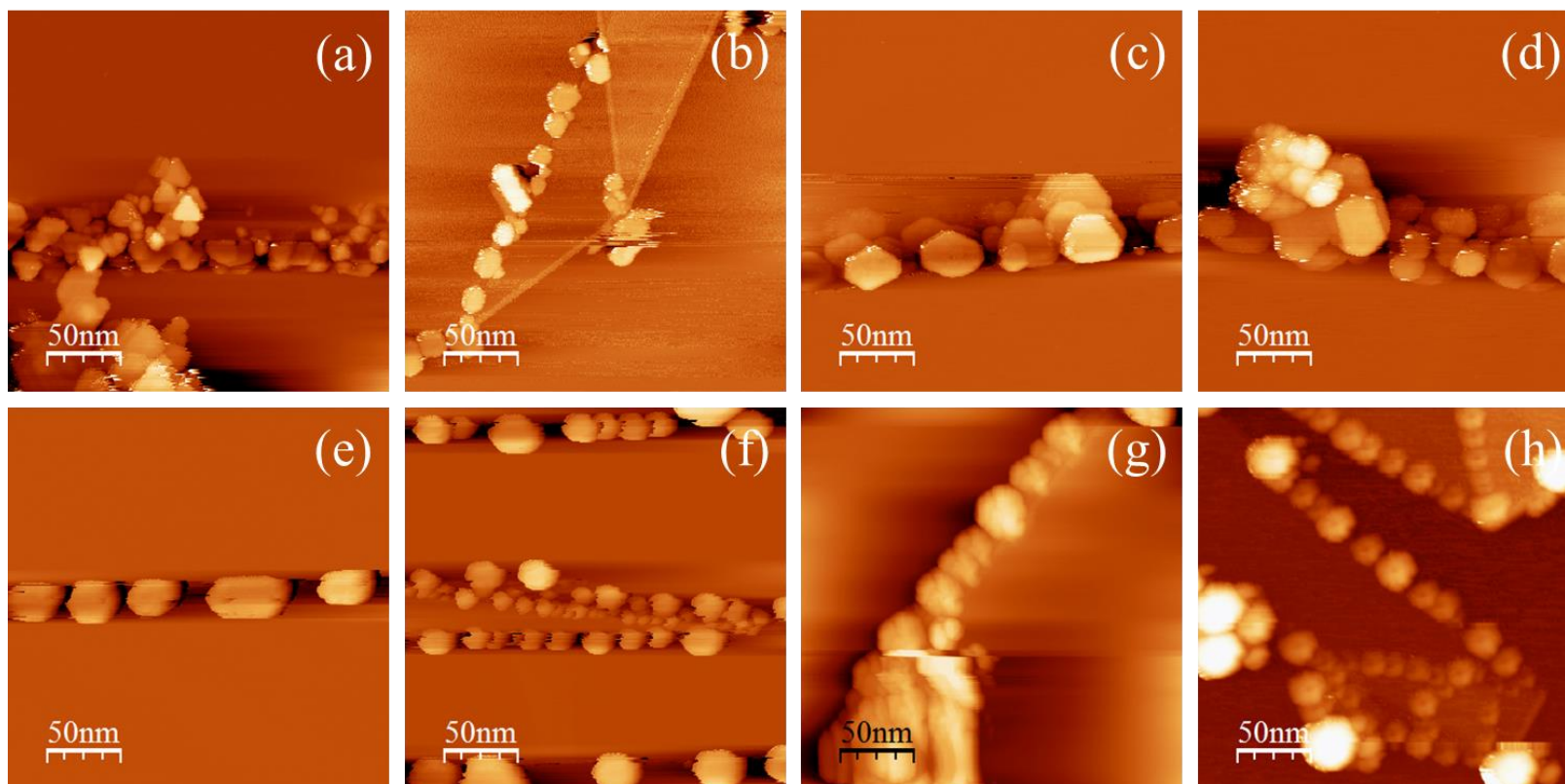


Figure A2. STM images of Au on graphite (0001) surface following seven incremental anneals ranging from 400 K to 900 K, in 100 K increments and a 950 K anneal. The triangular morphology changes to hexagonal after the first anneal at 400 K and the Au migrates to the step edges. (a) 300 K; (b) 400 K; (c) 500 K; (d) 600 K; (e) 700 K; (f) 800 K; (g) 900 K; (h) 950 K. All images 250 nm x 250 nm.

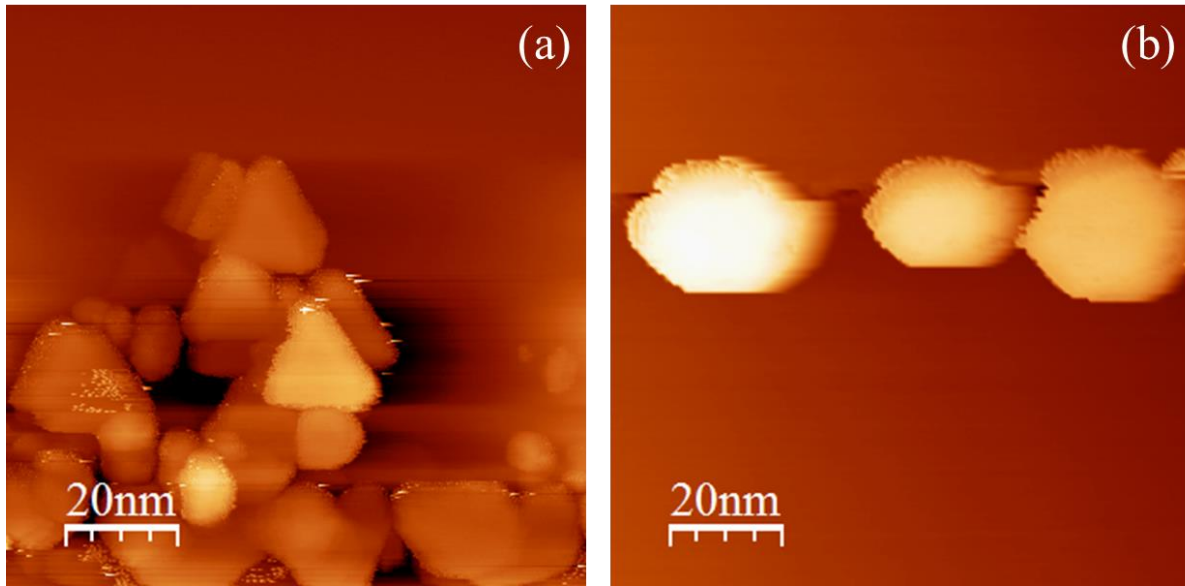


Figure A3. STM images of Au on graphite illustrating the island morphology shift from triangles to hexagons. (a) Triangles are present after a 3 minute, 26 W room temperature deposition. (b) Hexagons are present after annealing to 800 K for 15 minutes. Both images 100 nm x 100 nm.

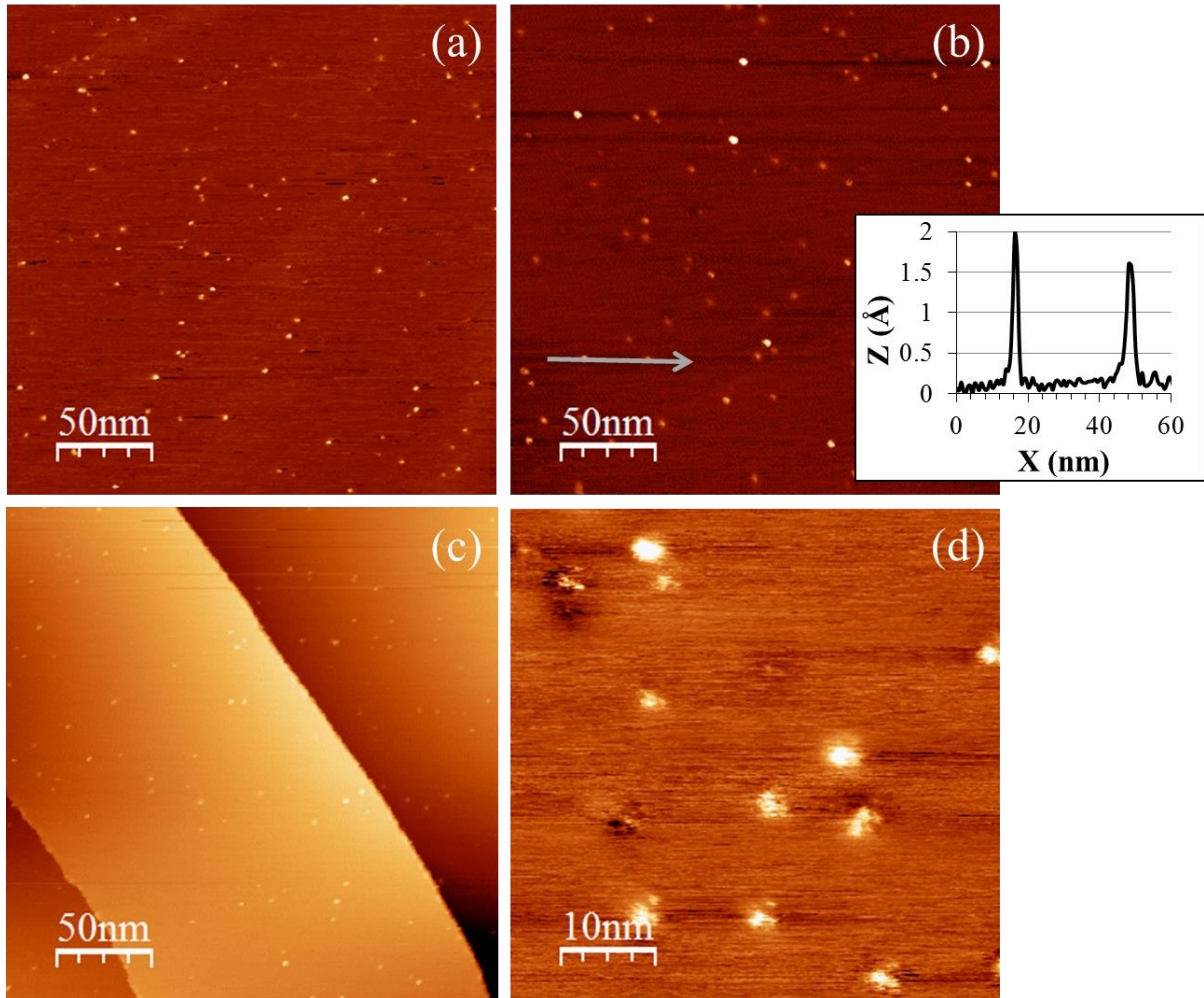


Figure A4. STM images of Pt on graphite deposited at room temperature illustrating the small circular islands and small amount of Pt at the step edges. (a)-(c) 64 W for 20 minutes. (d) 75 W for 20 minutes. The line profile offset in (b) shows two islands on the surface. Images (a)-(c) 250 nm x 250 nm. Image (d) 50 nm x 50 nm.

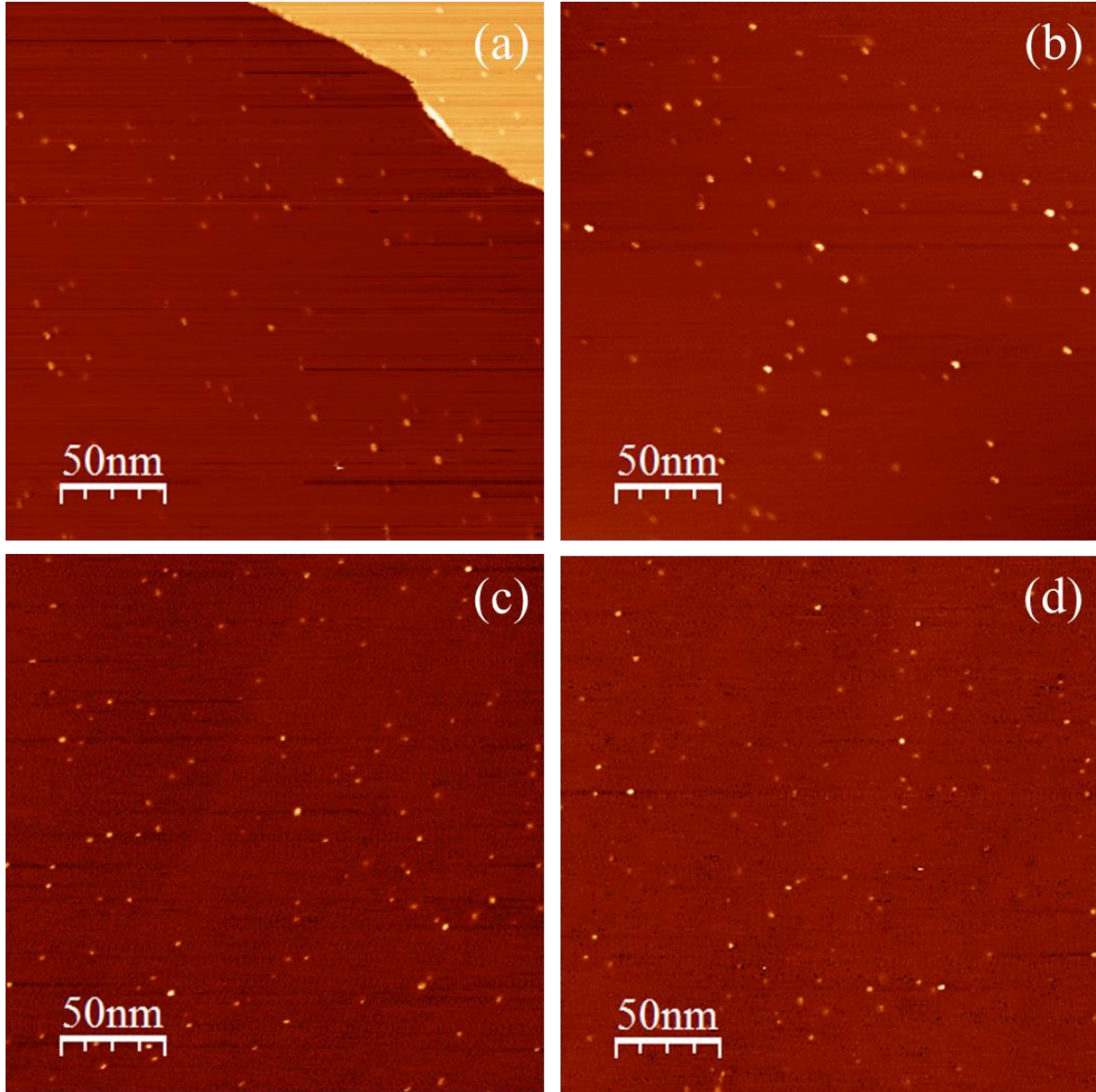


Figure A5. STM images of Pt on graphite deposited at room temperature, 64 W for 20 minutes. Average island density is 1.5×10^{-3} islands/nm² and average coverage is 0.041 ML. All images 250 nm x 250 nm.

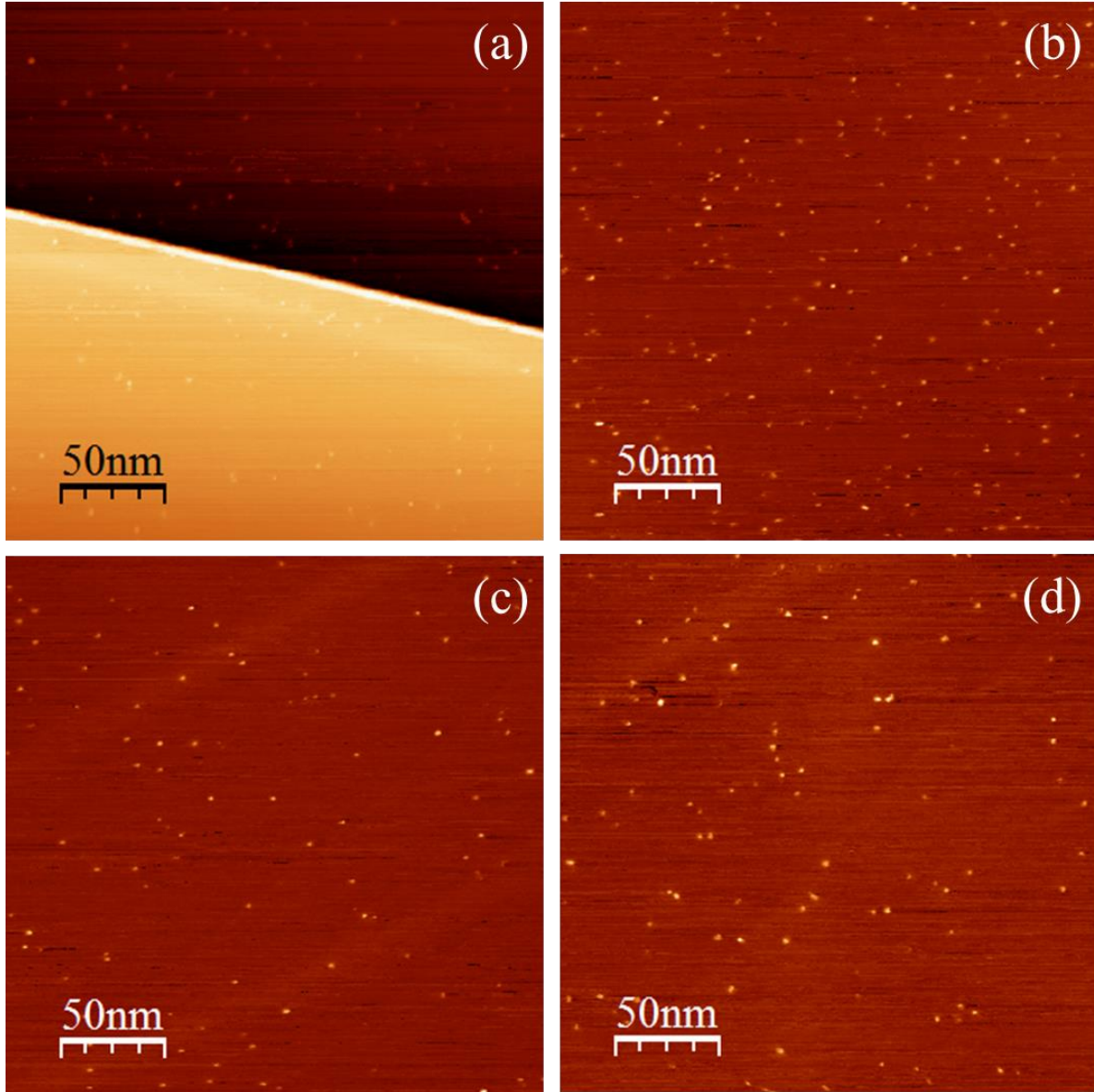


Figure A6. STM images of Pt on graphite deposited at room temperature, 75 W for 20 minutes. Average island density is 2.0×10^{-3} islands/nm² and average coverage is 0.055 ML. All images 250 nm x 250 nm.

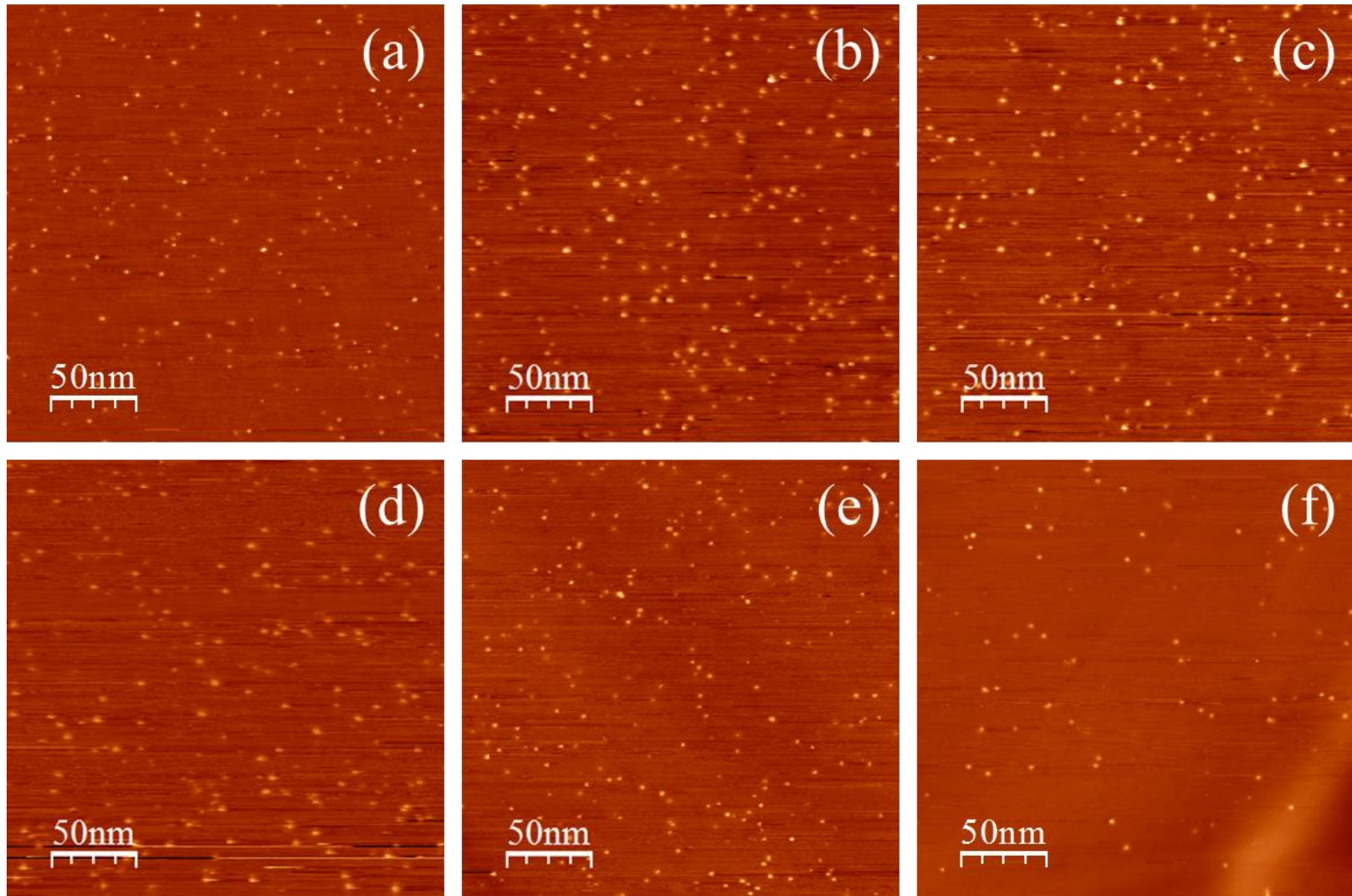


Figure A7. Pt on HOPG room temperature deposition followed by incremental anneals of 400 K to 1300 K, in 100 K increments (a) 300 K; (b) 400 K; (c) 500 K; (d) 600 K; (e) 700 K; (f) 800 K. All images 250 nm x 250 nm.

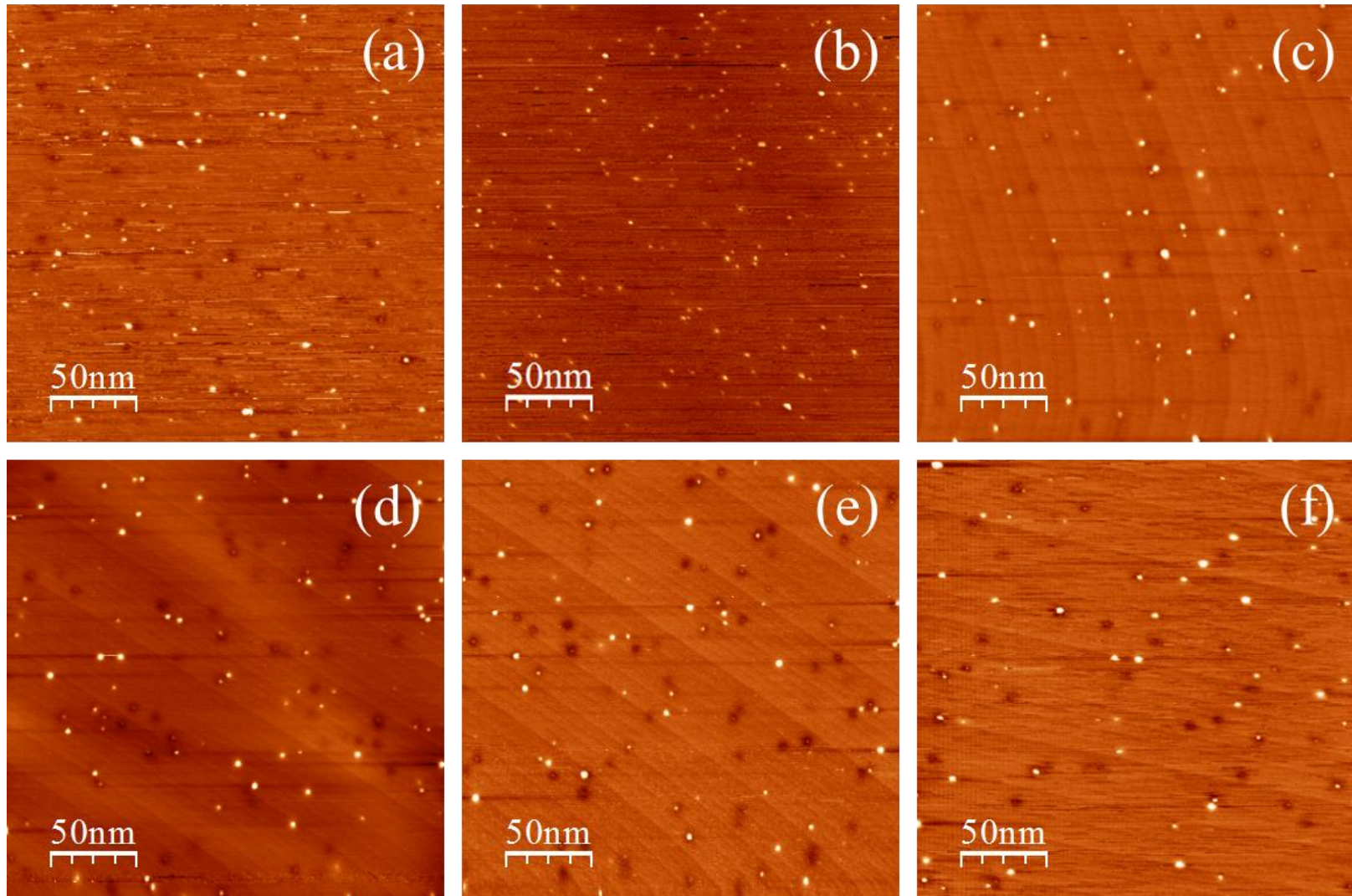


Figure A8. Pt on HOPG room temperature deposition followed by incremental anneals of 400 K to 1300 K, in 100 K increments (a) 900 K; (b) 950 K; (c) 1000 K; (d) 1100 K; (e) 1200 K; (f) 1300 K. All images 250 nm x 250 nm.

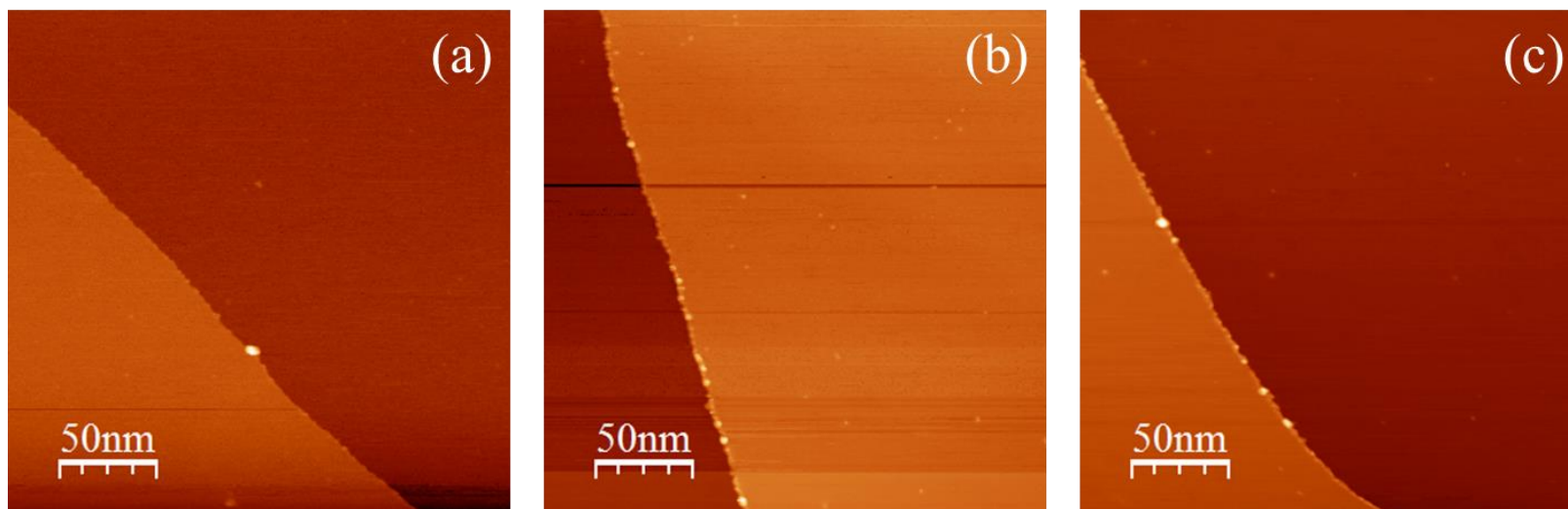


Figure A9. STM images of Pt on graphite at step edges after higher temperature anneals (>900 K). (a) 950 K. (b) 1000 K. (c) 1100 K. (d) 1300 K. All images 250 nm x 250 nm.

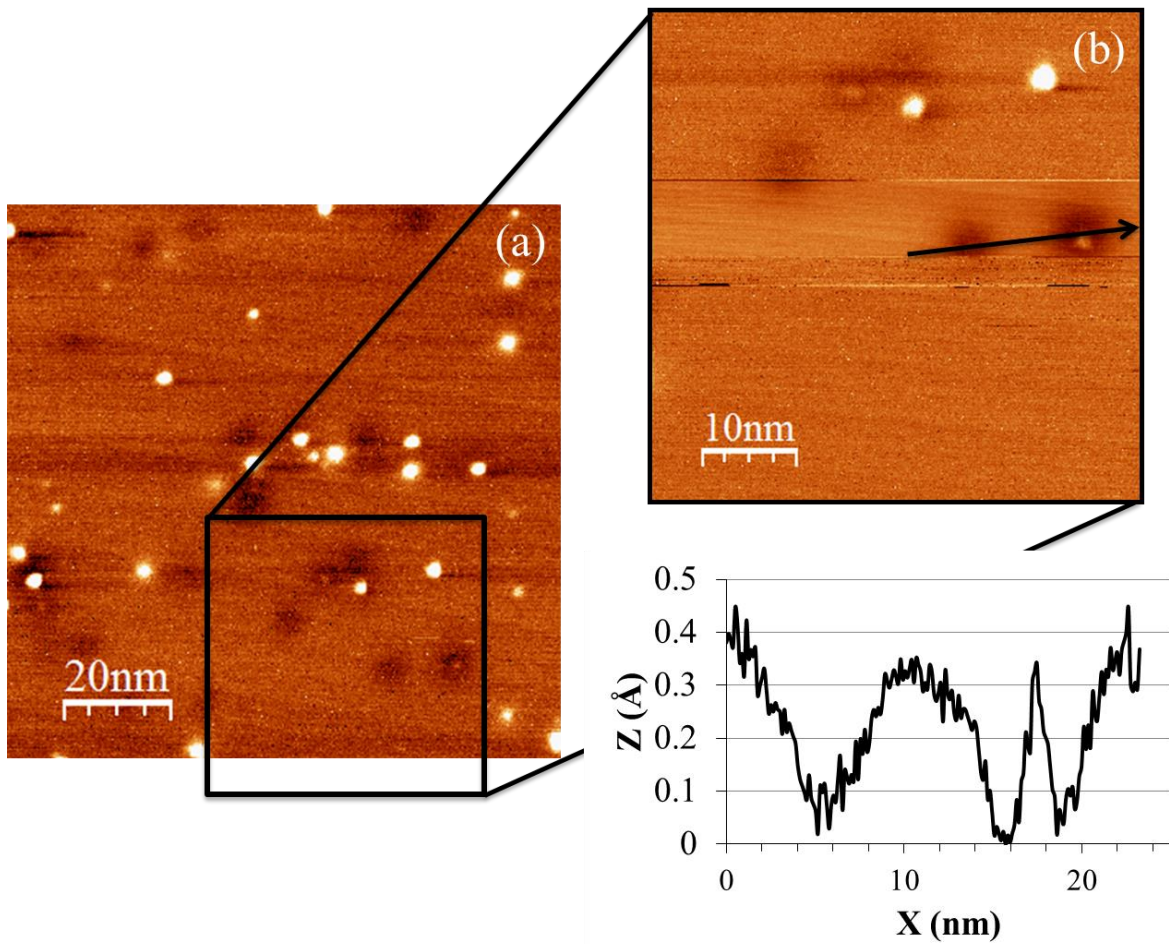


Figure A10. STM images of the depressions seen on the surface after high temperature annealing. (a) 100 nm x 100 nm. (b) 50 nm x 50 nm.

References

- ¹C. M. Wayman and T. P. Darby, "Nucleation and growth of gold films on graphite: II. The effect of substrate temperature," *Journal of Crystal Growth* **28**, 53 (1975).
- ²E. L. Evans, O. P. Bahl and J. M. Thomas, "The decoration of, and epitaxial growth of gold on, graphite surfaces," *Carbon* **5**, 587 (1967).
- ³R. Anton and I. Schneidereit, "In situ TEM investigations of dendritic growth of Au particles on HOPG," *Physical Review B* **58**, 13874 (1998).
- ⁴R. Anton and P. Kreuzer, "In situ TEM evaluation of the growth kinetics of Au particles on highly oriented pyrolytic graphite at elevated temperatures," *Physical Review B* **61**, 16077 (2000).
- ⁵L. Strong, D. F. Evans and W. L. Gladfelter, "Morphology of gold islands on highly oriented pyrolytic graphite as studied by scanning tunneling microscopy," *Langmuir* **7**, 442 (1991).
- ⁶B. Blum, R. C. Salvarezza and A. J. Arvia, "Vapor-deposited gold film formation on highly oriented pyrolytic graphite. A transition from pseudo-two-dimensional branched island growth to continuous film formation," *Journal of Vacuum Science & Technology B* **17**, 2431 (1999).
- ⁷E. Ganz, K. Sattler and J. Clarke, "Scanning tunneling microscopy of the local atomic structure of two-dimensional gold and silver islands on graphite," *Physical Review Letters* **60**, 1856 (1988).
- ⁸E. Ganz, K. Sattler and J. Clarke, "Scanning tunneling microscopy of Cu, Ag, Au, and Al adatoms, small clusters, and islands on graphite," *Surface Science* **219**, 33 (1989).
- ⁹D. Appy, H. Lei, C.-Z. Wang, M. C. Tringides, D.-J. Liu, J. W. Evans and P. A. Thiel, "Transition metals on the (0001) surface of graphite: Fundamental aspects of adsorption, diffusion, and morphology," *Progress in Surface Science* **89**, 219 (2014).
- ¹⁰A. R. Howells, L. Hung, G. S. Chottiner and D. A. Scherson, "Effects of substrate defect density and annealing temperature on the nature of Pt clusters vapor deposited on the basal plane of highly oriented pyrolytic graphite," *Solid State Ionics* **150**, 53 (2002).
- ¹¹G. W. Clark and L. L. Kesmodel, "Ultrahigh vacuum scanning tunneling microscopy studies of platinum on graphite," *Journal of Vacuum Science & Technology B* **11**, 131 (1993).
- ¹²J. Xhie, K. Sattler, U. Müller, N. Venkateswaran and G. Raina, "Periodic charge-density modulations on graphite near platinum particles," *Physical Review B* **43**, 8917 (1991).
- ¹³G. Ramos-Sanchez and P. B. Balbuena, "Interactions of platinum clusters with a graphite substrate," *Physical Chemistry Chemical Physics* **15**, 11950 (2013).

APPENDIX B

E-BEAM HEATER TEMPERATURE CALIBRATION

An Omicron dual filament e-beam heater is installed on the manipulator head of the DOE chamber (currently located in 224 Spedding Hall) and it allows heating of samples on a single plate sample holder up to 1300 K. In March 2014, I performed temperature calibrations on a blank single plate tantalum (Ta) sample holder using three separate measuring sources: a manipulator thermocouple, a remote thermocouple and an optical pyrometer.

The manipulator thermocouple is permanently attached at the end of the manipulator head. The temperature reading of this thermocouple is always lower than the actual sample temperature as there is a temperature gradient between the sample and the location of the thermocouple. The second device, the remote thermocouple, is a Type K thermocouple, most effective for temperatures between 300 K and 700 K. The thermocouple is mounted on a separate flange with a manual manipulator which allows the user to lower the thermocouple directly onto the sample surface for temperature measurements. This temperature reading is also lower than that of the actual sample as the ball at the end of the thermocouple wires is a heat sink. The third device, the optical pyrometer, is hand-held and measures the sample temperature via line of sight through a chamber window. The pyrometer is only usable for temperatures above 800 K and must be set to the correct emissivity of the sample (ϵ). Emissivity values are easily found online.¹ For this calibration, we used $\epsilon_{\text{Ta}} = 0.14$.

In order to get a correct value for temperatures below 800 K, we calibrated the manipulator and remote thermocouple readings against the pyrometer and extrapolated the

curve for lower temperatures. The estimated curve is extrapolated based on the ratio of the temperature difference between the manipulator and remote thermocouple readings divided by the temperature difference between the pyrometer and manipulator thermocouple readings. This ratio is fairly constant over the pyrometer's output range, so we assume this relationship holds at lower temperatures. Figure B1 shows the calibration curve of temperature vs. power for the e-beam heater. Figure B2 shows an expanded view of the calibration curve for temperatures 300 K to 500 K.

Figures

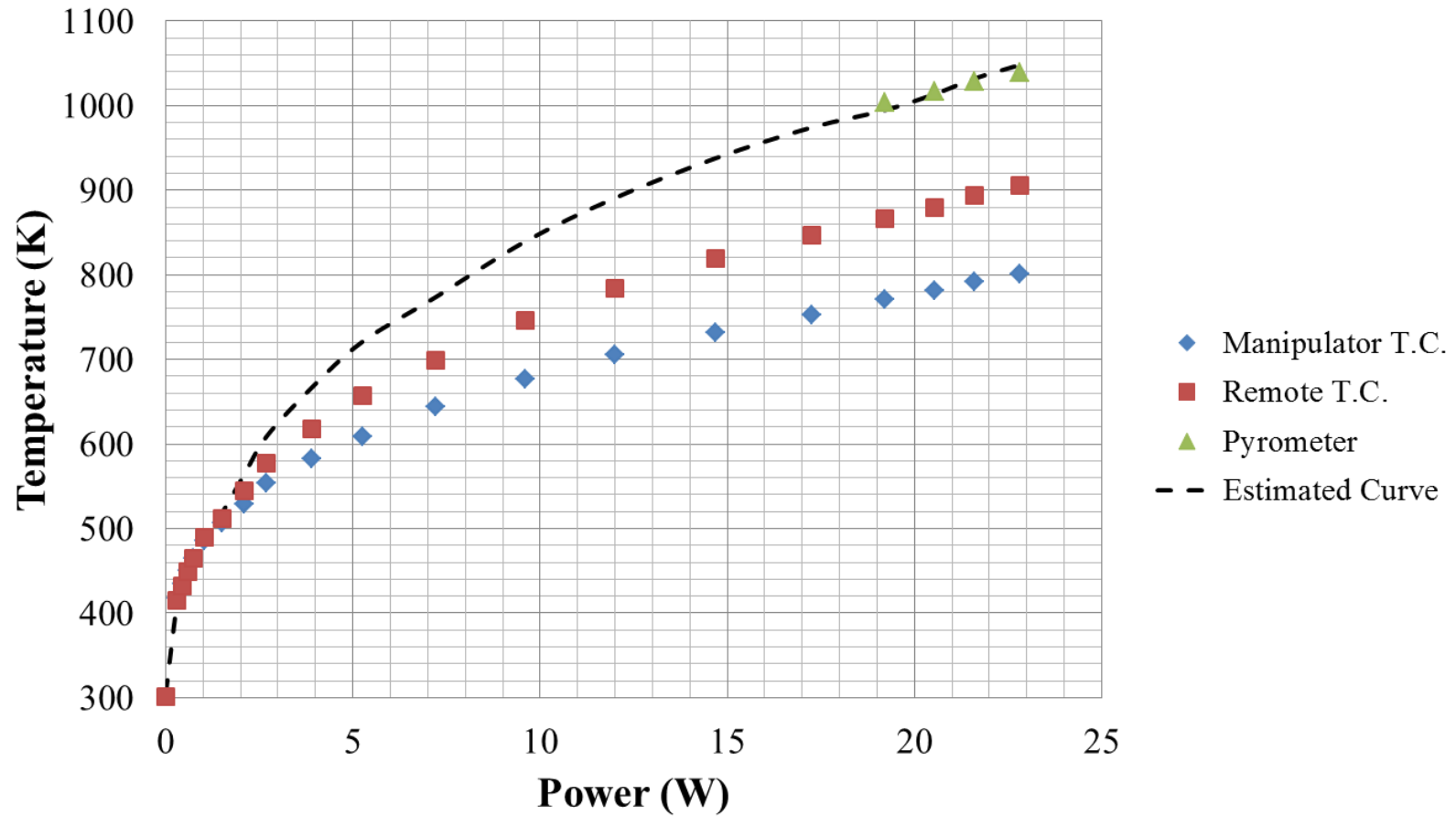


Figure B1. Heating calibration curve for a blank Ta sample plate in the e-beam heater of the manipulator. Estimated curve is forced through origin.

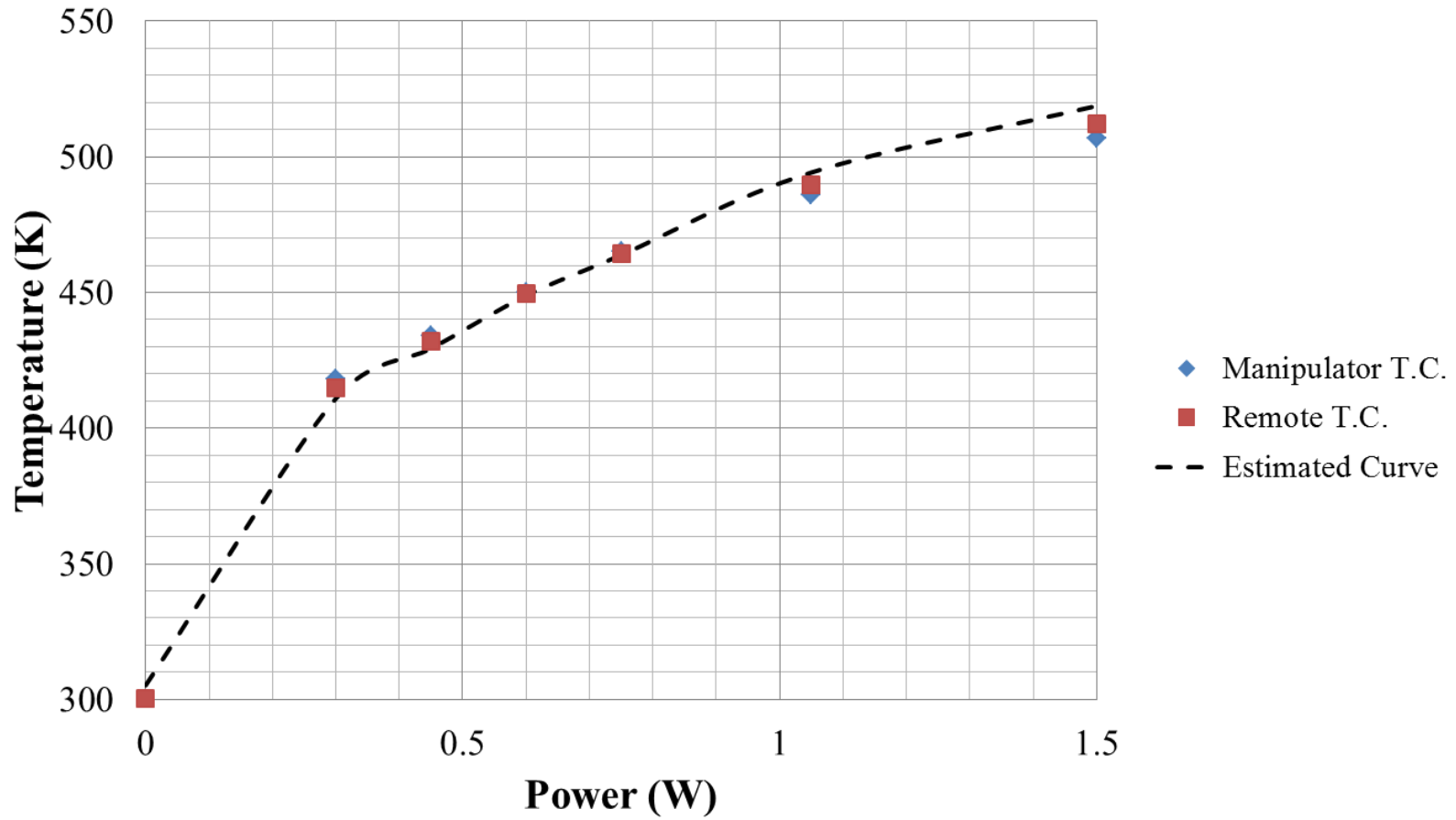


Figure B2. Expanded view of heating calibration curve for a blank Ta sample plate in the e-beam heater of the manipulator for temperatures 300 K to 500 K. Estimated curve is forced through origin.

References

¹Emissivity of Common Materials;
<http://www.omega.com/literature/transactions/volume1/emissivitya.html#t> March 8, 2014.

APPENDIX C

EXPERIMENTAL DATABASE

Abbreviations

HOPG	Highly-Oriented Pyrolytic Graphite
DOE	Department of Energy
SPH	Spedding Hall
ZYA	grade of graphite
Instru.	Instrument
STM	Scanning Tunneling Microscopy
XPS	X-ray Photoelectron Spectroscopy
min	minute
sec	second
dep	deposition
addt'l	additional
L	Langmuir
LEED	Low-energy Electron Diffraction
SEM	Scanning Electron Microscopy
EDX	Energy Dispersive X-ray
LT-STM	Low Temperature Scanning Tunneling Microscopy
Mass Spec.	Mass Spectrometer
TPD	Temperature Programmed Desorption

Table 1. NaAu₂ samples

Sample	Ames Laboratory Batch #	Description	Current Condition
A	XYY-1-61	Ames Lab Materials Preparation Center	Heavily used; in vacuum desiccator; needs re-polishing
B	DLS-9-5	Ames Lab Materials Preparation Center	Heavily used w/ gas exposures; in vacuum desiccator; needs re-polishing
C	DLS-9-5	Ames Lab Materials Preparation Center	Moderately used; in vacuum desiccator; needs re-polishing
D	DLS-9-5	Ames Lab Materials Preparation Center	Moderately used w/ TPD; in vacuum desiccator; needs re-polishing

Table 2. Dy/HOPG experiments conducted at Iowa State University (DOE Chamber - 224 SPH)

Sample	Date	Images/ Spectrum	Instru.	Filename	Details	Book #, Page #	Notes
HOPG-ZYA-4	1/26/2014	M1 - M13	STM	20140126_clean ZYA	Scan of clean surface	Bk 1, pg 76	sample previously used with Pt dep; Turbo On
		M1 - M15	STM	20140126_Dy 10 min dep 19W	19W for 10 min	Bk 1, pg 76	too much Dy!!!
HOPG-ZYA-4	2/3/2014	M1 - M5	STM	20140203_clean ZYA	Scan of clean surface	Bk 1, pg 77	Turbo On
		M1 - M10	STM	20140203_Dy 19W 1 min dep	19W for 1 min	Bk 1, pg 78	still too much Dy
HOPG-ZYA-4	2/4/2014	M1 - M3	STM	20140204_clean ZYA	Scan of clean surface	Bk 1, pg 78	Turbo On
		M1 - M22	STM	20140204_Dy 16W 5 min dep	16W for 5 min	Bk 1, pg 78	too much Dy
HOPG-ZYA-4	2/5/2014	M1 - M9	STM	20140205_clean ZYA	Scan of clean surface	Bk 1, pg 79	Turbo On
		M1 - M7	STM	20140205_Dy 16W 30 sec dep	16W for 30 sec	Bk 1, pg 79	still too much Dy
HOPG-ZYA-4	2/6/2014	M1 - M4	STM	20140206_clean ZYA	Scan of clean surface	Bk 1, pg 79	Turbo On
		M1 - M21	STM	20140206_Dy 14W 1 min dep	14W for 1 min	Bk 1, pg 79	possible evap. parameters
HOPG-ZYA-5	7/2/2014	M1 - M14	STM	20140702_ZYA_clean	Scan of clean surface	Bk 2, pg 10	previously unused sample; Turbo On
HOPG-ZYA-5	7/3/2014	M1 - M14	STM	20140703_Dy 15sec dep	14W for 15 sec	Bk 2, pg 10	shutter may have been partially open; excess Dy
		overview, Dy4d, C1s	XPS	20140703_Dy 15 sec dep	14W for 15 sec	Bk 2, pg 10	Mg Source
		overview, Dy4d, C1s	XPS	20140703_Dy 15 sec dep_02	14W for 15 sec	Bk 2, pg 11	Mg Source
		overview, Dy4d, C1s	XPS	20140703_Dy 15 sec dep_03	14W for 15 sec	Bk 2, pg 11	Mg Source
		overview, Dy4d, C1s	XPS	20140703_Dy 15 sec dep_04	14W for 15 sec	Bk 2, pg 11	Mg Source
HOPG-ZYA-5	7/7/2014	M1 - M10	STM	20140707_ZYA clean	Scan of clean surface	Bk 2, pg 12	Turbo On
		M1 - M5	STM	20140707_Dy 15 sec dep	14W for 15 sec	Bk 2, pg 12	noise and tip issues
HOPG-ZYA-5	7/8/2014	M1 - M11	STM	20140708_Pt-Ir tip test	Scan to test new Pt-Ir tip	Bk 2, pg 13	
HOPG-ZYA-5	7/9/2014	M1 - M23	STM	20140709_ZYA clean	Scan of clean surface	Bk 2, pg 13-14	Turbo On
HOPG-ZYA-5	7/10/2014	M1 - M10	STM	20140710_Dy 15 sec dep	14W for 15 sec	Bk 2, pg 14	Turbo On/Off
		M1 - M7	STM	20140710_Dy 30 sec	add'l 14W for 15 sec	Bk 2, pg 15	Turbo Off

Table 2. Dy/HOPG experiments continued

Sample	Date	Images/ Spectrum	Instru.	Filename	Details	Book #, Page #	Notes
HOPG-ZYA-5	7/15/2014	M1 - M14	STM	20140715_ZYA clean	Scan of clean surface	Bk 2, pg 16	Turbo On
HOPG-ZYA-5	7/16/2014	M1 - M18	STM	20140716_Dy 30 sec dep	14W for 30 sec	Bk 2, pg 17	Turbo On
HOPG-ZYA-5	7/21/2014	M1 - M21	STM	20140721_clean ZYA	Scan of clean surface	Bk 2, pg 18	Turbo On
HOPG-ZYA-5	7/28/2014	M1	STM	20140728_ZYA_after bake clean	Scan of clean surface	Bk 2, pg 19	after chamber bake and outgassing; Turbo On
		M1 - M5	STM	20140728_Dy 1 min 16W	16W for 1 min	Bk 2, pg 20	Turbo On
		overview, Dy4d, C1s	XPS	20140728_ZYA w Dy_01	after STM	Bk 2, pg 20	Mg Source
HOPG-ZYA-5	7/29/2014	M1 - M7	STM	20140729_ZYA clean	Scan of clean surface	Bk 2, pg 20	Turbo On
HOPG-ZYA-5	7/30/2014	M1 - M13	STM	20140730_ZYA Dy 16W 15 sec	16W for 15 sec	Bk 2, pg 21	Turbo On/Off
		M1 - M8	STM	20140730_ZYA Dy 16W 30 sec T	add'l 16W for 15 sec	Bk 2, pg 21	Turbo Off
		M1 - M11	STM	20140730_ZYA Dy 16W 1 min T	add'l 16W for 30 sec	Bk 2, pg 21	Turbo Off
HOPG-ZYA-5	7/31/2014	M1 - M6	STM	20140731_ZYA Dy sit overnight	sat in chamber overnight	Bk 2, pg 22	Turbo On
		M1 - M11	STM	20140731_ZYA Dy 16W 2 min T	add'l 16W for 1 min	Bk 2, pg 22	Turbo On
HOPG-ZYA-5	8/5/2014	M1 - M8	STM	20140805_ZYA clean	Scan of clean surface	Bk 2, pg 23	Turbo On
HOPG-ZYA-5	8/19/2014	M1 - M4	STM	20140819_clean ZYA	Scan of clean surface	Bk 2, pg 24	bad tip; Turbo On
HOPG-ZYA-5	8/20/2014	M1 - M15	STM	20140820_clean ZYA	Scan of clean surface	Bk 2, pg 25	Turbo On
HOPG-ZYA-5	8/21/2014	M1 - M28	STM	20140821_Dy 15 W 15 sec	15W for 15 sec	Bk 2, pg 25	Turbo On
		M1 - M14	STM	20140821_Dy 15W 30 sec addtl	add'l 15W for 30 sec	Bk 2, pg 26	Turbo On
HOPG-ZYA-5	8/25/2014	M1 - M7	STM	20140825_clean ZYA	Scan of clean surface	Bk 2, pg 26	Turbo On
HOPG-ZYA-6	8/29/2014	M1 - M2	STM	20140829_clean ZYA-D	Scan of clean surface	Bk 2, pg 28	sample previously used with Cu dep; Turbo On

Table 2. Dy/HOPG experiments continued

Sample	Date	Images/ Spectrum	Instru.	Filename	Details	Book #, Page #	Notes
HOPG-ZYA-7	9/2/2014	M1 - M9	STM	20140902_clean ZYA-E	Scan of clean surface	Bk 2, pg 30	previously unused sample; Turbo On
		M1 - M24	STM	20140902_Dy 15W 15sec	15W for 15 sec	Bk 2, pg 30	Turbo On
HOPG-ZYA-7	9/11/2014	M1 - M7	STM	20140911_clean ZYA-E	Scan of clean surface; tip check	Bk 2, pg 35	Turbo On
HOPG-ZYA-7	9/13/2014	M1 - M5	STM	20140913_clean ZYA-E	Scan of clean surface; tip check	Bk 2, pg 35	Turbo On
HOPG-ZYA-7	9/16/2014	M1 - M2	STM	20140916_Dy 15W 45sec overnight	addt'l 15W for 30 sec	Bk 2, pg 36	Turbo On
HOPG-ZYA-7	9/17/2014	M1 - M7	STM	20140917_clean ZYA-E	Scan of clean surface	Bk 2, pg 36	Turbo On
		M1 - M15	STM	20140917_Dy 15W 1 min ZYA-E	15W for 1 min	Bk 2, pg 37	Turbo On
		M1 - M13	STM	20140917_400K anneal_Dy ZYA-E	after 400K, 15 min anneal	Bk 2, pg 37	Turbo On
HOPG-ZYA-7	9/22/2014	M1 - M9	STM	20140922_clean ZYA-E	Scan of clean surface	Bk 2, pg 39	Turbo On
HOPG-ZYA-7	9/27/2014	M1 - M10	STM	20140927_clean ZYA-E	Scan of clean surface	Bk 2, pg 41	Turbo On
HOPG-ZYA-7	10/8/2014	M1 - M3	STM	20141008_clean ZYA-E	Scan of clean surface; tip check	Bk 2, pg 43	Turbo On
		M1 - M3	STM	20141008_clean ZYAE	Scan of clean surface; tip check	Bk 2, pg 43	Turbo On
HOPG-ZYA-7	10/9/2014	M1 - M20	STM	20141009_clean ZYA-E	Scan of clean surface	Bk 2, pg 44	Turbo On
HOPG-ZYA-7	10/10/2014	M1 - M20	STM	20141010_Dy 15W 1min ZYA-E	15W for 1 min	Bk 2, pg 44	Turbo On
		M1 - M24	STM	20141010_ZYA-E wDy 750K anneal	after 750K, 15 min anneal	Bk 2, pg 45	Turbo On
HOPG-ZYA-7	10/28/2014	M1 - M10	STM	20141028_clean ZYA-E	Scan of clean surface	Bk 2, pg 47	Turbo On
		M1 - M13	STM	20141028_Dy 15W 1min ZYA-E	15W for 1 min	Bk 2, pg 48	Turbo On
		M1 - M23	STM	20141028_ZYA-E 1100K	after 1100K heating	Bk 2, pg 48	Turbo On

Table 2. Dy/HOPG experiments continued

Sample	Date	Images/ Spectrum	Instru.	Filename	Details	Book #, Page #	Notes
HOPG-ZYA-7	10/30/2014	M1 - M10	STM	20141030_clean ZYA-E	Scan of clean surface	Bk 2, pg 49	Turbo On
		M1 - M21	STM	20141030_Dy 15W 1min	15W for 1 min	Bk 2, pg 49	Turbo On
		M1 - M10	STM	20141030_ZYA-E wDy 1100K anneal	after 1100K heating	Bk 2, pg 50	Turbo On
HOPG-ZYA-7	11/3/2014	M1 - M6	STM	20141103_clean ZYA-E	Scan of clean surface	Bk 2, pg 51	Turbo On
		M1 - M6	STM	20141103_ZYA-E wDy 20W+25W 20secT	Scan for Dy on HOPG	Bk 2, pg 51	determine power setting for ion damage experiments
HOPG-ZYA-8	11/10/2014	M1 - M7	STM	20141110_clean ZYA-E	Scan of clean surface	Bk 2, pg 53	previously unused sample; Turbo On
		M1 - M14	STM	20141110_Dy 25W 10sec ID#1	25W for 10 sec; HV/Fil ON/ON	Bk 2, pg 53	Turbo On
		M1 - M8	STM	20141110_clean ZYA-E 2	Scan of clean surface	Bk 2, pg 53	Turbo On
HOPG-ZYA-8	11/11/2014	M1 - M10	STM	20141111_clean ZYA-E ID#2	Scan of clean surface	Bk 2, pg 54	Turbo On
		M2 - M12	STM	20141111_Dy 25W 10sec ID#2	25W for 10 sec; HV/Fil OFF/ON	Bk 2, pg 54	Turbo On
		M1 - M8	STM	20141111_clean ZYA-E ID#3	Scan of clean surface	Bk 2, pg 55	Turbo On
		M1 - M9	STM	20141111_Dy 25W 10sec ID#3	25W for 10 sec; HV/Fil ON/OFF	Bk 2, pg 55	Turbo On
HOPG-ZYA-8	11/12/2014	M1 - M10	STM	20141112_clean ZYA-E ID#4	Scan of clean surface	Bk 2, pg 56	Turbo On
HOPG-ZYA-8	11/13/2014	M1 - M23	STM	20141113_Dy 25W 10sec ID#4	25W for 10 sec; HV/Fil OFF/OFF	Bk 2, pg 56	Turbo On
		M1 - M5	STM	20141113_clean ZYA-E ID#5	Scan of clean surface	Bk 2, pg 57	Turbo On
HOPG-ZYA-8	11/14/2014	M1 - M16	STM	20141114_Dy 25W 10sec ID#5	25W for 10 sec; HV/Fil ON/ON	Bk 2, pg 57	Turbo On
HOPG-ZYA-8	11/17/2014	M1 - M6	STM	20141117_clean ZYA-E	Scan of clean surface	Bk 2, pg 57	Turbo On
		M1 - M8	STM	20141117_shutter closed		Bk 2, pg 58	Check to make sure evaporator shutter in closed position (no metal dep)
HOPG-ZYA-8	12/1/2014	M1 - M12	STM	20141201_clean ZYA-E	Scan of clean surface	Bk 2, pg 61	Turbo On

Table 2. Dy/HOPG experiments continued

Sample	Date	Images/ Spectrum	Instru.	Filename	Details	Book #, Page #	Notes
HOPG-ZYA-8	12/4/2014	M1 - M4	STM	20141204_clean ZYA-E	Scan of clean surface	Bk 2, pg 62	Turbo On
HOPG-ZYA-8	12/6/2014	M1 - M10	STM	20141206_clean ZYA-E	Scan of clean surface	Bk 2, pg 62	Turbo On
HOPG-ZYA-8	12/8/2014	M1 - M24	STM	20141208_Dy 25W 10sec	25W for 10 sec; HV/Fil ON/OFF	Bk 2, pg 63	Turbo On
		M1 - M28	STM	20141208_Dy 25W 600K 5min	after 600K anneal for 5 min	Bk 2, pg 63	
HOPG-ZYA-8	12/10/2014	M1 - M12	STM	20141210_clean ZYA-E	Scan of clean surface	Bk 2, pg 64	Turbo On
		M1 - M12	STM	20141210_clean ZYA-E after O2 test	Scan of clean surface; after 20L O ₂ exposure	Bk 2, pg 64	Turbo On
HOPG-ZYA-8	12/11/2014	M1 - M19	STM	20141211_Dy 25W 10sec	25W for 10 sec; HV/Fil ON/OFF	Bk 2, pg 65	Turbo On
		M1 - M29	STM	20141211_Dy 25W 800K 5min	after 800K anneal for 5 min	Bk 2, pg 65	
		M1 - M24	STM	20141211_Dy 25W 800K O2 exp	after 20L O ₂ exposure (after 800K anneal)	Bk 2, pg 66	Turbo On
HOPG-ZYA-8	12/16/2014	M1 - M14	STM	20141216_clean ZYA-E	Scan of clean surface	Bk 2, pg 66-67	Turbo On
HOPG-ZYA-8	12/17/2014	M1 - M22	STM	20141217_Dy 25W 10sec	25W for 10 sec; HV/Fil ON/OFF	Bk 2, pg 67	Turbo On
		M1 - M20	STM	20141217_Dy 25W 20L O2	after 20L O ₂ exposure	Bk 2, pg 67	Turbo On
		overview, Dy4d, C1s	XPS	20141217_ZYA-E wDy + O2	25W for 10 sec + 20L O ₂ ; HV/Fil ON/OFF	Bk 2, pg 68	Mg Source
		O1s	XPS	20141217_O1s	25W for 10 sec + 20L O ₂ ; HV/Fil ON/OFF	Bk 2, pg 68	Mg Source
HOPG-ZYA-8	1/6/2015	M1 - M11	STM	20150106_clean ZYA-E	Scan of clean surface	Bk 2, pg 69	Turbo On
HOPG-ZYA-8	1/8/2015	M1 - M29	STM	20150108_Dy 23W 10sec	23W for 10 sec; HV/Fil ON/OFF	Bk 2, pg 69	Turbo On

Table 2. Dy/HOPG experiments continued

Sample	Date	Images/ Spectrum	Instru.	Filename	Details	Book #, Page #	Notes
HOPG-ZYA-8	1/9/2015	M1 - M18	STM	20150109_clean ZYA-E	Scan of clean surface	Bk 2, pg 70	Turbo On
		M1 - M28	STM	20150109_Dy 25W 10sec	25W for 10 sec; HV/Fil ON/OFF	Bk 2, pg 70	Turbo On
HOPG-ZYA-8	1/12/2015	M1 - M16	STM	20150112_clean ZYA-E	Scan of clean surface	Bk 2, pg 71	Turbo On
		M1 - M32	STM	20150112_Dy 29W 10sec	29W for 10 sec; HV/Fil ON/OFF	Bk 2, pg 71	Turbo On
		overview, Dy4d, C1s	XPS	20150112_ZYA-E wDy 29W	29W for 10 sec; HV/Fil ON/OFF	Bk 2, pg 71	Mg Source
HOPG-ZYA-8	1/14/2015	M1 - M18	STM	20150114_clean ZYA-E	Scan of clean surface	Bk 2, pg 72	Turbo On
		M1 - M28	STM	20150114_Dy 33W 10sec	33W for 10 sec; HV/Fil ON/OFF	Bk 2, pg 72	Turbo On
HOPG-ZYA-8	1/15/2015	M1 - M19	STM	20150115_clean ZYA-E	Scan of clean surface	Bk 2, pg 73	Turbo On
HOPG-ZYA-8	1/16/2015	M1 - M31	STM	20150116_Dy 37W 10sec	37W for 10 sec; HV/Fil ON/OFF	Bk 2, pg 73	Turbo On
		overview, Dy4d, C1s	XPS	20150116_ZYA-E wDy 37W	37W for 10 sec; HV/Fil ON/OFF	Bk 2, pg 74	Mg Source
		overview, Dy4d, C1s	XPS	20150116_ZYA wDy 37W+26W	addt'l 26W for 10 sec; HV/Fil ON/OFF	Bk 2, pg 74	Mg Source
HOPG-ZYA-8	1/22/2015	M1 - M16	STM	20150122_clean ZYA-E	Scan of clean surface	Bk 2, pg 75	Turbo On
HOPG-ZYA-8	1/23/2015	M1 - M28	STM	20150123_Dy 25W 10sec	25W for 10 sec; HV/Fil ON/OFF	Bk 2, pg 75	Turbo On
		M1 - M27	STM	20150123_Dy 20L O2 Exp	after 20L O ₂ exposure	Bk 2, pg 75-76	Turbo On
HOPG-ZYA-8	1/28/2015	M1 - M20	STM	20150128_clean ZYA-E	Scan of clean surface	Bk 2, pg 76	Turbo On
HOPG-ZYA-8	1/29/2015	M1 - M34	STM	20150129_Dy 25W 10sec	25W for 10 sec; HV/Fil ON/OFF	Bk 2, pg 77	Turbo On
		M1 - M34	STM	20150129_Dy 25W 700K 5min	after 700K anneal for 5 min	Bk 2, pg 77	
HOPG-ZYA-8	1/31/2015	M1 - M19	STM	20150131_clean ZYA-E	Scan of clean surface	Bk 2, pg 78	Turbo On

Table 2. Dy/HOPG experiments continued

Sample	Date	Images/ Spectrum	Instru.	Filename	Details	Book #, Page #	Notes
HOPG- ZYA-8	2/2/2015	M1 - M28	STM	20150202_Dy 25W 10sec	25W for 10 sec; HV/Fil ON/OFF	Bk 2, pg 79	Turbo On
		M1 - M41	STM	20150202_Dy 25W 20L O ₂ + 400K	after 20L O ₂ exposure w/ 400K anneal	Bk 2, pg 79	Turbo On

Table 3. Au/HOPG experiments conducted at Iowa State University (DOE Chamber - 224 SPH)

Sample	Date	Images/ Spectrum	Instru.	Filename	Details	Book #, Page #	Notes
HOPG-ZYA-1	6/30/2013	M1 - M5	STM	20130630_tip at. res.	Check tip for atomic resolution	Bk 1, pg 36	previously unused sample
HOPG-ZYA-1	7/1/2013	M1 - M19	STM	20130701_at res	Check tip for atomic resolution	Bk 1, pg 36	
HOPG-ZYA-2	7/6/2013	M1 - M23	STM	20130706_at res_clean surface	Check tip for atomic resolution; clean surface	Bk 1, pg 39	previously unused sample; Sample in double decker; Turbo On
		M1 - M7	STM	20130706_after sputter	45 sec sputter at 100eV	Bk 1, pg 39	Turbo On
		M1 - M5	STM	20130706_after sputter and heat	addt'l 45 sec sputter at 100eV, 5 min heating 655K	Bk 1, pg 40	Turbo On
HOPG-ZYA-2	7/7/2013	M1 - M18	STM	20130707_after 2nd heating	addt'l 30 min heating 660K	Bk 1, pg 40	Turbo On
		M1 - M8	STM	20130706_after 3rd heating	addt'l 30 min heating 660K	Bk 1, pg 41	poor tunneling; Turbo On
		M1 - M8	STM	20130707_test	Check new tip for atomic resolution	Bk 1, pg 41	
HOPG-ZYA-2	7/27/2013	M1 - M9	STM	20130727_ZYA clean	Scan of clean surface	Bk 1, pg 42	Turbo On
		M1 - M4	STM	20130727_ZYA after 30 min Au dep	22W for 30 min	Bk 1, pg 42	not many islands; tip issues; Turbo On
HOPG-ZYA-2	7/28/2013	M1 - M7	STM	20130728_addtl 30 min Au dep	addt'l 22W for 30 min	Bk 1, pg 43	tip issues; no gold seen; Turbo On
HOPG-ZYA-3	7/30/2013	M1 - M7	STM	20130730_clean surface ZYA	Scan of clean surface	Bk 1, pg 44	previously unused sample; Turbo On
		M1 - M16	STM	20130730_after 10 min Au dep	23.8W for 10 min	Bk 1, pg 44	possible islands and build up on step edges; Turbo On

Table 3. Au/HOPG experiments continued

Sample	Date	Images/ Spectrum	Instru.	Filename	Details	Book #, Page #	Notes
HOPG-ZYA-3	7/31/2013	M1 - M4	STM	30130731_clean surface ZYA	Scan of clean surface	Bk 1, pg 44	Turbo On
		M1 - M6	STM	20130731_after 20 min Au dep	23.8W for 20 min	Bk 1, pg 45	at step edges?; no islands; Turbo On
		M1	STM	20130731_addtl 20 min Au dep	addt'l 23.8W for 20 min	Bk 1, pg 45	rough surface; tunneling issues; Turbo On
HOPG-ZYA-3	8/1/2013	M1 - M5	STM	20130801_clean ZYA	Scan of clean surface	Bk 1, pg 45-46	poor tunneling; Turbo On
HOPG-ZYA-3	8/3/2013	M1 - M6	STM	20130803_tip test	Scan to test tip tunneling	Bk 1, pg 46	poor tunneling; Turbo On
		M1 - M3	STM	20130803_tip test 2	Scan to test tip tunneling	Bk 1, pg 46	poor tunneling; Turbo On
HOPG-ZYA-3	8/4/2013	M1 - M4	STM	20130804_tip test	Scan to test tip; clean surface	Bk 1, pg 47	Turbo On
		M1 - M11	STM	20130804_after 10 min Au dep	23.8W for 10 min	Bk 1, pg 47	possible tiny islands; Turbo On
		M1 - M6	STM	20130804_addtl 10 min Au Dep	addt'l 23.8W for 10 min	Bk 1, pg 48	small islands; Turbo On
HOPG-ZYA-3	8/5/2013	M1 - M7	STM	20130805_Au on HOPG		Bk 1, pg 48	Turbo On
		M1 - M16	STM	20130805_addtl 10 min Au dep 30 min total	addt'l 23.8W for 10 min	Bk 1, pg 48	hard to image; blobs on surface; Turbo On
		M1 - M26	STM	20130805_addtl 10 min Au dep 25W	addt'l 25W for 10 min	Bk 1, pg 48	large clusters and triangular islands!; Turbo On
HOPG-ZYA-3	8/6/2013	M1 - M8	STM	20130806_clean ZYA	Scan of clean surface	Bk 1, pg 49	Turbo On
		M1 - M6	STM	20130806_after 10 min Au dep	25W for 10 min	Bk 1, pg 49	tall islands; Turbo On

Table 3. Au/HOPG experiments continued

Sample	Date	Images/ Spectrum	Instru.	Filename	Details	Book #, Page #	Notes
HOPG-ZYA-3	8/7/2013	M1 - M10	STM	20130807_clean ZYA	Scan of clean surface	Bk 1, pg 50	
		M1	STM	20130807_1 min Au dep	25W for 1 min	Bk 1, pg 50	no islands
			STM	-	4 addt'l min	Bk 1, pg 51	still no islands
HOPG-ZYA-3	8/8/2013	M1 - M8	STM	20130808_clean ZYA	Scan of clean surface	Bk 1, pg 51	
		M1 - M11	STM	20130808_after 7 min Au dep	25W for 7 min	Bk 1, pg 51	where is the gold?
HOPG-ZYA-3	8/9/2013	M1 - M12	STM	20130809_clean ZYA	Scan of clean surface	Bk 1, pg 52	
		M1 - M14	STM	20130809_after 5 min Au dep	25W for 5 min	Bk 1, pg 52	islands in blobs
HOPG-ZYA-3	8/10/2013	M1 - M7	STM	20130810_clean ZYA	Scan of clean surface	Bk 1, pg 53	Turbo On
		M1 - M9	STM	20130810_after 3 min Au dep	25W for 3 min	Bk 1, pg 53	island blobs; Turbo Off
		M1 - M28	STM	20130810_after Au dep incremental heating	incremental heatings 400K-600K	Bk 1, pg 53-54	400K: M1-M10; 500K: M11-M18; 600K: M19-M28; Turbo Off
HOPG-ZYA-3	8/12/2013	M1 - M13	STM	20130812_clean ZYA	Scan of clean surface	Bk 1, pg 54	Turbo On
		M1 - M16	STM	20130812_after 3 min Au dep	26W for 3 min	Bk 1, pg 55	Turbo On
		M1 - M39	STM	20130812_incremental heating with Au	incremental heatings 400K-600K	Bk 1, pg 55-56	400K: M1-M11; 500K: M12-M30; 600K: M31-M39; 16 hour break between 400K and 500K anneals; Turbo On

Table 3. Au/HOPG experiments continued

Sample	Date	Images/ Spectrum	Instru.	Filename	Details	Book #, Page #	Notes
HOPG- ZYA-3	8/14/2013	M1 - M7	STM	20130814_clean ZYA	Scan of clean surface	Bk 1, pg 56	Turbo On
		M1 - M10	STM	20130814_after 3 min Au dep	26W for 3 min	Bk 1, pg 56	island blobs; Turbo On
		M1 - M33	STM	20130814_incremental heating with Au	incremental heatings 700K-900K	Bk 1, pg 57	700K: M1-M10; 800K: M11-M23; 900K: M24-M33; sat overnight after 900K anneal/before scanning; Turbo On
HOPG- ZYA-3	8/19/2013	M1 - M39	STM	20130819_clean ZYA	Scan of clean surface; tip prep	Bk 1, pg 57- 58	Turbo On
HOPG- ZYA-3	8/20/2013	M1 - M15	STM	20130820_3 min Au dep	25W for 3 min	Bk 1, pg 58	island blobs, step edge decoration; Turbo On
		M1 - M62	STM	20130820_incremental heating w/Au	incremental heatings 700K-950K	Bk 1, pg 59- 60	700K: M1-M20; 800K: M21-M35; 900K: M36-M54; 950K: M55-M62; Turbo Off

Table 4. Pt/HOPG experiments conducted at Iowa State University (DOE Chamber - 224 SPH)

Sample	Date	Images/ Spectrum	Instru.	Filename	Details	Book #, Page #	Notes
HOPG-ZYA-3	8/29/2013	M1 - M13	STM	20130829_clean ZYA	Scan of clean surface	Bk 1, pg 60	sample previously used with Au dep
		M1 - M12	STM	20130829_Pt dep test 10 min	48W for 10 min	Bk 1, pg 61	nothing seen
		M1 - M4	STM	20130829_Pt test 2 addtl 10 min	addtl 54W for 10 min	Bk 1, pg 61	nothing seen, possible Pt on tip
HOPG-ZYA-3	8/30/2013	M1 - M5	STM	20130830_Pt test 3 addtl 10 min	addtl 61W for 10 min	Bk 1, pg 61	small islands seen, not big enough yet
HOPG-ZYA-3	9/3/2013	M1 - M16	STM	20130903_clean ZYA	Scan of clean surface	Bk 1, pg 62	
		M1 - M11	STM	20130903_15 min Pt dep	61W for 15 min	Bk 1, pg 62-63	small islands seen, still not big enough
HOPG-ZYA-3	9/4/2013	M1 - M11	STM	20130904_addtl 15 min Pt dep	addtl 62W for 15 min	Bk 1, pg 63	small islands
HOPG-ZYA-3	9/5/2013	M1 - M11	STM	20130905_clean ZYA	Scan of clean surface	Bk 1, pg 63	
		M1 - M16	STM	20130905_15 min Pt dep	64W for 15 min	Bk 1, pg 64	small islands
HOPG-ZYA-3	9/6/2013	M1 - M32	STM	20130906_clean ZYA	Scan of clean surface	Bk 1, pg 64	
HOPG-ZYA-3	9/7/2013	M1 - M7	STM	20130907_after 20 min Pt dep	64W for 20 min	Bk 1, pg 65	islands seen, heat next
		M1 - M42	STM	20130907_incremental heating with Pt	incremental heatings 400-600K	Bk 1, pg 65-66	400K: M1-12; 500K: M13-M26; 600K: M27-M42
HOPG-ZYA-3	9/10/2013	M1 - M8	STM	20130910_clean ZYA	Scan of clean surface	Bk 1, pg 66	
		M1 - M14	STM	20130910_20 min Pt dep	64W for 20 min	Bk 1, pg 66	
		M1 - M9	STM	20130910_heated to 950K after Pt dep	after heating to 950K	Bk 1, pg 67	

Table 4. Pt/HOPG experiments continued

Sample	Date	Images/ Spectrum	Instru.	Filename	Details	Book #, Page #	Notes
HOPG-ZYA-3	9/11/2013	M1 - M6	STM	20130911_clean ZYA	Scan of clean surface	Bk 1, pg 67	
HOPG-ZYA-3	9/12/2013	M1 - M6	STM	20130912_20 min Pt dep	64W for 20 min	Bk 1, pg 67	where is Pt?
		M1 - M4	STM	20130912_addtl 20 min dep 40 total	addtl 64W for 20 min	Bk 1, pg 68	where is Pt?
		M1 - M5	STM	20130912_60 min total Pt power change	addtl 66W for 20 min	Bk 1, pg 68	Pt island present with higher dep power
HOPG-ZYA-4	9/13/2013	M1 - M10	STM	20130913_clean ZYA	Scan of clean surface	Bk 1, pg 69	previously unused sample
HOPG-ZYA-4	9/16/2013	M1 - M13	STM	20130916_clean ZYA	Scan of clean surface	Bk 1, pg 70	
HOPG-ZYA-4	9/17/2013	M1 - M102	STM	20130917_Pt dep and incremental heating	72W for 20 min; incremental heatings 300K-950K	Bk 1, pg 70-72	300K: M1-M13; 400K: M14-28; 500K: M29-M39; 600K: M40-M49; 700K: M50-M61; 800K: M62-M78; 900K: M79-M90; 950K: M91-M102; Turbo Off
HOPG-ZYA-2	9/20/2013	M1 - M8	STM	20130920_clean ZYA	Scan of clean surface	Bk 1, pg 73	sample previously used with Au dep
HOPG-ZYA-2	9/21/2013	M1 - M98	STM	20130921_Pt on ZYA incremental heating	75W for 20 min; incremental heatings 300K; 800K-1300K	Bk 1, pg 73-75	300K: M1-M13; 800K: M14-M26; 900K: M27-M41; 1000K: M42-M59; 1100K: M60-M73; 1200K: M74-M86; 1300K: M87-M98; Turbo Off

Table 5. NaAu₂ experiments conducted at EMPA (ESCA Chamber - Dübendorf, Switzerland)

Sample	Date	Spectrum/ Image	Instru.	Filename	Details	Book #, Page #	Notes
A	4/7/2014	overview	XPS	20140407_NaAu2_A_as transferred in	Sample alignment	Bk 1, pg 106	Al Source; Grazing 60° Emission; re-polished by Deborah L. Schlagele March 28, 2014; 1µm in thickness
		overview	XPS	20140407_NaAu2_A_10minspu tt_10minanneal160C	10 min sputter, 10 min anneal 435K	Bk 1, pg 106	Al Source; Grazing 60° Emission
A	4/8/2014	overview	XPS	20140408_NaAu2_A_20minspu tt_20minanneal160C	addt'l 10 min sputter, addt'l 10 min anneal 435K	Bk 1, pg 107	Al Source; Grazing 60° Emission
		overview	XPS	20140408_NaAu2_A_35minspu tt_20minanneal330C	addt'l 10 min sputter, 20 min anneal 605K	Bk 1, pg 107	Al Source; Grazing 60° Emission
		25.4eV - 103eV, 130eV	LEED	20140408_Sample A	15 min sputter, 20 min anneal 605K	Bk 1, pg 107	first spots ~13.4eV, final spots ~160eV
A	4/9/2014	overview, Au4f, O1s, Na1s	XPS	20140409_NaAu2_A_60minspu tt_20minanneal380C	10 min sputter, 20 min anneal 655K	Bk 1, pg 108	Al Source; Normal and Grazing 60° Emission
		overview, Au4f, Na1s	XPS	20140409_NaAu2_A_70minspu tt_20minanneal430C	10 min sputter, 20 min anneal 705K	Bk 1, pg 108-109	Al Source; Normal and Grazing 60° Emission
A	4/11/2014	M1 - M23	STM	20140411_NaAu2_A_15minspu t_20minanneal430C	Scan of surface after one 10 min sputter, one 705K 20 min anneal	Bk 1, pg 109	
		overview, Au4f, Na1s	XPS	20140411_NaAu2_A_15minspu t_20minanneal480C	10 min sputter, 20 min anneal 480C (753K)	Bk 1, pg 110	Al Source; Normal and Grazing 60° Emission
A	4/14/2014	M1 - M26	STM	20140414_NaAu2_A_30minspu tt_40minanneal480C	Scan of surface after one 15 min sputter, one 480C (753K) 20 min anneal	Bk 1, pg 110	possible Au(110) (2x1) reconstruction
		overview, Au4f, Na1s	XPS	20140414_NaAu2_A_15minspu tt_20minanneal495C	Sample alignment; after 15 min sputter, 20 min anneal 495C (768K)	Bk 1, pg 111	Al Source; Normal and Grazing 60° Emission

Table 5. NaAu₂ experiments EMPA continued

Sample	Date	Spectrum/ Image	Instru.	Filename	Details	Book #, Page #	Notes
A	4/15/2014	M1 - M42	STM	20140415_NaAu2_A_30minspu tt_40minanneal495C	Scan of surface after one 15 min sputter, one 495C (768K) 20 min anneal	Bk 1, pg 112	possible Au(111) reconstruction [herringbone]
A	4/16/2014	overview, Au4f, Na1s	XPS	20140416_NaAu2_A_65minspu tt_20minanneal230C	65 min sputter, 20 min anneal 230C (503K)	Bk 1, pg 112	Al Source; Normal and Grazing 60° Emission
		overview, Au4f, Na1s	XPS	20140416_NaAu2_A_15minspu tt	15 min sputter	Bk 1, pg 113	Al Source; Normal and Grazing 60° Emission
A	4/17/2014	overview, Au4f, Na1s	XPS	20140417_NaAu2_A_3minspu tt_20minanneal230C	3 min sputter, 20 min anneal 230C (503K)	Bk 1, pg 113-114	Al Source; Normal and Grazing 60° Emission
		overview, Au4f, Na1s	XPS	20140417_NaAu2_A_60mingra zingspu	60 min sputter at grazing angle	Bk 1, pg 114	Al Source; Normal and Grazing 60° Emission
A	4/18/2014	overview, Au4f, Na1s	XPS	20140418_NaAu2_A_16hrannea l160C	16 hour anneal 160C (433K)	Bk 1, pg 115	Al Source; Normal and Grazing 60° Emission
A	4/22/2014		SEM- EDX	20140422_NaAu2_A		Bk 1, pg 118	mapping taken by Dr. Juan-Ramon Sanchez
A	5/8/2014	overview, Au4f, Na1s	XPS	20140508_NaAu2_A_as_in_rep olished	after re-polish	Bk 1, pg 128	Al Source; Normal and Grazing 60° Emission; sample finger repolished by Alessandra Beni May 6, 2014
A	4/8/2015	overview	XPS	20150408_NaAu2_A_as is_008	after sitting in ESCA chamber 1 year	Bk 2, pg 83	Al Source; Normal Emission
		overview	XPS	20150408_NaAu2_A_as is_011	after sitting in ESCA chamber 1 year	Bk 2, pg 83	Al Source; Normal Emission
		overview	XPS	20150408_NaAu2_A_as is_012	after sitting in ESCA chamber 1 year	Bk 2, pg 83	Al Source; Normal Emission

Table 5. NaAu₂ experiments EMPA continued

Sample	Date	Spectrum/ Image	Instru.	Filename	Details	Book #, Page #	Notes
B	5/6/2014	overview, Au4f, Na1s	XPS	20140506_NaAu2_B_as_in	as transferred into chamber	Bk 1, pg 126	Al Source; Normal and Grazing 60° Emission; previous light sputtering and 400K anneals
B	5/7/2014	overview, Au4f, Na1s	XPS	20140507_NaAu2_B_10minSput_40minAnn220C	two 5 min sputters, 20 min anneal 220C (493K) cycles	Bk 1, pg 127	Al Source; Normal and Grazing 60° Emission
		27.0eV - 100.5eV	LEED	20140507_Sample B	5 min sputter, 20 min anneal 220C (493K)	Bk 1, pg 127-128	first spots ~15eV, final spots ~156eV
B	5/11/2014	Au4f, Na1s	XPD	20140511_NaAu2_B_XPD	XPD of surface	Bk 1, pg 129	Al Source; High resolution scan
B	5/13/2014	overview, Au4f, Na1s, O1s	XPS	20140513_NaAu2_B_5minSput_20minAnn220C_Clean	5 min sputter; 20 min anneal 220C (493K)	Bk 1, pg 129-130	Al Source; Normal, Grazing 60°, Grazing 80° Emission
		overview, Au4f, Na1s, O1s	XPS	20140513_NaAu2_B_1L_O2	1L O ₂ exposure	Bk 1, pg 130-131	Al Source; Normal, Grazing 60°, Grazing 80° Emission
B	5/14/2014	overview, Au4f, Na1s, O1s	XPS	20140514_NaAu2_B_5minSput_20minAnn220C_Clean	5 min sputter; 20 min anneal 220C (493K)	Bk 1, pg 131	Al Source; Normal, Grazing 60°, Grazing 80° Emission
		overview, Au4f, Na1s, O1s	XPS	20140514_NaAu2_B_5L_O2	5L O ₂ exposure	Bk 1, pg 132	Al Source; Normal, Grazing 60°, Grazing 80° Emission
		overview, Au4f, Na1s, O1s	XPS	20140514_NaAu2_B_10L_O2	add'l 10L O ₂ exposure	Bk 1, pg 132-133	Al Source; Normal, Grazing 60°, Grazing 80° Emission
		overview, Au4f, Na1s, O1s	XPS	20140514_NaAu2_B_35L_O2	add'l 35L O ₂ exposure	Bk 1, pg 133	Al Source; Normal, Grazing 60°, Grazing 80° Emission
		overview, Au4f, Na1s, O1s	XPS	20140514_NaAu2_B_50L_O2	add'l 50L O ₂ exposure	Bk 1, pg 134	Al Source; Normal, Grazing 60°, Grazing 80° Emission

Table 5. NaAu₂ experiments EMPA continued

Sample	Date	Spectrum/ Image	Instru.	Filename	Details	Book #, Page #	Notes
B	5/15/2014	overview, Au4f, Na1s, O1s	XPS	20140515_NaAu2_B_O2_sit_14 hrs	sit overnight	Bk 1, pg 134-135	Al Source; Normal, Grazing 60°, Grazing 80° Emission
		overview, Au4f, Na1s, O1s	XPS	20140515_NaAu2_B_100L_O2	add'l 100L O ₂ exposure	Bk 1, pg 135-136	Al Source; Normal, Grazing 60°, Grazing 80° Emission
B	5/15/2014	overview, Au4f, Na1s, O1s	XPS	20140515_NaAu2_B_10minSpu t_40minAnn220C_Clean	two 5 min sputters, 20 min anneal 220C (493K) cycles	Bk 1, pg 136	Al Source; Normal, Grazing 60°, Grazing 80° Emission
B	5/16/2014	overview, Au4f, Na1s, O1s	XPS	20140516_NaAu2_B_1L_O2	1L O ₂ exposure	Bk 1, pg 137	Al Source; Normal, Grazing 60°, Grazing 80° Emission
		overview, Au4f, Na1s, O1s	XPS	20140516_NaAu2_B_1L(2L)_O 2	add'l 1L O ₂ exposure	Bk 1, pg 137-138	Al Source; Normal, Grazing 60°, Grazing 80° Emission
		overview, Au4f, Na1s, O1s	XPS	20140516_NaAu2_B_3L_O2	add'l 3L O ₂ exposure	Bk 1, pg 138-139	Al Source; Normal, Grazing 60°, Grazing 80° Emission
		overview, Au4f, Na1s, O1s	XPS	20140516_NaAu2_B_5L_O2	add'l 5L O ₂ exposure	Bk 1, pg 139	Al Source; Normal, Grazing 60°, Grazing 80° Emission
		overview, Au4f, Na1s, O1s	XPS	20140516_NaAu2_B_15L_O2	add'l 15L O ₂ exposure	Bk 1, pg 139-140	Al Source; Normal, Grazing 60°, Grazing 80° Emission
		overview, Au4f, Na1s, O1s	XPS	20140516_NaAu2_B_25L_O2	add'l 25L O ₂ exposure	Bk 1, pg 140-141	Al Source; Normal, Grazing 60°, Grazing 80° Emission
		Au4f, Na1s, O1s	XPD	20140516_NaAu2_B_50L_O2_ XPD	XPD of surface after 50L oxygen exposure	Bk 1, pg 141	Al Source

Table 5. NaAu₂ experiments EMPA continued

Sample	Date	Spectrum/ Image	Instru.	Filename	Details	Book #, Page #	Notes
B	5/19/2014	overview, Au4f, Na1s, O1s, C1s	XPS	20140519_NaAu2_B_10minS_4 0minA220C_Clean	two 5 min sputters, 20 min anneal 220C (493K) cycles	Bk 1, pg 141-142	Al Source; Normal, Grazing 60°, Grazing 80° Emission
B	5/20/2014	overview, Au4f, Na1s, O1s, C1s	XPS	20140520_NaAu2_B_1L_CO	1L CO exposure	Bk 1, pg 142-143	Al Source; Normal, Grazing 60°, Grazing 80° Emission
		overview, Au4f, Na1s, O1s, C1s	XPS	20140520_NaAu2_B_19L_CO	add'l 19L CO exposure	Bk 1, pg 143-144	Al Source; Normal, Grazing 60°, Grazing 80° Emission
		overview, Au4f, Na1s, O1s, C1s	XPS	20140520_NaAu2_B_30L_CO	add'l 30L CO exposure	Bk 1, pg 144-145	Al Source; Normal, Grazing 60°, Grazing 80° Emission
		overview, Au4f, Na1s, O1s, C1s	XPS	20140520_NaAu2_B_100L_CO	add'l 100L CO exposure	Bk 1, pg 145-146	Al Source; Normal, Grazing 60°, Grazing 80° Emission
		27.0eV - 100.5eV, 132.0eV	LEED	20140520_Sample B w CO	150L CO exposure	Bk 1, pg 146	first spots ~16eV, final spots ~160eV
B	5/21/2014	overview, Au4f, Na1s, O1s, C1s	XPS	20140521_NaAu2_B_3minS_20 minA220C_Clean	3 min sputter; 20 min anneal 220C (493K)	Bk 1, pg 146-147	Al Source; Normal, Grazing 60°, Grazing 80° Emission
		overview, Au4f, Na1s, O1s, C1s	XPS	20140521_NaAu2_B_100L_CO _220C	100L CO exposure at 220C (493K)	Bk 1, pg 147-148	Al Source; Normal, Grazing 60°, Grazing 80° Emission

Table 5. NaAu₂ experiments EMPA continued

Sample	Date	Spectrum/ Image	Instru.	Filename	Details	Book #, Page #	Notes
B	5/22/2014	overview, Au4f, Na1s, O1s, C1s	XPS	20140522_NaAu2_B_60min_in _air	60 min in air	Bk 1, pg 148-149	Al Source; Normal, Grazing 60°, Grazing 80° Emission
		overview, Au4f, Na1s, O1s, C1s	XPS	20140522_NaAu2_B_10minS_4 0minA220C	two 5 min sputters, 20 min anneal 220C (493K) cycles	Bk 1, pg 149-150	Al Source; Normal, Grazing 60°, Grazing 80° Emission
		overview, Au4f, Na1s, O1s, C1s	XPS	20140522_NaAu2_B_100L_H2 O	100L H ₂ O exposure	Bk 1, pg 150-151	Al Source; Normal, Grazing 60°, Grazing 80° Emission
		overview, Au4f, Na1s, O1s, C1s	XPS	20140522_NaAu2_B_200L_H2 O	add'l 100L H ₂ O exposure	Bk 1, pg 151-152	Al Source; Normal, Grazing 60°, Grazing 80° Emission
B	5/23/2014	overview, Au4f, Na1s, O1s, C1s	XPS	20140523_NaAu2_B_10minS_4 0minA220C	two 5 min sputters, 20 min anneal 220C (493K) cycles	Bk 1, pg 152-153	Al Source; Normal, Grazing 60°, Grazing 80° Emission
		overview, Au4f, Na1s, O1s, C1s	XPS	20140523_NaAu2_B_10L_H2O	10L H ₂ O exposure	Bk 1, pg 153-154	Al Source; Normal, Grazing 60°, Grazing 80° Emission
		overview, Au4f, Na1s, O1s, C1s	XPS	20140523_NaAu2_B_100L_H2 O	add'l 90L H ₂ O exposure	Bk 1, pg 154	Al Source; Normal, Grazing 60°, Grazing 80° Emission
		overview, Au4f, Na1s, O1s, C1s	XPS	20140523_NaAu2_B_500L_H2 O	add'l 400L H ₂ O exposure	Bk 1, pg 155	Al Source; Normal, Grazing 60°, Grazing 80° Emission
		overview, Au4f, Na1s, O1s, C1s	XPS	20140523_NaAu2_B_2000L_H 2O	add'l 1500L H ₂ O exposure	Bk 1, pg 155-156	Al Source; Normal, Grazing 60°, Grazing 80° Emission
		27.0eV - 100.5eV	LEED	20140523_Sample B w H2O	2000L H ₂ O exposure	Bk 1, pg 156	No pattern seen

Table 5. NaAu₂ experiments EMPA continued

Sample	Date	Spectrum/ Image	Instru.	Filename	Details	Book #, Page #	Notes
B	5/25/2014	overview, Au4f, Na1s, O1s, C1s	XPS	20140525_NaAu2_B_10minS_4 0minA220C	two 5 min sputters, 20 min anneal 220C (493K) cycles	Bk 2, pg 1	Al Source; Normal, Grazing 60°, Grazing 80° Emission
		27.0eV - 100.5eV, 132.0eV	LEED	20140525_Sample B w O2	50L H ₂ O exposure	Bk 2, pg 2	No pattern seen
B	5/26/2014	27.0eV - 100.5eV, 132.0eV	LEED	20140526_Sample B Clean	two 5 min sputters, 20 min anneal 220C (493K) cycles	Bk 2, pg 3	Very faint pattern seen; 27.0eV and 28.5eV only
		overview, Au4f, Na1s, O1s, C1s	XPS	20140526_NaAu2_B_8minS_40 minA220C	two 4 min sputters, 20 min anneal 220C (493K) cycles	Bk 2, pg 3	Al Source; Normal, Grazing 60°, Grazing 80° Emission
		overview, Au4f, Na1s, O1s, C1s	XPS	20140526_NaAu2_B_100L_O2	100L O ₂ exposure	Bk 2, pg 4	Al Source; Normal, Grazing 60°, Grazing 80° Emission
		overview, Au4f, Na1s, O1s, C1s	XPS	20140526_NaAu2_B_100L_O2 _0.5WAnn	20 min 0.5W anneal	Bk 2, pg 5	Al Source; Normal, Grazing 60°, Grazing 80° Emission
		overview, Au4f, Na1s, O1s, C1s	XPS	20140526_NaAu2_B_100L_O2 _0.85WAnn	add'l 20 min 0.85W anneal	Bk 2, pg 6	Al Source; Normal, Grazing 60°, Grazing 80° Emission
		overview, Au4f, Na1s, O1s, C1s	XPS	20140526_NaAu2_B_100L_O2 _2.6WAnn	add'l 20 min 2.6W anneal	Bk 2, pg 7	Al Source; Normal, Grazing 60°, Grazing 80° Emission
B	5/27/2014	overview, Au4f, Na1s, O1s, C1s	XPS	20140527_NaAu2_B_10minS_4 0minA220C	two 4 min sputters, 20 min anneal 220C (493K) cycles	Bk 2, pg 8	Al Source; Normal, Grazing 60°, Grazing 80° Emission
		overview, Au4f, Na1s, O1s, C1s	XPS	20140527_NaAu2_B_10minS	10 min sputter only	Bk 2, pg 9	Al Source; Normal, Grazing 60°, Grazing 80° Emission

Table 5. NaAu₂ experiments EMPA continued

Sample	Date	Spectrum/ Image	Instru.	Filename	Details	Book #, Page #	Notes
B	4/3/2015	overview	XPS	20150403_NaAu2B_3minSput_15minAnn200C	3 min sputter, 15 min anneal 200C (473K)	Bk 2, pg 80	Mg Source; Normal Emission; sample finger repolished by Alessandra Beni February 2015
		overview	XPS	20150403_NaAu2_B_6minS_30minA200C	two 3 min sputter, 15 min anneal 200C (473K) cycles	Bk 2, pg 81	Mg Source; Normal Emission
B	4/6/2015	overview	XPS	20150406_NaAu2_B_9minS_45minA200C	3 min sputter, 15 min anneal 200C (473K)	Bk 2, pg 81	Mg Source; Normal Emission
B	4/7/2015	M1 - M47	STM	20150407_NaAu2B_9minS_45minA200C	Scan of surface after 9 min of sputtering and 45 min of annealing 200C (473K)	Bk 2, pg 82	
B	4/8/2015	overview	XPS	20150408_NaAu2_B_9minS_45minA200C	sit overnight	Bk 2, pg 83	Mg Source; Normal Emission
		overview	XPS	20150408_NaAu2_B_9minS_45minA200CAI		Bk 2, pg 83	Al and Mono Al Source; Normal Emission
		overview, Au4f, Na1s, O1s, C1s	XPS	20150408_NaAu2_B_12minS_60minA200C	3 min sputter, 15 min anneal 200C (473K)	Bk 2, pg 84	Mg Source; Normal Emission
B	4/13/2015	overview, Au4f, Na1s, O1s, C1s	XPS	20150413_NaAu2_B_12minS_60minA200C	sit over weekend	Bk 2, pg 86-87	Mg Source; Normal, Grazing 60°, Grazing 80° Emission
B	4/14/2015	overview, Au4f, Na1s, O1s, C1s	XPS	20150414_NaAu2_B_1L_O2	1L O ₂ exposure	Bk 2, pg 87-88	Mg Source; Normal, Grazing 60°, Grazing 80° Emission
		overview, Au4f, Na1s, O1s, C1s	XPS	20150414_NaAu2_B_2L_O2	add'l 1L O ₂ exposure	Bk 2, pg 88	Mg Source; Normal, Grazing 60°, Grazing 80° Emission
		overview, Au4f, Na1s, O1s, C1s	XPS	20150414_NaAu2_B_5L_O2	add'l 3L O ₂ exposure	Bk 2, pg 89	Mg Source; Normal, Grazing 60°, Grazing 80° Emission

Table 5. NaAu₂ experiments EMPA continued

Sample	Date	Spectrum/ Image	Instru.	Filename	Details	Book #, Page #	Notes
B	4/14/2015	overview, Au4f, Na1s, O1s, C1s	XPS	20150414_NaAu2_B_10L_O2	add'l 5L O ₂ exposure	Bk 2, pg 89-90	Mg Source; Normal, Grazing 60°, Grazing 80° Emission
		overview, Au4f, Na1s, O1s, C1s	XPS	20150414_NaAu2_B_25L_O2	add'l 15L O ₂ exposure	Bk 2, pg 90	Mg Source; Normal, Grazing 60°, Grazing 80° Emission
		overview, Au4f, Na1s, O1s, C1s	XPS	20150414_NaAu2_B_50L_O2	add'l 25L O ₂ exposure	Bk 2, pg 91	Mg Source; Normal, Grazing 60°, Grazing 80° Emission
B	4/15/2015	overview, Au4f, Na1s, O1s, C1s	XPS	20150415_NaAu2_B_18minS_90minA200C	two 3 min sputter, 15 min anneal 200C (473K) cycles	Bk 2, pg 92	Mg Source; Normal, Grazing 60°, Grazing 80° Emission
B	4/16/2015	overview, Au4f, Na1s, O1s, C1s	XPS	20150416_NaAu2_B_1L_O2	1L O ₂ exposure	Bk 2, pg 92-93	Mg Source; Normal, Grazing 60°, Grazing 80° Emission
		overview, Au4f, Na1s, O1s, C1s	XPS	20150416_NaAu2_B_2L_O2	add'l 1L O ₂ exposure	Bk 2, pg 93	Mg Source; Normal, Grazing 60°, Grazing 80° Emission
		overview, Au4f, Na1s, O1s, C1s	XPS	20150416_NaAu2_B_5L_O2	add'l 3L O ₂ exposure	Bk 2, pg 94	Mg Source; Normal, Grazing 60°, Grazing 80° Emission
		overview, Au4f, Na1s, O1s, C1s	XPS	20150416_NaAu2_B_10L_O2	add'l 5L O ₂ exposure	Bk 2, pg 94-95	Mg Source; Normal, Grazing 60°, Grazing 80° Emission
		overview, Au4f, Na1s, O1s, C1s	XPS	20150416_NaAu2_B_25L_O2	add'l 15L O ₂ exposure	Bk 2, pg 95	Mg Source; Normal, Grazing 60°, Grazing 80° Emission
		overview, Au4f, Na1s, O1s, C1s	XPS	20150416_NaAu2_B_50L_O2	add'l 25L O ₂ exposure	Bk 2, pg 96	Mg Source; Normal, Grazing 60°, Grazing 80° Emission

Table 5. NaAu₂ experiments EMPA continued

Sample	Date	Spectrum/ Image	Instru.	Filename	Details	Book #, Page #	Notes
B	4/16/2015	overview, Au4f, Na1s, O1s, C1s	XPS	20150416_NaAu2_B_O2_20minA200C	20 min anneal 200C (473K)	Bk 2, pg 96-97	Mg Source; Normal, Grazing 60°, Grazing 80° Emission
B	4/17/2015	overview, Au4f, Na1s, O1s, C1s	XPS	20150417_NaAu2_B_24minS_140minA200C	two 3 min sputter, 15 min anneal 200C (473K) cycles	Bk 2, pg 97-98	Mg Source; Normal, Grazing 60°, Grazing 80° Emission
B	4/20/2015	overview, Au4f, Na1s, O1s, C1s	XPS	20150420_NaAu2_B_1L_O2_A1	1L O ₂ exposure	Bk 2, pg 98-99	Al Source; Normal, Grazing 60°, Grazing 80° Emission
		overview, Au4f, Na1s, O1s, C1s	XPS	20150420_NaAu2_B_2L_O2_A1	add'l 1L O ₂ exposure	Bk 2, pg 99	Al Source; Normal, Grazing 60°, Grazing 80° Emission
		overview, Au4f, Na1s, O1s, C1s	XPS	20150420_NaAu2_B_5L_O2_A1	add'l 3L O ₂ exposure	Bk 2, pg 100	Al Source; Normal, Grazing 60°, Grazing 80° Emission
		overview, Au4f, Na1s, O1s, C1s	XPS	20150420_NaAu2_B_10L_O2_Al	add'l 5L O ₂ exposure	Bk 2, pg 100-101	Al Source; Normal, Grazing 60°, Grazing 80° Emission
		overview, Au4f, Na1s, O1s, C1s	XPS	20150420_NaAu2_B_25L_O2_Al	add'l 15L O ₂ exposure	Bk 2, pg 101	Al Source; Normal, Grazing 60°, Grazing 80° Emission
		overview, Au4f, Na1s, O1s, C1s	XPS	20150420_NaAu2_B_50L_O2_Al	add'l 25L O ₂ exposure	Bk 2, pg 102	Al Source; Normal, Grazing 60°, Grazing 80° Emission
B	4/21/2015	overview, Au4f, Na1s, O1s, C1s	XPS	20150421_NaAu2_B_32minS_170minA200C_Al	two 4 min sputter, 15 min anneal 200C (473K) cycles	Bk 2, pg 103	Al Source; Normal, Grazing 60°, Grazing 80° Emission
		overview, Au4f, Na1s, O1s, C1s	XPS	20150421_NaAu2_B_32minS_170minA200C_Mg	two 4 min sputter, 15 min anneal 200C (473K) cycles	Bk 2, pg 103-104	Mg Source; Normal, Grazing 60°, Grazing 80° Emission

Table 5. NaAu₂ experiments EMPA continued

Sample	Date	Spectrum/ Image	Instru.	Filename	Details	Book #, Page #	Notes
B	4/22/2015	overview, Au4f, Na1s, O1s, C1s	XPS	20150422_NaAu2_B_50L_O2_ Al	50L O ₂ exposure	Bk 2, pg 104	Al Source; Normal, Grazing 60°, Grazing 80° Emission
		overview, Au4f, Na1s, O1s, C1s	XPS	20150422_NaAu2_B_50L_O2_ Mg	50L O ₂ exposure	Bk 2, pg 105	Mg Source; Normal, Grazing 60°, Grazing 80° Emission
		overview, Au4f, Na1s, O1s, C1s	XPS	20150422_NaAu2_B_O2_20mi nA150C_Al	w/O ₂ after 20 min 423K anneal	Bk 2, pg 105-106	Al Source; Normal, Grazing 60°, Grazing 80° Emission
		overview, Au4f, Na1s, O1s, C1s	XPS	20150422_NaAu2_B_O2_20mi nA150C_Mg	w/O ₂ after 20 min 423K anneal	Bk 2, pg 106	Mg Source; Normal, Grazing 60°, Grazing 80° Emission
		overview, Au4f, Na1s, O1s, C1s	XPS	20150422_NaAu2_B_O2_20mi nA200C_Al	w/O ₂ after addt'l 20 min 473K anneal	Bk 2, pg 106-107	Al Source; Normal, Grazing 60°, Grazing 80° Emission
		overview, Au4f, Na1s, O1s, C1s	XPS	20150422_NaAu2_B_O2_20mi nA200C_Mg	w/O ₂ after addt'l 20 min 473K anneal	Bk 2, pg 107	Mg Source; Normal, Grazing 60°, Grazing 80° Emission
B	4/23/2015	overview, Au4f, Na1s, O1s, C1s	XPS	20150423_NaAu2_B_38minS_2 40minA200C_Al	two 3 min sputter, 15 min anneal 200C (473K) cycles	Bk 2, pg 108	Al Source; Normal, Grazing 60°, Grazing 80° Emission
		overview, Au4f, Na1s, O1s, C1s	XPS	20150423_NaAu2_B_38minS_2 40minA200C_Mg	two 3 min sputter, 15 min anneal 200C (473K) cycles	Bk 2, pg 109	Mg Source; Normal, Grazing 60°, Grazing 80° Emission

Table 5. NaAu₂ experiments EMPA continued

Sample	Date	Spectrum/ Image	Instru.	Filename	Details	Book #, Page #	Notes
B	4/24/2015	overview, Au4f, Na1s, O1s, C1s	XPS	20150424_NaAu2_B_20minA1 50C_A1	20 min, 423K anneal	Bk 2, pg 109-110	Al Source; Normal, Grazing 60°, Grazing 80° Emission
		overview, Au4f, Na1s, O1s, C1s	XPS	20150424_NaAu2_B_20minA1 50C_Mg	20 min, 423K anneal	Bk 2, pg 110	Mg Source; Normal, Grazing 60°, Grazing 80° Emission
		overview, Au4f, Na1s, O1s, C1s	XPS	20150424_NaAu2_B_20minA2 00C_A1	addt'l 20 min, 473K anneal	Bk 2, pg 111	Al Source; Normal, Grazing 60°, Grazing 80° Emission
		overview, Au4f, Na1s, O1s, C1s	XPS	20150424_NaAu2_B_20minA2 00C_Mg	addt'l 20 min, 473K anneal	Bk 2, pg 111-112	Mg Source; Normal, Grazing 60°, Grazing 80° Emission
B	4/28/2015	overview, Au4f, Na1s, O1s, C1s	XPS	20150428_NaAu2_B_10L_H2O _Mg	10L H ₂ O exposure	Bk 2, pg 113	Mg Source; Normal, Grazing 60°, Grazing 80° Emission
		overview, Au4f, Na1s, O1s, C1s	XPS	20150428_NaAu2_B_25L_H2O _Mg	addt'l 15L H ₂ O exposure	Bk 2, pg 113-114	Mg Source; Normal, Grazing 60°, Grazing 80° Emission
		overview, Au4f, Na1s, O1s, C1s	XPS	20150428_NaAu2_B_50L_H2O _Mg	addt'l 25L H ₂ O exposure	Bk 2, pg 114	Mg Source; Normal, Grazing 60°, Grazing 80° Emission
		overview, Au4f, Na1s, O1s, C1s	XPS	20150428_NaAu2_B_100L_H2 O_Mg	addt'l 50L H ₂ O exposure	Bk 2, pg 115	Mg Source; Normal, Grazing 60°, Grazing 80° Emission
		overview, Au4f, Na1s, O1s, C1s	XPS	20150428_NaAu2_B_250L_H2 O_Mg	addt'l 150L H ₂ O exposure	Bk 2, pg 115-116	Mg Source; Normal, Grazing 60°, Grazing 80° Emission
B	4/29/2015	overview, Au4f, Na1s, O1s, C1s	XPS	20150429_NaAu2_B_44minS_3 10minA200C	two 3 min sputter, 15 min anneal 200C (473K) cycles	Bk 2, pg 116-117	Mg Source; Normal, Grazing 60°, Grazing 80° Emission

Table 5. NaAu₂ experiments EMPA continued

Sample	Date	Spectrum/ Image	Instru.	Filename	Details	Book #, Page #	Notes
B	4/30/2015	overview, Au4f, Na1s, O1s, C1s	XPS	20150430_NaAu2_B_10L_H2O _Mg	10L H ₂ O exposure	Bk 2, pg 117-118	Mg Source; Normal, Grazing 60°, Grazing 80° Emission
		overview, Au4f, Na1s, O1s, C1s	XPS	20150430_NaAu2_B_25L_H2O _Mg	addt'l 15L H ₂ O exposure	Bk 2, pg 118	Mg Source; Normal, Grazing 60°, Grazing 80° Emission
		overview, Au4f, Na1s, O1s, C1s	XPS	20150430_NaAu2_B_50L_H2O _Mg	addt'l 25L H ₂ O exposure	Bk 2, pg 119	Mg Source; Normal, Grazing 60°, Grazing 80° Emission
		overview, Au4f, Na1s, O1s, C1s	XPS	20150430_NaAu2_B_100L_H2 O_Mg	addt'l 50L H ₂ O exposure	Bk 2, pg 119-120	Mg Source; Normal, Grazing 60°, Grazing 80° Emission
		overview, Au4f, Na1s, O1s, C1s	XPS	20150430_NaAu2_B_250L_H2 O_Mg	addt'l 150L H ₂ O exposure	Bk 2, pg 120	Mg Source; Normal, Grazing 60°, Grazing 80° Emission
B	5/1/2015	overview, Au4f, Na1s, O1s, C1s	XPS	20150501_NaAu2_B_50minS_3 40minA200C	two 3 min sputter, 15 min anneal 200C (473K) cycles	Bk 2, pg 121	Mg Source; Normal, Grazing 60°, Grazing 80° Emission
		overview, Au4f, Na1s, O1s, C1s	XPS	20150501_NaAu2_B_250L_H2 O	250L H ₂ O exposure	Bk 2, pg 122	Mg Source; Normal, Grazing 60°, Grazing 80° Emission
		overview, Au4f, Na1s, O1s, C1s	XPS	20150501_NaAu2_B_H2O_20m inA150C	w/H ₂ O after 20 min 423K anneal	Bk 2, pg 122-123	Mg Source; Normal, Grazing 60°, Grazing 80° Emission
		overview, Au4f, Na1s, O1s, C1s	XPS	20150501_NaAu2_B_H2O_20m inA200C	w/H ₂ O after 20 min 473K anneal	Bk 2, pg 123	Mg Source; Normal, Grazing 60°, Grazing 80° Emission

Table 5. NaAu₂ experiments EMPA continued

Sample	Date	Spectrum/ Image	Instru.	Filename	Details	Book #, Page #	Notes
B	5/4/2015	overview, Au4f, Na1s, O1s, C1s	XPS	20150504_NaAu2_B_56minS_4 10minA200C_Mg	two 3 min sputter, 15 min anneal 200C (473K) cycles	Bk 2, pg 124	Mg Source; Normal, Grazing 60°, Grazing 80° Emission
		overview, Au4f, Na1s, O1s, C1s	XPS	20150504_NaAu2_B_56minS_4 10minA200C_Al	two 3 min sputter, 15 min anneal 200C (473K) cycles	Bk 2, pg 125	Al Source; Normal, Grazing 60°, Grazing 80° Emission
		overview, Au4f, Na1s, O1s, C1s	XPS	20150504_NaAu2_B_50L_O2_ Mg	50L O ₂ exposure	Bk 2, pg 125-126	Mg Source; Normal, Grazing 60°, Grazing 80° Emission
B	5/5/2015	overview, Au4f, Na1s, O1s, C1s	XPS	20150505_NaAu2_B_50L_sit_o vernigh	sit overnight with O ₂	Bk 2, pg 126	Mg Source; Normal, Grazing 60°, Grazing 80° Emission
B	5/5/2015	overview, Au4f, Na1s, O1s, C1s	XPS	20150505_NaAu2_B_62minS_4 40minA200C	two 3 min sputter, 15 min anneal 200C (473K) cycles	Bk 2, pg 127	Mg Source; Normal, Grazing 60°, Grazing 80° Emission
		overview, Au4f, Na1s, O1s, C1s	XPS	20150505_NaAu2_B_100L_O2_ _423K	100L O ₂ exposure at 423K	Bk 2, pg 128	Mg Source; Normal, Grazing 60°, Grazing 80° Emission
B	5/5/2015	overview, Au4f, Na1s, O1s, C1s	XPS	20150505_NaAu2_B_det_10mi nS_10minA250C	10 min sputter and 10 min 523K anneal	Bk 2, pg 128	Mg Source; Normal Emission
B	5/6/2015	overview, Au4f, Na1s, O1s, C1s	XPS	20150506_NaAu2_B_deteriorat ed	20 min sputter and 20 min 700K anneal	Bk 2, pg 129	Mg Source; Normal, Grazing 60°, Grazing 80° Emission
		overview, Au4f, Na1s, O1s, C1s	XPS	20150506_NaAu2_B_deteriorat ed_50L_O2	50L O ₂ exposure	Bk 2, pg 130	Mg Source; Normal, Grazing 60°, Grazing 80° Emission
		overview, Au4f, Na1s, O1s, C1s	XPS	20150506_NaAu2_B_O2_20mi nA150C	20 min, 423K anneal	Bk 2, pg 130-131	Mg Source; Normal, Grazing 60°, Grazing 80° Emission

Table 5. NaAu₂ experiments EMPA continued

Sample	Date	Spectrum/ Image	Instru.	Filename	Details	Book #, Page #	Notes
B	5/6/2015	overview, Au4f, Na1s, O1s, C1s	XPS	20150506_NaAu2_B_O2_20minA200C	20 min, 473K anneal	Bk 2, pg 131	Mg Source; Normal, Grazing 60°, Grazing 80° Emission
B	5/11/2015	overview, Au4f, Na1s, O1s, C1s	XPS	20150511_NaAu2_B_deteriorated	20 min sputter and 30 min 700K anneal	Bk 2, pg 136-137	Mg Source; Normal, Grazing 60°, Grazing 80° Emission
B	5/12/2015	overview, Au4f, Na1s, O1s, C1s	XPS	20150512_NaAu2_B_deteriorated_surface	45 min sputter and 20 min 750K anneal	Bk 2, pg 138	Mg Source; Normal Emission
		overview, Au4f, Na1s, O1s, C1s	XPS	20150512_NaAu2_B_3minS_deteriorated	3 min sputter	Bk 2, pg 139	Mg Source; Normal Emission
		overview, Au4f, Na1s, O1s, C1s	XPS	20150512_NaAu2_B_10minA200C_deteriorated	10 min 473K anneal	Bk 2, pg 139	Mg Source; Normal, Grazing 60°, Grazing 80° Emission
B	5/13/2015	overview, Au4f, Na1s, O1s, C1s	XPS	20150513_NaAu2_B_deteriorated_50L_O2	50L O ₂ exposure	Bk 2, pg 140	Mg Source; Normal, Grazing 60°, Grazing 80° Emission
		overview, Au4f, Na1s, O1s, C1s	XPS	20150513_NaAu2_B_20minA150C	20 min, 423K anneal	Bk 2, pg 140-141	Mg Source; Normal, Grazing 60°, Grazing 80° Emission
		overview, Au4f, Na1s, O1s, C1s	XPS	20150513_NaAu2_B_20minA200C	20 min, 473K anneal	Bk 2, pg 141-142	Mg Source; Normal, Grazing 60°, Grazing 80° Emission
C	4/2/2014	overview	XPS	20140402_NaAu2_C_as_is	Sample alignment	Bk 1, pg 102	Al Source; Normal and Grazing 60° Emission
		overview	XPS	20140402_NaAu2_C_15min	15 min sputter	Bk 1, pg 102	Al Source; Grazing 60° Emission
		overview	XPS	20140402_NaAu2_C_30min	add'l 15 min sputter (30 min total)	Bk 1, pg 103	Al Source; Grazing 60° Emission

Table 5. NaAu₂ experiments EMPA continued

Sample	Date	Spectrum/ Image	Instru.	Filename	Details	Book #, Page #	Notes
C	4/2/2014	overview	XPS	20140402_NaAu2_C_60min	add'l 30 min sputter (60 min total)	Bk 1, pg 103	Al Source; Grazing 60° Emission
		overview	XPS	20140402_NaAu2_C_75minSput_10minAnn150C	add'l 15 min sputter; 10 min 150C (423K) anneal	Bk 1, pg 103	Al Source; Grazing 60° Emission
		overview	XPS	20140402_NaAu2_C_90minSput_10minanneal160C	add'l 15 min sputter; 10 min 160C (433K) anneal	Bk 1, pg 104	Al Source; Grazing 60° Emission
C	4/3/2014	overview	XPS	20140402_NaAu2_C_105minSput_13hAnn160C	add'l 15 min sputter; add'l 13 hour 136C (409K) anneal	Bk 1, pg 104	Al Source; Grazing 60° Emission
		13.3eV - 108.4eV	LEED	20140403_Sample C	10 min sputter, 10 min anneal 155C (428K)	Bk 1, pg 104-105	first spots ~13.2eV, final spots ~125eV
		M1 - M13	STM	20140403_NaAu2_C	Scan of surface after one 10 min sputter, one 160C (433K) 10 min anneal	Bk 1, pg 105	Turbo On
C	4/4/2014	M1 - M57	STM	20140404_NaAu2_C_135minSput_14.5hrann	Scan of surface after one 10 min sputter, one 160C (433K) 30 min anneal	Bk 1, pg 105	Turbo On
C	4/17/2014	Au4f, Na1s	XPD	20140417_NaAu2_C_15minSput_20minAnn205C	XPD of surface; after one 15 min sputter, one 205C (478K) 20 min anneal	Bk 1, pg 115	Al Source
C	4/18/2014	M1 - M21	STM	20140418_NaAu2_C_5minSput_20minAnn205C	Scan of surface after one 5 min sputter, one 205C (478K) 20 min anneal	Bk 1, pg 116	small terraces? Turbo On
		overview, Au4f, Na1s	XPS	20140418_NaAu2_C_5minSput_20minAnn205C	after STM	Bk 1, pg 116	Al Source; Normal and Grazing 60° Emission
C	4/21/2014	M1 - M29	STM	20140421_NaAu2_C_5minSput_20minAnn240C	Scan of surface after one 5 min sputter, one 240C (513K) 20 min anneal	Bk 1, pg 116	small terraces? Turbo On
		overview, Au4f, Na1s	XPS	20140421_NaAu2_C_5minSput_20minAnn240C	after STM	Bk 1, pg 117	Al Source; Normal and Grazing 60° Emission

Table 5. NaAu₂ experiments EMPA continued

Sample	Date	Spectrum/ Image	Instru.	Filename	Details	Book #, Page #	Notes
C	4/22/2014	M1 - M24	STM	20140422_NaAu2_C_5minSput _40minAnn210C	Scan of surface after one 5 min sputter, one 210C (483K) 40 min anneal	Bk 1, pg 117	Turbo On
		overview, Au4f, Na1s	XPS	20140422_NaAu2_C_5minSput _40minAnn210C	after STM	Bk 1, pg 117	Al Source; Normal and Grazing 60° Emission
C	4/23/2014	27.0eV - 100.5eV	LEED	20140423_Sample C	5 min sputter, 40 min anneal 215C (488K)	Bk 1, pg 118	first spots ~15eV, final spots ~115eV
		overview, Au4f, Na1s	XPS	20140423_NaAu2_C_5minSput _40minAnn215C	after LEED	Bk 1, pg 118	Al Source; Normal and Grazing 60° Emission
			SEM- EDX			Bk 1, pg 119	mapping taken by Dr. Juan-Ramon Sanchez
C	4/25/2014	27.0eV - 100.5eV	LEED	20140425_Sample C	5 min sputter, 20 min anneal 210C (483K)	Bk 1, pg 119	first spots ~13.5eV, final spots ~156.5eV
		M1 - M28	STM	20140425_NaAu2_C_5minSput _40minAnn260C	Scan of surface after one 5 min sputter, one 260C (533K) 40 min anneal	Bk 1, pg 120	Turbo On
		27.0eV - 100.5eV, 132.7eV	LEED	20140425_Sample C 260C	after STM	Bk 1, pg 120	first spots ~17eV, final spots ~148eV
		overview, Au4f, Na1s	XPS	20140425_NaAu2_C_5minSput _40minAnn260C	after STM & LEED	Bk 1, pg 120	Al Source; Normal and Grazing 60° Emission
C	4/28/2014	M1 - M29	STM	20140428_NaAu2_C_5minSput _60hrAnn200C	Scan of surface after one 5 min sputter, one 200C (473K) 60 hour anneal	Bk 1, pg 120	Turbo On
		27.0eV - 100.5eV	LEED	20140428_Sample C 60 hr anneal	after STM	Bk 1, pg 121	first spots ~16eV, final spots ~117eV
		overview, Au4f, Na1s	XPS	20140428_NaAu2_C_5minSput _60hrAnn200C	after STM & LEED	Bk 1, pg 121	Al Source; Normal and Grazing 60° Emission
C	4/29/2014	Au4f, Na1s	XPD	20140429_NaAu2_C_5minSput _60hrAnn200C_XPD	XPD of surface; after 200C (473K) 60 hour anneal	Bk 1, pg 121	Al Source

Table 5. NaAu₂ experiments EMPA continued

Sample	Date	Spectrum/ Image	Instru.	Filename	Details	Book #, Page #	Notes
C	5/2/2014	M1 - M104	LT-STM	20140502_NaAu2_C_475K_10minAnn	Scan of surface after two 10 min sputters, two 200C (475K) 10 min anneals	Bk 1, pg 124	ARPES Chamber
C	5/5/2014	overview	XPS	20140502_NaAu2_C_200C	Full grazing and full normal scans; after LT-STM	Bk 1, pg 125	Al Source; Normal and Grazing 60° Emission; ARPES Chamber
C	5/6/2014	overview, Au4f, Na1s, O1s, C1s	XPS	20140506_NaAu2_C_as_in_60min_in_air	60 min in air	Bk 1, pg 125	Al Source; Normal and Grazing 60° Emission
		overview, Au4f, Na1s	XPS	20140506_NaAu2_C_5minSput_20minAnn215C	sputter with 215C (490K) anneal	Bk 1, pg 126	Al Source; Normal and Grazing 60° Emission
C	4/6/2015	overview	XPS	20150406_NaAu2_C_3minS_15minA200C	3 min sputter, 15 min anneal 200C (473K)	Bk 2, pg 81	Al and Mg Sources; Normal Emission; sample finger repolished by Alessandra Beni February 2015
C	4/7/2015	M1 - M42	STM	20150407_NaAu2_C_3minSput_15minAnn200C	Scan of surface after 3 min of sputtering and 15 min of annealing 200C (473K)	Bk 2, pg 82	
C	4/9/2015	M1 - M107	STM	20150409_NaAu2_C_6minS_30minA200C_0.05rr	Scan of surface after 6 min of sputtering and 30 min of annealing 200C (473K)	Bk 2, pg 84-85	0.05 A/min cooling rate (for second 15 min anneal)
		overview, Au4f, Na1s, O1s, C1s	XPS	20150409_NaAu2_C_6minS_30minA200Crr0.05	3 min sputter, 15 min anneal 200C (473K)	Bk 2, pg 85	Mg Source; Normal and Grazing 60° Emission
C	4/10/2015	M1 - M91	STM	20150410_NaAu2_C_9minS_45minA200Crr0.05	Scan of surface after addt'l 3 min of sputtering and 15 min of annealing 200C (473K)	Bk 2, pg 85-86	0.05 A/min cooling rate
		overview, Au4f, Na1s, O1s, C1s	XPS	20150410_NaAu2_C_9minS_45minA200Crr05	3 min sputter, 15 min anneal 200C (473K)	Bk 2, pg 86	Mg Source; Normal and Grazing 60° Emission

Table 5. NaAu₂ experiments EMPA continued

Sample	Date	Spectrum/ Image	Instru.	Filename	Details	Book #, Page #	Notes
C	5/7/2015	overview, Au4f, Na1s, O1s, C1s	XPS	20150507_NaAu2_C_12minS_6 0minA200C	3 min sputter, 15 min anneal 200C (473K)	Bk 2, pg 132	Mg Source; Normal, Grazing 60°, Grazing 80° Emission
C	5/8/2015	overview, Au4f, Na1s, O1s, C1s	XPS	20150508_NaAu2_C_1L_CO2	1L CO ₂ exposure	Bk 2, pg 133	Mg Source; Normal, Grazing 60°, Grazing 80° Emission
		overview, Au4f, Na1s, O1s, C1s	XPS	20150508_NaAu2_C_10L_CO2	addt'l 9L CO ₂ exposure	Bk 2, pg 133-134	Mg Source; Normal, Grazing 60°, Grazing 80° Emission
		overview, Au4f, Na1s, O1s, C1s	XPS	20150508_NaAu2_C_50L_CO2	addt'l 40L CO ₂ exposure	Bk 2, pg 135	Mg Source; Normal, Grazing 60°, Grazing 80° Emission
		overview, Au4f, Na1s, O1s, C1s	XPS	20150508_NaAu2_C_150L_CO 2	addt'l 100L CO ₂ exposure	Bk 2, pg 135-136	Mg Source; Normal, Grazing 60°, Grazing 80° Emission
C	5/11/2015	overview, Au4f, Na1s, O1s, C1s	XPS	20150511_NaAu2_C_15minS_7 5minA200C	3 min sputter, 15 min anneal 200C (473K)	Bk 2, pg 137	Mg Source; Normal, Grazing 60°, Grazing 80° Emission
C	5/12/2015	overview, Au4f, Na1s, O1s, C1s	XPS	20150512_NaAu2_C_peak broadness comparison	for peak broadness comparison	Bk 2, pg 138	Mono Al Source; Normal, Grazing 60°, Grazing 80° Emission; Pass Energy = 20.0eV
D	4/29/2014	M1 - M78	LT- STM	20140429_NaAu2_D_775K_4cy cles	Scan of surface after four cycles of 10 min sputter, 500C (773K) flash anneals	Bk 1, pg 122	flat areas, "bubbled" surface; ARPES Chamber
		M1 - M62	LT- STM	20140429_NaAu2_D_775K_10 minAnn	Scan of surface after two cycles of 10 min sputter, 500C (773K) 10 min anneals	Bk 1, pg 122	unknown source causing vibration; ARPES Chamber

Table 5. NaAu₂ experiments EMPA continued

Sample	Date	Spectrum/ Image	Instru.	Filename	Details	Book #, Page #	Notes
D	4/30/2014	overview	XPS	20140429_NaAu2_D_500C	10 min sputters, 500C (773K) 10 min anneals	Bk 1, pg 123	Al Source; Normal and Grazing 60° Emission; ARPES Chamber
		M1 - M54	LT-STM	20140430_NaAu2_D_825K_10 minAnn	Scan of surface after two cycles of 10 min sputter, 550C (823K) 10 min anneals	Bk 1, pg 123	possible terraces? "bubbled" surface; ARPES Chamber
D	5/1/2014	M1 - M66	LT-STM	20140501_NaAu2_D_825K_15 minAnn	Scan of surface after two cycles of 10 min sputter, 550C (823K) 15 min anneals	Bk 1, pg 124	possible terraces? "bubbled" surface; ARPES Chamber
D	5/2/2014	overview	XPS	20140501_NaAu2_D_500C	10 min sputters, 550C (823K) 10 min anneals	Bk 1, pg 124	Al Source; Normal and Grazing 60° Emission; ARPES Chamber

Table 6. NaAu₂ experiments conducted at Iowa State University (DOE Chamber – 224 SPH or TPD Chamber – 217 SPH)

Sample	Chamber	Date	Spectrum/ Image	Instru.	Filename	Details	Book #, Page #	Notes
A	DOE	3/6/2014	M1 - M20	STM	20140306_quick scan rm temp	Scan of surface after one sputter, no anneal	Bk 1, pg 84	Turbo On; rough (expected)
A	DOE	3/9/2014	M1 - M18	STM	20140309_400K anneal	Scan of surface after one sputter, one 400K anneal	Bk 1, pg 88	Turbo On; fast ramp rate; smoother?
A	DOE	3/10/2014	M1 - M18	STM	20140310_400K anneal	Scan of surface after one sputter, one 400K anneal	Bk 1, pg 88	Turbo On; slow ramp rate; smoother?
			M1 - M16	STM	20140310_400K anneal #2	Scan of surface after one sputter, one 400K flash anneal	Bk 1, pg 89	Turbo On; slower ramp rate
			M1 - M9	STM	20140310_450K anneal	Scan of surface after one sputter, one 450K flash anneal	Bk 1, pg 89	Turbo On
A	DOE	3/11/2014	M1 - M9	STM	20140311_500K anneal	Scan of surface after one sputter, one 500K flash anneal	Bk 1, pg 90	Turbo On
			M1 - M9	STM	20140311_550K anneal	Scan of surface after one sputter, one 550K flash anneal	Bk 1, pg 91	Turbo On
A	DOE	3/12/2014	M1 - M9	STM	20140312_600K anneal	Scan of surface after one sputter, one 600K flash anneal	Bk 1, pg 92	Turbo On; large features!!
A	DOE	3/13/2014	M1 - M14	STM	20140313_650K anneal	Scan of surface after one sputter, one 650K flash anneal	Bk 1, pg 92	Turbo On; large features, some clumps
			M1 - M18	STM	20140313_700K anneal	Scan of surface after one sputter, one 700K flash anneal	Bk 1, pg 93	Turbo On
A	DOE	3/14/2014		Mass Spec	20140314_Na check	Mass spec during peak of heating	Bk 1, pg 93	Pressure was high! Na present?, it was not
			M1 - M25	STM	20140314_750K anneal	Scan of surface after one sputter, one 750K flash anneal	Bk 1, pg 93-94	Turbo On

Table 6. NaAu₂ experiments ISU continued

Sample	Chamber	Date	Spectrum/ Image	Instru.	Filename	Details	Book #, Page #	Notes
A	DOE	3/15/2014		Mass Spec	20140315_Na check	Mass spec during peak of heating	Bk 1, pg 94	Pressure was high! Na present?, it was not
			M1 - M26	STM	20140315_800K anneal	Scan of surface after one sputter, one 800K flash anneal	Bk 1, pg 94	Turbo On
A	DOE	3/16/2014		Mass Spec	20140316_Na check	Mass spec during peak of heating	Bk 1, pg 95	Pressure was high! Na present?, it was not
			M1 - M25	STM	20140316_850K anneal	Scan of surface after one sputter, one 850K flash anneal	Bk 1, pg 95	Turbo On
A		3/21/2014	overview, Au4f, Na1s, O1s, C1s	XPS	files: Angeregg XPS - mar2114	as in, several 1 min etches + depth profiling	Bk 1, pg 97	Done by Jim Anderegg
A		3/27/2014	overview	Auger	files: Angeregg Auger - mar272014	as in, depth profiling, EDS	Bk 1, pg 100	Done by Jim Anderegg
B	DOE	3/25/2014	overview	XPS	20140325_NaAu2 as transferred_Al	as transferred in	Bk 1, pg 98	Al Source
			overview	XPS	20140325_NaAu2 as transferred_Mg	as transferred in	Bk 1, pg 98	Mg Source
			M1 - M29	STM	20140325_NaAu2 as transferred	Scan of surface as transferred in after XPS	Bk 1, pg 98	Turbo On; flatter with rough patches
B	DOE	3/26/2014	overview, Au4f, Na1s, O1s, C1s	XPS	20140326_01	3 min sputter	Bk 1, pg 98-99	Mg Source
			M1 - M23	STM	20140326_400K	Scan of surface after one sputter and one 400K flash anneal	Bk 1, pg 99	Turbo On; rough surface

Table 6. NaAu₂ experiments ISU continued

Sample	Chamber	Date	Spectrum/ Image	Instru.	Filename	Details	Book #, Page #	Notes
B	DOE	3/27/2014		Mass Spec	20140327_Na check	Mass spec during peak of heating	Bk 1, pg 101	Pressure was high! Na present?, it was not
	DOE		M1 - M34	STM	20140327_400K 10 min	Scan of surface after one sputter and one 400K 10 min anneal	Bk 1, pg 101	Turbo On; rough(!) surface
D	TPD	9/9/2014		TPD	20140909a	Heating Rate: 2K/s	Bk 2, pg 32	
				TPD	20140909b	Heating Rate: 2K/s	Bk 2, pg 32	
				TPD	20140909c	Heating Rate: 2K/s	Bk 2, pg 32	
				TPD	20140909d	Heating Rate: 2K/s	Bk 2, pg 32	
				TPD	20140909e	Heating Rate: 2K/s	Bk 2, pg 32	
				TPD	20140909f	Heating Rate: 2K/s	Bk 2, pg 32	
				TPD	20140909g	Heating Rate: 2K/s	Bk 2, pg 33	
				TPD	20140909h	Heating Rate: 2K/s	Bk 2, pg 33	
				TPD	20140909i	Heating Rate: 2K/s	Bk 2, pg 33	
				TPD	20140909j	Heating Rate: 2K/s	Bk 2, pg 33	Mass spec turned off between runs J and K
				TPD	20140909k	Heating Rate: 2K/s	Bk 2, pg 33	
				TPD	20140909l	Heating Rate: 2K/s	Bk 2, pg 33	
				TPD	20140909m	Heating Rate: 0.5K/s	Bk 2, pg 33	
				TPD	20140909n	Heating Rate: 0.5K/s	Bk 2, pg 33	
				TPD	20140909o	Heating Rate: 0.5K/s	Bk 2, pg 34	
				TPD	20140909p	Heating Rate: 4K/s	Bk 2, pg 34	
	TPD	20140909q	Heating Rate: 4K/s	Bk 2, pg 34				
	TPD	20140909r	Heating Rate: 4K/s	Bk 2, pg 34				
	TPD	20140909s	Heating Rate: 2K/s	Bk 2, pg 34				

Table 6. NaAu₂ experiments ISU continued

Sample	Chamber	Date	Spectrum/ Image	Instru.	Filename	Details	Book #, Page #	Notes
D	TPD	11/24/2014		TPD	20141124_NaAu2_1L_CO	Heating Rate: 5K/s; after 1L CO exposure	Bk 2, pg 59	
				TPD	20141124_NaAu2_20L_CO	Heating Rate: 5K/s; after 20L CO exposure	Bk 2, pg 59	
				TPD	20141124_NaAu2_100L_CO	Heating Rate: 5K/s; after 100L CO exposure	Bk 2, pg 59	
D	TPD	11/25/2014			-	3 min sputter, 15 min anneal 475K	Bk 2, pg 59	
				TPD	20141125_NaAu2_10sec_O2	Heating Rate: 5K/s; after dosing 10 sec with O ₂	Bk 2, pg 60	
				TPD	20141125_NaAu2_50sec_O2	Heating Rate: 5K/s; after dosing 50 sec with O ₂	Bk 2, pg 60	
				TPD	20141125_NaAu2_100sec_O2	Heating Rate: 5K/s; after dosing 100 sec with O ₂	Bk 2, pg 60	
	TPD	20141125_NaAu2_200sec_O2	Heating Rate: 5K/s; after dosing 200 sec with O ₂	Bk 2, pg 60				
D	TPD	12/3/2014		TPD	20141203_NaAu2_O2&CO	Heating Rate: 6K/s; after dosing 100 sec with O ₂ followed by 100L CO	Bk 1, pg 167	M. Wallingford Lab Notebook
					-	3 min sputter, 15 min anneal 475K	Bk 1, pg 167	M. Wallingford Lab Notebook
				TPD	20141203_NaAu2_O2_20 min	Heating Rate: 6K/s; after dosing 20 min with O ₂	Bk 1, pg 167	M. Wallingford Lab Notebook
D	TPD	12/5/2014		TPD	-	3 min sputter, 15 min anneal 475K	Bk 1, pg 168	M. Wallingford Lab Notebook
				TPD	20141205_NaAu2_O2_20 min_100L_CO	Heating Rate: 6K/s; after dosing 20 min with O ₂ followed by 100L CO	Bk 1, pg 168	M. Wallingford Lab Notebook
				TPD	-	3 min sputter, 15 min anneal 475K	Bk 1, pg 168	M. Wallingford Lab Notebook
				TPD	20141205_NaAu2_O2_20 min	Heating Rate: 6K/s; after dosing 20 min with O ₂	Bk 1, pg 168	M. Wallingford Lab Notebook

Table 6. NaAu₂ experiments ISU continued

Sample	Chamber	Date	Spectrum/ Image	Instru.	Filename	Details	Book #, Page #	Notes
D	TPD	12/5/2014		TPD	20141205_NaAu2b	Heating Rate: 6K/s; 3 min sputter, 20 min anneal 420K	Bk 1, pg 168	M. Wallingford Lab Notebook
D	TPD	12/9/2014		TPD	-	3 min sputter, 20 min anneal 420K	Bk 1, pg 169	M. Wallingford Lab Notebook
				TPD	20141209_NaAu2_20min O2_COduring	Heating Rate: 6K/s; after dosing 20 min with O ₂ followed by CO	Bk 1, pg 169	Backfilled to 1x10 ⁻⁹ Torr CO during TPD run; M. Wallingford Lab Notebook
				TPD	-	3 min sputter, 20 min anneal 420K	Bk 1, pg 169	M. Wallingford Lab Notebook
				TPD	20141209_NaAu2_20min O2&100LCO	Heating Rate: 6K/s; after dosing 20 min with O ₂ followed by 100L CO	Bk 1, pg 169	M. Wallingford Lab Notebook
D	TPD	12/10/2014		TPD	-	3 min sputter, 20 min anneal 420K	Bk 1, pg 170	M. Wallingford Lab Notebook
				TPD	20141210_NaAu2_20min O2	Heating Rate: 6K/s; after dosing 20 min with O ₂	Bk 1, pg 170	Issue with TPD program; M. Wallingford Lab Notebook
D	TPD	12/11/2014		TPD	20141211_NaAu2_clean_1	Heating Rate: 6K/s; 3 min sputter, 20 min anneal 420K	Bk 1, pg 170	M. Wallingford Lab Notebook
				TPD	20141211_NaAu2_20min O2_1	Heating Rate: 6K/s; after dosing 20 min with O ₂	Bk 1, pg 170	M. Wallingford Lab Notebook
				TPD	-	3 min sputter, 20 min anneal 420K	Bk 1, pg 170	M. Wallingford Lab Notebook
				TPD	20141211_NaAu2_20min O2_2	Heating Rate: 6K/s; after dosing 20 min with O ₂	Bk 1, pg 170	M. Wallingford Lab Notebook
				TPD	-	3 min sputter, 20 min anneal 420K	Bk 1, pg 170	M. Wallingford Lab Notebook
				TPD	20141211_NaAu2_20min O2_3	Heating Rate: 6K/s; after dosing 20 min with O ₂	Bk 1, pg 171	M. Wallingford Lab Notebook

Table 6. NaAu₂ experiments ISU continued

Sample	Chamber	Date	Spectrum/ Image	Instru.	Filename	Details	Book #, Page #	Notes
D	TPD	12/11/2014		TPD	-	3 min sputter, 20 min anneal 420K	Bk 1, pg 171	M. Wallingford Lab Notebook
				TPD	20141211_NaAu2_20min O2&CO_1	Heating Rate: 6K/s; after dosing 20 min with O ₂ followed by 100L CO	Bk 1, pg 171	M. Wallingford Lab Notebook
D	TPD	12/15/2014		TPD	20141215_NaAu2_clean_1	Heating Rate: 6K/s; 3 min sputter, 20 min anneal 420K	Bk 1, pg 171	begin Na depletion; M. Wallingford Lab Notebook
				TPD	20141215_NaAu2_100LC O_1	Heating Rate: 6K/s; after 100L CO exposure	Bk 1, pg 171	M. Wallingford Lab Notebook
				TPD	-	3 min sputter, 20 min anneal 420K	Bk 1, pg 171	M. Wallingford Lab Notebook
				TPD	20141215_NaAu2_100LC O_2	Heating Rate: 6K/s; after 100L CO exposure	Bk 1, pg 171	M. Wallingford Lab Notebook
				TPD	-	3 min sputter, 20 min anneal 420K	Bk 1, pg 171	M. Wallingford Lab Notebook
				TPD	20141215_NaAu2_100LC O_3	Heating Rate: 6K/s; after 100L CO exposure	Bk 1, pg 171	M. Wallingford Lab Notebook
D	TPD	12/16/2014		TPD	-	3 min sputter, 20 min anneal 420K	Bk 1, pg 171	M. Wallingford Lab Notebook
				TPD	20141216_NaAu2_20min sO2&100LCO_1	Heating Rate: 6K/s; after dosing 20 min with O ₂ followed by 100L CO	Bk 1, pg 171	M. Wallingford Lab Notebook
				TPD	-	3 min sputter, 20 min anneal 420K	Bk 1, pg 171	M. Wallingford Lab Notebook
				TPD	20141216_NaAu2_20min sO2&100LCO_2	Heating Rate: 6K/s; after dosing 20 min with O ₂ followed by 100L CO	Bk 1, pg 172	M. Wallingford Lab Notebook
				TPD	20141216_NaAu2_clean_1	Heating Rate: 6.5K/s; 3 min sputter, 20 min anneal 420K	Bk 1, pg 172	M. Wallingford Lab Notebook

Table 6. NaAu₂ experiments ISU continued

Sample	Chamber	Date	Spectrum/ Image	Instru.	Filename	Details	Book #, Page #	Notes
D	TPD	12/24/2014		TPD	-	3 min sputter, 20 min anneal 420K	Bk 1, pg 172	M. Wallingford Lab Notebook
				TPD	20141224_NaAu2_20min O2_100LCO_1	Heating Rate: 6K/s; after dosing 20 min with O ₂ followed by 100L CO	Bk 1, pg 172	M. Wallingford Lab Notebook
				TPD	20141224_NaAu2_clean_1	Heating Rate: 7K/s; 3 min sputter, 20 min anneal 420K	Bk 1, pg 172	M. Wallingford Lab Notebook
D	TPD	12/30/2014		TPD	20141230_NaAu2_clean_1		Bk 1, pg 173	Issues with mass spec., turned off/on; M. Wallingford Lab Notebook
				TPD	20141230_NaAu2_clean_2	Heating Rate: 6K/s; 3 min sputter, 20 min anneal 420K	Bk 1, pg 173	M. Wallingford Lab Notebook
				TPD	20141230_NaAu2_20min sO2_100LCO_1	Heating Rate: 6K/s; after dosing 20 min with O ₂ followed by 100L CO	Bk 1, pg 173	M. Wallingford Lab Notebook
				TPD	-	3 min sputter, 20 min anneal 420K	Bk 1, pg 173	M. Wallingford Lab Notebook
				TPD	20141230_NaAu2_20min sO2_100LCO_2	Heating Rate: 6K/s; after dosing 20 min with O ₂ followed by 100L CO	Bk 1, pg 173	M. Wallingford Lab Notebook
				TPD	20141230_NaAu2_clean_3	Heating Rate: ?K/s; 3 min sputter, 20 min anneal 420K	Bk 1, pg 174	M. Wallingford Lab Notebook
D	TPD	12/31/2014		TPD	-	3 min sputter, 20 min anneal 420K	Bk 1, pg 174	M. Wallingford Lab Notebook
				TPD	20141321_NaAu2_clean_6K_1	Heating Rate: 6K/s	Bk 1, pg 174	M. Wallingford Lab Notebook
				TPD	20141321_NaAu2_clean_6K_2	Heating Rate: 6K/s	Bk 1, pg 174	M. Wallingford Lab Notebook
				TPD	20141321_NaAu2_clean_6K_3	Heating Rate: 6K/s	Bk 1, pg 174	M. Wallingford Lab Notebook

Table 6. NaAu₂ experiments ISU continued

Sample	Chamber	Date	Spectrum/ Image	Instru.	Filename	Details	Book #, Page #	Notes
D	TPD	12/31/2014		TPD	20141321_NaAu2_clean_2K_1	Heating Rate: 2K/s	Bk 1, pg 174	M. Wallingford Lab Notebook
				TPD	20141321_NaAu2_clean_2K_2	Heating Rate: 2K/s	Bk 1, pg 174	M. Wallingford Lab Notebook
				TPD	20141321_NaAu2_clean_4K_1	Heating Rate: 4K/s	Bk 1, pg 174	M. Wallingford Lab Notebook
				TPD	20141321_NaAu2_clean_4K_2	Heating Rate: 4K/s	Bk 1, pg 174	M. Wallingford Lab Notebook
				TPD	20141231_NaAu2_20min O2_CO_1	after dosing 20 min with O ₂ , heat to 350K, hold, expose CO	Bk 1, pg 174	Pressures of CO: 1x10 ⁻⁹ Torr and 1x10 ⁻⁸ Torr; M. Wallingford Lab Notebook

Table 7. Mantis evaporator calibration, Cu pocket, conducted at Iowa State University (DOE Chamber – 224 SPH)

Sample	Date	Spectrum/ Image	Instr.	Filename	Details	Book #, Page #	Notes
Cu Foil	6/14/2013	overview, C1s, O1s	XPS	20130614_Cu Foil_1Spu-1Ann	21 min sputter, 30 min anneal 810K	Bk 1, pg 20	Mg Source
		M1 - M16	STM	20130614_Cu Foil_Clean	Scan of surface for terraces	Bk 1, pg 20	
Cu Foil	6/15/2013	M1 - M16	STM	20130615_Cleaned more	Scan of surface for terraces	Bk 1, pg 21	
		M1 - M3	STM	20130615_5 sec Cu dep	23.5W for 5 sec	Bk 1, pg 21	no islands seen
		M1 - M4	STM	20130615_10 sec addtl Cu dep	23.5W for 15 sec	Bk 1, pg 22	no islands seen
		overview, C1s, O1s, Cu2p	XPS	20130615_Cu Foil_5Spu-5Ann	four addtl 9 min sputter, 30 min anneal 810K cycles	Bk 1, pg 22	Mg Source
Cu Foil	6/16/2013	M1 - M10	STM	20130616_Cu Clean	Scan of surface to look for terraces and clean surface	Bk 1, pg 22	
		M1 - M10	STM	20130616_Cleaned more	Scan of surface to look for terraces and clean surface	Bk 1, pg 23	
Cu Foil	6/17/2013	M1 - M16	STM	20130617_Cleaned	Scan of surface to look for terraces and clean surface	Bk 1, pg 23	
Cu Foil	6/18/2013	M1 - M20	STM	20130618_Cleaned 870K	Scan of surface to look for terraces and clean surface	Bk 1, pg 24	
		M1 - M5	STM	20130618_after 5 min Cu dep	23.5W for 5 min	Bk 1, pg 24-25	
Cu Foil	6/19/2013	M1 - M8	STM	20130619_more 870K cleaning	Scan of surface to look for terraces and clean surface	Bk 1, pg 25	
		M1 - M10	STM	20130619_after 10 min Cu dep	23.5W for 10 min	Bk 1, pg 26	Islands!!
		overview, C1s, O1s, Cu2p	XPS	20130619_Cu Foil clean check	surface cleanliness check	Bk 1, pg 26	Mg Source
Cu Foil	6/20/2013		STM	20130620_parameter test	Test for new V and nA parameters	Bk 1, pg 27	
Cu Foil	6/22/2013	M1 - M4	STM	20130622_new tip	Testing new tip for imaging quality	Bk 1, pg 28	

Table 7. Mantis evaporator calibration continued

Sample	Date	Spectrum/ Image	Instr.	Filename	Details	Book #, Page #	Notes
Cu Foil	6/23/2013	M1 - M7	STM	20130622_clean surface	Scan of surface to look for terraces and clean surface	Bk 1, pg 29	
		M1 - M30	STM	20130622_after 1 min Cu dep	23.5W for 1 min	Bk 1, pg 29	Cu on Cu Foil calibration
		M1 - M27	STM	20130622_addtl 1 min_2 min total Cu dep	addt'l 23.5W for 1 min	Bk 1, pg 29-30	Cu on Cu Foil calibration
		M1 - M19	STM	20130622_addtl 2 min_4 min total Cu dep	addt'l 23.5W for 2 min	Bk 1, pg 30	Cu on Cu Foil calibration
Cu Foil	6/25/2013	M1 - M5	STM	20130625_clean	Scan of surface to look for terraces	Bk 1, pg 31	
		M1 - M25	STM	20130625_after 15 min Cu dep	23.5W for 15 min	Bk 1, pg 32	Cu on Cu Foil calibration
Cu Foil	6/27/2013	M1 - M4	STM	20130627_clean test	Scan of surface to look for terraces and clean surface	Bk 1, pg 33	
		M1 - M6	STM	20130627_clean surface	Scan of surface to look for terraces and clean surface	Bk 1, pg 33	
Cu Foil	6/29/2013	M1 - M6	STM	20130629_clean surface	Scan of surface to look for terraces and clean surface	Bk 1, pg 35	
		M1 - M53	STM	20130629_after 10 min Cu dep	23.5W Cu for 10 min; 7.5L O ₂	Bk 1, pg 35	Cu on Cu Foil calibration; M17 - M53 with O ₂
Cu Foil	7/2/2013	M1 - M11	STM	20130702_clean surface	Scan of surface to look for terraces and clean surface	Bk 1, pg 37	
		M1 - M4	STM	20130702_Cu control	23.5W for 10 min	Bk 1, pg 37	experiment failed bad tunneling
Cu Foil	7/3/2013	M1 - M5	STM	20130703_clean surface	Scan of surface to look for terraces and clean surface	Bk 1, pg 38	
		M1 - M8	STM	20130703_O2 Cu Control	23.5W for 10 min	Bk 1, pg 38	experiment failed bad tunneling

ACKNOWLEDGEMENTS

I would like to begin by expressing my sincere gratitude to Professor Patricia A. Thiel for welcoming me into her research group. As a wonderful mentor she has given me much guidance, advice, encouragement and support throughout my graduate studies. Because of this I feel confident in my future professional opportunities.

I would like to thank the members of the Thiel group, former and current, for their advice, help and encouragement. Thank you for the positive and fun working environment.

I would like to thank the nanotech@surfaces group in Dübendorf, Switzerland, especially Oliver Gröning and Roland Widmer, for allowing me to visit and to conduct research as well as welcoming me into the group. Thank you to Okan Deniz for training me on the ESCA chamber and always being available to help and to answer any questions.

I would like to thank Jim Anderegg for many fruitful discussions and guidance about XPS and Auger. Thank you to Deborah “Devo” Schlagel for providing our NaAu₂ samples as well as performing countless sample re-polishings, taking XRD spectra and answering questions.

I would like to thank Jim Evans, Huaping Lei and Linlin Wang for their assistance with theoretical calculations for both of my projects. Their contributions provide a more complete picture on what is occurring in each of the projects.

I would like to thank my friends, especially April Larson and Kelly Rach, for providing support, encouragement, and numerous visits to get me out of the lab throughout my time at Iowa State.

Finally, I would like to thank my family for their unconditional love and support throughout my graduate studies. Thank you for always encouraging me and boosting my confidence when I needed it.

Parts of this work were performed at the Ames Laboratory under contract number DE-AC02-07CH11358 with the U.S. Department of Energy. The document number assigned to this thesis/dissertation is IS-T 3154.